

# UNIVERSITA' DEGLI STUDI DI PARMA



## Dottorato di ricerca in Scienza e Tecnologia dei Materiali Innovativi

Ciclo XXIV

# Functionalization of zinc oxide nanostructures

Coordinatore:  
Chiar.mo Prof. Enrico Dalcanale

Supervisor:  
Dott. Andrea Zappettini

Dottorando: Marco Villani



**Where is the wisdom that we have lost in knowledge?  
Where is the knowledge we have lost in information?**

**Thomas Stearns Elliot**

**The best way to get a good idea is to get a lot of ideas**

**Linus Pauling**



# Table of contents

---

List of abbreviations .....	IV
List of figures .....	VII
List of tables .....	XI
<b>Chapter 1: Introduction .....</b>	<b>1</b>
<b>Chapter 2: Materials properties and applications .....</b>	<b>8</b>
2.1 Zinc oxide nanostructures .....	8
2.1.1 Structural properties .....	9
2.1.2 Optical properties .....	14
2.1.3 Applications .....	16
2.2 Synthesis of semiconductor nanoparticles.....	25
2.2.1 Nucleation, growth and dimensional control .....	27
2.2.1a Homogeneous nucleation .....	27
2.2.1b Heterogeneous nucleation.....	28
2.2.1c Growth .....	29
2.2.1d Dimensional control .....	30
2.2.2 Cadmium sulphide .....	33
2.2.2a Hot injection method .....	34
2.2.2b Chemical batch deposition.....	36
2.2.2c Remarks.....	38
2.2.3 Iron Oxides .....	41
2.2.3a Synthesis of Fe <sub>3</sub> O <sub>4</sub> NP .....	46
2.2.3b Hydrolysis in Aqueous Solutions .....	47
2.2.3c Synthesis in organic solvents .....	49

2.3 Organic Molecules .....	61
2.3.1 Porphyrins .....	61
2.3.2 Phthalocyanines .....	63
2.3.3 Applications .....	65
<b>Chapter 3: Experimental .....</b>	<b>72</b>
3.1 Synthetic procedures .....	72
3.1.1 Growth of ZnO nanostructures .....	72
3.1.1a ZnO tetrapods .....	73
3.1.1b ZnO nanorods .....	75
3.1.2 Solution growth of nanoparticles .....	77
3.1.3 Supersonic Molecular Beam Deposition .....	77
3.2 Characterization techniques .....	80
3.2.1 Optical Properties .....	80
3.2.1a Absorbance .....	80
3.2.1b Photoluminescence .....	83
3.2.2 Structural Characterizations .....	86
3.2.2a XRD .....	86
3.2.2b TEM .....	88
3.2.3 Magnetic Characterization .....	89
3.2.3a AGFM .....	92
3.2.3b VSM .....	93
3.2.4 Functional Characterizations .....	93
3.2.4a Gas sensing .....	93
3.2.4b Photocatalytic activity .....	97
<b>Chapter 4: Results - functionalized materials .....</b>	<b>104</b>
4.1 Cadmium Sulphide .....	104
4.1.1 Synthesis of CdS nanoparticles .....	105
4.1.2 CdS functionalization of ZnO tetrapods .....	111

4.1.2a	Synthesis and structural characterization .....	111
4.1.2b	Photoluminescence .....	114
4.1.2c	Photocurrent .....	118
4.1.2d	Photocatalytic activity .....	119
4.1.2e	Gas sensing .....	121
4.1.2f	Final remarks .....	122
4.1.3	CdS functionalization of ZnO nanorods .....	123
4.2	Iron oxides .....	129
4.2.1	Synthesis of Fe <sub>3</sub> O <sub>4</sub> nanoparticles .....	130
4.2.1a	Synthesis by co-precipitation .....	130
4.2.1b	Synthesis in organic solvents .....	138
4.2.2	Fe <sub>3</sub> O <sub>4</sub> functionalization of ZnO tetrapods .....	146
4.3	Organics on ZnO nanorods.....	159
4.3.1	TiOPc functionalization of ZnO nanorods .....	159
4.3.2	Dual functionalization of ZnO nanorods .....	168
4.3.3	TPP functionalization of ZnO nanorods .....	175
4.3.4	Preliminary study on hole conducting material .....	177
4.3.5	Final remarks .....	181
<b>Chapter 5:</b>	<b>Conclusions .....</b>	<b>187</b>
	Cadmium sulphide .....	187
	Iron Oxides .....	189
	Organics .....	191
<b>List of publications</b>	<b>.....</b>	<b>194</b>
<b>Aknowledgement</b>	<b>.....</b>	<b>195</b>

# List of abbreviations

---

$A^0$	neutral acceptor
$a_B$	Bohr radius
AGFM	alternate gradient field magnetometer
AZO	aluminum-doped zinc oxide
BXC	bound exciton complex (exciton bound to donor / acceptor)
CB	conduction band
CBD	chemical bath deposition
$D^0/D^+$	neutral / ionized donor
DBSA	dodecyl benzoic sulfonic acid
DEG	diethylenglycole
DLE	deep levels emission
DMF	N,N-dimethylformamide
DSSC	dye sensitized solar cell
ED	electron diffraction
EDX	energy dispersive x-ray spectrometry
$E_s$	surface energy
ETA	extremely thin absorber (solar cell)
$E_v$	volume energy
$E_x$	exciton energy
$E_{xb}$	exciton binding energy
fcc	face centered cubic
FM	ferromagnetism
FX	free exciton
GL	green luminescence, referred to the wide ZnO emission peaked around 500 nm
hcp	hexagonal closed packing



HREM	high resolution TEM
HSC	hybrid solar cell
IPA	isopropyl alcohol
$K_{SP}$	solubility product equilibrium constant
MEK	methylethylketone
MOX	metal oxides
MPc	metal phthalocyanines
MRI	magnetic resonance imaging
NBE	near band edge
NP	nanoparticles
NR	nanorods
OA	oleylamine
ODE	octadecene
$O_i$	oxygen interstitial
OSC	organic solar cells
PDT	photo-dynamic therapy
PEC	photo electrochemical cells
PEDOT	poly 3,4-ethylenedioxythiophene
PEG	polyethylene glycol
PEO	polyethylene oxide
PL	photoluminescence
PMAO	Poly(maleic anhydride- <i>alt</i> -1-octadecene)
PSS	polystyrenesulfonate
PV	photovoltaic
PVA	polyvinyl alcohol
PVP	polyvinylpyrrolidone
$r^*$	critical radius (nucleation)
$R_y^*$	Rydberg energy

SEM	scanning electron microscopy
SPM	superparamagnetism
SuMBD	supersonic molecular beam deposition
TBPA	tertbutylphosphonic acid
TCO	transparent conducting oxide
TEM	transmission electron microscopy
TiOPc	titanyl phthalocyanine
TOPO	trioctylphosphine oxide
TP	tetrapods
TPP	5,10,15,20-Tetrakis(pentafluorophenyl)-porphyrin
VB	valence band
VdW	Van der Waals
V <sub>O</sub>	oxygen vacancy
VSM	vibrating sample magnetometer
V <sub>Zn</sub>	zinc vacancy
WZ	wurtzite
XRD	x-ray diffraction
XSC	excitonic solar cell
Zn <sub>i</sub>	zinc interstitial
ZB	zinc blende

# List of figures

---

<b>Figure 1.1</b>	Number of publication containing “ZnO nano*” in the title .....	2
<b>Figure 2.1</b>	Different morphologies of ZnO nanostructures .....	9
<b>Figure 2.2</b>	The hexagonal WZ structure of ZnO pointing out Zn tetrahedral coordination .....	10
<b>Figure 2.3</b>	The rock salt and zinc blend phases of ZnO .....	11
<b>Figure 2.4</b>	Energy levels of native defects in ZnO .....	12
<b>Figure 2.5</b>	Calculated defect formation energies for main native point defects in ZnO .....	13
<b>Figure 2.6</b>	Typical room temperature PL spectrum of ZnO .....	14
<b>Figure 2.7</b>	Low temperature PL spectrum of bulk ZnO .....	15
<b>Figure 2.8</b>	ZnO TP “film” and single ZnO TP contacted on oxidized Si substrate .....	17
<b>Figure 2.9</b>	Different elements in a ZnO NR based XSC and band gap alignment .....	18
<b>Figure 2.10</b>	Balance between surface and volume energy as a function of particle dimension .....	28
<b>Figure 2.11</b>	La Mer diagram .....	31
<b>Figure 2.12</b>	Experimental set-up and reaction scheme for the hot-injection method .....	35
<b>Figure 2.13</b>	Highly monodispersed CdS NP assembled in a hexagonal superlattice .....	35
<b>Figure 2.14</b>	Crystal structure of hematite .....	43
<b>Figure 2.15</b>	Crystal structure of magnetite .....	44
<b>Figure 2.16</b>	Crystal structure of cubic maghemite .....	45
<b>Figure 2.17</b>	Dimensional dispersion in magnetite NP obtained through water based synthesis .....	48
<b>Figure 2.18</b>	High temperature synthesis of magnetite nanocrystals in coordinating solvents .....	51
<b>Figure 2.19</b>	Magnetite NP with good dimensional control over a wide range of dimensions .....	51
<b>Figure 2.20</b>	Structure of water dispersible iron oxide nanocrystals .....	52
<b>Figure 2.21</b>	TEM image of maghemite NP and hexagonal close-packed NP superlattice .....	53
<b>Figure 2.22</b>	STEM and HREM image of 11 nm maghemite NP .....	54
<b>Figure 2.23</b>	TEM images of iron oxide nanoparticles .....	54
<b>Figure 2.24</b>	Free-base porphyrin macrocycle .....	62
<b>Figure 2.25</b>	Typical absorbance spectrum and HOMO-LUMO symmetry of porphyrin molecule .....	63
<b>Figure 2.26</b>	Optical absorption spectra of TiOPc and CuPc thin films .....	64
<b>Figure 2.27</b>	XSC hybrid cell based on inorganic NR and organic polymer .....	67
<b>Figure 3.1</b>	Different ZnO morphologies grown by our group at IMEM institute .....	73
<b>Figure 3.2</b>	Simplified sketch of the synthesis reactor .....	74
<b>Figure 3.3</b>	SEM images of different TP growths reflecting different dimensions .....	74
<b>Figure 3.4</b>	Scheme of the main reaction steps to grow ZnO nanorods .....	75
<b>Figure 3.5</b>	SEM images of the starting ZnO seeding film and oriented ZnO NR .....	76
<b>Figure 3.6</b>	The wet-chemistry synthetic apparatus .....	77

<b>Figure 3.7</b>	SuMBD experimental apparatus .....	78
<b>Figure 3.8</b>	Sketch of the SuMBD source .....	78
<b>Figure 3.9</b>	AFM micrographs of TiOPc thin films deposited on SiO <sub>2</sub> by SuMBD .....	79
<b>Figure 3.10</b>	Valence and conduction bands of ZnO in the vicinity of the fundamental bandgap .....	81
<b>Figure 3.11</b>	Indirect band gap semiconductor .....	81
<b>Figure 3.12</b>	Absorption spectra of CdS nanoparticles with different dimensions .....	82
<b>Figure 3.13</b>	Schematic drawing of the excitonic states .....	84
<b>Figure 3.14</b>	ZnO PL spectra at low temperature (10K) and different BXC recombinations . .....	85
<b>Figure 3.15</b>	Schematic representation of the PL setup .....	85
<b>Figure 3.16</b>	The Bragg-Brentano $\theta$ - $\theta$ geometry .....	88
<b>Figure 3.17</b>	Powder XRD pattern of ZnO TP with a typical wurtzite structure .....	88
<b>Figure 3.18</b>	HREM image of ZnO TP nanostructure .....	89
<b>Figure 3.19</b>	Magnetization curves of (A) ferromagnetic and (B) superparamagnetic material .....	91
<b>Figure 3.20</b>	Schematic view of a AGF magnetometer .....	92
<b>Figure 3.21</b>	Schematic drawing of the working principle of a chemoresistive gas sensor .....	94
<b>Figure 3.22</b>	Simplified sketch of the gas sensor device and the actual device .....	95
<b>Figure 3.23</b>	Schematic representation of the gas sensing measuring equipment .....	95
<b>Figure 3.24</b>	A generic conductance vs. time curve of a gas sensor .....	96
<b>Figure 3.25</b>	Definition of sensitivity of a sensor .....	96
<b>Figure 3.26</b>	Schematic view of the photocatalytic process .....	97
<b>Figure 3.27</b>	Band alignment of common semiconductors and standard redox potentials .....	98
<b>Figure 3.28</b>	Absorbance spectra of reference MB and photo-degraded MB .....	100
<b>Figure 4.1.1</b>	SEM image of highly polydispersed CdS NP (sample CdS1) .....	105
<b>Figure 4.1.2</b>	XRD analysis on the sample CdS1 .....	107
<b>Figure 4.1.3</b>	CdS nanoparticles aggregates (sample CdS2) .....	108
<b>Figure 4.1.4</b>	XRD analysis on the sample CdS2 .....	108
<b>Figure 4.1.5</b>	Small grains CdS NP (sample CdS3) .....	109
<b>Figure 4.1.6</b>	XRD spectrum of small CdS NP (sample CdS3) .....	109
<b>Figure 4.1.7</b>	TEM analysis of sample CdS3 .....	110
<b>Figure 4.1.8</b>	SEM and EDX analysis of as synthesized sample CdS@ZnO .....	111
<b>Figure 4.1.9</b>	TEM analysis of the sample CdS@ZnO .....	112
<b>Figure 4.1.10</b>	HREM image, FT and intensity map of CdS crystallites on a TP arm tip .....	113
<b>Figure 4.1.11</b>	XRD analysis on the CdS@ZnO TP core-shell structure .....	114
<b>Figure 4.1.12</b>	PL spectra of (A) CdS NP and (B) coupled compound CdS@ZnO TP .....	115
<b>Figure 4.1.13</b>	Schematic sketch of a type-II heterojunction between CdS and ZnO .....	116
<b>Figure 4.1.14</b>	TEM analysis on a sample CdS@ZnO-2 grown with excess of precursors .....	117
<b>Figure 4.1.15</b>	Comparison between different CdS “layers”: core-shell and spot-like .....	117
<b>Figure 4.1.16</b>	Photocurrent spectrum of CdS@ZnO TP core-shell compared to bare ZnO TP .....	118
<b>Figure 4.1.17</b>	Absorbance spectra of samples after 1 hour illumination at 442nm .....	120

<b>Figure 4.1.18</b>	Dynamic response of <u>CdS@ZnO-2</u> gas-sensor .....	122
<b>Figure 4.1.19</b>	SEM view of as grown NR and CdS functionalized NR .....	125
<b>Figure 4.1.20</b>	TEM analysis of CdS functionalized NR .....	126
<b>Figure 4.2.1</b>	XRD spectrum of Fe <sub>3</sub> O <sub>4</sub> NP (sample NPH) .....	133
<b>Figure 4.2.2</b>	Absorption spectrum of magnetite and maghemite NP and picture of samples .....	134
<b>Figure 4.2.3</b>	XRD spectrum of magnetite NP obtained with the co-precipitation method .....	136
<b>Figure 4.2.4</b>	M(H) VSM measurement for samples synthesized via co-precipitation method .....	137
<b>Figure 4.2.5</b>	XRD pattern of NP4 synthesized though the hot injection method .....	139
<b>Figure 4.2.6</b>	TEM analysis on the sample NP4.....	140
<b>Figure 4.2.7</b>	VSM measurement on the sample NP4 .....	141
<b>Figure 4.2.8</b>	XRD pattern of sample NP5, prepared via heating-up method .....	142
<b>Figure 4.2.9</b>	STEM analysis on the sample obtained by heating-up method (NP5) .....	143
<b>Figure 4.2.10</b>	STEM image magnetite NP and the statistic on NP dimensions .....	143
<b>Figure 4.2.11</b>	ED of magnetite NP and angular integration (NP5) .....	144
<b>Figure 4.2.12</b>	Hysteresis loop of NP5 showing a SPM behavior .....	145
<b>Figure 4.2.13</b>	Resuming M(H) graph for all different NP synthesized .....	146
<b>Figure 4.2.14</b>	XRD samples of coupled nanostructures magnetite NP on ZnO TP .....	148
<b>Figure 4.2.15</b>	XRD spectrum of as-grown NP and annealed NP– ZnO TP coupled material .....	149
<b>Figure 4.2.16</b>	FE-SEM analysis of coupled compound magnetite ZnO TP .....	149
<b>Figure 4.2.17</b>	TEM analysis on sample TPM1 .....	150
<b>Figure 4.2.18</b>	Hysteresis loop for the sample TPM1 showing a ferromagnetic behavior .....	151
<b>Figure 4.2.19</b>	TEM analyses on the Fe <sub>3</sub> O <sub>4</sub> functionalized ZnO TP (sample TPM5).....	152
<b>Figure 4.2.20</b>	Magnetization curve of the sample TPM5.....	153
<b>Figure 4.2.21</b>	PL spectra of bare and functionalized ZnO TP at RT and 20K .....	154
<b>Figure 4.3.1</b>	XRD spectrum of c-axis oriented (A) AZO film, (B) ZnO NR grown on AZO .....	161
<b>Figure 4.3.2</b>	SEM view of the different ZnO layer constituting the photoanode .....	162
<b>Figure 4.3.3</b>	Scheme of SuMBD deposition on two different samples of ZnO nanorods .....	163
<b>Figure 4.3.4</b>	Picture and sketch of ZnO NR sensitized with SuMBD deposited TiOPc .....	164
<b>Figure 4.3.5</b>	SEM image of as-grown ZnO NR and TiOPc deposition (90°) on ZnO NR .....	164
<b>Figure 4.3.6</b>	STEM-HAADF image of a TiOPc-sensitized ZnO NR .....	165
<b>Figure 4.3.7</b>	Zero-loss TEM and HREM images of TiOPc sensitized ZnO NR .....	165
<b>Figure 4.3.8</b>	EDX analysis of TiOPc sensitized ZnO NR .....	166
<b>Figure 4.3.9</b>	Absorption and emission spectra of TiOPc .....	167
<b>Figure 4.3.10</b>	Simplified sketch of a double functionalized photoanode .....	169
<b>Figure 4.3.11</b>	Absorption spectrum of SuMBD–grown TiOPc and H <sub>2</sub> TTP(F) thin films .....	169
<b>Figure 4.3.12</b>	Absorption and emission spectra of 50 nm TTP film deposit by SuMBD .....	171
<b>Figure 4.3.13</b>	STEM images on TiOPc + TPP dual sensitized ZnO NR .....	172
<b>Figure 4.3.14</b>	EDX mapping and STEM image of irregular TTP layers around ZnO NR .....	172

<b>Figure 4.3.15</b>	PL spectra of dual-sensitized photoanode .....	173
<b>Figure 4.3.16</b>	STEM (left) and TEM (middle, right) images on H <sub>2</sub> TPP(F) sensitized ZnO NR .....	175
<b>Figure 4.3.17</b>	PL spectra of porphyrin-sensitized photoanode measured in different zones .....	176
<b>Figure 4.3.18</b>	ZnO NR based hybrid solar cell and band gap alignment .....	177
<b>Figure 4.3.19</b>	Chemical structure of PEDOT:PSS and sketch of the ZnO NR-PEDOT hybrid cell .....	178
<b>Figure 4.3.20</b>	SEM image and AFM measurement of PEDOT-sensitized ZnO NR .....	179
<b>Figure 4.3.21</b>	I/V dark measurement to verify the ohmicity of gold tip moving contacts .....	180
<b>Figure 4.3.22</b>	I/V characteristic in dark and under illumination of the hybrid junction .....	180

# List of tables

---

<b>Table 2.1</b>	Free and bound exciton recombinations and related properties. ....	16
<b>Table 2.2</b>	Crystallographic data for iron oxide phases.....	41
<b>Table 4.1.1</b>	List of tested solvents for the dispersion of ZnO nanostructures .....	105
<b>Table 4.2.1</b>	XRD reflections for maghemite and magnetite .....	132
<b>Table 4.2.2</b>	Summary of magnetite NP produced via co-precipitation method .....	135
<b>Table 4.2.3</b>	Summary of coupled compounds magnetite NP – ZnO TP .....	147

# 1 Introduction

---

Nanotechnology, which sets out to explore and manipulate reality at the molecular level, is widely recognized as a key technology that will drive economic growth and standards of living in the twenty-first century. What we are currently seeing is the beginning of a revolution, caused by our ability to work on the same scale as nature [1]. This is the result of almost five decades in which miniaturization has been a commitment for scientists and the research in nanotechnology has been largely funded by governments and private corporations. According to a study by Global Industry Analysts Inc. [2], the global market for products incorporating nanotechnology is projected to grow at a compound annual growth rate of 11.1% between 2010 and 2015 and will reach the impressive sum of US\$2.4 trillion, that is roughly 1/25 of the current world gross domestic product [3].

Since the discovery of carbon nanotubes in 1991 [4], significant progress has already been made in the field of zero- (0D), one- (1D) and two-dimensional (2D) nanomaterials and nanostructures. Studies on new physical properties and applications of nanomaterials and nanostructures are possible only when nanostructured materials are made available with desired size, morphology, crystal microstructure and chemical composition [5]. The fabrication of materials at the nanoscale can be used to enhance and exploit properties that become stronger under conditions of reduced dimensionality; in fact size reduction can lead to a whole range of new physico-chemical properties and a wealth of potential applications.

Nanotechnology allows the miniaturization of current and new instruments, sensors and machines that will greatly impact the world we live in. Possible examples include: computers with amazing power that compute algorithms to mimic human brain, biosensors that warn us at the early stage of a disease, target-specific drugs that automatically attack the diseased cells *on site*, nano-robots that can repair internal damage and remove chemical toxins in human bodies, nano-scaled electronics that constantly monitor our local environment [5].

In general, there are two theoretically distinct approaches to the creation of nanostructures and related devices, which are commonly known as *top-down* and *bottom-up*. In the top-down approach, small features are patterned in bulk materials by a combination of lithography, etching and deposition, to form functional devices. The top-down approach has been unexpectedly successful in many venues, with microelectronics being perhaps the best example today. While the technique developments continue to push forward the resolution limits of the top-down approach, these improvements in resolution are associated with a near exponential increase in the



manufacturing costs. This economic limitation and other scientific problems related to the top-down approach have motivated efforts worldwide to search for new strategies to meet the demand for nanoscale structures. The bottom-up approach represents a powerful alternative to conventional top-down methods. In the bottom-up approach functional electronic structures are assembled from chemically synthesized, well-defined nanoscale building blocks, much like the way nature uses proteins and other macromolecules to construct complex biological systems. So, in this approach lithography is substituted by nanometer-scale synthesis, functionalization and assembly.

Put into this perspective, ZnO is nowadays a key technological material and a promising building block for functional devices. The lack of a center of symmetry in wurtzite lead to an extremely interesting material that exhibits both semiconducting and piezoelectric behavior together with a large exciton binding energy. Moreover ZnO probably has the richest family of nanostructures among all materials, both in structures and in properties [6]. In the last decade significant efforts have been made to investigate zinc oxide nanostructures and a large number of research groups turn their investigations to ZnO for (opto)electronic, photovoltaic, piezotronics, photoreactive and sensing devices, as proved by the increasing number of scientific papers during the last decade (Figure 1.1).

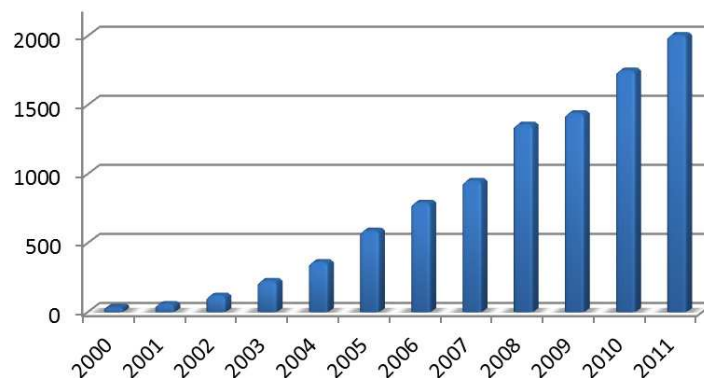


**Figure 1.1** Number of publications containing “ZnO nano\*” in the title.  
Source: ISI Web of Science.

Although ZnO properties are much interesting themselves, the functionalization of ZnO nanostructures – by means of surface functionalization as well as the creation of heterostructures combining different materials (organic / inorganic, metals, semiconductors, insulators...) – paves the way to the creation of novel functional materials that exhibit unique new properties or the enhancement of the pre-existent ones. Actually, to tailor and engineer material properties is the calling for a material scientist and coupling different materials at the nanoscale is the key to the fabrication of multifunctional devices.

This thesis deals with the functionalization of ZnO nanostructures, tetrapods (TP) and nanorods (NR) in particular, which have been grown by our group at IMEM Institute through a non-catalyzed CVD technique. My research, in particular, focused on different kinds of functionalization in order to tailor the properties of the resulting material towards different applicative fields, namely gas sensing devices, photocatalytic systems and photovoltaic cells. Herein this Thesis describes the functionalization of ZnO nanostructures with different materials belonging to three specific classes:

- II-VI semiconductor (cadmium sulphide)
- Magnetic materials (magnetite)
- Organic molecules (phthalocyanine and porphyrin)

Out of this brief introduction, the Thesis is basically divided in three parts, an overview chapter describing the different materials, their chemical and physical properties and main applicative fields (Ch. 2); the experimental section (Ch. 3) which concisely presents synthesis and characterization techniques of both starting and functionalized materials and the discussion of meaningful results obtained in the functionalization (Ch. 4). Finally conclusions and future perspectives are depicted in Ch. 5.

More in detail, the cadmium sulphide (CdS) functionalization of ZnO TP is aimed to create an heterojunction for photoenergy conversion applications. Although the use of CdS to extend the fraction of visible light to be collected by the heterostructure is not new, the present work focuses on a new synthetic approach. This is required since, despite of the huge variety of literature-proposed methods for CdS synthesis, none of them can be considered optimal for ZnO functionalization. In fact, on the one hand, CdS aqueous-based synthesis requires alkaline or acidic environments that invariably etch the ZnO surface [7–9]; on the other, high temperature syntheses in organic solvents require the presence of ligands or surfactant to effectively control the CdS dimension. Unfortunately such polymers / molecules would likely be trapped at the interface limiting the heterojunction performance [10–15]. Hence, an *in-situ* deposition of CdS on ZnO TP, *without* the need of any surface passivating agent, is presented in Chapter 4.1. This paves the way to use the composite nanostructured material in photocatalytic (degradation of organic pollutants, photo-induced water splitting), and gas sensing applications [16–23]. Taking into account the research on the functionalization of ZnO TP, the following section (Ch. 4.2) briefly extends the CdS deposition to ZnO NR, which are promising nanostructures for photovoltaic applications [7,

24–27], since they show excellent transport properties [28,29] and allow a continuous path for the electrons (as opposite to ZnO TP which shows hopping/percolative transport [30,31]).

Chapter 4.2 deals with the functionalization ZnO TP with magnetite nanoparticles. The study is aimed to extrinsically *add* superparamagnetic properties to ZnO and obtain a multifunctional magnetic material that still preserves all ZnO own peculiar characteristics, *e.g.* luminescence and surface reactivity, in particular. The possibility to intentionally “switch” *off* or *on* the magnetization is a great advantage for many applications. For example, consider a set of nanostructures dispersed in a liquid medium, the superparamagnetic behavior permits to avoid magnetic-induced aggregation and have stable suspensions over long periods (months) but, when needed, it is also possible to activate aggregation at a given time / position by applying an external magnetic field to drive, transport or collect these nanostructures to a specific target. This turns out particularly interesting for biomedicine, since ZnO nanostructures are considered to be biocompatible (at least those with sizes larger than 100 nm) [32], and display a very high quantum efficiency for singlet oxygen production [33,34]. In fact they are currently being studied for selective destruction of tumor cells and drug delivery applications [32]. Moreover the functionalization with magnetite may be exploited to develop filter-free photocatalytic systems wherein the catalyst is collected by magnetic separation [35–38].

A third example of functionalization concerns organic molecules, as depicted in Chapter 4.3. The study has been carried out in collaboration with colleagues at IMEM Trento, in the frame of “D.A.F.N.E.” project, which is devoted to the study of hybrid materials for photovoltaic applications. One of the challenging issues in excitonic photovoltaic cells deals with the optimization of the absorbing layer in order to collect a vast fraction of the incident light. Owing to the limited absorption width of organic molecules and polymers, only a small fraction of the solar flux can be harvested by a single-layer bulk heterojunction photovoltaic cell. Furthermore, the low charge-carrier mobility of most organic materials limits the thickness of the active layer, since the exciton diffusion length in most organic semiconductors is in the order of  $3 \div 10$  nm [39–42]. One promising strategy to overcome both the limited absorption and the low exciton diffusion in organic materials, is to couple organics with inorganic semiconductor nanostructures (mainly TiO<sub>2</sub> and ZnO). In these hybrid heterostructures a thin organic layer (  $\sim 10$  nm ) is used to achieve an efficient exciton separation at the interface, transferring electrons to ZnO conduction band. The use of nanostructures with high surface-to-volume ratio induces scattering phenomena of the incident light and enables multiple trapping processes at the interface that assure significant light absorption in the dye molecule, even when the organic thickness is limited to a few nanometers. This lowers

the recombination probability inside the organic layer, extends carriers lifetime and consequently enhances the efficiency of the hybrid solar cell [43].

Different organic molecules (phthalocyanines and porphyrins) have been deposited by researchers at IMEM Trento throughout a tailor-made supersonic molecular beam apparatus. The aim of the project is the sensitization, and the characterization, of ZnO NR to investigate the hybrid nanostructure as a hybrid photo-anode for future photovoltaic applications. As a matter of fact, ZnO solar cells have shown relatively low overall conversion efficiencies when compared with TiO<sub>2</sub>-based systems. The limited performance in ZnO-based DSSC may be explained by the instability of ZnO in acidic dye (i.e., protons from the dyes cause the dissolution of Zn atoms at ZnO surface, resulting in the formation of excessive Zn<sup>2+</sup>/dye agglomerates) and the slow electron-injection kinetics from dye to ZnO [44]. Consequently, molecular beam deposition is an attractive alternative to wet impregnation, since it preserves the ZnO surface and, by varying the kinetic energy of the beam, it is possible to promote chemical bonds at the interface. Driven by the high directionality of SuMBD deposition, the goal is to deposit two distinct molecules, with convenient absorption range, on the surface of a single ZnO NR, in order to collect a wider spectrum of incident light. Photovoltaic, however, is not the only applicative field where sensitized ZnO NR can be employed in. According to literature, either porphyrin [33,45,46], ZnO [33,34] and the resulting hybrid material [47] have been well established as materials for singlet oxygen production, hence they can be used in photocatalytic systems as well as in nano-medicine. If porphyrins are known to be biocompatible, ZnO nanowires have been shown to be biodegradable and, to eventually dissolve into Zn<sup>2+</sup> ions that can be adsorbed by the body and become part of the nutritional cycle: thereby ZnO NR have been proposed for *in vivo* bio-sensing and bio-detection applications [48].

## References

- [1] Tim Harper, CEO of CMP Cientifica (the Europe's largest nanotechnology information provider).
- [2] <http://www.reuters.com/article/2011/11/17/idUS139697+17-Nov-2011+MW20111117>
- [3] [http://en.wikipedia.org/wiki/List\\_of\\_countries\\_by\\_GDP\\_%28nominal%29](http://en.wikipedia.org/wiki/List_of_countries_by_GDP_%28nominal%29)
- [4] S. Iijima: *Nature*, 1991, **354**, 56
- [5] G. Cao, *Nanostructures and nanomaterials*, 2004, Imperial College Press
- [6] Z.L. Wang, *J. Phys.: Condens. Matter*, 2004, **16**, R829
- [7] Y. Tak, S.J. Hong, J.S. Lee, *Cryst. Growth Des*, 2009, **9** (6), 2627
- [8] H. Horiuchi, R. Katoh, K. Hara, M. Yanagida, S. Murata, H. Arakawa, M. Tachiya, *J. Phys. Chem. B*, 2003, **107**, 2570
- [9] H. Zheng, X.L. Du, Q. Luo, J.F. Jia, C.Z. Gu, Q.K. Xue, *Thin Solid Films*, 2007, **515**, 3967
- [10] S. Rühle, M. Shalom, and A. Zaban, *ChemPhysChem*, 2010, **11**, 2290
- [11] Y.J. Shen, Y.L. Lee, *Nanotechnology*, 2008, **19**, 045602
- [12] Y. Zhou, F.S. Riehle, Y. Yuan, H.F. Schleiermacher, M. Niggemann, G. A. Urban, M. Krüger, *Appl. Phys. Lett.*, 2010, **96**, 013304
- [13] I. Mora-Serò, S. Giménez, T. Moehl, F. Fabregat-Santiago, T. Lana-Villareal, R. Gómez, J. Bisquert, *Nanotechnology*, 2008, **19**, 424007
- [14] J. Chen, J. L. Song, X. W. Sun, W. Q. Deng, C. Y. Jiang, W. Lei, J. H. Huang, R. S. Liu, *Appl. Phys. Lett.*, 2009, **94**, 153115
- [15] I. Robel, V. Subramanian, M. Kuno, P. V. Kamat, *J. Am. Chem. Soc.*, 2006, **128**, 2385
- [16] Y. Tak, H. Kim, D. Lee and K. Yong, *Chem. Commun.*, 2008, 4585
- [17] J. Nayak, S.N. Sahu, J. Kasuya, S. Nozaki, *Applied Surface Science*, 2008, **254**, (22), 7215
- [18] P. Kundu, P. A. Deshpande, G. Madras and N. Ravishankar, *J. Mater. Chem.*, 2011, **21**, 4209
- [19] X. Wang, G. Liu, G. Q. Lu, H.-M. Cheng, *international journal of hydrogen energy*, 2010, **35**, 8199
- [20] X. Wang et. al., *Energy Environ. Sci.*, 2011, **4**, 3976
- [21] S. Wei, Z. Shao, X. Lu, Y. Liu, L. Cao, Y. He, *J. Environ. Sci.*, 2009, **21** (7), 991
- [22] G. Wang, X. Yang, F. Qian, J. Z. Zhang and Y. Li, *Nano Lett.*, 2010, **10** (3), 1088
- [23] M. Villani, D. Calestani, L. Lazzarini, L. Zanotti, R. Mosca, A. Zappettini, *J. Mater. Chem.*, 2012, *In press*
- [24] Y. Zang, T. Xie, T. Jiang, X. Wei, S. Pang, X. Wang, D. Wang, *Nanotechnology*, 2009, **20**, 155707
- [25] Y. Tak, S. J. Hong, J. S. Lee, and K. Yong, *J. Mater. Chem.*, 2009, **19**, 5945
- [26] G. Guerguerian, F. Elhordoy, C. J. Pereyra, R. E. Marotti, F. Martin, D. Leinen, J. R. Ramos-Barrado and E. A. Dalchiale, *Nanotechnology*, 2011, **22**, 505401
- [27] C. Luan et al, *Nanoscale Res Lett.*, 2011, **6** (1), 340
- [28] W. Park, J. S. Kim, G. C. Yi, M. H. Bae, and H.J. Lee, *Appl. Phys. Lett.*, 2004, **85**, 5052

- [29] P.C. Chang, Z. Fan, C.J. Chien, D. Stichtenoth, C. Ronning, J. G. Lu, *Appl. Phys. Lett.*, 2006, **89**, 133113
- [30] Q. Zhang, C. S. Dandeneau, X. Zhou, and G. Cao, *Adv. Mater.*, 2009, **21**, 4087
- [31] K. D. Benkstein, N. Kopidakis, J. van de Lagemaat, A. J. Frank, *J. Phys. Chem. B*, 2003, **107**, 7759
- [32] J.W. Rasmussen, E. Martinez, P. Louka, and D.G. Wingett, *Expert Opin Drug Deliv*, 2010, **7** (9), 1063
- [33] M.C. DeRosa, R.J. Crutchley, *Coordination Chemistry Reviews*, 2002, **233-234**, 351
- [34] Y. Yamamoto, N. Imai, R. Mashima, R. Konaka, M. Inoue, W. C. Dunlap, *Methods in Enzymology*, 2000, **319**, 29
- [35] S. Xu, W. Shangguan, J. Yuan, M. Chen, J. Shi and Z. Jiang, *Nanotechnology*, 2008, **19**, 095606
- [36] M. Ye, Q. Zhang, Y. Hu, J. Ge, Z. Lu, L. He, Z. Chen, Y. Yin, *Chem. Eur. J.*, 2010, **16**, 6243
- [37] F. Chen, Y. Xie, J. Zhao, G.Lu, *Chemosphere*, 2010, **44**, 1159
- [38] A. Lu, W. Schmidt, N. Matoussevitch, B. Spliethoff, B. Tesche, E. Bill, W. Kiefer, F. Schüth, *Angew. Chem. Int. Ed.*, 2004, **43**, 4303
- [39] S.R. Scully, and M.D McGehee, *J. Appl. Phys.*, 2006, **100**, 034907
- [40] D.E. Markov et al., *Phys. Rev. B*, 2005, **72**, 045216
- [41] P. Peumans et al., *J. Appl. Phys.*, 2003, **93**, 3693
- [42] A. Hadipour, B. De Boer, P.W.M. Blom, *Adv. Funct. Mater.*, 2008, **18**, 169
- [43] J. Liu, S. Wang, Z. Bian, M. Shan, and C. Huang, *Appl. Phys. Lett.*, 2009, **94**, 173107
- [44] Q. Zhang, C. S. Dandeneau, X. Zhou, G. Cao, *Adv. Mater.*, 2009, **21**, 1
- [45] M. Krieg, D. G. Whitten, *J. Am. Chem. Soc.*, 1984, **106** (8), 2477
- [46] B. Ventura, A. Degli Esposti, B. Koszarna, D. T. Gryko and L. Flamigni, *New J. Chem.*, 2005, **29**, 1559
- [47] Y. Liu, Y. Zhang, S. Wang, C. Pope, and W. Chen, *Appl. Phys. Lett.*, 2008, **92**, 143901
- [48] J. Zhou, N. Xu, Z.L. Wang, *Adv. Mater.*, 2006, **18**, 2432

# 1 Introduction

---

Nanotechnology, which sets out to explore and manipulate reality at the molecular level, is widely recognized as a key technology that will drive economic growth and standards of living in the twenty-first century. What we are currently seeing is the beginning of a revolution, caused by our ability to work on the same scale as nature [1]. This is the result of almost five decades in which miniaturization has been a commitment for scientists and the research in nanotechnology has been largely funded by governments and private corporations. According to a study by Global Industry Analysts Inc. [2], the global market for products incorporating nanotechnology is projected to grow at a compound annual growth rate of 11.1% between 2010 and 2015 and will reach the impressive sum of US\$2.4 trillion, that is roughly 1/25 of the current world gross domestic product [3].

Since the discovery of carbon nanotubes in 1991 [4], significant progress has already been made in the field of zero- (0D), one- (1D) and two-dimensional (2D) nanomaterials and nanostructures. Studies on new physical properties and applications of nanomaterials and nanostructures are possible only when nanostructured materials are made available with desired size, morphology, crystal microstructure and chemical composition [5]. The fabrication of materials at the nanoscale can be used to enhance and exploit properties that become stronger under conditions of reduced dimensionality; in fact size reduction can lead to a whole range of new physico-chemical properties and a wealth of potential applications.

Nanotechnology allows the miniaturization of current and new instruments, sensors and machines that will greatly impact the world we live in. Possible examples include: computers with amazing power that compute algorithms to mimic human brain, biosensors that warn us at the early stage of a disease, target-specific drugs that automatically attack the diseased cells *on site*, nano-robots that can repair internal damage and remove chemical toxins in human bodies, nano-scaled electronics that constantly monitor our local environment [5].

In general, there are two theoretically distinct approaches to the creation of nanostructures and related devices, which are commonly known as *top-down* and *bottom-up*. In the top-down approach, small features are patterned in bulk materials by a combination of lithography, etching and deposition, to form functional devices. The top-down approach has been unexpectedly successful in many venues, with microelectronics being perhaps the best example today. While the technique developments continue to push forward the resolution limits of the top-down approach, these improvements in resolution are associated with a near exponential increase in the

manufacturing costs. This economic limitation and other scientific problems related to the top-down approach have motivated efforts worldwide to search for new strategies to meet the demand for nanoscale structures. The bottom-up approach represents a powerful alternative to conventional top-down methods. In the bottom-up approach functional electronic structures are assembled from chemically synthesized, well-defined nanoscale building blocks, much like the way nature uses proteins and other macromolecules to construct complex biological systems. So, in this approach lithography is substituted by nanometer-scale synthesis, functionalization and assembly.

Put into this perspective, ZnO is nowadays a key technological material and a promising building block for functional devices. The lack of a center of symmetry in wurtzite lead to an extremely interesting material that exhibits both semiconducting and piezoelectric behavior together with a large exciton binding energy. Moreover ZnO probably has the richest family of nanostructures among all materials, both in structures and in properties [6]. In the last decade significant efforts have been made to investigate zinc oxide nanostructures and a large number of research groups turn their investigations to ZnO for (opto)electronic, photovoltaic, piezotronics, photoreactive and sensing devices, as proved by the increasing number of scientific papers during the last decade (Figure 1.1).

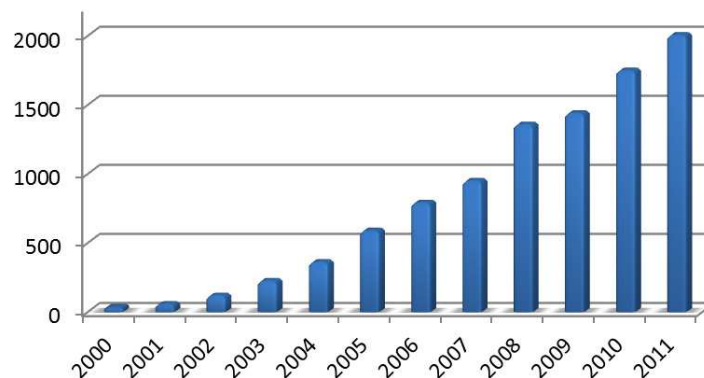


**Figure 1.1** Number of publications containing “ZnO nano\*” in the title.  
Source: ISI Web of Science.

Although ZnO properties are much interesting themselves, the functionalization of ZnO nanostructures – by means of surface functionalization as well as the creation of heterostructures combining different materials (organic / inorganic, metals, semiconductors, insulators...) – paves the way to the creation of novel functional materials that exhibit unique new properties or the enhancement of the pre-existent ones. Actually, to tailor and engineer material properties is the calling for a material scientist and coupling different materials at the nanoscale is the key to the fabrication of multifunctional devices.



This thesis deals with the functionalization of ZnO nanostructures, tetrapods (TP) and nanorods (NR) in particular, which have been grown by our group at IMEM Institute through a non-catalyzed CVD technique. My research, in particular, focused on different kinds of functionalization in order to tailor the properties of the resulting material towards different applicative fields, namely gas sensing devices, photocatalytic systems and photovoltaic cells. Herein this Thesis describes the functionalization of ZnO nanostructures with different materials belonging to three specific classes:

- II-VI semiconductor (cadmium sulphide)
- Magnetic materials (magnetite)
- Organic molecules (phthalocyanine and porphyrin)

Out of this brief introduction, the Thesis is basically divided in three parts, an overview chapter describing the different materials, their chemical and physical properties and main applicative fields (Ch. 2); the experimental section (Ch. 3) which concisely presents synthesis and characterization techniques of both starting and functionalized materials and the discussion of meaningful results obtained in the functionalization (Ch. 4). Finally conclusions and future perspectives are depicted in Ch. 5.

More in detail, the cadmium sulphide (CdS) functionalization of ZnO TP is aimed to create an heterojunction for photoenergy conversion applications. Although the use of CdS to extend the fraction of visible light to be collected by the heterostructure is not new, the present work focuses on a new synthetic approach. This is required since, despite of the huge variety of literature-proposed methods for CdS synthesis, none of them can be considered optimal for ZnO functionalization. In fact, on the one hand, CdS aqueous-based synthesis requires alkaline or acidic environments that invariably etch the ZnO surface [7–9]; on the other, high temperature syntheses in organic solvents require the presence of ligands or surfactant to effectively control the CdS dimension. Unfortunately such polymers / molecules would likely be trapped at the interface limiting the heterojunction performance [10–15]. Hence, an *in-situ* deposition of CdS on ZnO TP, *without* the need of any surface passivating agent, is presented in Chapter 4.1. This paves the way to use the composite nanostructured material in photocatalytic (degradation of organic pollutants, photo-induced water splitting), and gas sensing applications [16–23]. Taking into account the research on the functionalization of ZnO TP, the following section (Ch. 4.2) briefly extends the CdS deposition to ZnO NR, which are promising nanostructures for photovoltaic applications [7,

24–27], since they show excellent transport properties [28,29] and allow a continuous path for the electrons (as opposite to ZnO TP which shows hopping/percolative transport [30,31]).

Chapter 4.2 deals with the functionalization ZnO TP with magnetite nanoparticles. The study is aimed to extrinsically *add* superparamagnetic properties to ZnO and obtain a multifunctional magnetic material that still preserves all ZnO own peculiar characteristics, *e.g.* luminescence and surface reactivity, in particular. The possibility to intentionally “switch” *off* or *on* the magnetization is a great advantage for many applications. For example, consider a set of nanostructures dispersed in a liquid medium, the superparamagnetic behavior permits to avoid magnetic-induced aggregation and have stable suspensions over long periods (months) but, when needed, it is also possible to activate aggregation at a given time / position by applying an external magnetic field to drive, transport or collect these nanostructures to a specific target. This turns out particularly interesting for biomedicine, since ZnO nanostructures are considered to be biocompatible (at least those with sizes larger than 100 nm) [32], and display a very high quantum efficiency for singlet oxygen production [33,34]. In fact they are currently being studied for selective destruction of tumor cells and drug delivery applications [32]. Moreover the functionalization with magnetite may be exploited to develop filter-free photocatalytic systems wherein the catalyst is collected by magnetic separation [35–38].

A third example of functionalization concerns organic molecules, as depicted in Chapter 4.3. The study has been carried out in collaboration with colleagues at IMEM Trento, in the frame of “D.A.F.N.E.” project, which is devoted to the study of hybrid materials for photovoltaic applications. One of the challenging issues in excitonic photovoltaic cells deals with the optimization of the absorbing layer in order to collect a vast fraction of the incident light. Owing to the limited absorption width of organic molecules and polymers, only a small fraction of the solar flux can be harvested by a single-layer bulk heterojunction photovoltaic cell. Furthermore, the low charge-carrier mobility of most organic materials limits the thickness of the active layer, since the exciton diffusion length in most organic semiconductors is in the order of  $3 \div 10$  nm [39–42]. One promising strategy to overcome both the limited absorption and the low exciton diffusion in organic materials, is to couple organics with inorganic semiconductor nanostructures (mainly TiO<sub>2</sub> and ZnO). In these hybrid heterostructures a thin organic layer (  $\sim 10$  nm ) is used to achieve an efficient exciton separation at the interface, transferring electrons to ZnO conduction band. The use of nanostructures with high surface-to-volume ratio induces scattering phenomena of the incident light and enables multiple trapping processes at the interface that assure significant light absorption in the dye molecule, even when the organic thickness is limited to a few nanometers. This lowers

the recombination probability inside the organic layer, extends carriers lifetime and consequently enhances the efficiency of the hybrid solar cell [43].

Different organic molecules (phthalocyanines and porphyrins) have been deposited by researchers at IMEM Trento throughout a tailor-made supersonic molecular beam apparatus. The aim of the project is the sensitization, and the characterization, of ZnO NR to investigate the hybrid nanostructure as a hybrid photo-anode for future photovoltaic applications. As a matter of fact, ZnO solar cells have shown relatively low overall conversion efficiencies when compared with TiO<sub>2</sub>-based systems. The limited performance in ZnO-based DSSC may be explained by the instability of ZnO in acidic dye (i.e., protons from the dyes cause the dissolution of Zn atoms at ZnO surface, resulting in the formation of excessive Zn<sup>2+</sup>/dye agglomerates) and the slow electron-injection kinetics from dye to ZnO [44]. Consequently, molecular beam deposition is an attractive alternative to wet impregnation, since it preserves the ZnO surface and, by varying the kinetic energy of the beam, it is possible to promote chemical bonds at the interface. Driven by the high directionality of SuMBD deposition, the goal is to deposit two distinct molecules, with convenient absorption range, on the surface of a single ZnO NR, in order to collect a wider spectrum of incident light. Photovoltaic, however, is not the only applicative field where sensitized ZnO NR can be employed in. According to literature, either porphyrin [33,45,46], ZnO [33,34] and the resulting hybrid material [47] have been well established as materials for singlet oxygen production, hence they can be used in photocatalytic systems as well as in nano-medicine. If porphyrins are known to be biocompatible, ZnO nanowires have been shown to be biodegradable and, to eventually dissolve into Zn<sup>2+</sup> ions that can be adsorbed by the body and become part of the nutritional cycle: thereby ZnO NR have been proposed for *in vivo* bio-sensing and bio-detection applications [48].

## References

- [1] Tim Harper, CEO of CMP Cientifica (the Europe's largest nanotechnology information provider).
- [2] <http://www.reuters.com/article/2011/11/17/idUS139697+17-Nov-2011+MW20111117>
- [3] [http://en.wikipedia.org/wiki/List\\_of\\_countries\\_by\\_GDP\\_%28nominal%29](http://en.wikipedia.org/wiki/List_of_countries_by_GDP_%28nominal%29)
- [4] S. Iijima: *Nature*, 1991, **354**, 56
- [5] G. Cao, *Nanostructures and nanomaterials*, 2004, Imperial College Press
- [6] Z.L. Wang, *J. Phys.: Condens. Matter*, 2004, **16**, R829
- [7] Y. Tak, S.J. Hong, J.S. Lee, *Cryst. Growth Des*, 2009, **9** (6), 2627
- [8] H. Horiuchi, R. Katoh, K. Hara, M. Yanagida, S. Murata, H. Arakawa, M. Tachiya, *J. Phys. Chem. B*, 2003, **107**, 2570
- [9] H. Zheng, X.L. Du, Q. Luo, J.F. Jia, C.Z. Gu, Q.K. Xue, *Thin Solid Films*, 2007, **515**, 3967
- [10] S. Rühle, M. Shalom, and A. Zaban, *ChemPhysChem*, 2010, **11**, 2290
- [11] Y.J. Shen, Y.L. Lee, *Nanotechnology*, 2008, **19**, 045602
- [12] Y. Zhou, F.S. Riehle, Y. Yuan, H.F. Schleiermacher, M. Niggemann, G. A. Urban, M. Krüger, *Appl. Phys. Lett.*, 2010, **96**, 013304
- [13] I. Mora-Serò, S. Giménez, T. Moehl, F. Fabregat-Santiago, T. Lana-Villareal, R. Gómez, J. Bisquert, *Nanotechnology*, 2008, **19**, 424007
- [14] J. Chen, J. L. Song, X. W. Sun, W. Q. Deng, C. Y. Jiang, W. Lei, J. H. Huang, R. S. Liu, *Appl. Phys. Lett.*, 2009, **94**, 153115
- [15] I. Robel, V. Subramanian, M. Kuno, P. V. Kamat, *J. Am. Chem. Soc.*, 2006, **128**, 2385
- [16] Y. Tak, H. Kim, D. Lee and K. Yong, *Chem. Commun.*, 2008, 4585
- [17] J. Nayak, S.N. Sahu, J. Kasuya, S. Nozaki, *Applied Surface Science*, 2008, **254**, (22), 7215
- [18] P. Kundu, P. A. Deshpande, G. Madras and N. Ravishankar, *J. Mater. Chem.*, 2011, **21**, 4209
- [19] X. Wang, G. Liu, G. Q. Lu, H.-M. Cheng, *international journal of hydrogen energy*, 2010, **35**, 8199
- [20] X. Wang et. al., *Energy Environ. Sci.*, 2011, **4**, 3976
- [21] S. Wei, Z. Shao, X. Lu, Y. Liu, L. Cao, Y. He, *J. Environ. Sci.*, 2009, **21** (7), 991
- [22] G. Wang, X. Yang, F. Qian, J. Z. Zhang and Y. Li, *Nano Lett.*, 2010, **10** (3), 1088
- [23] M. Villani, D. Calestani, L. Lazzarini, L. Zanotti, R. Mosca, A. Zappettini, *J. Mater. Chem.*, 2012, *In press*
- [24] Y. Zang, T. Xie, T. Jiang, X. Wei, S. Pang, X. Wang, D. Wang, *Nanotechnology*, 2009, **20**, 155707
- [25] Y. Tak, S. J. Hong, J. S. Lee, and K. Yong, *J. Mater. Chem.*, 2009, **19**, 5945
- [26] G. Guerguerian, F. Elhordoy, C. J. Pereyra, R. E. Marotti, F. Martin, D. Leinen, J. R. Ramos-Barrado and E. A. Dalchiale, *Nanotechnology*, 2011, **22**, 505401
- [27] C. Luan et al, *Nanoscale Res Lett.*, 2011, **6** (1), 340
- [28] W. Park, J. S. Kim, G. C. Yi, M. H. Bae, and H.J. Lee, *Appl. Phys. Lett.*, 2004, **85**, 5052

- [29] P.C. Chang, Z. Fan, C.J. Chien, D. Stichtenoth, C. Ronning, J. G. Lu, *Appl. Phys. Lett.*, 2006, **89**, 133113
- [30] Q. Zhang, C. S. Dandeneau, X. Zhou, and G. Cao, *Adv. Mater.*, 2009, **21**, 4087
- [31] K. D. Benkstein, N. Kopidakis, J. van de Lagemaat, A. J. Frank, *J. Phys. Chem. B*, 2003, **107**, 7759
- [32] J.W. Rasmussen, E. Martinez, P. Louka, and D.G. Wingett, *Expert Opin Drug Deliv*, 2010, **7** (9), 1063
- [33] M.C. DeRosa, R.J. Crutchley, *Coordination Chemistry Reviews*, 2002, **233-234**, 351
- [34] Y. Yamamoto, N. Imai, R. Mashima, R. Konaka, M. Inoue, W. C. Dunlap, *Methods in Enzymology*, 2000, **319**, 29
- [35] S. Xu, W. Shangguan, J. Yuan, M. Chen, J. Shi and Z. Jiang, *Nanotechnology*, 2008, **19**, 095606
- [36] M. Ye, Q. Zhang, Y. Hu, J. Ge, Z. Lu, L. He, Z. Chen, Y. Yin, *Chem. Eur. J.*, 2010, **16**, 6243
- [37] F. Chen, Y. Xie, J. Zhao, G.Lu, *Chemosphere*, 2010, **44**, 1159
- [38] A. Lu, W. Schmidt, N. Matoussevitch, B. Spliethoff, B. Tesche, E. Bill, W. Kiefer, F. Schüth, *Angew. Chem. Int. Ed.*, 2004, **43**, 4303
- [39] S.R. Scully, and M.D McGehee, *J. Appl. Phys.*, 2006, **100**, 034907
- [40] D.E. Markov et al., *Phys. Rev. B*, 2005, **72**, 045216
- [41] P. Peumans et al., *J. Appl. Phys.*, 2003, **93**, 3693
- [42] A. Hadipour, B. De Boer, P.W.M. Blom, *Adv. Funct. Mater.*, 2008, **18**, 169
- [43] J. Liu, S. Wang, Z. Bian, M. Shan, and C. Huang, *Appl. Phys. Lett.*, 2009, **94**, 173107
- [44] Q. Zhang, C. S. Dandeneau, X. Zhou, G. Cao, *Adv. Mater.*, 2009, **21**, 1
- [45] M. Krieg, D. G. Whitten, *J. Am. Chem. Soc.*, 1984, **106** (8), 2477
- [46] B. Ventura, A. Degli Esposti, B. Koszarna, D. T. Gryko and L. Flamigni, *New J. Chem.*, 2005, **29**, 1559
- [47] Y. Liu, Y. Zhang, S. Wang, C. Pope, and W. Chen, *Appl. Phys. Lett.*, 2008, **92**, 143901
- [48] J. Zhou, N. Xu, Z.L. Wang, *Adv. Mater.*, 2006, **18**, 2432

## 2 Materials properties and applications

---

### 2.1 Zinc oxide nanostructures

Zinc oxide (ZnO) is an inorganic compound that usually appears as a white powder, nearly insoluble in water, which is widely used as an additive into numerous materials and products including plastics, ceramics, glass, cement, rubber, lubricants, paints, adhesives, sealants, pigments, foods, batteries, ferrites, fire retardants, etc. ZnO is present in the Earth crust as a mineral zincite; however, most ZnO used commercially is produced synthetically. In materials science, ZnO is often called a II–VI semiconductor because zinc and oxygen belong to the 2nd and 6th groups of the periodic table, respectively. This semiconductor has several favorable properties: good transparency, high electron mobility, wide bandgap, strong room temperature luminescence, piezoelectricity etc. Those properties are already used in emerging applications for transparent electrodes in liquid crystal displays and in energy-saving or heat-protecting windows. Electronic applications of ZnO as thin-film transistor and light-emitting diode are forthcoming as of 2011 [source:<http://compoundsemiconductor.net/csc/features-details/19732885/LEDs:-ZnO-prepares-to-leap-from-lab-to-fa.html>].

The research on ZnO started in the 1930s [1] and it has featured as subject of thousands of research papers until today. This early period is reviewed and documented, *e.g.* in [2–4] but the research peaked around the end of the 1970s and the beginning of the 1980s. Then the interest faded away, partly because it was not possible to dope ZnO both n- and p-type, which is an indispensable prerequisite for optoelectronics applications, partly because the interest moved to structures of reduced dimensionality, like quantum wells, which were at that time almost exclusively based on the III–V system such as GaAs / Al<sub>1-x</sub>Ga<sub>x</sub>As.

The emphasis of ZnO research at that time was essentially on bulk samples covering topics like growth, doping, transport properties, deep centers, band structure, excitons, bulk – and surface – polaritons, luminescence, high excitation or many-particle effects and lasing. The results of this first research period are reviewed [5–7] and entered in data collections [8] or textbooks on semiconductor optics [9]. Nowadays the interest in ZnO structures has drastically increased: intense research by many different groups has focused on novel nanostructures with different shapes (Figure 2.1) ranging from nanobelts (A), (B), (C); to nanocombs (D); from nanorings (E), (F) to hierarchical nanowire junction arrays (G) and nanonails (H).

Besides these fancy nanostructures, which turn out interesting because allow researchers to better understand some key points in the crystal growth of ZnO nanostructures, other morphologies have been widely investigated in different application fields: these are nanorods (NR) and nanotetrapods (TP) (refer to Ch. 2.1.3 for discussion and applications).

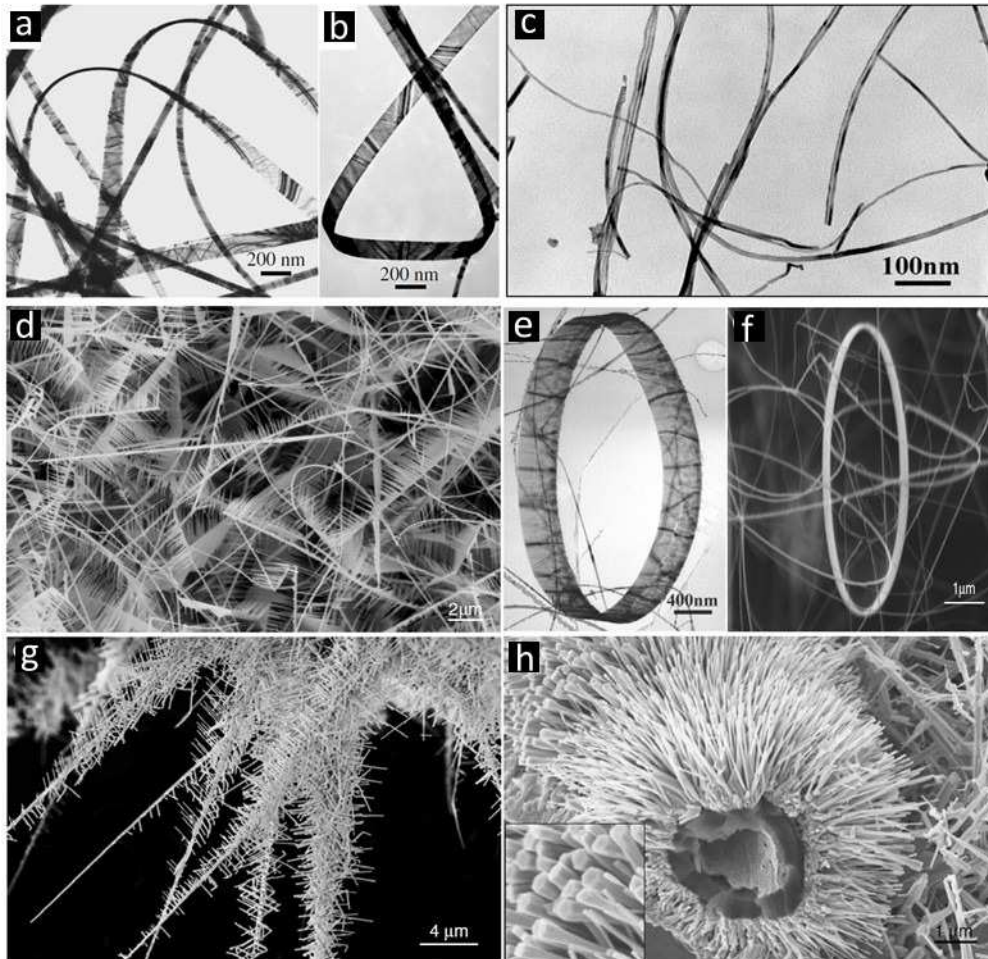


**Figure 2.1** Different morphologies of ZnO nanostructures. Adapted from [10].

### 2.1.1 Structural properties

At ambient pressure and temperature, ZnO crystallizes in the wurtzite (WZ) structure, as shown in Figure 2.2: the point group is  $6mm$  (Hermann-Mauguin notation) or  $C_6^v$  (Schoenflies notation), and the space group is  $P63mc$  or  $C_6^v$ , lattice parameters are  $a = 3.296$  and  $c = 5.2065$  Å and their ratio  $c/a \sim 1.60$  is close to the ideal value for hexagonal cell  $c/a = 1.633$ . The zinc atoms are tetrahedrally coordinated to four oxygen atoms, with the oxygen anions occupying the octahedral sites. The structure can be described as a number of alternating planes composed of  $O^{2-}$  and  $Zn^{2+}$  ions, stacked alternately along the  $c$ -axis (Figure 2.2). The largely ionic bonding together with

tetrahedral coordination in ZnO and non-central symmetric structure result in interesting piezoelectric and pyroelectric properties. Due to this ionicity, zinc and oxygen planes bear electric charge (positive and negative, respectively). Therefore, to maintain electrical neutrality, those planes reconstruct at atomic level in most similar materials, but not in ZnO: its surfaces are atomically flat, stable and exhibit no reconstruction. This anomaly of ZnO is not fully explained yet. The most common polar surface is the basal plane. The oppositely charged ions produce positively charged Zn-(0001) and negatively charged O-(000-1) surfaces, resulting in a normal dipole moment and spontaneous polarization along the c-axis as well as a divergence in surface energy. To maintain a stable structure, the polar surfaces generally have facets or exhibit massive surface reconstructions, but ZnO  $\pm(0001)$  are exceptions: they are atomically flat, stable and without reconstruction [11]. Efforts to understand the superior stability of the ZnO  $\pm(0001)$  polar surfaces are at the forefront of research in today's surface physics [12–15]. The other two most commonly observed facets for ZnO are (2-1-10) and (01-10), which are non-polar surfaces and have lower energy than the (0001) facets.

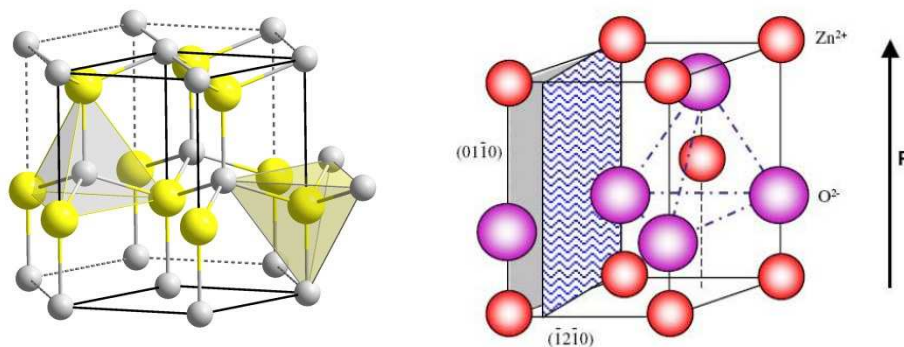


**Figure 2.2** The hexagonal WZ structure of ZnO pointing out Zn tetrahedral coordination.

Similarly to what was observed for other II-VI compounds (ZnS, CdSe, CdS, and MnS) [16–20], the ZB phase has been found as the nucleus in the initiation of ZnO nanostructures (*e.g.* tetrapods and nanowires) [21-25] but it is rather unstable and quickly transforms into the WZ (thermodynamically stable) phase once the crystal becomes bigger. The symmetry of the ZB structure is given by space group  $F43m$  in the Hermann–Mauguin notation and  $T_d^2$  in the Schoenflies notation and is composed of two interpenetrating face-centered cubic (*fcc*) sublattices shifted along the body diagonal by one-quarter of the length of the body diagonal (Figure 2.3). There are four atoms per unit cell and every Zn atom is tetrahedrally coordinated with four O atoms, and vice versa. Because of the tetrahedral coordination of WZ and ZB structures, the four nearest neighbors and 12 next-nearest neighbors have the same bond distance in both structures. Like other II–VI semiconductors, ZnO WZ can be transformed to the rocksalt (NaCl) structure at relatively modest external hydrostatic pressures. The reason for this is that the reduction of the lattice dimensions causes the interionic Coulomb interaction to favor the ionicity over the covalent



nature. The space group symmetry of the rocksalt type of structure is  $Fm\bar{3}m$  in the Hermann–Mauguin notation and  $O_h$  in the Schoenflies notation, and the structure is sixfold coordinated (Figure 2.3).

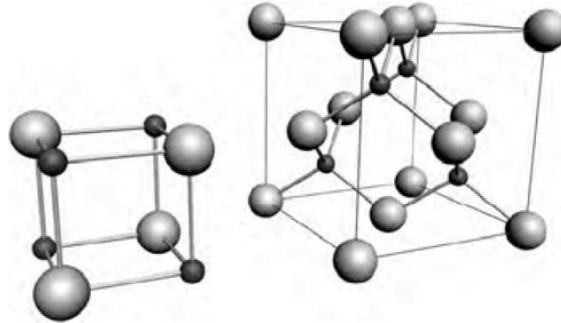
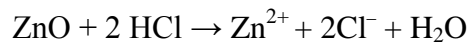


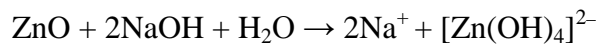
**Figure 2.3** The rock salt (left) and ZB (right) phases of ZnO. O atoms are shown as white spheres, Zn atoms as black spheres.

Crystalline zinc oxide is thermo-chromic, changing from white to yellow when heated and in air reverting to white on cooling. This is caused by a very small loss of oxygen at high temperatures to form the non-stoichiometric  $Zn_{1+x}O$ , where at 800 °C,  $X = 0.00007$ .

Zinc oxide is an amphoteric oxide. It is nearly insoluble in water and alcohol, but it is soluble in (degraded by) most acids, such as hydrochloric acid:



Bases also degrade the solid to give soluble zincates:



Despite its simple chemical formula, ZnO has a very rich defect chemistry [26]. Defect studies have been considered for more than 40 years, but now need revisiting in the context of novel applications using nanostructured materials. In nanostructured ZnO (as well as in other materials), the small length scales and large surface-to-volume ratio mean that surface defects play a stronger role in controlling properties. It is important to understand the relative dominance of carriers introduced by the doping over native defects. ZnO has a relatively open structure, with a hexagonal close packed lattice where Zn atoms occupy half of the tetrahedral sites. All the octahedral sites are empty. Hence, there are plenty of sites for ZnO to accommodate intrinsic (namely Zn interstitials) defects and extrinsic dopants. There are a number of intrinsic defects with different ionization energies. According to the Kröger–Vink notation:  $i$  = interstitial site,  $Zn$  = zinc,  $O$  = oxygen, and  $V$  = vacancy. The terms indicate the atomic sites, and superscripted terms indicate charges, where a dot indicates positive charge, a prime indicates negative charge, and a cross indicates zero charge, with the charges in proportion to the number of symbols. Figure 2.4 shows the defect states within the bandgap of ZnO.

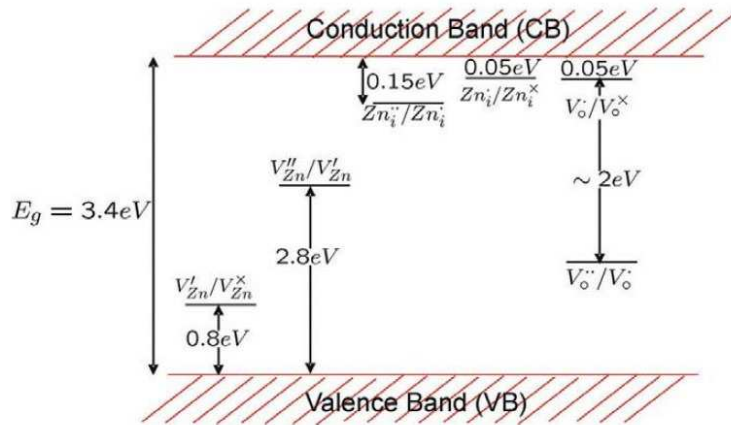
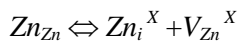


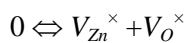
**Figure 2.4** Energy levels of native defects in ZnO. Adapted from [26].

The donor defects are :  $Zn_i^{••}$ ,  $Zn_i^{•}$ ,  $Zn_i^X$ ,  $V_o^{••}$ ,  $V_o^{•}$ ,  $V_o$ , the acceptor defects are:  $V_{Zn}''$ ,  $V_{Zn}'$  and the defect ionization energies vary from  $\sim 0.05$  to  $2.8$  eV [27]. Most ZnO has *n*-type character, even in the absence of intentional doping. Native defects such as O vacancy ( $V_o$ ) or Zn interstitial ( $Zn_i$ ) are often assumed to be the origin of this [28], but the subject remains controversial. Zn interstitials and oxygen vacancies are known to be the predominant ionic defect types, however, which defect dominates in native, undoped ZnO, is still a matter of great controversy [29–31]. As shown below, since both defects donate two electrons, it is difficult to distinguish one from the other using electrical measurements.

Zn interstitials come from the Frenkel reaction:



The oxygen vacancies arise from the Schottky reaction:



Further ionization reactions and equilibrium constants are [27,29]:



The concentration of point defects depends on their formation energies, these have been calculated by several groups of theorists and the results generally agree [32,33]. Recently, Jannotti and Walle [34,35], calculated the formation energy of ZnO point defects for the two limiting zinc chemical

potential values (a)  $\mu_{\text{Zn}} = \mu_{\text{Zn}}^0$  high zinc partial pressure resulting in a Zn-rich crystal; (b) high oxygen partial pressure:  $\mu_{\text{Zn}} = \mu_{\text{Zn}}^0 + \Delta H_{\text{ZnO}}^f$  (assuming that under thermal equilibrium  $\mu_{\text{Zn}} + \mu_{\text{O}} = \Delta H_{\text{ZnO}}^f$ ). The lowest formation energy values are shown in Figure 2.5: the zero of the Fermi level is set to the top of the valence band. Kinks for each defect indicate transitions between different charge states (0, 1, 2).

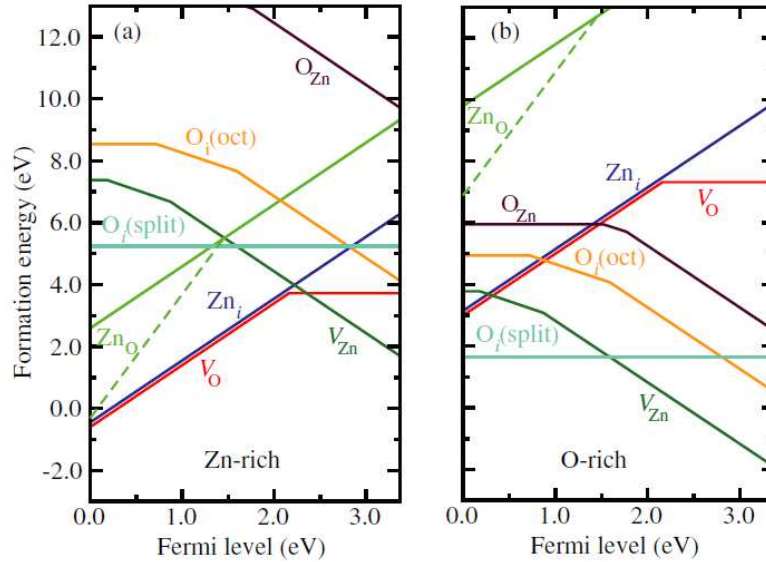


**Figure 2.5** Calculated defect formation energies for main native point defects in ZnO as a function of Fermi level under (A) zinc rich conditions and (B) oxygen-rich conditions [35].

The authors' investigation of native point defects in ZnO is based on density functional theory and, opposite to other works [30,36–39], Jannotti and Walle conclude that  $V_{\text{O}}$ , which have most often been cited as the cause of unintentional doping, are deep rather than shallow donors (red line) and have high formation energies in *n*-type ZnO and are therefore unlikely to form.  $Z_{\text{i}}$  are shallow donors, but they also have high formation energies in *n*-type ZnO (blue line) and are fast diffusers with migration barriers as low as 0.57 eV; therefore they are unlikely to be stable.  $Z_{\text{nO}}$  are also shallow donors but their high formation energies – even under Zn-rich conditions – render them unlikely to be stable under equilibrium conditions. Authors have identified a different low-energy atomic configuration for  $Z_{\text{nO}}$  that may play a role under non-equilibrium conditions such as irradiation (green dotted line).  $O_{\text{Zn}}$  have very high formation energies (purple line) and are unlikely to exist in measurable concentrations under equilibrium conditions.  $O_{\text{i}}$  have high formation energies (orange); they can occur as electrically neutral split interstitials ( $O_{\text{i}}$  split) in semi-insulating and *p*-type materials or as deep acceptors at octahedral interstitial sites in *n*-type ZnO (light blue line). Finally, authors consider  $V_{\text{Zn}}$  as deep acceptors (compensating centers in *n*-type ZnO) and ascribe to them the frequently observed green luminescence [35]. However, note that these formation energies are calculated for bulk ZnO at thermodynamic equilibrium and may not reflect the real-life conditions occurring during the growth of ZnO nanostructures, because of the

high degree of supersaturation typically needed. Controllable n-type doping is easily achieved by substituting Zn with group-III elements Al, Ga, In or by substituting oxygen with group-VII elements chlorine or iodine while reliable p-type doping of ZnO remains difficult. This problem originates from low solubility of p-type dopants and their compensation by abundant n-type impurities, and it is pertinent not only to ZnO, but also to similar compounds GaN and ZnSe. Measurement of p-type in "intrinsically" n-type material is also not easy because inhomogeneity results in spurious signals. Several laboratories have reported p-type ZnO, but their results were difficult to reproduce in other laboratories and hence remain controversial. An elegant summary of all of these efforts is documented by Look and Claflin [40]. The highest room-temperature electron mobility for a bulk ZnO single crystal grown by vapor-phase transport method is reported to be about  $205 \text{ cm}^2/\text{V}\cdot\text{s}$  with a carrier concentration of  $6.0 \cdot 10^{16} \text{ cm}^{-3}$  [41], while, in high crystalline nanostructures, like NR grown by catalyst-free MO-VPE, the reported electron mobility is as high as  $3000 \text{ cm}^2/\text{V}\cdot\text{s}$  [42].

### 2.1.2 Optical properties

Optical properties and processes in ZnO were extensively studied many decades ago [43–60]. The renewed interest in ZnO is enhanced by its prospects in optoelectronics applications owing to its direct wide band gap of 3.37 eV (at room temperature) with large exciton energy of 60 meV and efficient radiative recombination. The strong exciton binding energy, which is much larger than that of GaN (25 meV) and the thermal energy at room temperature (25 meV), can ensure an efficient exciton emission at room temperature under low excitation energy. As a consequence, ZnO is recognized as a promising photonic material in the blue-UV region. According to literature reports, the room temperature PL spectrum typically consists of a UV emission band and a broad “green” luminescence (GL) band, as shown in Figure 2.6.

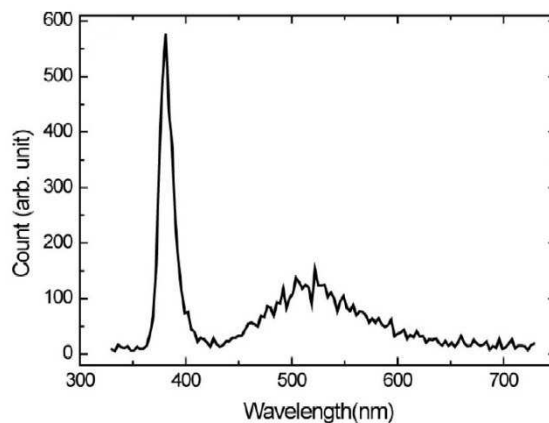


**Figure 2.6** Typical room temperature PL spectrum of ZnO. The NBE emission lies in the UV region (380 nm) and the defect related broad band in the visible (520 nm).

The UV emission band is related to a near band-edge (NBE) transition of ZnO, namely the recombination of the free excitons (FX) and bound exciton complexes (BXC), while the broad emission band between 420 and 700 nm is due to deep level emission (DLE). It is worth noting that this *green* luminescence band (GL, as other authors refer to it) is observed nearly in all samples regardless of growth conditions. The DLE is widely considered a defect emission band but there is still no agreement about its chemistry. Defects represent one of the controversial areas of semiconductors, and ZnO is no exception, as the measurement techniques are not able to correlate electrical or optical manifestation of defects to their origin precisely. The DLE band has been attributed to several defects in the crystal structure such as O-vacancy ( $V_O$ ) [36-39], Zn-vacancy ( $V_{Zn}$ ) [34,35,61-64], O-interstitial ( $O_i$ ) [65], Zn-interstitial ( $Zn_i$ ) [66] and O-antisite ( $O_{Zn}$ ) [67]. Other authors attribute GL band to complex defect involving mostly singly ionized oxygen vacancies ( $V_O^\bullet$ ) [69-72], for example, Vanheusden [38] ascribes GL to radiative transitions from the  $V_O$  donor level, located near the CB, to the VB (D-h type recombination); other authors from  $V_O$  or another donor level to deep  $V_{Zn}$  acceptor level (DAP recombination) [73,74], Kohan from conduction band to the  $V_{Zn}$  acceptor ( $e-A$  type) [75], others report intra-center transitions between two states of  $V_O$  [76] in analogy to what is reported for other oxides, like CaO and MgO [77]. The bottom line is that the green luminescence band strongly depends on growth method and a wide agreement about its origin still lacks among the scientific community.

At low cryogenic temperatures the NBE emission is the dominant radiative channel. Figure 2.7 shows a typical photoluminescence spectrum of n-type bulk ZnO measured at 4.2 K [78]. The luminescence spectrum extends from the UV band edge to the green / orange spectral range. The lines dominating the spectrum originate from BXC recombinations (excitons bound to neutral donors ( $D^0X$ ) and/or acceptors ( $A^0X$ )) followed by longitudinal optical (LO) phonon replicas with an energy separation of 72 meV.

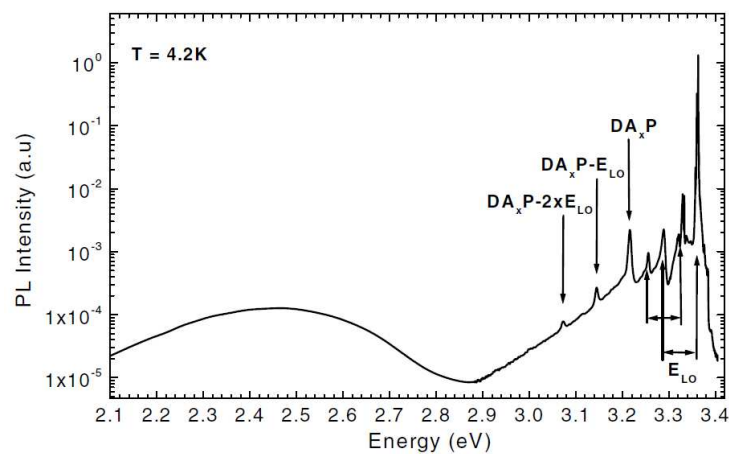


**Figure 2.7** Low temperature ( $T=4.2K$ ) PL spectrum (HeCd excitation) of bulk ZnO showing excitonic, donor acceptor pair (DAP) and deep level emission [78].

The free exciton emission with the A–valence band (FXA), positioned at 3.375 eV, can be seen. And a donor-acceptor-pair (DAP) transition around 3.22 eV is found, which is again followed by phonon replicas. Until now, up to eleven excitonic recombinations where excitons bind to neutral donors and / or acceptors have been observed [44,45,79–81]. The positions of these eleven prominent PL lines in the UV range are listed in Table 2.1, however the chemical nature of the donor and acceptor species still remains unclear.

line	wavelength (nm)	energy (eV)	localisation energy (meV)	donor binding energy (meV)	chemical identity
$A_L^*$	367.12	3.3772			
$A_T^*$	367.26	3.3759			
$I_0$	367.63	3.3725	3.4		
$I_1$	367.71	3.3718	4.1		
$I_{1a}$	368.13	3.3679	8.0		
$I_2^{**}$	368.19	3.3674	8.5		
$I_3^{**}$	368.29	3.3665	9.4		
$I_{3a}$	368.34	3.3660	9.9		
$I_4$	368.34	3.3628	13.1	46.1	H
$I_5$	368.86	3.3614	14.5		
$I_6$	368.92	3.3608	15.1	51.55	Al
$I_{6a}$	368.96	3.3604	15.5	53	
$I_7$	369.01	3.3600	15.9		
$I_8$	369.03	3.3598	16.1	54.6	Ga
$I_{8a}$	369.08	3.3593	16.6		
$I_9$	369.37	3.3567	19.2	63.2	In
$I_{10}$	369.76	3.3531	22.8	72.6	
$I_{11}$	370.28	3.3484	27.5		

**Table 2.1** Free and bound exciton recombinations and related properties. Adapted from [78].

### 2.1.3 Applications

Zinc oxide nanostructures are important technological materials because of their unique properties and potential applications in future nano-electronics, optoelectronics and sensing. Herein is reported a brief list of devices fabricated using ZnO nanostructures as building blocks:

- depletion- and enhancement-mode FET transistors [82–91]
- homojunction LEDs [92–95]
- single nanowire LEDs [96–98]
- hybrid LEDs with p-type polymer [99–102]
- single nanowire cantilevers [103,104]
- lasers [105–110]
- biosensors [111–120]
- piezo nano-generators [121–125]
- hydrogen storage applications [126,127]

In addition to the aforementioned applications, herein a brief overview of ZnO-based gas sensors and photovoltaic (PV) cell devices is reported. ZnO nanostructures have been indeed widely investigated for sensing applications because of their high sensitivity to the chemical environment and high surface area that strongly influences electronic processes. For example ZnO nanowires display high sensitivity even at room temperature, whereas thin-film gas sensors often need to be operated at elevated temperatures. The sensing process is governed by oxygen vacancies on the surface that influence the electronic properties of ZnO. Upon oxidation, via adsorption of molecules such as  $\text{NO}_2$  at vacancy sites that accept electrons, electrons are withdrawn and effectively depleted from the conduction band, leading to a reduction of conductivity. On the other hand, reducing molecules such as  $\text{H}_2$  can react with surface-adsorbed oxygen, leaving behind an electron and a higher conductivity (for a more comprehensive discussion see Ch. 3.2.4a).

The challenge is to sense certain gases selectively. A ZnO NR  $\text{H}_2$  sensor has been developed [128] and the sensitivity of this sensor was improved by sputter deposition of Pd clusters on the ZnO surface. The addition of Pd appears to be effective in the catalytic dissociation of  $\text{H}_2$  into atomic hydrogen, increasing the sensitivity of the device: the sensor detects hydrogen concentrations down to 10 ppm in  $\text{H}_2$  at room temperature, whereas there is no response to  $\text{O}_2$ . By exposing the sensor to air or  $\text{O}_2$ , the conductance recovers to 95% after 20 s [129]. Other researchers used a thick film of ZnO NP for  $\text{H}_2$  sensing [130]. A sensitivity of  $10 \div 1000$  ppm  $\text{H}_2$  was achieved for a Pt-impregnated and 3% Co-doped, ZnO nanoparticle film, at a working temperature of 125 °C.  $\text{O}_2$ ,  $\text{NO}_2$ , and  $\text{NH}_3$  oxidizing sensors in a field-effect transistor geometry of single nanowires have also been demonstrated [131,132]. The oxygen sensitivity is higher for smaller diameter nanowires and can be modulated by the gate voltage. Desorption of adsorbed  $\text{NO}_2$  molecules is observed when a large negative gate voltage is applied. This can be used as a method to refresh the sensor to its original level. An ethanol sensor with good sensitivity and fast response at 300 °C has been demonstrated using Pt interdigitated electrodes [133].

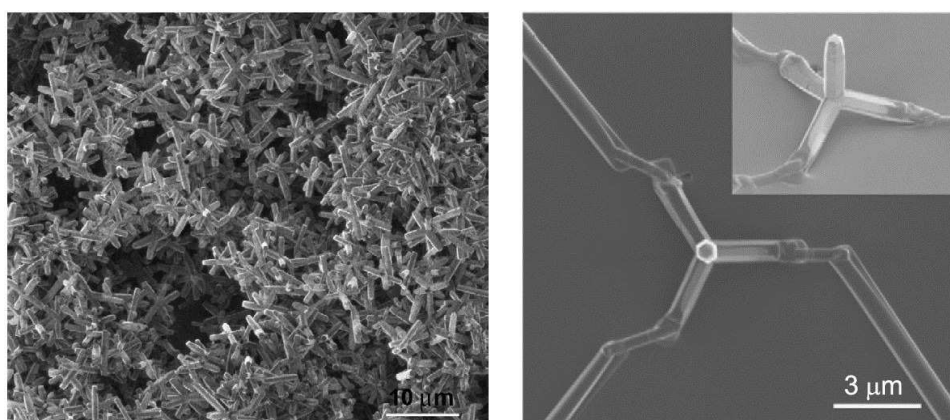


**Figure 2.8** ZnO TP “film” (left) and single ZnO TP contacted on oxidized Si substrate (right). Adapted from [135].

TP films prepared in a flow of humidified Ar show excellent performance in sensing ethanol with a short response time [134]. Lupan and co-workers [135] fabricated a single ZnO TP gas sensor by in situ lift-out technique (Figure 2.8) and studied its ultraviolet (UV) and gas sensing properties demonstrating a fast UV recovery time ( $\sim 20$  s) and good response towards 100ppm of reducing gases like  $H_2$ , i-butane and CO.

Besides gas sensors, ZnO nanostructures are particularly interesting as n-type conductor (or TCO) in excitonic solar cells (XSC), *e.g.* in extremely thin absorber (ETA) and dye sensitized solar cells (DSSC). ZnO has recently emerged as a promising candidate due to its semiconducting properties which are very similar to the most used semiconductor oxide,  $TiO_2$ , but the possibility of obtaining ZnO nanostructures by easy and low-cost techniques renders ZnO a unique and even more interesting alternative [136]. In PV applications, TP employment is far less interesting than NR. TP “film” conduction is dominated by surface transport and hopping takes place, especially at the interface between different TP, thus limiting the mobility. On the other hand, NR are almost ideal structures in XSC. They have high surface / volume ratio, a “corrugated” surface that helps photon absorption and, above all, excellent electron transport properties confirmed by a mobility as high as  $3000\text{ cm}^2/\text{V}\cdot\text{s}$  (when not exposed to air, refer to [42] for details), higher than those of the state-of-the-art planar Si MOSFETs (less than  $1000\text{ cm}^2/\text{V}\cdot\text{s}$ ).

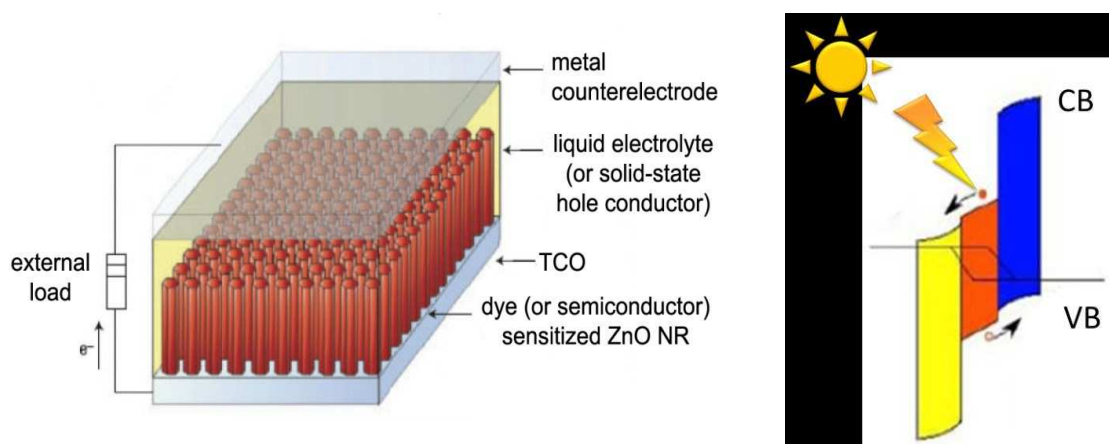


**Figure 2.9** Different elements in a ZnO NR based XSC (left) adapted from [137]. Band gap alignment (right), adapted from [138].

A XSC consist typically of three active elements: a transparent n-type material, a thin absorbing layer (*e.g.* an organic dye in DSSC, a inorganic semiconductor in ETA) and a p-type material. Incident photons are absorbed inside the thin layer (orange in Figure 2.9, right) creating an exciton that diffuses to the interface and separates, transferring the electron to the CB of n-type material (blue in Figure 2.9, right) and then to the TCO; the hole is injected to the VB of p-type material (yellow in Figure 2.9, right), then collected to the metal counter electrode. A schematic view of a XSC based on ZnO NR and band alignment are reported in Figure 2.9.



Despite of the excellent electronic performance of ZnO nanostructures, the use in DSSC is still limited because of ZnO poor chemical stability in both acidic and alkaline environment (often needed to anchor the dye to semiconductor surface). The sensitization process follows the diffusion of the dye, adsorption on the ZnO surface, dissolution of Zn surface atoms and formation of [Dye–Zn<sup>2+</sup>] complex [139]. Such complexes are thought to be responsible for the poor electron injection from the dye [139–141]. However, it must be noted that the issue of ZnO instability arises from the use of dyes previously developed and engineered specifically for TiO<sub>2</sub>, which offers far better performances in aggressive environment. Research on ZnO NR based DSSC is still an hot topic [142–144] albeit reported efficiencies are quite low (1-2% in most cases). Up to now, the best light-to-electricity conversion efficiency ( $\eta$ ) of a DSSC based on ZnO nanostructures is found to be 6.06%, under 100 mW/cm<sup>2</sup> illumination [145].

Since the ETA-solar cell concept was proposed in 2000 by Konenkamp *et al.* [146], continuous and progressive improvements have been achieved. After some interesting reports on the integration of different materials in the ETA-solar cell architecture [147], Lévy-Clément *et al.* [148] demonstrated in 2005 the experimental feasibility of the concept for ZnO/CdSe/CuSCN solar cells (efficiency,  $\eta \sim 2.3\%$  under 360 W/m<sup>2</sup> illumination) based on ZnO nanowire arrays. In 2008, Dittrich's group [149] also used ZnO nanowire arrays as building blocks for ZnO/In<sub>2</sub>S<sub>3</sub>/CuSCN ETA-solar devices, reaching conversion efficiencies up to 3.4%. Similar efficiencies were also reported in the last two years for devices based on nanocrystalline TiO<sub>2</sub> using Sb<sub>2</sub>S<sub>3</sub> as a light absorber, keeping CuSCN as a hole collector [150-152]. Slightly higher conversion efficiencies (up to 5%) have been recently reported using TiO<sub>2</sub> with different hole conductor materials, such as spiro–OmeTAD [153] and P3HT [154]. As concerns ZnO, it is worth mentioning the study reported by Tak *et al.* who functionalized ZnO NR with CdS to extend light absorption in the visible region and produced a ZnO/CdS core-shell nanowire heterostructure array [155]: the cell has a high short-circuit photocurrent density of 7.23 mA/cm<sup>2</sup> with a power conversion efficiency of 3.53% under AM 1.5G illumination at 100 mW/cm<sup>2</sup>. Finally, to my knowledge, the efficiency record, for a ZnO NR based ETA–solar cell, is currently reported by Krunk *et al.* with 4.2% for a ZnO/In<sub>2</sub>S<sub>3</sub>/CuInS<sub>2</sub> nanowire array [156].

## References

- [1] C. W. Bunn, *Proc. Phys. Soc.*, 1935, **47**, 835
- [2] P. H. Miller, *Proc. Int. Conf. on Semiconducting Materials*, 1950, Butterworths Scientific Publications, London, p. 172
- [3] H. E. Brown, *Zinc Oxide, Properties and Applications*, 1976, The New Jersey Zinc Company, New York
- [4] H. Heiland, E. Mollwo, and F. Stöckmann, *Solid State Phys.*, 1959, **8**, 191
- [5] W. Hirschwald *et al*, *Curr. Top. Mater. Sci.*, 1981, **7**, 143
- [6] C. Klingshirn and H. Haug, *Phys. Rep.*, 1981, **70**, 315
- [7] B. Hönerlage, R. Lévy, J. B. Grun, C. Klingshirn, and K. Bohnert, *Phys. Rep.*, 1985, **124**, 161
- [8] Landolt-Börnstein New Series, Group III, Vol. 17B, 22, 41B, edited by U. Rössler (Springer, Heidelberg, Berlin, 1999)
- [9] C. Klingshirn, *Semiconductor Optics*, 3rd edn., 2007, Springer, Heidelberg, Berlin
- [10] Z. L. Wang, *J. Phys.: Condens. Matter*, 2004, **16**, R829
- [11] B. Meyer and D. Marx, *Phys. Rev. B*, 2003, **67**, 035403
- [12] P. W. Tasker, *J. Phys. C: Solid State Phys.*, 1979, **12**, 4977
- [13] O. Dulub, U. Diebold and G. Kresse. *Phys. Rev. Lett.*, 2003, **90**, 016102
- [14] A. Wander, F. Schedin, P. Steadman, A. Norris, R. McGrath, T.S. Turner, G. Thornton, N.M. Harrison, *Phys. Rev. Lett.*, 2001, **86**, 3811
- [15] V. Staemmler, K. Fink, B. Meyer, D. Marx, M. Kunat, S.G. Girol, U. Burghaus and C. Woll, *Phys. Rev. Lett.*, 2003, **90**, 106102
- [16] Y. W. Jun, Y. Y. Jung, and J. Cheon, *J. Am. Chem. Soc.*, 2002, **124**, 615
- [17] D. J. Milliron, S.M. Hughes, Y. Cui, L. Manna, J. Li, L. W. Wang, and A. P. Allivisatos, *Nature* 2004, **430**, 190
- [18] M. Chen, Y. Xie, J. Lu, Y. Xiong, S. Zhang, Y. Qian, X. Liu, *J. Mater. Chem.* 2002, **12**, 748
- [19] J. Gong, S. Yang, H. Huang, J. Duan, H. Liu, X. Zhao, R. Zhang, Y. Du, *Small*, 2006, **2**, 732
- [20] Q. Pang *et al*, *Chem. Mater.* 2005, **17**, 5263
- [21] C. Y. Yeh, Z.W. Lu, S. Froyen, A. Zunger, *Phys. Rev. B*, 1992, **46**, 10086
- [22] R. W. G. Wyckoff, *Crystal Structure*, vol. 1, 2nd ed., Interscience, New York, 1963
- [23] E. Parthe, *Crystal Chemistry of Tetrahedral Structures*, Gordon and Breach, New York, 1964
- [24] Y. Ding, Z. L. Wang, T. Sun, and J. Qiu, *Appl. Phys. Lett.* 2007, **90**, 153510
- [25] L. Lazzarini, G. Salviati, F. Fabbri, *ACS Nano*, 2009, **3** (10), 3158
- [26] F. A. Kröger, *The Chemistry of Imperfect Crystals.*, 1974, 2nd Edition, North Holland, Amsterdam, 73
- [27] J. Han *et al.*, *J. Eur. Ceram. Soc.*, 2002, **22**, 49
- [28] D. C. Look, J.W. Hemsky and J.R. Sizelove, *Phys. Rev. Lett.*, 1999, **82**, 2552
- [29] L. Schmidt-Mende and J. L. MacManus-Driscoll, *Materials Today*, 2007, **10** (5), 40
- [30] M. Willander, O. Nur, J. R. Sadaf, M. I. Qadir, S. Zaman, A. Zainelabdin, N. Bano and I. Hussain, *Materials*, 2010, **3**, 2643

- [31] Y. Gong, T. Andelman, G. F. Neumark, S. O'Brien, I. L. Kuskovsky, *Nanoscale Res Lett*, 2007, **2**, 297
- [32] A. F. Kohan, G. Ceder, D. Morgan, C.G. Van de Walle, *Physical Review B: Condensed Matter*, 2000, **61**, 15019
- [33] C. G. Van de Walle, *Physica B*, 2001, **899**, 308
- [34] A. Janotti and C.G. Van de Walle, *Appl. Phys. Lett.*, 2005, **87**, 122102
- [35] A. Janotti and C.G. Van de Walle, *Phys. Rev. B*, 2007, **76**, 165202
- [36] R. Djelloul, A. Rabadanov, *Turk J Phys*, 2004, **28**, 309
- [37] P. H. Kasai, *Phys. Rev.*, 1963, **130**, 989
- [38] K: Vanheusden, W. L. Warren, C. H. Seager, D. R. Tallant, J. A. Voigt, and B. E. Gnade, *J. Appl. Phys.*, 1996, **79**, 7983
- [39] S. Yamauchi, Y. Goto, and T. Hariu, *J. Cryst. Growth*, 2004, **260**, 1
- [40] D. C. Look, B. Claflin, *phys. stat. sol. (b)*, 2004, **241** (3), 624
- [41] D. C. Look, D.C. Reynolds, J.R. Sizelove, R.L. Jones, C.W. Litton, G. Cantwell, W.C. Harsch, *Solid State Communications*, 1998, **105**, 399
- [42] W. Park, J. S. Kim, G. C. Yi, M. H. Bae, and H.J. Lee, *Appl. Phys. Lett.* 2004, **85**, 5052
- [43] D. C. Reynolds and T.C. Collins, *Physical Review*, 1969, **185**, 1099
- [44] D. G. Thomas, *Journal of Physics and Chemistry of Solids*, 1960, **15**, 86
- [45] J. J. Hopfield, *Journal of Physics and Chemistry of Solids*, 1960, **15**, 97
- [46] Y. S. Park, C. W. Litton, T. C. Collins, D. C. Reynolds, *Physical Review*, 1965, **143**, 512
- [47] B. Segall, *Physical Review*, 1967, **163**, 769
- [48] R. Dinges, D. Froehlich, B. Staginnus, W. Staude, *Phys. Rev. Lett.*, 1970, **25**, 922
- [49] R. J. Collins, D. A. Kleinman, *Journal of Physics and Chemistry of Solids*, 1959, **11**, 190
- [50] R. L. Weiher, *Physical Review*, 1966, **152**, 736
- [51] W. S. Bear, *Physical Review*, 1967, **154**, 785
- [52] W. L. Bond, *J. Appl. Phys.*, 1965, **3**, 1674
- [53] W. Y. Liang, A. D. Yoffe, *Phys. Rev. Lett.*, 1968, **20**, 59
- [54] A. R. Hutson, *J. Appl. Phys.*, 1961, **32**, 2287
- [55] J. L. Freeouf, *Phys. Rev. B*, 1973, **7**, 3810
- [56] O. F. Schirmer, D. Zwingel, *Solid State Communications*, 1970, **8**, 1559
- [57] J. J. Hopfield, D. G. Thomas, *Physical Review Letters*, 1965, **15**, 22
- [58] R. E. Stephens, I. H. Malitson, *J. Research National Bureau of Standards*, 1952, **49**, 249
- [59] Y. S. Park, J. R. Schneider, *Journal of Applied Physics*, 1968, **39**, 3049
- [60] G. E. Heiland, Mollwo, F. Stockmann, *Solid State Physics*, 1959, **8**, 191
- [61] M. Liu, A.H. Kitai, P. Mascher, *J. Lumin.* 1992, **54**, 35
- [62] E. G. Bylander, *J. Appl. Phys.*, 1978, **49**, 1188
- [63] G. Yang, X. Du, J. Wang, B. Wang, Y. Liu, D. Zhang, D. Liu, H. Liu, S. Yang, *J. Cryst. Growth*, 2003, **252**, 275
- [64] O. D. Jayakumar, V. Sudarsan, C. Sudakar, R. Naik, R. K. Vatsa, A. K. Tyagi, *Scripta Materialia*, 2010, **62**, 662

- [65] J. Zhong, A.H. Kitai, P. Mascher, W. Puff, *J. Electrochem. Soc.*, 1993, **140**, 3644
- [66] R. Bahskar, et.al., *Indian Journal of Pure and Applied Physics*, 2009, **47**, 772
- [67] B. Lin and Z. Fu, *Appl. Phys. Lett.*, 2001, **79** (7), 943
- [68] N. O. Korsunskaya, L.V. Borkovskaya, B.M. Bulakh, Khomenkova, V.I. Kushnirenko, and I.V. Markevich, *Journal of Luminescence*, 2003, **733**, 102
- [69] S. A. Studenikin, N. Golego, M. Cocivera, *Appl. Phys.*, **84** (4), 2287
- [70] K. Vanheusden, W.L. Warren, C.H. Seager, D.R. Tallant, J.A. Voigt, B.E. Gnade, *J. Appl. Phys.*, 1996, **79**, 7983
- [71] F. H. Leiter, H.R. Alves, N.G. Romanov, D.M. Hoffman, B.K. Meyer, *Phys. B*, 2003, **201**, 340
- [72] X. L. Wu, G. G. Siu, C. L. Fu, and H. C. Ong, *Appl. Phys. Lett.*, 2001, **78**, 2285
- [73] B. Guo, Z.R. Qiu, K.S. Wong, *Appl. Phys. Lett.*, 2003, **82**, 2290
- [74] H. J. Egelhaaf and D. Oelkrug, *J. Cryst. Growth*, 1996, **161**, 190
- [75] A. F. Kohan, G. Ceder, D. Morgan and G.C. Van de Walle, *Phys. Rev. B*, 2000, **61**, 15019
- [76] F. H. Leiter, H.R. Alves, A. Hofstaetter, D.M. Hoffmann, B.K. Meyer, *phys. stat. sol. (b)*, 2001, **226**, R4
- [77] P. Edel, C. Hennies, Y. Merle, D'Aubigne, R. Romestain, and Y. Twarowski, *Phys. Rev. Lett.*, 1972, **28**, 1268
- [78] B. K. Meyer et al., *phys. stat. sol. (b)*, 2004, **241**, 231
- [79] D. C. Reynolds and T.C. Collins, *Physical Review*, 1969, **185**, 1099
- [80] E. Tomzig and H. Helbig, *J. Lumin.*, 1976, **14**, 403
- [81] D. C. Reynolds, C. W. Litton, and T. C. Collins, *Phys. Rev.* 1965, **140**, A1726
- [82] Z. Y. Fan, D. W. Wang, P. C. Chang, W. Y. Tseng, J. G. Lu, *Appl. Phys. Lett.*, 2004, **85**, 5923
- [83] Z. Y. Fan and J. G. Lu, *Appl. Phys. Lett.* 2005, **86**, 123510
- [84] P. C. Chang, Z. Fan, C.J. Chen, D. Stichtenoth, C. Ronning, J.G. Lu, *Appl. Phys. Lett.* 2006, **89**, 133113
- [85] Y. W. Heo, L.C. Tien, Y. Kwon, D.P. Norton, S.J. Pearton, B. S. Kang, F. Ren, *Appl. Phys. Lett.*, 2004, **85**, 2274
- [86] J. Goldberger, D. J. Sirbuly, M. Law, and P. Yang, *J. Phys. Chem. B*, 2005, **109**, 9
- [87] W. I. Park, J.S. Kim, G.C. Yi, M.H. Bae, and H.J. Lee, *Appl. Phys. Lett.* 2004, **85**, 5052
- [88] S. Ju, K. Lee, D. B. Janes, M.-H. Yoon, A. Facchetti, and T. J. Marks, *Nano Lett.* 2005, **5**, 2281
- [89] W. K. Hong, D.K. Hwang, I.K. Park, G. Jo, S. Song, S.J. Park, T. Lee, B.J. Kim, E. A. Stach, *Appl. Phys. Lett.* 2007, **90**, 243103
- [90] Y. K. Park, H. S. Choi, J.H. Kim, J.H. Kim and Y.B. Hahn, *Nanotechnology*, 2011, **22**, 185310
- [91] P. Atanasova, D. Rothenstein, J. J. Schneider, R. C. Hoffmann, S. Dilfer, S. Eiben, C. Wege, H. Jeske, J. Bill, *Adv. Mater.*, 2011, **23**, 4918
- [92] G. T. Du, W. F. Liu, J. M. Bian, L. Z. Hu, H. W. Liang, X. S. Wang, A. M. Liu, and T. P. Yang, *Appl. Phys. Lett.*, 2006, **89**, 052113
- [93] M. T. Chen, M.P. Lu, Y.J. Wu, J. Song, C Y. Lee, M. Y. Lu, *Nano Lett.*, 2010, **10** (11), 4387
- [94] J. C. Sun, J. Z. Zhao, H. W. Liang, J. M. Bian, L. Z. Hu, H. Q. Zhang, X. P. Liang, W. F. Liu, and G. T. Du, *Appl. Phys. Lett.* 2007, **90**, 121128

- [95] X. Dong, H. C. Zhu, B. L. Zhang, X. P. Li, G. T. Du, *Semicond. Sci. Technol.*, 2007, **22**, 1111
- [96] J. Bao *et al.*, *Nano Lett.*, 2006, **6**, 1719
- [97] Y. Q. Bie *et al.*, *Adv. Mater.*, 2010, **22**, 4284
- [98] M. A. Zimmler, T. Voss, C. Ronning, and F. Capasso, *Appl. Phys. Lett.* 2009, **94**, 241120
- [99] C. Y. Chang, F.C. Tsao, C.J. Pan, G.C. Chi, H.T. Wang, *Appl. Phys. Lett.* 2006, **88**, 173503
- [100] R. Könenkamp *et al.*, *Nano Lett.*, 2005, **5**, 2005
- [101] A. El-Shaer, A. Dev, J.P. Richters, S.R. Waldvogel, J. Waltermann, W. Schade, T. Voss, *Phys. Status Solidi B*, 2010, **247** (6), 1564
- [102] Y. He, J. A. Wang, X. B. Chen, *J. Nanopart. Res.*, 2010, **12**, 169
- [103] W. Lee, *et al.*, *Acta Mater.*, 2004, **52**, 3949
- [104] M. A. Khaderbad, *et al.*, *Nanotechnology*, 2012, **23**, 025501
- [105] M. H. Huang, *et al.*, *Science*, 2001, **292**, 1897
- [106] K. Govender, *et al.*, *Adv. Mater.*, 2002, **14**, 1221
- [107] J. H. Choy *et al.*, *Adv. Mater.*, 2003, **15**, 1911
- [108] D. Vanmaekelbergh and L. K. van Vugt, *Nanoscale*, 2011, **3**, 2783
- [109] D. J. Gargas, M. E. Toimil-Molares and P. Yang, *J. Am. Chem. Soc.*, 2009, **131** (6), 2125–2127
- [110] S. Chu *et al.*, *Nature Nanotechnology*, 2011, **6**, 506
- [111] B. S. Kang, F. Ren, Y.W. Heo, L.C. Tien, D.P. Norton, S.J. Pearton, *Appl. Phys. Lett.*, 2005, **86**, 112105
- [112] P. D. Batista and M. Mulato, *Appl. Phys. Lett.*, 2005, **87**, 143508
- [113] R. Bashir, J. Z. Hilt, O. Elibol, A. Gupta and N. A. Peppas, *Appl. Phys. Lett.*, 2002, **81**, 3091
- [114] A. Wei, X.W. Sun, J.X. Wang, Y. Lei, X.P. Cai, C.M. Li, Z.L. Dong and W. Huang, *Appl. Phys. Lett.*, 2006, **89**, 123902
- [115] N. Kumar, A. Dorfman and J. Hahm, *Nanotechnology*, 2006, **17**, 2875
- [116] X. Cai, N. Klauke, A. Glidle, P. Cobbold, G.L. Smith, J.M. Cooper, *Anal. Chem.*, 2002, **74**, 908
- [117] M. Ahmad, C. Pan, L. Gan, Z. Nawaz and J. Zhu, *J. Phys. Chem. C*, 2010, **114**, 243
- [118] Y. T. Wang, L. Yu, Z. Q. Zhu, J. Zhang, J. Z. Zhu, C. Fan, *Sens. Actuators, B*, 2009, **136**, 332
- [119] T. Kong, Y. Chen, Y. Ye, K. Zhang, Z. Wang and X. Wang, *Sens. Actuators, B*, 2009, **138**, 344
- [120] X. W. Sun, J. X. Wang and A. Wei, *J. Mater. Sci. Technol.*, 2008, **24**, 649
- [121] Z. L. Wang, and J.H. Song, *Science*, 2006, **312** , 242
- [122] K. Momeni, G. M. Odegard, and R. S. Yassar, *J. Appl. Phys.* 2010, **108**, 114303
- [123] C. T. Pan, Z.H. Liu, Y.C. Chen, C.F. Liu, *Sensors and Actuators A: Physical*, 2010, **159** (1), 96
- [124] C. Majidi, M. Haataja and D. J. Srolovitz, *Smart Mater. Struct.*, 2010, **19**, 055027
- [125] A. Kumar, H. Gullapalli, K. Balakrishnan, A. Botello-Mendez, R. Vajtai, M. Terrones, P.M. Ajayan, *Small*, 2011, **7** (15), 2173
- [126] Q. Wan, C. L. Lin, X. B. Yu and T. H. Wang, *Appl. Phys. Lett.*, 2004, **84**, 124
- [127] P. Hui, L. Jizhong, S. Han, F. Yuanping, P. Cheekok, L. Jianyi, *Nanotechnology*, 2006, **17**, 2963
- [128] H. T. Wang *et al.*, *Appl. Phys. Lett.*, 2005, **86**, 243503
- [129] L. C. Tien *et al.*, *Appl. Phys. Lett.*, 2005, **87**, 222106

- [130] C. S. Rout et al., *Solid State Commun.*, 2006, **138**, 136
- [131] Z. Fan et al., *Appl. Phys. Lett.*, 2004, **85**, 5923,
- [132] Z. Fan and J.G. Lu, *Appl. Phys. Lett.*, 2005, **86**, 123510
- [133] Q. Wan et al., *Appl. Phys. Lett.*, 2004, **84**, 3654
- [134] C. Xiangfeng et al., *Chem. Phys. Lett.*, 2005, **401**, 426
- [135] O. Lupan, L. Chowa, G. Chaid, *Sensors and Actuators B*, 2009, **141**, 511–517
- [136] L. E. Greene, M. Law, J. Goldberger, F. Kim, J. C. Johnson, Y. Zhang, R. J. Saykally, P. Yang, *Angew. Chem., Int. Ed.*, 2003, **42** (26), 3031
- [137] L. E. Greene, J.C. Johnson, R. Saykally, P.D. Yang, *Nat. Mater.* 2005, **4**, 455
- [138] R. Tena-Zaera, A. Katty, S. Bastide, C. Lévy-Clément, B. O'Regan and V. Muñoz-Sanjosé. *Thin Solid Films*, 2005, **483**, 372
- [139] I. Gonzalez-Valls and M. Lira-Cantu, *Energy Environ. Sci.*, 2009, **2**, 19–34
- [140] K. Keis, C. Bauer, G. Boschloo, A. Hagfeldt, K. Westermark, H. Rensmo, H. Siegbahn, *J. Photochem. Photobiol., A*, 2002, **148**, 57
- [141] M. Quintana, T. Edvinsson, A. Hagfeld and G. Boschloo, *J. Phys. Chem. C*, 2007, **111**, 1035
- [142] S. H. Ko et al., *Nano Lett.*, 2011, **11**, 666
- [143] S. Chu, Dongdong Li, P.-C. Chang, and J. G. Lu, *Nanoscale Res Lett.*, 2011, **6** (1), 38
- [144] E. Guillen, E. Azaceta, L. M. Peter, A. Zukal, R. Tena-Zaera and J. A. Anta, *Energy Environ. Sci.*, 2011, **4**, 3400
- [145] C. Y. Lin, Y.H. Lai, H. W. Chen, J. G. Chen, C. W. Kung, R. Vittala, K. C. Ho, *Energy Environ. Sci.*, 2011, **4**, 3448
- [146] K. Ernst, M.C. Lux-Steiner, R. Konenkamp, *16th European Photovoltaic Solar Energy Conference*, 2000, 63–66
- [147] K. Ernst, A. Belaidi and R. Könenkamp, *Semicond. Sci. Technol.*, 2003, **18**, 475
- [148] C. Lévy-Clément, R. Tena-Zaera, M. A. Ryan, A. Katty and G. Hodes, *Adv. Mater.*, 2005, **17**, 1512–1515
- [149] A. Belaidi, T. Dittrich, D. Kieven, J. Tornow, K. Schwarzburg and M. Lux-Steiner, *Phys. Status Solidi RRL*, 2008, **2**, 172
- [150] Y. Itzhaik, O. Niitsoo, M. Page and G. Hodes, *J. Phys. Chem. C*, 2009, **113**, 4254
- [151] C. Choné and G. Larramona, *French Patent 2899385*, (05 October, 2007)
- [152] S. Nezu, G. Larramona, C. Chon, A. Jacob, B. Delatouche, D. Péré and C. Moisan, *J. Phys. Chem. C*, 2010, **114**, 6854
- [153] S. J. Moon, Y. Itzhaik, J.-H. Yum, S. M. Zakeeruddin, G. Hodes and M. Grätzel, *J. Phys. Chem. Lett.*, 2010, **1**, 1524
- [154] J. A. Chang, J.H. Rhee, S.H. Im, Y.H. Lee, H.J. Kim, S.I. Seok, M.K. Nazeeruddin and M. Grätzel, *Nano Lett.*, 2010, **10**, 2609
- [155] Y. Tak, S.J. Hong, J.S. Lee and K. Yong, *J. Mater. Chem.*, 2009, **19**, 5945
- [156] I. Mora-Seró, S. Giménez, F. Fabregat-Santiago, E. Azaceta, R. Tena-Zaera and J. Bisquert, *Phys. Chem. Chem. Phys.*, 2011, **13**, 7162

## 2.2 Synthesis of semiconductor nanoparticles

Research on nanoparticles, including synthesis, characterization of the structural, chemical and physical properties, assembly into 1-, 2- and 3-dimensional architectures, represents a fundamental cornerstone of nanoscience and nanotechnology because of their application in various fields of technology. Many different synthesis techniques gave access to nanomaterials with a wide range of compositions, well-defined and uniform crystallite sizes, unprecedented crystallite shapes, and complex assembly properties. Although gas-phase processes are successfully employed for production of large quantities of nanopowders [1–3], it seems that liquid-phase syntheses are more flexible with regard to the controlled variation of structural, compositional, and morphological features of the final nanomaterials. Liquid phase routes include co-precipitation, hydrolytic as well as non-hydrolytic sol-gel processes, hydrothermal or solvothermal methods, template synthesis and bio-mimetic approaches [4]. However, often the synthesis protocol for a targeted material involves not just one, but a combination of several of these methods.

The synthesis of particles with control over size, shape and size distribution is not a special feature of nanoscience, but has been an integral part of colloid chemistry for decades. However, for quite a while, most efforts invested in the preparation of uniform, finely dispersed particles were essentially considered as due to the curiosity of colloid scientists, and, with the exception of polymer colloids (latexes), without any practical significance [5,6]. With the advent of nanoscience this attitude has changed completely. Nowadays, there is no doubt about the fundamental role of uniform powders in many areas of science and technology. Parallel to the development of highly advanced analytical tools, enabling the characterization of small structures with atomic resolution, the size of the targeted objects and devices decreased rapidly below the 100 nm limit. The preparation of nanostructures on such a small size scale makes great demands to the synthesis methodology and therefore it is a great challenge to develop a “synthetic chemistry” of nanoparticles that is as precise as that used to make molecules [7]. Two strategies are generally pursued to prepare nanostructures: the *top-down* approach, using physical methods such as photolithography and related techniques, and the *bottom-up* employing physical and chemical approaches. Miniaturization by lithographic techniques is mainly driven by microelectronics industry and has reached a level, at which feature sizes of around 10 nm can be generated [8,9]. However, upon down-scaling the costs associated with lithography equipment and operating facilities rapidly increase, and the features achievable are on the one hand rather coarse and irregular on an atomic scale, and on the other hand difficult to extend onto non-planar surfaces or to 3D structures. The *bottom-up* approach, making use of both specific and non-covalent interactions (e.g. hydrogen bonding, electrostatic and van der Waals – VdW – interactions)

between molecules or colloidal particles to assemble discrete nanoscale structures, represents a valuable alternative on the way to further miniaturization of electronic devices and to the fabrication of complex 3D architectures [10-11]. The use of nanoparticles as building blocks has the advantage that highly advanced synthesis methodologies provide control over crystallite size and shape with a precision well beyond that of *top-down* lithography. The *bottom-up* assembly of nanoparticles may prove to be a solution to the technological challenges faced by the semiconductor industry [12].

From a scientific point of view, the use of nanoparticles as “artificial atoms” to form spatial arrays, extending over several length scales, is particularly fascinating because these superlattices are expected to have unprecedented and striking collective properties resulting from the interactions between the nano-building blocks that cannot be found in the individual constituents, thus opening up an almost indefinite playground to design novel multi-component materials [13–16].

The availability of reproducible colloidal synthesis protocols for nanoparticles whose compositional, structural, morphological and surface characteristics are well-defined and uniform, is a prerequisite on the way to such complex superstructures. Research on the preparation of inorganic nanoparticles and nanostructures has always been, and still will be, at the heart of nanoscience for the next few years. The significance of nanoparticle synthesis is also reflected in the fact that many groundbreaking findings that can be regarded as milestones in the history of nanoscience are directly related to synthetic work, for example the discovery of carbon nanotubes [17], the synthesis of well-defined quantum dots [18], or the shape control of CdSe nanocrystals [19]. The size – and shape – dependent physical and chemical properties of semiconductor nanoparticles [20–22] as well as the increased surface-to-volume ratio of nanoscale materials in general raised expectations for a better performance of nanomaterials compared to their bulk counterparts in many applications. Intensive works on semiconductor-doped glasses [23], on the photocatalytic properties of colloidal CdS [24,25] and on the “absorption of light in a semiconductor sphere” [26] finally resulted in the description of the quantum size effect more than 25 years ago. Brus et al. found that CdS crystallites in the size range of a few nanometers did not have the electronic spectra of the bulk material, even though they exhibited the same unit cell and bond length as the bulk material [27]. These findings opened up a new and exciting possibility to tailor the chemical and physical properties of a material: new applications and properties are a result of controlling crystallite size and shape on a nanometer scale rather than of altering the composition [28].



## 2.2.1 Nucleation, growth and dimensional control

### 2.2.1a Homogeneous nucleation

According to simple solubility considerations, a precipitate will be formed when the product of the concentrations of anions and cations exceeds the solubility product. From another point of view, phase transformation occurs when the free energy of the new phase is lower than that of the initial (metastable) phase. However, there are many examples where the ion product exceeds  $K_{sp}$ , yet no precipitation occurs - the phenomenon of supersaturation. The solubility product also does not provide information on how the particles of the precipitate form - nucleation. Nucleation involves various physical processes, and both thermodynamic and kinetic aspects must be considered.

Homogeneous nucleation can occur due to local fluctuations in the solution, whether in concentration, temperature, or other variables. The first stage in growth is collision between individual ions or molecules to form embryos (embryos are nuclei that are intrinsically unstable against redissolution). Embryos grow by collecting individual species (may be ions, atoms, or molecules in general) that collide with them. They may also grow by collisions between embryos; however, unless the embryo concentration is large, this is less likely [29].

These embryos may redissolve in the solution before they have a chance to grow into stable particles (nuclei). Because of the high surface areas, and therefore high surface energies of such small nuclei, they are very reactive and thermodynamically unstable against redissolution (critical nuclei). They may, however, be kinetically stabilized by low temperatures, which increase their lifetime, possibly enough for them to grow to a size where they are thermodynamically stable. This is an important reason why smaller particles can be formed at lower temperatures in a precipitation reaction; the subcritical embryos last long enough to grow into stable particles, while at higher temperatures they would redissolve, reducing the density of nuclei. This results in an increase of the particle size, since there is more reactant per nucleus.

The critical radius,  $r^*$ , is the size where the embryo (critical nucleus) has a ½ chance of either redissolving or growing into a stable nucleus; it is determined by the balance between the surface energy required to form the embryo and the energy released when a spherical particle is formed [30]:

$$E_S = 4\pi R^2 \sigma$$
$$E_V = \frac{4}{3}\pi R^3 \rho L$$

Where  $\sigma$  is the surface energy per unit area  $\rho$  is the density of the solid phase and  $L$  the heat of the solution. The balance between  $E_S$  and  $E_V$  is shown in Figure 2.10. The typical size of  $r^*$  is about 100 units, between 1 and 2 nm in diameter. Solvent molecules can adsorb on the embryos too, and

change their surface energy: the critical radius will therefore depend not only on the material of the nucleating phase but also on the solution content.

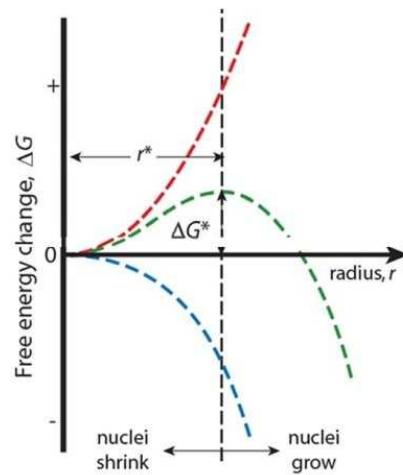


**Figure 2.10** Balance between surface and volume energy as a function of particle dimension.

### 2.2.1b Heterogeneous Nucleation

In heterogeneous nucleation, subcritical embryos (or even individual ions) can adsorb onto the substrate. The energy required to form an interface between the embryo and the solid substrate will usually be less than that required for homogeneous nucleation, where no such interface exists. Therefore heterogeneous nucleation is energetically preferred over homogeneous nucleation and can occur near equilibrium saturation conditions, compared with the high degree of supersaturation often required for homogeneous nucleation. These subcritical nuclei can grow, either by surface diffusion or by material addition from solution. It should also be noted that nuclei that are subcritical in solution may be supercritical when adsorbed on a substrate. This is a consequence of reduced contact between nucleus and solution as well as stabilization of the adsorbed nucleus [29]. It was noted earlier that even individual ions may adsorb onto a surface. More specifically, depending on the surface chemistry of the substrate, individual ions or molecular species may actually be chemisorbed, creating a nucleus for reaction and further growth. Pure homogeneous nucleation is probably less common than might appear from the above discussion. Because of the greater ease of nucleation on a solid phase than homogeneously, any solid matter in the solution will act as a preferential nucleation center.

### 2.2.1c Growth

Once (stable) nuclei have formed, there are several ways in which they can increase in size. One is a continuation of the process of embryo growth discussed earlier: adsorption of ionic species from the solution onto the nucleus. Crystal growth of this type can be considered a self-assembling process. Thus for CdS, either  $\text{Cd}^{2+}$  or  $\text{S}^{2-}$  will adsorb – since a crystal, and in particular a polar one, is made up of different faces, the adsorption properties of each may be different – and therefore both types of ions may adsorb to give an additional CdS *unit*.

This process can continue until either all the ions of any one type are used up or growth is blocked, *e.g.*, by aggregation or by blocking of the crystal surface by a foreign adsorbed species. Another mechanism for crystal growth is known as Ostwald ripening. If a small nucleus or embryo is close to a larger crystal, the ions formed by (partial) dissolution of the smaller and less stable crystal can be incorporated into the larger crystal. As the smaller crystal becomes even smaller, its dissolution will become ever more favorable and eventually it will disappear. The result is that the larger crystals grow at the expense of the smaller ones [32].

If the concentration of particles is sufficiently high, then the probability of collisions between these particles becomes high. This can result in either aggregation or coalescence. When two particles approach each other, the VdW force of attraction between them will often cause them to stick together. This can continue until a large particle (large in relation to the original particle size) comprising the individual particles has formed. This is the process of aggregation, and the resulting large particle is called an *aggregate*. (in colloidal chemistry, the alternative terms of *flocculation* and *floc* are often encountered). The properties of the aggregate may be similar to those of the individual particles in some ways (such as X-Ray diffraction peak broadening, quantum size effects) and very different in others (*e.g.*, light scattering, sedimentation). In an aggregate, there are grain boundaries between individual crystallites. However, in some cases, particularly if the temperature is high enough to allow appreciable diffusion of the crystal atoms, surface diffusion may occur where two (or more) particles have aggregated, resulting in the formation of a neck. This is termed *coalescence*, and may continue until one large particle is formed from the original two or more particles [29].

If nucleation occurs in a very short time, whereas growth occurs separately, often over a much longer time but without further nucleation, then the size distribution is likely to be narrow, since all the original nuclei should be of similar size and grow at the same rate. The opposite case, where nucleation and growth occur simultaneously, usually results in a wide size distribution. Homogeneous nucleation normally requires a supersaturated solution, while growth can occur close to the saturation concentration. Therefore rapid nucleation can occur if a large supersaturation is rapidly reached. This nucleation lowers the concentration of reactants below that needed to cause further nucleation. If one of the reactants is supplied at a low concentration *after*

nucleation has occurred (such as by *in situ* homogeneous formation in the solution), then growth can occur without further nucleation, resulting in a narrow size distribution.

### 2.2.1d Dimensional control

The requirements for monodispersity are a high rate of nucleation, leading to the burst formation of nuclei in a short period, an initial fast rate of growth of these nuclei to reduce the concentration below the nucleation concentration rapidly and an eventual slow rate of growth leading to a long growth period compared to the nucleation period.

While investigating the formation of sulfur suspensions, La Mer [32] postulated the necessity of temporal separation of the nucleation and growth phases for the formation of monodisperse colloids. La Mer burst nucleation is described with reference to the La Mer plot shown below (Figure 2.11), which describes the evolution of supersaturation ( $S$ ) with time, where supersaturation is defined as the ratio between the monomer concentration in the *solution* and the equilibrium monomer *surface* concentration.

During phase I, the supersaturation lies somewhere below the critical supersaturation required for the kinetic barrier to homogenous nucleation to be surpassed and nucleation to occur ( $S = S_c$ ). During phase II some event increases the supersaturation of solution above the critical level, and the rate of nucleation increases to some finite level. In the case where further monomer is not supplied to replace that consumed in nucleation, the supersaturation will eventually fall back below the critical supersaturation, causing further nucleation to cease. Phase III is now entered, where monomer continues to be consumed solely by growth of existing particles until eventually equilibrium is reached ( $S = 1$ ). Provided that Phase II (nucleation) is brief, and temporally distinct from Phase III (growth), all nuclei emerge from Phase II with a uniform size – a condition identified as a prerequisite for monodispersity of particles at the end of Phase III (growth) [33]. When the monomer concentration falls below the critical level for nucleation (critical supersaturation level), nucleation ends. A colloidal particle growth can be considered as a sequence of monomer diffusion towards the surface followed by reaction of the monomers at the surface of the nanocrystal.

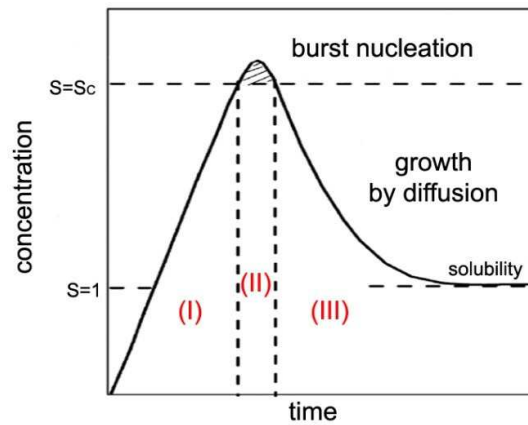


**Figure 2.11** La Mer diagram. Adapted from [32].

The interfacial energy (the energy associated with an interface due to differences between the chemical potential of atoms in an interfacial region and atoms in neighboring bulk phases) plays a key role in the growth process. For a solid species present at a solid / liquid interface, the chemical potential of a particle increases with decreasing particle size and the equilibrium solute concentration for a small particle is much higher than for a large particle, as described by the Gibbs–Thompson equation [34]:

$$\ln\left(\frac{S_C}{S_\infty}\right) = \gamma V \left( \frac{R_1^{-1} + R_2^{-1}}{kT} \right)$$

Where  $S_C$  and  $S_\infty$  are the solubility of a curved solid surface and a flat surface respectively.  $\gamma$  is the surface energy,  $V$  the volume of the particle and  $R$  are the curvature radii of the surface / particle. The equilibrium concentration of the nanocrystal in the liquid phase is dependent on the local curvature of the solid phase. The resulting concentration gradients lead to transport of the solute from the small particles to the larger particles. Differences in the local equilibrium concentrations, due to variations in curvature, set up concentration gradients provide the driving force for the growth of larger particles at the expense of smaller particles [35]. This coarsening effects, controlled either by mass transport or diffusion, are often referred as the Ostwald ripening process. It is the most predominant growth mechanism and was first quantified by Lifshitz and Slyozov [36], followed by a related work by Wagner [37], known as the LSW theory. Beside the theoretical formulation, the key idea of separating the nucleation stage and growth process in time is often used to obtain nearly monodisperse particles. In most of the cases in recent times, synthesis has been carried out by injecting one of the components into the remaining ones, in a very short time (see the Ch. 2.2.2a). This is to ensure that the entire nucleation takes place in that short time, followed by a much slower growth process, thereby attempting to separate the two stages temporally.

So, the key to achieve efficient control of particle growth, is to decouple the nucleation and growth processes. Primary particles grow by addition of soluble species coming from the solution. These species attach themselves at the surface and, if necessary, diffuse along the surface to the position corresponding to a minimum energy.

Nanometric particles are subject to Brownian motion and hence often collide with one another. Then they tend to associate via weak bonds (agglomeration) or strong bonds (aggregation) to form larger particles. This is the well-known phenomenon leading to flocculation in colloidal dispersions. To avoid such processes, which lead to the formation of polydispersed powders, collisions between primary particles must be avoided [31].

VdW forces are the primary source of attraction between colloidal particles. These forces are always present between particles of similar composition. Therefore, a colloidal dispersion is said to be stable only when a sufficiently strong repulsive force counteracts VdW attraction [38]. There are three different possible origins for VdW forces: permanent dipole-permanent dipole (Keesom) forces, the permanent dipole-induced dipole (Debye) interactions and transitory dipole-transitory dipole (London) forces. The first two are very short-range interactions, but the London forces are longer range attractions. Since only London forces contribute to the long-range attraction between colloidal particles, the magnitude and range of the Van der Waals–London (VdWL) attraction are decisive in determining strategies for stabilizing colloid particles. For many colloid systems, the range of significant VDWL attraction is between 5 and 10 nm. Since there are always strong, long-range attractive forces between similar colloidal particles, it is necessary to provide a long range repulsion between the particles to impart stability. This repulsion should be at least as strong as the attractive force and comparable in range of the attractive interaction. Stability can be obtained by surrounding colloidal particles:

- with an electrical double layer (electrostatic or charge stabilization).
- with adsorbed or chemically attached polymeric molecules (steric stabilization).

Combination of the first two stabilization mechanisms lead to electro-steric stabilization (ionic polymers).

An effective way to counterbalance the VDWL attraction between colloidal particles in polar liquids is to provide the particles with Coulombic repulsion. In liquid dispersion media, ionic groups can adsorb to the surface of a colloidal particle through different mechanisms to form a charged layer. To maintain electroneutrality, an equal number of counterions with the opposite charge will surround the colloidal particles and give rise to overall charge-neutral double layers. In charge stabilization, it is the mutual repulsion of these double layers surrounding particles that provides stability.

Charge stabilization is not effective in media of low dielectric constant (the vast majority of organic solvents), and steric stabilization is required to maintain dispersed particles in a stable non-flocculated state. Steric stabilization relies on the adsorption of a layer of polymer chains on the surface of the particle. For polymers with molecular weights  $> 10000$ , the chain dimensions are comparable to, or in excess of, the range of the VDWL attraction. Hence, as long as they can generate repulsion, these polymer molecules can be used to impart colloid stability.

As particles approach each other these adsorbed polymeric chains intermingle and in so doing they lose a degree of freedom which they would otherwise possess [31,33]. This loss of freedom is expressed, in thermodynamic terms, as a reduction in entropy, which is unfavorable and provides the necessary barrier to prevent further attraction. Alternatively one can consider that, as the chains intermingle, solvent is forced out from between particles. This leads to an imbalance in solvent concentration which is resisted by osmotic pressure tending to force solvent back between the particles, thus maintaining their separation.

The use of a steric stabilizer rather than an electrostatic one has to be considered in each case, however steric stabilization has several distinct advantages: it is relatively insensitive to the presence of electrolytes (while the electrostatic is strongly dependent on the ionic strength of the solution) and is effective in both aqueous and non-aqueous dispersion media (since it's insensitive to the solvent dielectric constant).

## 2.2.2 Cadmium sulphide

During the past two decades, the synthesis or preparation of II–VI semiconductor nanoparticles has experienced an enormous development, to the point where the published material related to the topic has become virtually unmanageable. It all started in the early 1980s [39–46] where the absorption spectrum of a colloidal solution of size-quantized CdS nanocrystals were reported for the first time. The absorption onset is shifted considerably to higher energies with respect to the bulk bandgap of CdS (515 nm). In addition, the sol emits light upon excitation at 390 nm, which was also a matter of investigation in this report. The first correct interpretation of the observed blue shift of the absorption as a quantum mechanical effect stems from Brus [47] when, in the framework of the effective mass approximation, the shift in kinetic energy of the charge carriers due to their spatial restriction to the volume of the nanometer-sized semiconductors was calculated. Incidentally, it should be noted that comparable experimental [48] and theoretical studies [49] were carried out almost simultaneously on the I–VII compound CuCl in the Soviet Union. Since then hundreds of scientific papers have been published on about the surface

chemistry, photodegradation, and catalytic processes in colloidal semiconductor particles. In 1993, another milestone in the preparation of II–VI semiconductor nanocrystals was the study of Murray, Norris and Bawendi [18], whose synthesis was based on the pyrolysis of organometallic reagents after injection into a hot coordinating solvent. This approach is currently known as the hot injection method.

### 2.2.2a Hot injection method

In 1993, Murray et al. published the synthesis of monodisperse CdX (X=S,Se, Te) nanocrystallites in molten trioctylphosphine oxide (TOPO) [18]. This work provided the basis for the so-called *hot-injection* method, which involves the injection of a room-temperature (“cold”) solution of precursor molecules into a hot solvent in the presence of surfactants [50] (Figure 2.12). The fast injection of the precursor induces a high degree of supersaturation, resulting in a short burst of nucleation. During the nucleation process the precursor concentration in the solution decreases abruptly. The drop in temperature, due to the injection of the “cold” reactants, and the low concentration of unreacted remaining precursor prevent any further nucleation events. In a next step, the temperature is carefully increased to a value which allows the slow growth of the nuclei to larger nanoparticles, however still suppresses further nucleation. The separation of nucleation and growth is a prerequisite to synthesizing monodispersed nanoparticles [52], and therefore the hot-injection method generally leads to nanoparticles with a narrow size distribution of  $\sigma \sim 10\%$ . If size distributions narrower than 5% are required, then a size-selection process has usually to be applied. The surfactants, typically consisting of a coordinating head group and a long alkyl chain, adsorb reversibly to the surfaces of the growing nanoparticles, and thus provide a dynamic organic capping layer that stabilizes the nanoparticles in solution and also mediates their growth [53]. The use of surfactants with selectivity towards specific crystal faces, or mixtures of surfactants with different binding affinities to the nanocrystal surface allow excellent control over crystal size, size distribution and morphology [54].

Finally, the nanocrystals can be precipitated by adding a nonsolvent. After their separation from the reaction liquid, the nanoparticles can be redispersed in suitable, usually apolar, organic solvents, forming stable colloidal suspensions. The surfactants used during the synthesis and now attached to the surface of the nanocrystals can be exchanged against other ones in a post-synthetic step, allowing not only the chemical modification of the surface properties of the nanoparticles in general, but also the tailoring of the dispersibility behavior in different solvents [55].



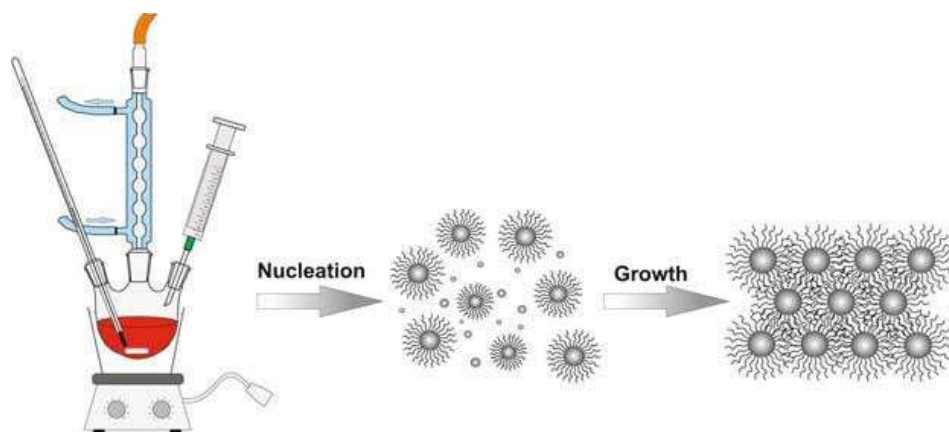


**Figure 2.12** Experimental set-up and reaction scheme for the hot-injection method [51].

Recently, Zhang *et al.* [56] reported the formation of highly monodispersed and regular shaped CdS NP using thioacetamide (TAA) and cadmium stearate as sulfur and cadmium sources respectively, through a hot-injection method. CdS NP were controllably synthesized by adjusting reaction conditions, such as reaction time, injection / growth temperatures and TAA concentration. Dodecylamine, a strong electron-donating long-chain alkyl amine, was selected as the reaction solvent, not only because its nucleophilicity facilitates to generate reactive sulfur species from TAA, but because it can dissolve readily TAA at relatively low temperature such as 30°C and thus facilitate the formation and hot injection of homogeneous TAA stock solution. TEM images of CdS NP self-assembled NP into a hexagonal superlattice is shown in Figure 2.13.

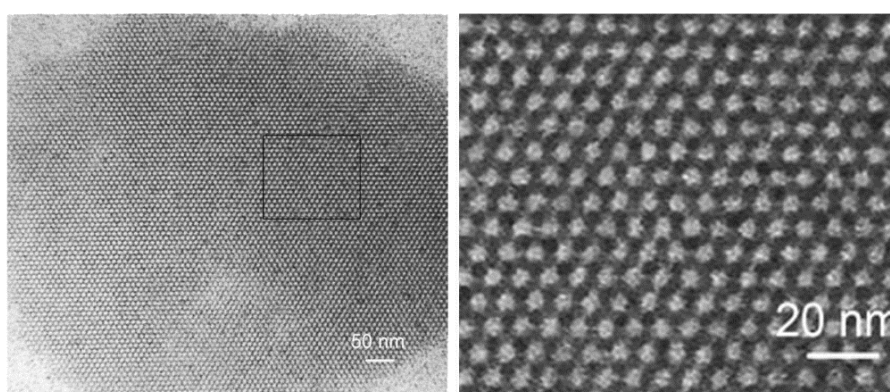


**Figure 2.13** Highly monodispersed CdS NP assembled in a closed-packed hexagonal superlattice. Low magnification (left) and high magnification view (right). Adapted from [56].

The hot-injection method proved to be particularly versatile for preparing II-VI and III-V semiconductor nanocrystals [50,52], furthermore it has also been extended to the synthesis of metal oxides NP too (refer to Ch. 2.2.3b for further reading).

## 2.2.2b Chemical Bath Deposition (CBD)

Whereas hot-injection is nowadays the leading technique to produce semiconductor NP, CBD is widely used to deposit semiconductor thin films. CBD in fact refers to the deposition of films on a solid substrate from a reaction occurring in a solution (almost always aqueous). Using the prototypical CdS as an example, a Cd salt in solution can be converted to CdS by adding sulphide ions (e.g., as  $\text{H}_2\text{S}$  or  $\text{Na}_2\text{S}$ ); CdS immediately precipitates (unless the solution is very dilute – a few millimolar or less – in which case CdS often forms as a colloidal sol). Another pathway for CdS formation, one that does not require free sulphide ions, is decomposition of a Cd-thiocomplex (a compound that binds to Cd through a sulphur atom) [29].

In CBD, the trick (or at least one of them) is to control the rate of these reactions so that they occur slowly enough to allow the CdS either to form gradually on the substrate or to diffuse there and adhere to the substrate itself (or other solid phases suspended in the solution, heterogeneous nucleation) rather than aggregate into larger particles in solution and precipitate out (homogeneous nucleation).

This rate control can be accomplished by a slow release of sulphide ions in the deposition solution. The rate of dissociation of sulphide, and therefore reaction rate, can be controlled through a number of parameters, in particular the concentration of sulphide-forming precursor, solution temperature, and pH.

The CdS forms through a number of different possible pathways: simple ionic reaction between  $\text{Cd}^{2+}$  and sulphide ion; topotactic conversion of  $\text{Cd}(\text{OH})_2$ , which may be present in the deposition solution, to CdS by sulphide; and decomposition of a complex between Cd (whether as a free ion or as a Cd compound, e.g.,  $\text{Cd}(\text{OH})_2$ ) and the sulphide precursor (often thiourea, which, like other chalcogenide precursors, also acts as a complexant for metal ions).

Although CBD can be carried out in both acidic and alkaline solutions, most CBD reactions have been carried out in alkaline solutions. Therefore to prevent (at least bulk) precipitation of metal hydroxides in the deposition solution, the metal ion must be complexed. There is a very wide range of possible complexing agents available; the most used are intermediate in complexing strength – not too weak, in order to prevent bulk precipitation of hydroxide, but not too strong, which may prevent interaction with the desired substrate (i.e. glass, growing film or another solid phase) altogether.

Even if CBD technique is very versatile and applies to a wide variety of materials (selenides, phosphides, sulphides, oxides, tellurides, halides...) there are two main mechanism to explain how it takes place [29]:

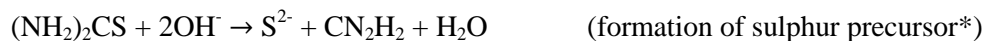
- *Ion-by-Ion Mechanism:*

The simplest mechanism, often assumed to be the operative one in general, is commonly called the ion-by-ion mechanism, since it occurs by sequential ionic reactions.

The basis of this mechanism is simply given by:  $\text{Cd}^{2+} + \text{S}^{2-} \rightarrow \text{CdS}$

When the ion product  $[\text{Cd}^{2+}][\text{S}^{2-}]$  exceeds  $10^{-28}$  ( $K_{\text{sp}}$  the solubility product), then, neglecting kinetic problems of nucleation, CdS will form as a solid phase. If the reaction is carried out in alkaline solution (by far the most common case), then a complex (ammonia) is needed to keep the metal ion in solution and to prevent the hydroxide from precipitating out. Alkaline environment is not mandatory but it enhances dramatically deposition rate.

Since the decomposition of the chalcogenide precursor can be controlled over a very wide range (by temperature, pH, concentration), the rate of CdS formation can likewise be well controlled. Of course, the CdS should form a film on the substrate and (at least ideally) not precipitate in the solution.



(\*The cyanamide ( $\text{CN}_2\text{H}_2$ ) can decompose further to urea and then to ammonium carbonate)

- *Hydroxide Mechanism:*

In this case, the initial step in the deposition is adhesion of the hydroxide to the substrate. This hydroxide is then converted into CdS by reacting with sulphur (precursor), forming a primary deposit of CdS clusters. As the reaction proceeds more  $\text{Cd}(\text{OH})_2$ , CdS and partially converted hydroxide diffuses / convects to the substrate where it deposits on the surface. Since the initial nucleation of hydroxide occurs homogeneously in the solution, the CdS also is formed homogeneously and therefore usually precipitates out in the solution to a large extent. This precipitation occurs if the isolated crystals aggregate to a sufficient extent to form large flocs.



Hydroxide mechanism is widely used as a standard protocol to form CdS thin films on glass. This is because of ammonia complexing properties that helps  $\text{Cd}^{2+}$  ions to stick into the substrate and promotes adhesion [29], moreover the alkaline solution helps thiourea dissociation and reduces the

deposition time of the growing film. For ion-by-ion growth, when no alkaline solution is used, the dissociation rate of thiourea is the kinetic limiting stage hence accurate control of temperature (that regulates  $S^{2-}$  concentration) can be used to avoid bulk precipitation.

It is known from previous work [57] that thiourea thermally decomposes without the need of neither acidic or alkaline environment to produce ammonium and thiocyanate ions. A possible reaction intermediate to the formation of CdS is reported to be [58]:



### 2.2.2c Remarks

Solution chemistry is the most versatile and highly flexible technique to tune the size, the shape and dimensional distribution of nanocrystals. Since Murray [18] studies, the hot injection method has become the leading synthetic route to the formation of highly monodisperse semiconductor nanostructures: compound variety is huge, from metal to semiconductor, while with regards to the morphology, case record is even more extensive. The main advantage of the injection method concerns the possibility to obtain *single* nanostructures surrounded by ligands that help the dispersion in the chosen “solvent”. Moreover, interactions between ligand molecules drives the deposition of ordered superstructures upon controlled solvent evaporation. When a deposition of (thin) film is the goal, the CBD process provides a facile and well-rounded approach for the deposition of many binary and ternary compounds, mainly in aqueous environment in both acidic and alkaline environment.

## References

- [1] A. Gurav, T. Kodas, T. Pluym, Y. Xiong, *Aerosol Sci. Technol.* 1993, **19**, 411
- [2] F. E. Kruis, H. Fissan, A. Peled, *J. Aerosol Sci.* 1998, **29**, 511
- [3] R. Strobel, S.E. Pratsinis, *J. Mater. Chem.* 2007, **17**, 4743
- [4] B. L. Cushing, V.L. Kolesnichenko, C.J. O'Connor, *Chem. Rev.* 2004, **104**, 3893
- [5] E. Matijevic, *Annu. Rev. Mater. Sci.* 1985, **15**, 483
- [6] E. Matijevic, *Chem. Mater.* 1993, **5**, 412
- [7] G. M. Whitesides, *Small* 2005, **1**, 172
- [8] B. D. Gates, Q. Xu, M. Stewart, D. Ryan, C. G. Willson, G. M. Whitesides, *Chem. Rev.* 2005, **105**, 1171
- [9] S. E. Thompson, S. Parthasarathy, *Materials Today* 2006, **9**, 20
- [10] G. A. Ozin, *Chem. Commun.*, 2000, **6**, 419
- [11] G. M. Whitesides, B. Grzybowski, *Science*, 2002, **295**, 2418
- [12] W. Lu, C.M. Lieber, *Nature Materials*, 2007, **6**, 841
- [13] C. B. Murray, C.R. Kagan, M.G. Bawendi, *Annu. Rev. Mater. Sci.*, 2000, **30**, 545
- [14] A. L. Rogach, D.V. Talapin, E.V. Shevchenko, A. Kornowski, M. Haase, H. Weller, *Adv. Funct. Mater.* 2002, **12**, 653
- [15] E. V. Shevchenko, D.V. Talapin, N.A. Kotov, S. O'Brien, C.B. Murray, *Nature*, 2006, **439**, 55
- [16] H. Zhang, E.W. Edwards, D. Wang, H. Mohwald, *Phys. Chem. Chem. Phys.*, 2006, **8**, 3288
- [17] S. Iijima, *Nature*, 1991, **354**, 56
- [18] C. B. Murray, D.J. Norris, M.G. Bawendi, *J. Am. Chem. Soc.*, 1993, **115**, 8706
- [19] X. G. Peng, L. Manna, W.D. Yang, J. Wickham, E. Scher, A. Kadavanich, A.P. Alivisatos, *Nature*, 2000, **404**, 59
- [20] A. Henglein, *Chem. Rev.*, 1989, **89**, 1861
- [21] A. P. Alivisatos, *J. Phys. Chem.*, 1996, **100**, 13226
- [22] C. Burda, X. Chen, R. Narayanan, M.A. El-Sayed, *Chem. Rev.*, 2005, **105**, 1025
- [23] A. I. Ekimov, A.A. Onushchenko, V.A. Tsekhomskii, *Fizika i Khimiya Stekla*, 1980, **6**, 511
- [24] M. Greatzel, K. Kalyanasundaram, E. Borgarello, D. Duonghong, *Angew. Chem. Int. Ed.*, 1981, **20**, 987
- [25] A. Henglein, B. Bunsenges., *Phys. Chem.* 1982, **86**, 301
- [26] A. L. Efros, *Sov. Phys. Semicond.*, 1982, **16**, 772
- [27] R. Rossetti, J.L. Ellison, J.M. Gibson, L.E. Brus, *J. Chem. Phys.* 1984, **80**, 4464
- [28] C. Burda, X. Chen, R. Narayanan, M.A. El-Sayed, *Chem. Rev.*, 2005, **105**, 1025
- [29] G. Hodes, *Chemical solution deposition of semiconductor films*, 2002, Marcel Dekker Inc., New York
- [30] T. Hyeon et al., *Angew. Chem. Int. Ed.*, 2007, **46**, 4630
- [31] R. Nagarajan, T. A. Hatton, *Nanoparticles: Synthesis, Stabilization, Passivation, and Functionalization*, 2008, American Chemical Society, Washington DC
- [32] V. K. LaMer and R. H. Dinegar, *J. Am. Chem. Soc.*, 1950, **72**, 4847

- [33] J. H. Beal, *Synthesis and Characterisation of Metal Chalcogenide Nanocrystals*, PhD Thesis 2009, Victoria University of Wellington
- [34] C. N. R. Rao, A. Müller, A. K. Cheetham, in *Nanomaterials Chemistry*, 2007, WILEY-VCH Verlag GmbH, Weinheim, Ch. 4.
- [35] T. Sugimoto, *Adv. Colloid Interface Sci.*, 1987, **28**, 165
- [36] I. M. Lifshitz, V. V. Slyozov, *J. Phys. Chem. Solids*, 1961, **19**, 35
- [37] C. Wagner, *Z. Elektrochem.*, 1961, **65**, 581
- [38] J. T. G. Overbeek, *Discuss. Faraday Soc.*, 1966, **42**, 7
- [39] K. Kalyanasundaram, E. Borgarello, D. Duonghong, and M. Graetzel, *Angew. Chem., Int. Ed. Engl.*, 1981, **20**, 987
- [40] J. R. Darwent and G. Porter, *J. Chem. Soc. Chem. Commun.*, 1981, 145
- [41] R. Rossetti and L.E. Brus, *J. Phys. Chem.*, 1982, **86**, 4470
- [42] D. Duonghong, J. Ramsden and M. Graetzel, *J. Am. Chem. Soc.*, 1982, **104**, 2977
- [43] J. Kuczynski and J.K. Thomas, *Chem. Phys. Lett.*, 1982, **88**, 445
- [44] M. A. Fox, B. Lindig, and C.C. Chem, *J. Am. Chem. Soc.*, 1982, **104**, 5828
- [45] A. Henglein, *Phys. Chem.*, 1982, **86**, 301
- [46] R. Katzschmann, R. Kranold and A. Rehfeld, *Phys. Status Solidi A*, 1977, **43**, K161
- [47] L. E. Brus, *J. Chem. Phys.*, 1983, **79**, 5566
- [48] A. I. Ekimov and A.A. Onushchenko, *Sov. Phys. - Semiconductors*, 1982, **16**, 775
- [49] A. L. Efros, *Sov. Phys. - Semiconductors*, 1982, **16**, 772
- [50] C. De Mello Donega, P. Liljeroth, D. Vanmaekelbergh, *Small*, 2005, **1**, 1152
- [51] M. Niederberger, N. Pinna, *Metal Oxide Nanoparticles in Organic Solvents*, 2009, Springer-Verlag, London Limited,
- [52] J. Park, J. Joo, S.G. Kwon, Y. Jang, T. Hyeon, *Angew. Chem. Int. Ed.*, 2007, **46**, 4630
- [53] C. Burda, X. Chen, R. Narayanan, M.A. El-Sayed, *Chem. Rev.* 2005, **105**, 1025
- [54] S. Kumar, T. Nann, *Small*, 2006, **2**, 316
- [55] A. H. Latham, M.E. Williams, *Acc. Chem. Res.* 2008, **41**, 411
- [56] L. J. Zhang, X.C. Shen,, H. Liang, S. Guo, Z. H. Liang, *Journal of Colloid and Interface Science* 2010, **342**, 236
- [57] W. H. R. Shaw, D.G. Walker, *Nature*, 1956, 5769
- [58] B. Ptaszyński, E. Skiba, J. Krystek, *Journal of Thermal Analysis and Calorimetry*, 2001, **65**, 231

## 2.2.3 Iron Oxides

Iron oxides have received increasing attention due to their extensive applications, such as magnetic recording media, catalysts, pigments, gas sensors, optical devices, and electromagnetic devices. They exist in a rich variety of structures (polymorphs), crystallographic phases (Table 2.2) and hydration states; therefore until recently, knowledge of the structural details, thermodynamics and reactivity of iron oxides has been lacking. Furthermore, physical (magnetic) and chemical properties commonly change with particle size and degree of hydration.

Compound	Crystallographic system	Space group	Stacking of close packed anions	Unit cell dimensions nm				Z
				a	b	c	$\beta^\circ$	
Goethite*	Orthorhombic	Pnma	ABAB [001]	0.9956	0.30215	0.4608		4
Lepidocrocite*	Orthorhombic	Bbmm	ABCABC [015]	0.3071	1.2520	0.3873		4
Akaganéite	Monoclinic	I2/m	bcc	1.056	0.3031	1.0483	90.63	8
Schwertmannite	Tetragonal	P4/m		1.066		0.604		
Feroxyhyte	Hexagonal	P3ml	ABAB [001]	0.293		0.456		2
$\delta$ -FeOOH	Hexagonal	P3ml	ABAB [001]	0.293		0.449		1
HP FeOOH	Orthorhombic	Pn2 <sub>1</sub> m		0.4932	0.4432	0.2994		2
Ferrihydrite	Hexagonal	P31c; P3	ABAB [001]	0.2955		0.937		4
Hematite	Hexagonal (Rhombohedral)	R $\bar{3}$ c	ABAB [001]	0.5034		1.3752		6
Magnetite	Cubic	Fd3m	ABCABC [111]	0.8396				8
Maghemite	Cubic	P4 <sub>3</sub> 2	ABCABC [111]	0.83474				8
	Tetragonal	P4 <sub>1</sub> 2 <sub>1</sub> 2		0.8347		2.501		24
Wüstite	Cubic	Fm3m		0.4302 (high Fe) 0.4275 (low Fe)				
$\epsilon$ -Fe <sub>2</sub> O <sub>3</sub>	Orthorhombic	Pna2 <sub>1</sub>		0.5095	0.879	0.9437		8
Fe(OH) <sub>2</sub>	Hexagonal	P3ml		0.3262		0.4596		1
Bernalite	Orthorhombic	Immm		0.7544	0.7560	0.7558		8

**Table 2.2** Crystallographic data for iron oxide phases [13].

In particular, magnetic iron oxide nanoparticles (magnetite, maghemite) with size up to 20 nm in diameter represent an important class of artificial nanostructured materials. Their magnetic properties change drastically with the sizes as magnetic anisotropic energy,  $KV$ , where  $K$  is the magnetic anisotropic constant and  $V$  is the particle volume, becomes comparable to the thermal energy,  $kT$ , resulting in moment randomization and superparamagnetism [1,2]. Such superparamagnetic nanoparticles have great potential for biomedical applications [3–8]. Their magnetic signal far exceeds that from any of the known bio-entities, making them readily identified in the ocean of biomolecules. Without external magnetic field, they show no net magnetic moment, facilitating their long-term stability in various dispersion media. They are smaller than or comparable to a cell (1–10  $\mu\text{m}$ ), a virus (20–450 nm), a protein (5–50 nm), or a

gene (2 nm wide and 10–100 nm long). These, plus their capability of being manipulated under an external magnetic field, provide controllable means of magnetically tagging of all biomolecules, leading to highly efficient bioseparation / biodelivery [7] and highly sensitive biolabeling and magnetic resonance imaging (MRI) contrast enhancement [8–10]. To apply superparamagnetic nanoparticles for biomedical applications, the nanoparticles should be monodisperse to have uniform physical and chemical properties for controlled biodistribution, bioelimination, and contrast effects. The magnetic nanoparticles should also have high magnetic moment, and can be so modified that they are capable of binding specifically to a biological entity and able to withstand various physiological conditions. Iron oxide nanoparticles, due to their chemical and magnetic stability and low level of toxicity in biological systems, have been widely tested for their use in biomedicine [3,11] as the body can process excess iron [12].

Iron oxide-based materials have been found to be good candidates as cheap and efficient catalysts too, especially in environmental catalysis where magnetite, maghemite and hematite are often used. Iron oxide NP have been used in the oxidation of CO and the oxidative pyrolysis of biomass [14] or biomass model compounds [15,16] and has been shown to be a very active (although unstable) catalyst for the oxygen evolution process as well as other related processes, such as water splitting, chlorine evolution, the oxidation of organic molecules, and the hydrogen peroxide decomposition [17]. Although direct photocatalytic water splitting is still a challenging problem, extensive efforts have been made to investigate iron oxides (hematite in particular) for hydrogen production [18–20]. Moreover, heterogeneous catalysts based on magnetic mixed iron oxides ( $\text{MO}\cdot\text{Fe}_2\text{O}_3$ ; M: Fe, Co, Cu, Mn) were used for the degradation of several synthetic dyes [21]. In the following is reported a brief description of the three iron oxide phases that have more relevance in the aforementioned applications, namely hematite, magnetite and maghemite.

### $\alpha\text{-Fe}_2\text{O}_3$ (hematite)

Hematite is the most stable iron oxide under ambient conditions. Because of its magnetic properties and chemical stability, hematite is a material with scientific and technological importance. Regarding the hematite crystals, a rhombohedrally centered hexagonal structure of corundum-type is well documented. The crystalline structure of hematite is featured by a close-packed oxygen lattice where  $\text{Fe}^{3+}$  ions occupy two thirds of the octahedral sites [12].  $\alpha\text{-Fe}_2\text{O}_3$  is a red compound, which crystallizes in the  $R\text{-}3c$  space group (refer to Figure 2.14 for crystal structure model). Like other iron oxides, superexchange leads to antiferromagnetic ordering in  $\alpha\text{-Fe}_2\text{O}_3$  [22]. Consequently, despite having a magnetic moment of 5  $\mu\text{B}$  / formula unit,  $\alpha\text{-Fe}_2\text{O}_3$  displays only very weak magnetization ( $\sim 0.36 \text{ A m}^2 \text{ kg}^{-1}$ ) above  $-13^\circ\text{C}$ , due to a slight canting of the antiparallel spins [23]. Its non-toxicity, low cost and relatively good stability render hematite a type of



desirable candidate material for various applications such as gas sensors, photoanodes for photo oxidation of water, and photocatalytic oxidation [25].

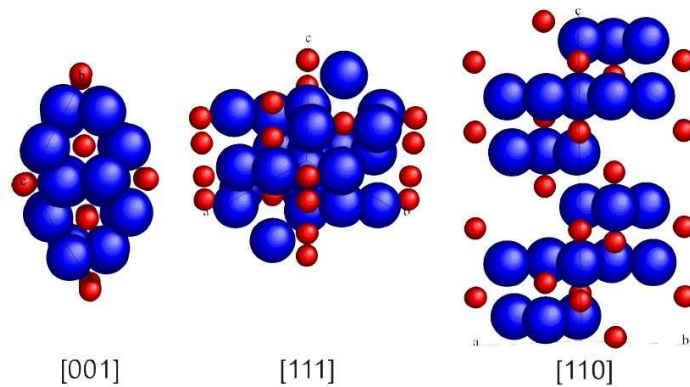


**Figure 2.14** Crystal structure of hematite. Iron is shown in red, oxygen is shown in blue [24].

### Fe<sub>3</sub>O<sub>4</sub> (magnetite)

The Fe<sub>3</sub>O<sub>4</sub> magnetic structure is composed of two magnetic sublattices (called A and B), the magnetic interaction is due to superexchange interactions mediated by the oxygen anions. In ferrimagnets, the magnetic moments of the A and B sublattices are not equal and result in a net magnetic moment. Ferrimagnetism is therefore similar to ferromagnetism. It exhibits all the hallmarks of ferromagnetic behavior- spontaneous magnetization, Curie temperatures, hysteresis, and remanence. However, ferro- and ferrimagnets have very different magnetic ordering [26]. Magnetite is a well-known ferrimagnetic material but it was considered a ferromagnet until Néel studies, in the 1940's, provided the theoretical framework for understanding ferrimagnetism.

Fe<sub>3</sub>O<sub>4</sub> (magnetite) is a black mixed Fe<sup>2+</sup> / Fe<sup>3+</sup> oxide, with an inverse spinel structure (Fe<sup>III</sup>[Fe<sup>II</sup>Fe<sup>III</sup>]O<sub>4</sub>, space group *Fd-3m*), in which one in eight of the tetrahedral holes in the oxide *fcc* lattice are occupied by Fe<sup>3+</sup> ions, and one in two of octahedral holes are occupied by Fe<sup>2+</sup> and Fe<sup>3+</sup> ions, in equal numbers (Figure 2.15). The large oxygen ions are close packed in a cubic arrangement and the smaller Fe ions fill in the gaps. There are 2 kind of gaps: tetrahedral site where Fe ion is surrounded by four oxygens and octahedral site in which Fe ion is surrounded by six oxygens. The tetrahedral and octahedral sites form the two magnetic sublattices, A and B respectively. The spins on the A sublattice are antiparallel to those on the B sublattice. The two crystal sites are very different and result in complex forms of exchange interactions of the iron ions between and within the two types of sites. The structural formula for magnetite is [Fe<sup>3+</sup>]<sub>A</sub>[Fe<sup>3+</sup>,Fe<sup>2+</sup>]<sub>B</sub> O<sub>4</sub>, this particular arrangement of cations on the A and B sublattice is called an inverse spinel structure. With negative AB exchange interactions, the net magnetic moment of magnetite is due to the B-site Fe<sup>2+</sup>. At room temperature electron hopping between Fe<sup>2+</sup> and Fe<sup>3+</sup>

ions in octahedral sites leads to moderate conductivity [27]. Below the so-called Verwey transition point, which occurs at 120 K, a distinct increase in resistivity is observed, which is attributed to localization of  $\text{Fe}^{2+}$  and  $\text{Fe}^{3+}$  ions. Accompanying the increase in resistivity is a structural alteration from cubic to monoclinic symmetry, and the disappearance of magnetocrystalline anisotropy. [28]. Superexchange leads to antiferromagnetic coupling between each sublattice (tetrahedral and octahedral sites), resulting in an overall observed magnetic moment of  $4.1 \mu\text{B}$  / formula unit, results due to the imbalance of the 30 two sublattices (ferrimagnetism). The Néel temperature of the phase is  $577^\circ\text{C}$ , and the saturation magnetization of the bulk material is  $84 \text{ A m}^2 \text{ kg}^{-1}$  [22].

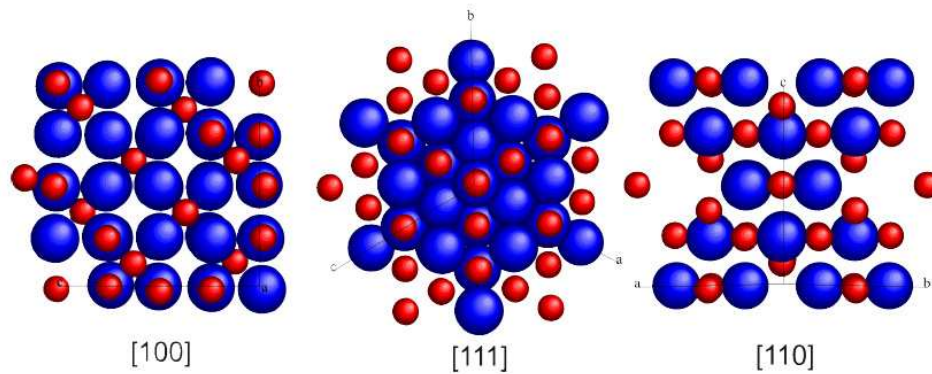


**Figure 2.15** Crystal structure of magnetite ( $Fd-3m$ ). Iron is shown in red, oxygen is shown in blue [24].

### $\gamma\text{-Fe}_2\text{O}_3$ (maghemite)

$\gamma\text{-Fe}_2\text{O}_3$  (maghemite) is a metastable brown solid with a defect spinel structure. Within each unit cell there are  $21\frac{1}{2}$   $\text{Fe}^{3+}$  ions, eight of which occupy tetrahedral sites. The remaining are distributed randomly in the octahedral sites *i.e.* there are  $2\frac{2}{3}$  cation vacancies distributed in octahedral sites [29]. Ordering of the cation vacancies can result in either a primitive cubic base structure ( $P4_232$ ), or tetrahedral symmetry superlattice ( $P4_12_12$ ) with a tripling of the cell in the  $c$  direction ( $c = 3a$ ) [30]. The formation of a solid solution of  $\text{Fe}_3\text{O}_4 + \gamma\text{-Fe}_2\text{O}_3$  has been also observed, where the  $fcc$  symmetry of the spinel was retained [31]. The crystal structure model for  $\gamma\text{-Fe}_2\text{O}_3$  containing randomly located vacancies, where the  $Fd-3m$  space group is retained, is essentially identical to  $\text{Fe}_3\text{O}_4$ , and is shown above in Figure 2.15. Shown below is the crystal structure model for the primitive cubic ( $P4_132$ ) alteration (Figure 2.16). Oxidation of  $d^6 \text{Fe}^{2+}$  to  $d^5 \text{Fe}^{3+}$  increases the observed magnetic moment to  $5.0 \mu\text{B}$ , however the saturation magnetization at  $74 \text{ Am}^2\text{kg}^{-1}$  is slightly lower than that of  $\text{Fe}_3\text{O}_4$  [22]. When heated under vacuum  $\gamma\text{-Fe}_2\text{O}_3$  can be converted to  $\text{Fe}_3\text{O}_4$ , but when heated in air, it will convert to  $hcp \alpha\text{-Fe}_2\text{O}_3$ .

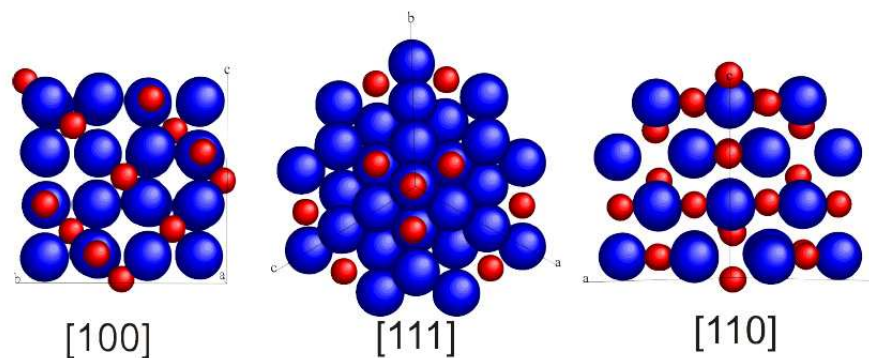


**Figure 2.16** Crystal structure of cubic maghemite ( $P4_32$ ). Iron is shown in red, oxygen in blue [24].

Both maghemite and magnetite exhibit a spinel crystal structure, but while the latter contains both  $\text{Fe}^{2+}$  and  $\text{Fe}^{3+}$  cations, in maghemite all the iron cations are in trivalent state, and the charge neutrality of the cell is guaranteed by the presence of cation vacancies. It is widely accepted in the literature from X-ray [32–34], neutron diffraction [35–37], Mössbauer [33,38] and magnetization studies [39–41] that the cation vacancies are distributed on the octahedral cation sites in the molecular formula of  $(\text{Fe}^{3+})[\text{Fe}^{3+}_{5/3}\square_{1/3}]\text{O}_4$ , where  $\square$  denotes a vacancy [42]. The nature and degree of ordering of the iron vacancies in the octahedral sites has been the subject of investigations for several decades. If the cation vacancies were randomly distributed over the octahedral sites, as it was initially assumed, the space group would be  $Fd3m$  like in magnetite [43]. The first indication of a departure from the  $Fd3m$  symmetry was reported by Haul and Schoon [44], who noticed extra reflections in the powder diffraction pattern of maghemite prepared by oxidizing magnetite.

The *partial* ordering of vacancies forms a structure basically similar to that of  $\text{LiFe}_5\text{O}_8$  (space group  $P4_32$ ) with vacancies concentrated on the site corresponding to Li [45]. Van Oosterhout and Rooijmans [46] first suggested a spinel tetragonal superstructure with  $c/a = 3$ , where the Fe atoms are *completely* ordered. A neutron diffraction study by Greaves [30] confirmed a higher degree of ordering than the one implied by the cubic  $P4_32$  structure, and described this departure as a tetragonal distortion. The positions of the vacancies in the fully ordered maghemite structure were obtained by Shmakov *et al.* [47] using synchrotron X-ray diffraction. This ordered maghemite structure has the tetragonal space group  $P4_12_12$  with  $a = 8.347 \text{ \AA}$  and  $c = 25.042 \text{ \AA}$  (spinel cubic cell tripled along the  $c$  axis). The ion coordinates in the  $P4_12_12$  structure have been refined in 2007 by Jorgensen *et al.* based on synchrotron X-ray powder diffraction data [48].

Despite this progress in the structure determination of maghemite, the phenomenon of vacancy ordering in the lattice is not yet fully understood. It is not clear, for example, under which conditions, if any, vacancy disorder occurs. It has been suggested that the degree of ordering depends on crystal size, and that very small particles of maghemite do now show vacancy ordering [49,50], although a recent investigation of needle-shaped maghemite nanoparticles with average size  $240 \text{ nm} \times 30 \text{ nm}$  has found the same tetragonal distortion with space group  $P4_12_12$  as in the

*completely* ordered crystal [51]. Belin *et al.* observed crystallographic order of ions and vacancies ( $P4_132$ ) even at 9 nm [52]. Other authors observed that vacancy order ( $P4_132$ ) could be present in maghemite particles larger than 5 nm in diameter depending on the preparation method [53]. However, the thermodynamics of vacancy ordering in maghemite has not been investigated so far, because of the difficulty to control experimentally the level of ordering of the iron vacancies. Grau-Crespo and co-workers present a computational investigation of the energetics of vacancy ordering in maghemite. They show that a fully ordered structure with tetragonal space group  $P4_12_12$ , is indeed the most stable configuration, among all the possible ionic arrangements that are compatible with the partially disordered  $P4_332$  structure, because of most favorable electrostatic contribution (minimal Coulombic repulsion between Fe(III) cations) [42]. However it must be noted that DFT+U calculation is referred to the bulk at the thermodynamic equilibrium and deviations are expected in nanostructures. In fact in most synthetic procedures the growth of nanocrystals takes place in non-equilibrium conditions. Moreover the presence of antisite-type disorder and surface effects in nanocrystals could contribute to deviation from the ideal ordering of the vacancies.

### 2.2.3a Synthesis of $Fe_3O_4$ NP

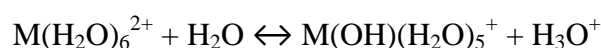
In principle, synthetic approaches developed for preparation of iron oxide NP are not different from the approaches used for other metals. The reduction of the crystal dimensionality to the nanometer scale brings a new degree of complexity to their synthesis. Moreover, many precursors in traditional solution precipitation reactions for the preparation of metals and metal oxides are ionic compounds. Solution reactions involving ions are usually fast, which complicates control over kinetics and morphology of the products. A great variety of ligands gives rise to metal complexes with different molecular and electronic structures and therefore different stability constants, reactivity, and kinetics. Furthermore, using covalent metal-containing compounds (organometallic, etc.) which react and / or decompose only at elevated temperatures yielding metals or metal oxides, new chemical reactions with different mechanisms and different kinetics can be introduced (*e.g.* refer to *heating-up* method section in this chapter).

As a general consideration, production of NP with uniform size and shape is possible under conditions of accurate control over kinetics of their nucleation, growth, and coarsening (refer to Ch. 2.2.2 for general guidelines). The best control is achieved when all the three steps are separated in time; namely, the nucleation must be finished by the time when the growth begins. There has been much interest in the development of synthetic methods to produce high-quality iron oxide systems. The synthesis of controlled size magnetic nanoparticles is described in multiple

publications. High-quality iron oxide nanomaterials have been generated using high-temperature solution phase methods similar to those used for semiconductor quantum dots (see ref. [54] for a comprehensive review). Other synthesis methods such as polyol-mediated, sol-gel [55] and sonochemical [56] were also proposed. The effectiveness of the non-aqueous routes for the production of well-calibrated iron oxide nanoparticles was shown in [57]. Herein are reported, in details, two classes of synthetic procedures that prompt a guideline for the production of magnetite nanoparticles as described in Ch. 4.2, namely aqueous-based (hydrolysis) and organic-based (coordinating solvent) synthesis.

### 2.2.3b Hydrolysis in aqueous solution

Among the variety of literature-proposed methods for the synthesis of magnetic iron oxide nanoparticles [58-60], the co-precipitation method is the most effective technique for preparing aqueous dispersions of iron oxide nanoparticles because the synthesis is conducted in water. In fact, all transition metal ions undergo hydrolysis in aqueous solutions:



How far this equilibrium goes to the right, can be determined from the corresponding metal-hydroxide complex formation constant. In a practical sense, in order to initiate condensation of hydroxide complexes into the nuclei, the acid formed as a byproduct of hydrolysis, must be neutralized. These nuclei act as seeds for further condensation until they grow large enough for precipitation. Variation in size and shape of the nanoparticles was observed under conditions of strict control of acidity and ionic strength in aqueous solutions containing no complexing agents [61,62]. These variables influence the electrostatic surface charge density of the nanoparticles, the interfacial tension, and consequently their surface energy.

Precipitation from basic aqueous solutions is widely reported and applied for the preparation of magnetite NP [61,63–66]. In fact, a common synthetic approach to produce small nanocrystals of magnetite (hydrodynamic radius  $\sim 6$  nm) is based on co-precipitation starting from Fe(II) / Fe(III) salts in 1:2 ratio. A continuous mixing of 0.1 M metal ion solutions with 1.0 M  $NH_3(aq)$  at room temperature, followed by heating the resulted solution at 75°C for 1 min [67]:



However precipitation by means of careful acidification is reported too [63] and the adsorption of  $H^+$  at the particle surfaces has been found to help the NP dispersion thanks to electrostatic repulsion: the excessive positive charge at the surface effectively stabilizes the colloid [68]. In both acidic and alkaline environments, the experimental challenge in the synthesis of  $Fe_3O_4$  by co-precipitation lies in control of the particle size and thus achieving a narrow particle size distribution. Size tailoring of magnetite particles (*e.g.* the *mean* diameter) can be obtained over a

large range at nanometric scale ( $1.5 \div 15$  nm) by controlling pH and ionic strength of the solution [61], but particles prepared by co-precipitation method tend to be rather polydispersed as shown in Figure 2.17.

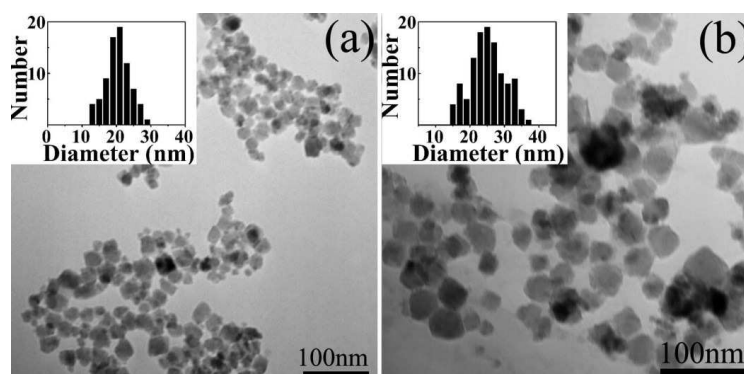


**Figure 2.17** Dimensional dispersion in magnetite NP obtained through water based synthesis [65].

Vayssières and co-workers [61], found that the higher the pH and the ionic strength of the solution are, the smaller the particle size is: above a critical pH value, which depends on the ionic strength and the temperature, the secondary particle growth by Ostwald ripening does not take place anymore. The stabilization of nanoparticles seems to result from thermodynamics rather than kinetics. According to Chao Hui *et al.* [65] adding to the solution a soluble, but chemically inert salt ( $\text{NaNO}_3$ ), *i.e.* increasing the ionic strength of the solution, leads to smaller particles size due to the formation of a large number of seeds (electrostatic stabilization lowers the dimension of the critical radius,  $r^*$ ), which provides high particle concentration and yielded small particles. For example, the diameter of 20 nm  $\text{Fe}_3\text{O}_4$  particles was obtained in 10 M  $\text{NaNO}_3$ , while the size of 40 nm particles can be formed without  $\text{NaNO}_3$ . As a general consideration, an unavoidable problem associated with particles in this size range is their intrinsic instability over longer periods of time: the smaller the particles, the less stable the colloidal system is, from the thermodynamic point of view [69–72]. To overcome this limitation, coating of particle surface can effectively prevent the adhesion of colliding particles during thermal motion, thus results in enhanced resistance against particle aggregation. In aqueous medium, electrostatic, steric and mixed stabilization layers can be used (refer to Ch.2.2.1 c and d) [73] and, as a rule of thumb, thicker coating provides better stability. This is especially true in the case of magnetic fluids: it is important to keep an appropriate spacing between magnetic NP (typically 2–3 nm), to overcome both VdW interactions and magnetic-induced agglomeration [74]. Significant advances in preparing monodisperse magnetite nanoparticles, of different sizes, have been made by the use of organic additives as stabilizing and / or reducing agents. The variety of such coatings ranges from hydrophilic polymers (poly(vinyl-pyrrolidone) [75–78], poly(ethylene glycol) [79–86], starch [87,88]), amphiphilic co-polymers (vinyl alcohol / vinyl amine [89], ethyl methacrylate / ethylene glycol

methacrylate [90]), chelating aminoacids [91] or ammonium salts (*e.g.* tetramethylammonium hydroxide) [92]. Polymers are known to effectively passivate NP surface and are directly involved in their biocompatibility, but they show important hydrodynamic sizes too, that may limit their tissular diffusion, so that extensive studies were performed on small-molecule ligands. Carboxylic acid and amine functional groups have been shown to provide chemisorption onto the particle surfaces [93–95]. In particular, Portet [96] studied non-polymeric coatings with carboxylic, sulfonic, phosphonic, and phosphoric acid functional groups: the strongest binding with attached iron oxide NP was determined for phosphonates moieties, in general, and molecules with bis-phosphonates groups, in particular.

Lastly, water based synthesis has been proved to be an effective, scalable and factory-oriented strategy to produce Fe<sub>3</sub>O<sub>4</sub> NP on large scale, in ambient atmosphere and low temperatures. The possibility to use biocompatible coatings – without the need of ligand exchange – make this approach very interesting for biomedical applications. Unfortunately, up to now, NP dimensional control is rough so that, when a very narrow size distribution is needed (<5%), the synthesis in organic solvents provide a lab-scale alternative to co-precipitation method.

### 2.2.3c Synthesis in organic solvents

Alcohols are good alternatives for water as coordinating solvents possessing relatively high dielectric constant and high donor number. Polyols are even better than regular alcohols because they are more polar and they form stronger associates with metal ions. This is especially true for 1,2-diols, 1,2,3-triols, and diethylene glycol (DEG) which form chelates with metal ions. Synthesis is accomplished by the sequence of the following reactions: (a) metal ion–chelated alcohol complexes formation; (b) ligand deprotonation - alkoxide complexes formation; (c) high-temperature crystal nucleation and growth [97,98]. The rate of this reaction is highly dependent on temperature, ranging from indefinitely low at a room temperature to the instantaneous at 200–220 °C. This property is very useful, since it assures a fine control over the nucleation and the growth of the nanocrystals. In these conditions, no formation of iron oxides takes place at room temperature, all reagents can be premixed, and therefore any non-homogeneity of the product, due to reactions happening faster than the rate of mixing, is eliminated. Additionally, these conditions help achieving significant ordering in the crystal lattice of the metal oxide, which is the main responsible for the magnetic properties: most of the obtained nanoparticles are indeed single crystalline. Bigger nanocrystals of magnetite were obtained when the complexing strength of the medium was increased by replacement of DEG with structurally similar *N*-methyl-diethanolamine. The results indicate that the reaction is slower in a more complexing medium, and that the Ostwald

ripening (mass transfer) is presumably taking place, which makes it different from the original DEG-based system [99].

The function of the DEG is not only to be a solvent and a complexing / chelating agent, but also to be a stabilizing agent. As a result, even in hot solution during the synthesis, the nanocrystals remain in colloidal form and do not agglomerate. The agglomeration of the nanocrystals due to their high surface energy is a very common and difficult problem to overcome. It is usually addressed by adding a capping ligand in the reaction solution, by doing synthesis in surfactant micelles, or by providing the conditions for the adsorption of the solvated ions (electric double-layers formation), which would cause the electrostatic repulsion of the charged surfaces. In this method, DEG seems to act as a capping ligand, and a favorable medium for electric double-layer stabilization, so as a consequence the agglomeration is barely noticeable. Once precipitated, the nanocrystalline powders still contain the adsorbed DEG, and if kept under the DEG solvent they remain non-agglomerated for an indefinitely long time. The additional advantage of this method is that the “hot” inorganic chemistry, occurring when crystal cores are synthesized, does not interfere with the surface chemistry that can be done later under ambient conditions for the preparation of biocompatible nanocomposites [99]. In addition to DEG, polar aprotic solvents (*e.g.* 2-pyrrolidone) are used as reaction medium for preparation of magnetite nanoparticles by hydrolysis and partial reduction of Fe(III). [100] Refluxing the solutions of the sole precursor  $\text{FeCl}_3 \cdot 6\text{H}_2\text{O}$  (normal boiling point of 2-pyrrolidone is 245 °C) results in the formation of the colloids containing  $\text{Fe}_3\text{O}_4$  nanoparticles with sizes strongly dependent on reaction time: 4, 12, or 60 nm for 1, 10, and 24 h. The evidence occurred is that the hydrolysis reaction is promoted by trapping the byproduct HCl with amine, and the reduction of Fe(III) to Fe(II) is done with CO (both the amine and CO are *in situ* generated from 2-pyrrolidone). Remarkably, the solvent also plays a role of the colloid stabilizing medium; the precipitation of nanopowders has to be initiated by adding the 1:3 methanol / diethyl ether mixtures.

Besides alcohol-based synthesis, it is worth mentioning Jana *et al.* [101] that develop a general and simple strategy for controlling the size, shape, and size distribution of oxide nanocrystals. This is based on the thermal decomposition of metal fatty acid salts, the most common metal compounds compatible with non-aqueous solutions. The reaction system is generally composed of the metal fatty acid salts (*e.g.* iron oleate), the corresponding fatty acids (*e.g.* oleic acid), and a hydrocarbon solvent (*e.g.* ODE, benzyl ether). Such synthesis leads to the intermediate precursor (metal oleate) that is used for the synthesis of metal oxide nanoparticles through high-temperature pyrolysis. Interestingly, an accurate dimensional control can be achieved (Figure 2.18) because the metal-complex decomposition reaction can be completely quenched by lowering the temperature of the mixture to room temperature. This allows to study the growth of oxide nanocrystals and to follow the temporal evolution of the size and shape of the nanocrystals.



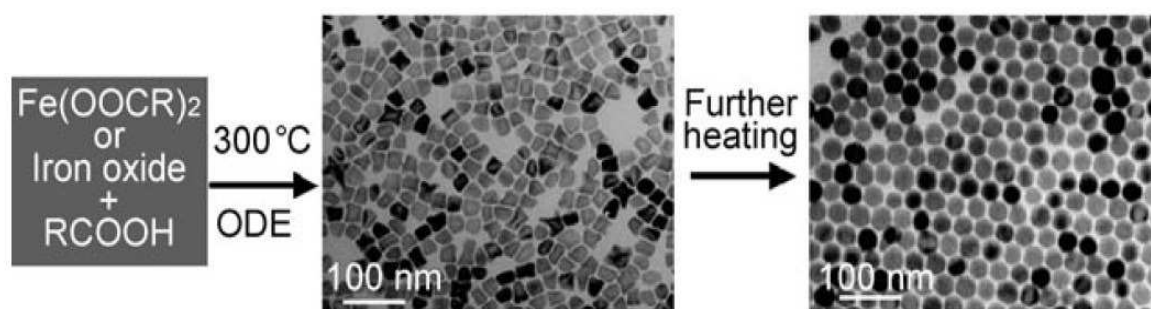


**Figure 2.18** High temperature synthesis of magnetite nanocrystals in coordinating solvents. The middle and right panels are TEM images of the as-synthesized nanocrystals taken at different reaction times [101].

Nearly monodispersed  $\text{Fe}_3\text{O}_4$  nanocrystals can be obtained in a large size range (3-50 nm) simply varying synthetic parameters (Figure 2.19): for example, the size and shape control of the nanocrystals is achieved by varying the reactivity and the precursors concentration; the reactivity can be tuned by changing the chain length and concentration of the ligands *i.e.* the fatty acids. Moreover, alcohols or primary amines, could be used as the activation reagents when a given metal fatty acid salt was not sufficiently active under selected reaction conditions. Finally, this method has been further applied to the growth of oxide nanocrystals of other magnetic metals in the fourth rows: *e.g.*  $\text{Cr}_2\text{O}_3$ ,  $\text{MnO}$ ,  $\text{Co}_3\text{O}_4$ , and  $\text{NiO}$ .

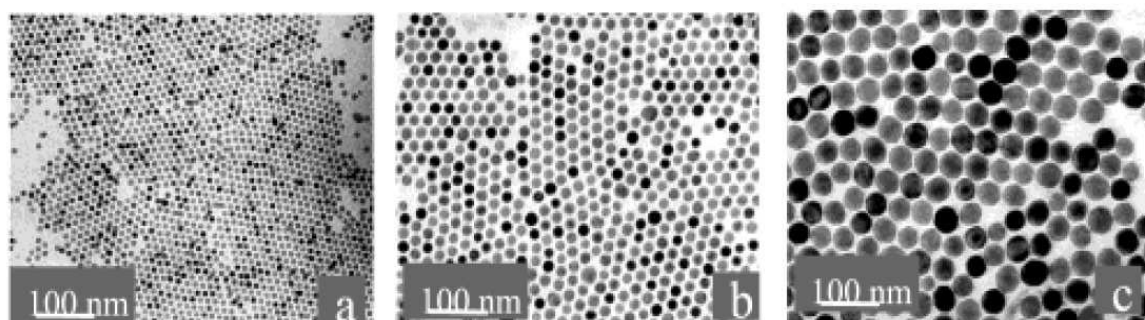


**Figure 2.19** Magnetite NP with good dimensional control over a wide range of dimensions [101].

Other studies focus on the ligands exchange in order to suspend in aqueous solutions the  $\text{Fe}_3\text{O}_4$  NP synthesized in organic solvents, to be used for example in biological and biomedical applications. For example,  $\alpha$ -cyclodextrin was used to transfer oleic acid stabilized iron oxide nanoparticles to aqueous phase, via forming an inclusion complex between surface-bound surfactants and  $\alpha$ -cyclodextrin [102]. Polymers were also applied to form oil-in-water micelles to encapsulated iron oxide nanocrystals inside [103], and a recent report [104] employed poly(ethyleneglycol)-terminated organic dendrons to exchange the original surface ligand (oleic acid) to make iron oxide nanocrystals dispersible in water. Lastly, other researchers [105] developed a facile method for completely transferring high quality monodisperse iron oxide nanocrystals from organic solvents to water (Figure 2.20).

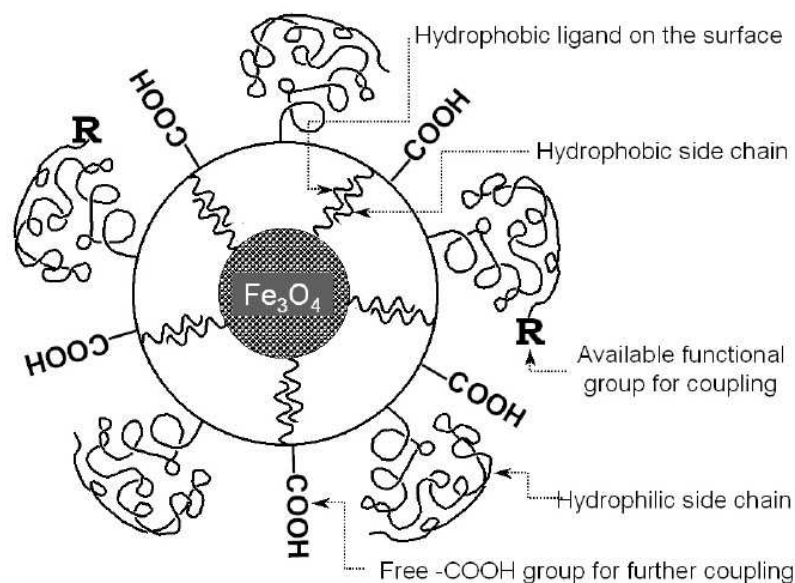


**Figure 2.20** Structure of water dispersible iron oxide NP (R is a functional group, e.g.  $-\text{COOH}$ ) [105].

More in detail, an amphiphilic copolymer made of Poly(maleic anhydride-*alt*-1-octadecene) (PMAO) and PEG is used for ligand exchange in water solution: hydrophobic chains are alternate with carboxyl group, useful for bioconjugation with biomolecules *i.e.* peptides, proteins, antibodies, and nucleic acids, through standard bioconjugation techniques [106].

Out of this introduction, pointing out the influence of different *reagents* for the production of highly-mondispersed crystalline NP, it is worth noting that there are two main *operative* approaches to deal with the synthesis in organic solvents, known as *hot-injection* and *heating-up* methods.

Names themselves are explanatory but, beside the apparent difference, they share common features and the respective synthesized nanostructures are often comparable (*i.e.* shape and dimensional control, crystallinity, magnetic properties).

### Hot injection method

Back in 1993 Murray developed a synthetic protocol to obtain monodispersed II-VI semiconductor NP, the so-called *hot-injection* method. The reader is invited to refer Ch. 2.2.2a for a review of the synthetic procedure, herein are reported just a few examples related to the synthesis of iron oxide nanoparticles.

The typical procedure involves the hot-injection of a metallorganic iron precursor (*e.g.*  $\text{Fe}(\text{CO})_5$ , iron (III) acetylacetonate) in an appropriate high boiling solvent (*e.g.* ODE, diphenyl ether, oleic acid, OA) in the presence of alcohol (reducing agent) and surfactant, in inert atmosphere. The thermal decomposition / reduction produces iron NP as reaction intermediate and the following oxidation by a chemical reagent leads to monodisperse magnetite nanoparticles [108,120]. As-

synthesized NP (Figure 2.21) are very uniform in shape and present a narrow size distribution. Maghemite NP can be obtained simply by the oxidation of as-grown magnetite NP at high temperature (250 °C), in oxygen atmosphere for 2 h [114]. Murray's successful synthetic scheme was later applied to a huge variety of materials, including metals, metal-alloys (Sn, Ni, In, Co, Pt, Fe, FePt, CoPt, CoPt<sub>3</sub>) and oxides (CoFe<sub>2</sub>O<sub>4</sub>, TiO<sub>2</sub>, BaTiO<sub>3</sub>, MnFe<sub>2</sub>O<sub>4</sub>, ZrO<sub>2</sub>, Cu<sub>2</sub>O, CeO<sub>2</sub>) [119].

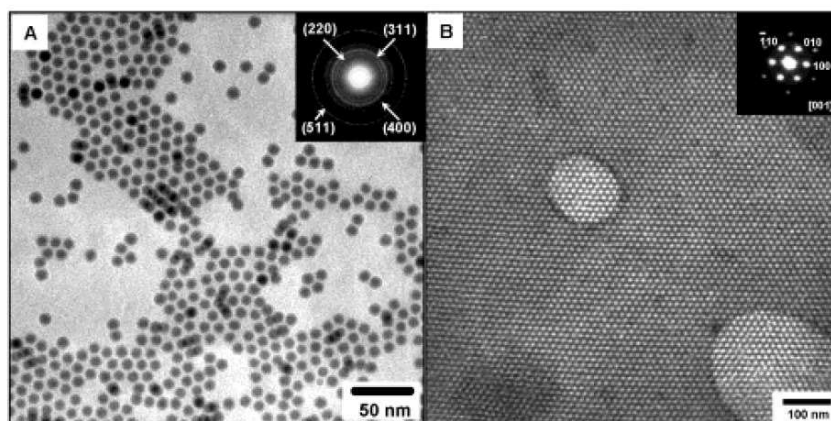


**Figure 2.21** (A) TEM image of maghemite NP, (B) hexagonal close-packed NP superlattice [121].

### Heating-up method

In the so-called *heating-up* method the reaction solution is prepared at low temperature using particular metal-salt complexes that shows self catalytic dissociation properties as the temperature is raised, so that an instant nucleation can take place, followed by the crystallization process, which finally leads to the formation of nanocrystals. The heating-up method is particularly advantageous for large-scale production, because of its simplicity [107]. Nevertheless, the size uniformity that can be achieved by this approach is comparable to the best results reported in literature (*e.g.* highly monodispersed NP obtained though the hot-injection method). The method was pioneered by Hyeon *et al.* [108] in 2001 for the synthesis of maghemite nanoparticles. Adapting a synthesis protocol previously published by Bentzon *et al.* for the preparation of iron oxide superlattices [109], the procedure involved the reaction of iron pentacarbonyl Fe(CO)<sub>5</sub> into a mixture of octyl ether and oleic acid at the moderate temperature of 100 °C, producing iron oleate complexes as precursor species (whose exact structure is however unknown). During the subsequent heating to reflux (around 300 °C) the iron oleate complex decomposes and metallic iron NP are formed (similarly to the hot-injection method). NP are then oxidized to  $\gamma$ -Fe<sub>2</sub>O<sub>3</sub> by a mild oxidant (*e.g.* trimethylamine oxide). The obtained nanocrystals are highly monodisperse, as reported in Figure 2.22. This seed-mediated growth is the most apparent strategy for the separation of nucleation and growth and has successfully been applied for the size-controlled synthesis of many different metal oxide nanoparticles.

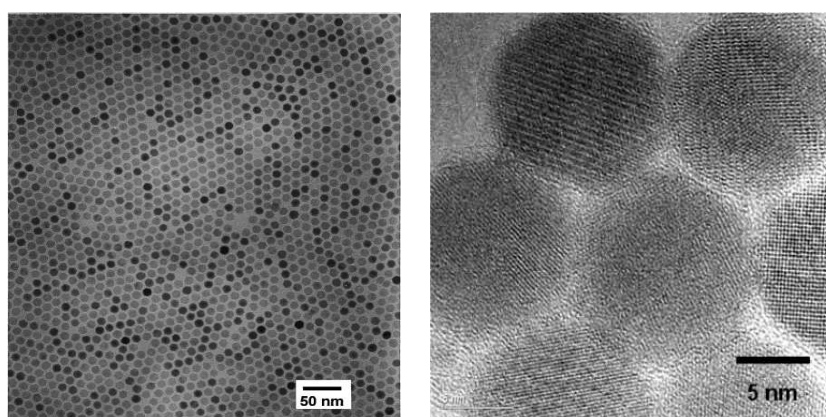


**Figure 2.22** STEM (left) and HREM (right) image of a 2D hexagonal assembly of maghemite NP [108].

More recently, seed-mediated growth has been employed for the synthesis of larger metallic nanoparticles on smaller seeds. For example, Buhro and co-workers reported the synthesis of monodisperse nanoparticles of Bi, Sn, and In using Au nanoclusters as seeds [110]. In addition, monodisperse nanoparticles of Au [111,112], Fe [113] and  $\text{Fe}_3\text{O}_4$  [114,115] have been synthesized following similar procedures. Finally, in 2005 Hyeon group succeeded in the synthesis of monodisperse iron nanoparticles with sub-nanometric accuracy [116] resulting in particle sizes of 6, 7, 9, 10, 12, 13, and 15 nm as reported in Figure 2.23. Starting from the seeded-mediated growth described above, after refluxing the mixtures generated from the various combinations of the iron nanoparticles and the iron oleate solutions, we were able to synthesize mixing solutions containing 1.5, 3.0, and 4.5 mmol of the iron oleate complex and appropriate amounts of pentacarbonyl iron and oleic acid in dioctyl ether at 400 K for 12 h.

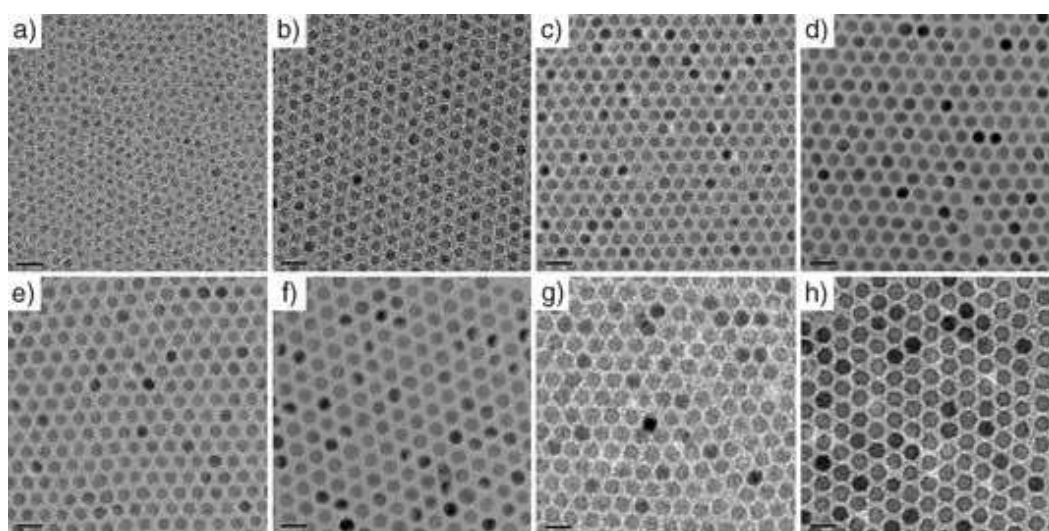


**Figure 2.23** TEM images of iron oxide NP with particle diameters of 6, 7, 8, 9, 10, 11, 12, 13 nm [116].

As a general consideration, the nucleation process persists as long as the supersaturation level is kept high enough to overcome the energy barrier for the nucleation (in the hot-injection this requirement is satisfied by the rapid injection). To keep the supersaturation level high, the monomer supply rate should be higher than, or equal to, the rate of the consumption of the monomer caused by the nucleation and growth of the nanocrystals. For the case of heating-up method, it was demonstrated that, as the thermal decomposition reaction of the precursor proceeds, the monomer supply rate increases very fast because the thermal decomposition of the metal-salt complex (*e.g.* iron oleate) follows the kinetic of autocatalytic reaction (*i.e.* a sigmoidal shaped curve in the reaction coordinate *vs* time diagram) [117,118]. Autocatalysis is a self-accelerating process in which the product reacts with the reactant to enhance the forward reaction and consequently the nucleation process is terminated before growth takes place. Hyeon and co-workers reached the conclusion that pentacarbonyl iron mainly contributes to nucleation, whereas the iron oleate complex, generated *in situ*, contributes exclusively to growth. They also found that the nucleation resulting from the thermal decomposition of pentacarbonyl iron takes place at relatively low temperature, whereas the growth derived from the decomposition of the iron oleate complex occurs at a higher temperature.

Due to its versatility, the heating-up method constitutes nowadays one of the most popular synthesis routes and consequently, a large number of metal oxide nanoparticles have been prepared and reported based on this approach [107,116].

### Remarks about hot injection and heating-up methods

Regarding the nucleation process, the main difference between the heating-up and the hot-injection method (with or without coordinating solvents) is the instantaneous supersaturation that is induced in the hot-injection method. Although the crystallization mechanisms underlying the control of the size distribution in the heating-up method are much less understood than in the hot-injection method, one would expect different growth kinetics for both methods. However, investigations in this direction did not yet show any significant differences, at least in comparison with other, more important reaction parameters (*e.g.* reaction temperature and surface capping agent above all).

This is a general remarks and could be extended to other materials too: in the case of ZnO nanoparticles for example, prepared by the thermal decomposition of zinc acetate in alkylamines in the presence of tert-butylphosphonic acid (TBPA), the UV-vis absorption spectra showed similar optical features for the final products prepared by the hot-injection and heating-up method, respectively [122]. On the other hand, it was found that TBPA was essential to keep the crystal size in the nanoscopic regime, and that the TBPA to zinc acetate ratio strongly influenced both the growth kinetics and the final crystal size. Comparison of the two methods was also drawn in the case of more complex morphologies like tetrapod-shaped maghemite nanocrystals [123]. The

heating-up method involved the addition of iron pentacarbonyl, dissolved in 1-octadecene, to the three surfactants oleic acid, oleylamine and hexadecane-1,2-diol in 1-octadecene at 100 °C, followed by heating to 240 °C for 1h. The hot-injection procedure was different in that the iron pentacarbonyl was rapidly injected into the hot surfactant mixture at 240°C. However, both methods resulted in the formation of rather similar  $\gamma$ -Fe<sub>2</sub>O<sub>3</sub> tetrapods, with the only difference that the arms of the tetrapods obtained by the hot injection are slightly thicker. In both methods, the main parameter determining the length of the arms of the tetrapods, is the concentration of the precursor. Finally, even though state-of-the-art nanostructures have been synthesized using organic solvents as reaction media, water based synthesis of Fe<sub>3</sub>O<sub>4</sub> NP offers several important advantages (e.g. low temperature, non polluting and non-toxic precursors, air stability) that render it a promising candidate for large scale integration, even if accurate dimensional control is still an open issue.

## References

- [1] A. H. Morrish. *The Physical Principles of Magnetism*, 1965, John Wiley, New York, Chap. 7
- [2] K. M. Unruh, C. L. Chien, *Nanomaterials: Synthesis, Properties and Applications*, 1996, Institute of Physics Publishing, New York, Chap. 14
- [3] U. Häfeli, W. Schütt, J. Teller, M. Zborowski. *Scientific and Clinical Applications of Magnetic Carriers*, 1997, Plenum Press, New York
- [4] Q. A. Pankhurst, J. Connolly, S. K. Jones, J. Dobson. *J. Phys. D: Appl. Phys.*, 2003, **36**, R167
- [5] P. Tartaj, M. P. Morales, S. Veintemillas-Verdaguer, T. González-Carreño, C. J. Serna. *J. Phys. D: Appl. Phys.*, 2003, **36**, R182
- [6] P. Tartaj, M. P. Morales, T. González-Carreño, S. Veintemillas-Verdaguer, C. J. Serna. *J. Magn. Mater.*, 2005, **28**, 290
- [7] T. Neuberger, B. Schöpf, H. Hofmann, M. Hofmann, B. Von Rechenber, *J. Magn. Mater.*, 2005, **293**, 483

- [8] O. Bomati-Miguel, M. P. Morales, P. Tartaj, J. Ruiz-Cabello, P. Bonville, M. Santos, X. Zhao, S. Veintemillas-Verdaguer, *Biomaterials*, 2005, **26**, 5695
- [9] H. T. Song, J.S. Choi, Y.M. Huh, Y. W. Jun, J. S. Suh, J. Cheon. *J. Am. Chem. Soc.*, 2005, **127**, 9992
- [10] Y. M. Huh *et al.*, *J. Am. Chem. Soc.* 2005, **127**, 12387
- [11] J. Xie, S. Peng, N. Brower, N. Pourmand, S. X.Wang, and S. Sun, *Pure Appl. Chem.*, 2006, **78** (5), 1003
- [12] V. K. Varadan, L. Chen, J. Xie, *Nanomedicine*, 2008, John Wiley & Sons, Ltd
- [13] R. M. Cornell and U. Schwertman, *The Iron Oxides, Structure, Properties, Reactions, Occurrences and Uses*. 2003, Weinheim: Wiley-VCH
- [14] P. Li, Miser D., Rabiei S., Yadav R., and Hajaligol M.R. *Appl. Catal. B: Environ.*, 2003, **43**, 151
- [15] P. Li *et al.*, In: *Nanotechnology in Catalysis*, 2004 Kluwer Academic / Plenu, New York, pp.515
- [16] E. J. Shin, M.R. Hajaligol, F. Rasouli, *Fuel*, 2004, **83** (11-12) 1445
- [17] M. Mohapatra and S. Anand, *International Journal of Engineering, Science and Technology*, 2010, **2**(8), 127
- [18] K. Sivula, R. Zboril, F. Le Formal, R. Robert, A. Weidenkaff, J. Tucek, J. Frydrych and M. Graetzel, *J. Am. Chem. Soc.*, 2010, **132** (21), 7436
- [19] K. Sivula, F. Le Formal, and M. Graetzel, *ChemSusChem*, 2011, **4**, 432
- [20] S. D. Tilley, M. Cornuz, K. Sivula, and M. Graetzel, *Angew. Chem. Int. Ed.*, 2010, **49**, 6405
- [21] P. Baldrian, V. Merhautová, J. Gabriel, F. Nerud, P. Stopka, M. Hrubý and M.J. Beneš, *J. Appl. Catal. B: Environ.*, 2006, **66** (3-4), 258
- [22] R. O'Handley, *Modern Magnetic Material: Principles and Applications*, 2000, John Wiley & Sons, New York, pp. 29
- [23] R. Nathans, S. J. Pickart, H. A. Alperin and P. J. Brown, *Physical Review A*, 1964, **136**, 1641
- [24] J. H. L. Beal, *Synthesis and Characterisation of Metal Chalcogenide Nanocrystals*, PhD Thesis, 2009, Victoria University of Wellington
- [25] X. P. Shen, H.J. Liu, L. Pan, K.M. Chen, J.M. Hong, Z. Xu, *Chemistry Letters*, 2004, **33**, 1128
- [26] M. Pal and A. De, in *Hybrid nanocomposite for nanotechnology*, 2009, Springer Science Business Media, p.478
- [27] E. J. W. Verwey, *Nature*, 1939, **144**, 327
- [28] F. Walz, *J. Phys.: Condens. Matter*, 2002, **14**, R285
- [29] G. A. Waychunas, *Review of Mineralogy*, 1991, **25**, 11
- [30] C. Greaves, *J. Solid State Chem.*, 1983, **49**, 325
- [31] G. A. Waychunas, *Review of Mineralogy*, 1991, **25**, 11
- [32] A. H. Latham, M.J. Wilson, P. Schiffer, M.E. Williams, *J. Am. Chem. Soc.*, 2006, **128**, 12632
- [33] D. Farrell, S.A. Majetich, J.P. Wilcoxon, *J. Phys. Chem. B*, 2007, **107**, 11022-11030
- [34] J. Van Wonerghem, S. Mørup, S.W. Charles, S. Wells, *J. Phys. Rev. Lett.*, 1985, **55**, 410
- [35] A. T. Fromhold, E.L. Cook, *Phys. Rev.*, 1967, **158**, 600

- [36] A. T. Fromhold, E.L. Cook, *Phys. Rev.*, 1967, **163**, 650
- [37] N. Cabrera, N.F. Mott, *Rep. Prog. Phys.*, 1949, **12**, 163
- [38] C. M. Wang, D.R. Baer, L.E. Thomas, J.E. Amonette, J. Antony, Y. Qiang, G. Duscher, *J. Appl. Phys.*, 2005, **98**, 094308
- [39] S. Peng, C. Wang, J. Xie, S. Sun, *J. Am. Chem. Soc.*, 2006, **128**, 10676
- [40] S. Peng, S. Sun, *Angew. Chem., Int. Ed.*, 2007, **46**, 1
- [41] A. D. Smigelskas, E.O. Kirkendall, *Trans. AIME*, 1947, **171**, 130
- [42] R. Grau-Crespo, A.Y. Al-Baitai, I. Saadoun and N.H. De Leeuw, *J. Phys.: Condens. Matter*, 2010, **22**, 255401
- [43] G. Hagg, *Z. Physik. Chem.*, 1935, **9B**, 95
- [44] R. Haul and T. Schoon, *Z. Physik. Chem.*, 1929, **44B**, 216
- [45] P. B. Braun, *Nature*, 1952, **170**, 1123
- [46] G. W. Van Oosterhout and C.J.M. Rooijmans, *Nature*, 1958, **181**, 44
- [47] A. N. Shmakov, G.N. Kryukova, S.V. Tsybulya, A.L. Chuvilin, L.P. Solovyeva, *J. Appl. Crystallogr.*, 1995, **28**, 141
- [48] J. E. Jorgensen, L. Mosegaard, L.E. Thomsen, T.R. Jensen, and J.C. Hanson, *J. Solid State Chem.*, 2007, **180**, 180
- [49] R. M. Cornell and U. Schwertman, *The Iron Oxides, Structure, Properties, Reactions, Occurrences and Uses*. 2003, Weinheim: Wiley-VCH
- [50] T. J. Bastow, A. Trinchi, M.R. Hill, R. Harris, T.H. Muster, *J. Magn. Mater.* 2009, **321**, 2677
- [51] Z. Somogyvari et al., *Applied Physics a-Materials Science & Processing*. 2002, **74**, S1077
- [52] T. Belin, N. Guigue-Millot, T. Caillot, D. Aymes, and J. C. Niepce, *Journal of Solid State Chemistry*, 2002, **163**, 459
- [53] M. P. Morales, S. Veintemillas-Verdaguer, M.I. Montero, C.J. Serna, *Chem. Mater.*, 1999, **11**, 3058
- [54] M. Mohapatra and S. Anand, *International Journal of Engineering, Science and Technology*, 2010, **2** (8), 127
- [55] C. Feldmann, H.-O. Jungk, *Angew.Chem., Int. Ed.*, 2001, **40**, 359
- [56] R. V. Kumar, Y. Koltypin, Y.S. Cohen, Y. Cohen, D. Aurbach, O. Palchik, I. Felner, A. Gedanken, *J. Mater. Chem.*, 2000, **10**, 1125
- [57] O. Li, H. Chen, H. Bao, M. Gao, *Chem. Mater.*, 2004, **16**, 1391
- [58] J. P. Ge, Y.X. Hu, M. Biasini, C.L. Dong, J.H. Guo, W.P. Beyermann, Y.D. Yin, *Chem. Eur. J.*, 2007, **13** (25), 7153
- [59] T. Hyeon, *Chemical Commun.*, 2002, **8**, 927
- [60] Y. Wenguang, Z. Tonglai, Z. Jianguo, G. Jinyu, W. Ruifeng, *Progress in Chemistry*, 2007, **19** (6), 884
- [61] L. Vayssieres, C. Chaneac, E. Tronc, J.P. Jolivet, *J. Colloid Interface Sci.*, 1998, **205**, 205
- [62] J.P. Jolivet, C. Froidefond, A. Pottier, C. Chaneac, S. Cassaignon, E. Tronc, P. Euzen, *J. Mater. Chem.*, 2004, **14**, 3281
- [63] Y. S. Kang, S. Risbud, J. F. Rabolt, and P. Stroeve, *Chem. Mater.*, 1996, **8**, 2209



- [64] H. Iida, K. Takayanagi, T. Nakanishi, T. Osaka, *J. Colloid Interface Sci.*, 2007, **314**, 274
- [65] C. Hui, C. Shen, T. Yang, L. Bao, J. Tian, H. Ding, C. Li, and H. J. Gao, *J. Phys. Chem. C*, 2008, **112**, 11336
- [66] Y. Zhu and Q. Wu, *Journal of Nanoparticle Research*, 1999, **1**, 393
- [67] V. S. Zaitsev, D.S. Filimonov, I.A. Presnyakov, R.J. Gambino, B. Chu, *J. Colloid Interface Sci.*, 1999, **212**, 49
- [68] L. Garcell, M.P. Morales, M. Vreuges, P. Tartaj, C.J. Serna, *J. Colloid Interface Sci.*, 1998, **205**, 470
- [69] E. Tombacz, A. Majzik, Z. S. Horvat, E. Illes, *Romanian Reports in Physics*, 2006, **58** (3), 281
- [70] E. Tombacz: Adsorption from Electrolyte Solutions, Ch.12. In: J. Tóth (Ed.) *Adsorption: Theory, Modeling, and Analysis*, Marcel Dekker, New York, 2002. pp. 711
- [71] E. J. W. Verwey, *Theory of the Stability of Lyophobic Colloids*, Elsevier, New York, 1947
- [72] R. E. Rosenweig: *Ferrohydrodynamics*, Cambridge Univ. Press, Cambridge, 1985
- [73] R. J. Hunter: *Foundations of Colloid Science*, Oxford University Press, New York, 2002
- [74] S. Odenbach, *Colloids Surfaces A*, 2003, **217**, 171
- [75] Y. Zhang, J.-Y. Liu, S. Ma, Y.-J. Zhang, X. Zhao, X.-D. Zhang, Z.-D. Zhang, *J Mater Sci: Mater Med*, 2010, **21**, 1205
- [76] C. K. Nair and D. Chandrasekharan, *Cancer Prevention Research*, 2008, **1** (7), Supplement
- [77] H. Y. Lee, N. H. Lim, J. A. Seo, S. H. Yuk, B. K. Kwak, G. Khang, H. Bang Lee, S. H. Cho, *J Biomed Mater Res Part B: Appl Biomater*, 2006, **79B**, 142
- [78] J. Neamtu, N. Verga, *Digest Journal of Nanomaterials and Biostructures*, 2011, **6** (3), 969
- [79] N. Tomašovičová, M.Koneracká, P.Kopčanský, M.Timko, V. Závěšová, *Measurement Science Review*, 2006, **6-2** (3), 63
- [80] M. M. Yallapu, S. P. Foy, T. K. Jain, V. Labhasetwar, *Pharm. Research*, 2010, **27**(11), 2283
- [81] Y. Zhang, J. Zhang, *Journal of Colloid and Interface Science*, 2005, **283** (2), 352
- [82] K. Hervè et al., *Nanotechnology*, 2008, **19**, 465608
- [83] N. Kohler, C. Sun, A. Fichtenholtz, J. Gunn, C. Fang, M.Q. Zhang, *Small*, 2006, **2**, 785
- [84] M. D. Butterworth, L. Illum, S.S Davis, *Colloids Surf. A*, 2001, **179**, 93
- [85] J. Xie, C. Xu, N. Kohler, Y. Hou, S. Sun, *Adv. Mater.*, 2007, **19**, 3163
- [86] S. Mondini, S. Cenedese, G. Marinoni, G. Molteni, N. Santo, C.L. Bianchi, A. Ponti, *J. Colloid Interface Sci.*, 2008, **322**, 173
- [87] D. K. Kim, M. Mikhaylova, F.H. Wang, J. Kehr, B. Bjelke, Y. Zhang, T. Tsakalacos, M. Muhammed, *Chem. Mater.*, 2003, **15** (23), 4343
- [88] J. S. Jiang, Z.F. Gan, Y. Yang, B. Du, M. Qian, P. Zhang, *J Nanopart Res*, 2009, **11**, 1321
- [89] A. Petri-Fink and H. Hofmann, *IEEE Trans. on Nanobioscience*, 2007, **6** (4), 289
- [90] C. Stefaniu, M. Chanana, H. Ahrens, D. Wang, G. Brezesinski and H. Möhwald, *Soft Matter*, 2011, **7**, 4267
- [91] G. Marinescu et al., *Journal of Nanoparticle Research*, 2006, **8** (6), 1045
- [92] F. Y. Cheng et al, *Biomaterials*, 2005, **26** (7), 729
- [93] N. Pinna, S. Grancharov, P. Beato, P. Bonville, M. Antonietti, M. Niederberger, *Chem Mater*,

- 2005, **17**, 3044
- [94] C. Wei, J. Wan, *J Colloid Interface Sci*, 2007, **305**, 366
- [95] Z. Li, H. Chen, H. Bao, M. Gao, *Chem. Mater.*, 2004, **16**, 1391
- [96] D. Portet, B. Denizot, E. Rump, J.J: Lejeune, P. Jallet, *J. Colloid Interface Sci.*, 2001, **238**, 37
- [97] D. Caruntu et al, *Inorg. Chem.*, 2002, **41**, 6137
- [98] D. Caruntu, G. Caruntu, C. Yuxi, C. O'Connor, G. Goloverda, V. Kolesnichenko, *Chem. Mater.*, 2004, **16**, 5527
- [99] S. P. Gubin, *Magnetic Nanoparticles*, WILEY-VCH Verlag GmbH & Co, Weinheim (2009)
- [100] M. Rajamathi, M. Ghosh, R. Seshadri, *Chem. Commun.*, 2002, 1152
- [101] N. R. Jana, Y. Chen, and X. Peng, *Chem. Mater.*, 2004, **16**, 3931
- [102] Y. Wang, J.F Wong, X. Teng, X.Z. Lin, H. Yang, *Nano Lett.*, 2003, **3**, 1555
- [103] B. S. Kim, J. M. Qiu, J. P. Wang and T. A. Taton, *Nano Lett.*, 2005, **5**, 1987
- [104] T. Pellegrino *et al.*, *Nano Lett.*, 2004, **4**, 703
- [105] W. W. Yu, E. Chang, C.M. Sayes, R. Drezek and V. L. Colvin, *Nanotechnology*, 2006, **17**, 4483
- [106] G. T. Hermanson, *Bioconjugate Techniques*, 1996, (San Diego, CA: Academic)
- [107] J. Park, J. Joo, S.G. Kwon, Y. Jang, T. Hyeon, *Angew. Chem. Int. Ed.*, 2007, **46**, 4630
- [108] T. Hyeon, S.S. Lee, J. Park, Y. Chung, H.B. Na, *J. Am. Chem. Soc.*, 2001, **123**, 12798
- [109] M. D. Bentzon, J. Vonwongerghem, A. Tholen, *Ultramicroscopy*, 1988, **24**, 67
- [110] H. Yu, P. C. Gibbons, K. F. Kelton, W. E. Buhro, *J. Am. Chem. Soc.*, 2001, **123**, 9198
- [111] N. R. Jana, X. Peng, *J. Am. Chem. Soc.*, 2003, **125**, 14280
- [112] J. P. Wilcoxon, P. P. Provencio, *J. Am. Chem. Soc.*, 2004, **126**, 6402.
- [113] D. Farrell, S. A. Majetich, J. P. Wilcoxon, *J. Phys. Chem. B*, 2003, **107**, 11022
- [114] S. Sun, H. J. Zeng, *J. Am. Chem. Soc.*, 2002, **124**, 8204
- [115] S. Sun, H. Zeng, D. B. Robinson, S. Raoux, P. M. Rice, S. X. Wang, G. Li, *J. Am. Chem. Soc.*, 2004, **126**, 273
- [116] J. Park, et al., *Angew. Chem.*, 2005, **117**, 2932
- [117] S. G. Kwon, Y. Piao, J. Park, S. Angappane, Y. Jo, N. M. Hwang, J.-G. Park, T. Hyeon, *J. Am. Chem. Soc.*, 2007, **129**, 12571
- [118] D. Dollimore, K. H. J. Tonge, *Inorg. Nucl. Chem.*, 1967, **29**, 621
- [119] T. Hyeon *et al.*, *Angew. Chem. Int. Ed.*, 2007, **46**, 4630
- [120] A. H. Lu, E. L. Salabas, and F. Schuth, *Angew. Chem. Int. Ed.*, 2007, **46**, 1222
- [121] J. Cheon, N.J. Kang, S.M. Lee, J.H. Lee, J.H. Yoon, S. J. Oh, *J. Am. Chem. Soc.*, 2004, **126**, 1950
- [122] P. D. Cozzoli, M.L. Curri, A. Agostiano, G. Leo, M. Lomascolo, *J. Phys. Chem. B*, 2003, **107**, 4756
- [123] P. D. Cozzoli, *et al.*, *Nano Lett.*, 2006, **6**, 1966

## 2.3 Organic Molecules

A particular class of organic molecules is the one characterized by the fact that  $\pi$  orbitals are close in space and can overlap: this occurs when two carbon double bonds are adjacent  $[-C=C-C=C-]$ , so that the  $\pi$ -system can experience a certain degree of delocalization. Organic molecules that belong to this class are called  $\pi$ -conjugated molecules, and this feature lead to some peculiar properties. Benzene, for instance, is a good example of  $\pi$ -conjugated molecule in which the highly delocalized  $\pi$ -orbitals increase its binding energy with respect to a cyclic-organic molecule with the same number of C atoms, i.e. cyclohexane. When  $\pi$ -conjugated orbitals overlap, depending on the conjugation length and the extension of such overlapping, the molecular bonding (HOMO) and anti-bonding (LUMO) orbitals turn into bands, so that their energy gap makes them semiconductors, rather than insulators. This property is of a great importance, since it opens the way to organic-based electronics and optoelectronics.

In the past decade, the growing attention in the field of materials for electronics and optoelectronics has been devoted to organic semiconductors, in particular, conjugated molecules or polymers. This interest is related to the high technological impact of these materials and their good prospects for use in the field of thin-film solar cells and display devices. In particular, two classes of organic molecules – porphyrins and phthalocyanines – have been selected for the present work because of their unique and tunable characteristics, together with chemical and structural stability, that make them particularly attractive as dye absorber in solar cells applications.

### 2.3.1 Porphyrins

The word *porphyrin* is derived from the greek *purphura* meaning purple, and all porphyrins are intensely colored [1]. Porphyrins comprise an important class of molecules that serve nature in a variety of ways. Porphyrins are important biological molecules whose functions range from oxygen transfer and storage (hemoglobin and myoglobin) to electron transfer (cytochrome C, cytochrome oxidase) to energy conversion (chlorophyll).

The common feature of all these molecules is the basic structure of the porphyrins macrocycle, which consists of a 16-atoms ring containing four nitrogen atoms, obtained by linking four tetrapyrrolic subunits with four methine bridges, as shown in Figure 2.24. If the macrocycle does not show any central atom, it is the so called free-base configuration: the four N atoms are non equivalent, two of them being bonded to H atoms and the other two showing a lone electron pair. The periphery of the ring can be functionalized with a variety of substituents that modulate both

the photophysical and the materials properties. Because of their exceptional and tunable optoelectronic properties, porphyrins have been studied for energy related applications ranging from energy storage to materials for organic solar cells (OSC) and to catalysis [2–7]. Substitution with perfluoro-alkane moieties and perfluoro-phenyl groups improve their supramolecular self-organizing properties as well as the robustness of porphyrinic materials [8].

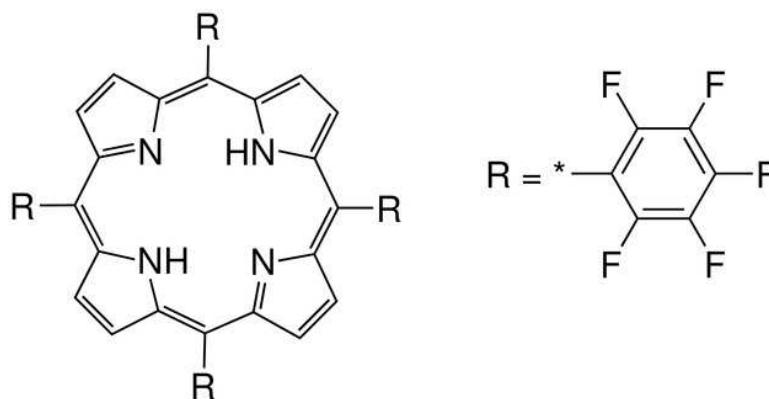


**Figure 2.24** Free base porphyrin macrocycle (R = H) and an example of substituent (R = perfluoro-phenyl) 5,10,15,20-Tetrakis(pentafluorophenyl)-porphyrin

The electronic absorption spectrum of a typical porphyrin consists of a strong transition to the second excited state ( $S_0 \rightarrow S_2$ ) at about 400 nm (corresponding to the so-called Soret or B band) due to optical transitions localized on the nitrogen atoms of the central macrocycle, and a weak transition to the first excited state ( $S_0 \rightarrow S_1$ ) at about 550 nm (the Q band) involving transitions from delocalized orbitals in the molecule (Figure 2.25, left). Usually, internal conversion from  $S_2$  to  $S_1$  is rapid so typically fluorescence is only detected from  $S_1$ , even if there are reports about Soret band emission [9,10]. The B and the Q bands both arise from  $\pi-\pi^*$  transitions and can be explained by considering the Gouterman four orbital model [11,12]. According to this theory, the absorption bands in porphyrin systems arise from transitions between two HOMO and two LUMO. The HOMO were calculated to be an  $a_{1u}$  and an  $a_{2u}$  orbital, while the LUMO were calculated to be a degenerate set of  $e_g$  orbitals (see Figure 2.25, right). A excited singlet state with an  $a_{1u}e_g$  configuration is formed by promoting an electron from the  $a_{1u}$  orbital to an  $e_g$  orbital ( $S_2$ , a singlet state with greater oscillator strength, giving rise to the Soret band). Likewise, an excited singlet state with an  $a_{2u}e_g$  configuration is formed by promoting an electron from the  $a_{2u}$  orbital to an  $e_g$  orbital ( $S_1$ , a lower energy singlet state with less oscillator strength, giving rise to the Q-bands). An electronic transition to the higher energy mixed state, the  $S_2$  state, is strongly allowed, whereas an electronic transition to the lower energy mixed state, the  $S_1$  state, is only weakly allowed. These excited singlet states mix to two new singlet states that are nearly 50:50 mixtures of the unmixed states. The closer in energy the unmixed states, the greater the degree of mixing. The greater the degree of mixing, the less intense the Q band relative to the Soret band [13].

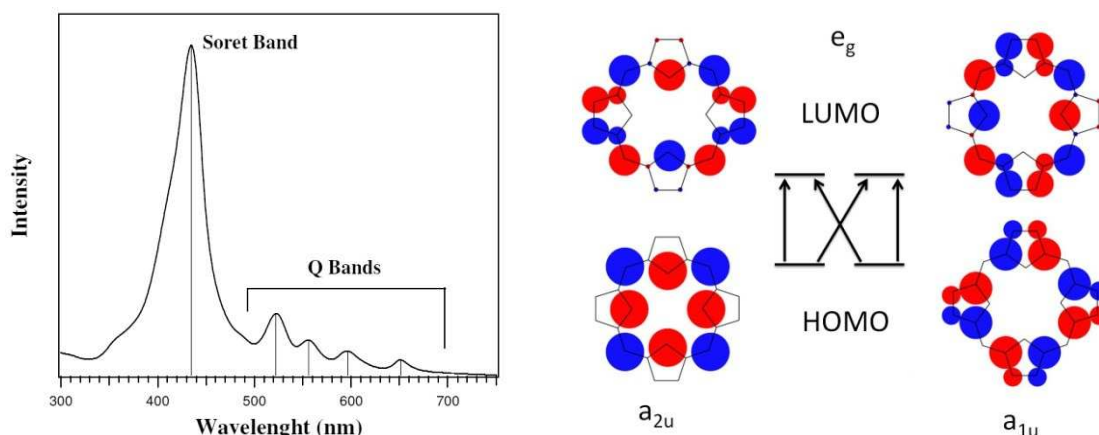


**Figure 2.25** Left: Typical absorbance spectrum of porphyrin molecule (left). Right: Symmetry of HOMO and LUMO for porphyrin molecule and schematic view of the Gouterman four orbital model and related transitions, adapted from [13].

Given the capabilities of porphyrins to bind and release gases and to act as active center in catalytic reactions in biological systems, porphyrin-based films on metal or semiconductor surfaces are extremely appealing as chemical and gas sensors [14–16] as well as nanoporous catalytic materials [17,18] in novel synthetic bio-mimetic devices. Moreover, the role of porphyrins in photosynthetic mechanisms indicates a good attitude of these molecules to mediate visible photon – electron energy transfer processes [19].

### 2.3.2 Phthalocyanines

Phthalocyanines are structurally related to porphyrins. Both feature four pyrrole-like subunits linked to form a 16-membered ring. Both porphyrins and phthalocyanines function as planar tetradentate dianionic ligands that bind metals through four inwardly projecting nitrogen centers. Such complexes are formally derivatives of  $Pc^{2-}$ , the conjugate base of free-base phthalocyanine. Traditionally, metal phthalocyanine (MPc) molecules, composed of a metal atom surrounded by a ligand ring, have been used as dyes and pigments. Recently, MPc molecules have shown great promise as components of light-emitting diodes, field-effect transistors, PV and single-molecule devices [20–22]. Moreover, phthalocyanines are among the most studied class of molecules for gas sensing applications too, since their electric properties strongly depend on the chemical composition of the surrounding atmosphere [23,24]. By virtue of their delocalized  $\pi$ -electron system they are good electron donors and show high sensitivity to oxidizing gases (thus may enhance the n-type response of inorganic semiconductor, *e.g.* ZnO and  $TiO_2$ ).

In particular, our attention focuses on titanyl phthalocyanine (TiOPc): it is a non-planar molecule consisting of four isoindole groups connected to a ring with the titanyl group in the center and the

O at the apex. The difference in electronegativity between Ti and O makes their bond polar and the molecule is thus an electric dipole with a moment amounting to 1.77 D [25]. The difference between HOMO and LUMO level is 1.7 eV and TiOPc exhibits a wide absorption spectrum in the visible range, a large nonlinear optical susceptibility [26], an ultrafast optical response, and a high photoconductivity [27,28]. Driven by these promising properties, an increasing interest has been devoted to exploit TiOPc as an active material in organic solar cells [29,30], while applications in organic light emitting diodes and as a conducting layer in organic field effect transistors have been investigated [31]. As is typical for many other organic molecules, optical and electronic properties of TiOPc thin films strongly depend on their structure and order. Therefore, the development of growth methods enabling appropriate control of the crystalline phase has crucial importance to fabricate devices with improved performances. Aiming at this purpose, several studies have been performed on the synthesis of TiOPc films. The optical absorption spectrum of the TiOPc films is characterized by two main broad bands (Figure 2.26, left): a B Soret band in the near-UV and a Q band in the visible region. Both of them include different components whose positions and intensities are known to be sensitive to the specific crystalline phase. In particular, the Q band, ranging from about 550 to 900 nm, is characterized by at least two components,  $Q_x$  (at the low wavelength side) and  $Q_y$  (at the high wavelength side), that are due to HOMO–LUMO transitions.

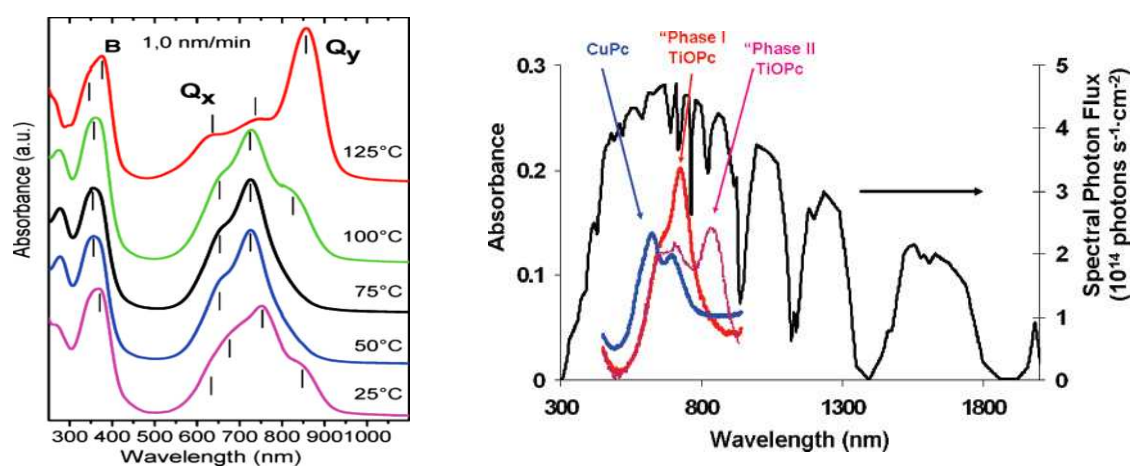


**Figure 2.26 Left:** Absorption spectra of TiOPc films grown by SuMBD at different substrate temperature [35]. **Right:** Absorption spectra for films of TiOPc and CuPc, relative to the AM 1.5 solar spectrum [36].

Their energy, according to Mizuguchi *et al.* [32], is strongly influenced by molecular distortion induced by  $\pi$ - $\pi$  interactions between adjacent molecules along the  $c$  axis. As a consequence, the absorption properties in the visible range are very sensitive to the crystalline structure, which determines the degree of overlap between orbitals of neighboring molecules. Even though, the literature is sometimes contradictory, mostly because of the different type and quality of the samples studied, different studies [32–34] give useful information about the UV-vis absorbance

spectroscopic signatures (fingerprints) of different crystalline phases. Amorphous films typically show  $Q_x$  and  $Q_y$  bands at 645–660 and 714–718 nm, respectively, while the main B band component is centered at 345–350 nm. Phase I films give rise to red-shifted  $Q_x$  and  $Q_y$  bands positioned at about 670 and 755–760 nm, respectively, with a B band main component at about 370 nm. Finally, phase II films show the highest separation between the Q bands, with an even higher red-shift of the  $Q_y$  component, so that the positions of the  $Q_x$  and  $Q_y$  bands are typically at 630–635 and at 845–850 nm, respectively, while the B band main component is shifted at 375–380 nm. The possibility to control the growth of TiOPc in different crystalline phases turns out particularly interesting in PV applications, where it can be used to tailor the degree of crystallinity and hence extend the absorption (in the visible range) to different spectral region (Figure 2.26, right).

### 2.3.3 Applications

Both porphyrins and phthalocyanines are promising molecules to be used as absorber in hybrid (or organic) excitonic solar cells (XSC). It is possible to separate existing solar cells into two distinct categories on the basis of their charge generation mechanisms: conventional solar cells and XSC. A fundamental difference between organic solar cells and conventional solar cells lies in the mechanism of charge generation: light absorption results in the formation of excitons rather than the free electron-hole pairs directly. XSC consists of cells in which light absorption results in the production of a transiently localized excited state that cannot thermally dissociate (because of binding energy exceeds  $kT$ ) in the chemical phase in which it was formed [37]. Examples of XSC include molecular semiconductor solar cells [38–41], conducting polymer solar cells [42–51], dye-sensitized solar cells (DSSC) [52–57], and quantum dot solar cells [58,59]. Today the PV technologies are currently dominated by inorganic semiconductor based solar cells. However, significant efforts have been made to research in the field of XSC since the manufacturing processes of traditional inorganic solar cells often involve elevated temperature, high vacuum, and numerous lithographic steps, resulting in high production costs and energy consumption. Alternatively, solar cells based on organic materials such as small molecules and conjugated polymers offer a cost-effective way to convert solar energy into electricity. In contrast to their inorganic counterparts, OSC have several advantages [60]. They are able to be manufactured by low-temperature processing: either from small molecules from the vapor phase, or polymers from solution. The organic materials are relatively inexpensive, and only 100–200 nm thick films are required due to the high optical absorption capabilities of organic semiconductors. Additionally, roll-to-roll processing like low cost printing techniques [61] can be used for manufacturing.

Nevertheless there are some drawbacks associated with OSC: one of the features differentiating OSC from their inorganic counterparts is the localized nature of excess charge carriers and excited states. Excess charges and excited states at room temperature can be thought of being localized on an individual small-molecule or polymer site, rather than being delocalized as they are in crystalline silicon [62].

In fact the probability for an excess charge sitting on one molecule to jump to a neighboring molecule is low in organic materials, such that those charges will (mainly electronically) polarize their environment before having made the jump, resulting in a polaron state. This polaron is even more unlikely to jump to a neighboring site since the charge is now dressed by its polarized environment. The polaron is therefore the relevant charge transport species which determines the energy level for transport of excess charges [63]. Similarly, absorption of light in organic semiconductors results in the generation of localized electronic excitations - referred to as polaron-excitons - rather than free electron-hole pairs as produced in many inorganic semiconductors. Organic optoelectronic devices such as solar cells take great benefit of interfaces (between different organic semiconductors as well hybrid interfaces with inorganic semiconductors) in order to manipulate excitons and polarons, amongst others to split the neutral excitons into free charge carriers [64].

Dissociation of photo-induced excitons is an essential process to produce photocurrent in organic solar cells [65]. In organic materials, excitons can be dissociated by interfaces [66], impurities, defects [67], and electric fields [68]. In XSC the interface has a dramatic influence, in fact an abrupt changes of the potential energy occur and strong local electrical fields are possible ( $E = -\text{grad } U$ ). To better understand the importance of exciton dissociation one should consider the fundamental mechanisms which lead towards photocurrent generation. Generally, the following steps take place: (a) photoexcitation of the dye molecules; (b) exciton diffusion inside the organic layer; (c) exciton break-up at the hybrid interface resulting in the generation of charge carriers; (d) drift of charge carriers in the internal field inside the organic layer; (e) collection of the charge carriers by the external electrodes leading towards current flow in the external circuit. Since the optical absorption efficiency of organic dyes is typically very high (e.g. for phthalocyanines  $\alpha \sim 10^5 \text{ cm}^{-1}$ ), the mechanisms of energy transfer, exciton break-up and charge carrier transport (steps (b) – (d) as described above) are generally considered as the most probable efficiency-limiting processes.[69].

In order to generate separated negative and positive charges, the excitons need to diffuse to the donor / acceptor interface. Since excitons are neutral species, their motion is not affected by any electric field and they diffuse *via* random hops driven by the concentration gradient. Note that the exciton diffusion lengths are typically around 10–20 nm for most conjugated polymers [70–72] and excitons that do not reach the donor / acceptor interface are lost for the energy conversion (recombination takes place) and have no contribution to the photocurrent. Hence, low exciton



diffusion and charge collection efficiency limit the improvement in PV performance due to the small exciton diffusion length and low carrier mobility of organic materials [73,74].

PV devices based on organic small molecular materials such as CuPc as donor and fullerene as acceptor have attracted a lot of attention in the recent past years because they offer the possibility of better charge separation at the hetero-interface, in a cost-effective device. The efficiencies of this kind of solar cells have been improved steadily since Tang [38] reported a bilayer device consisting of a donor and an acceptor layer [75]. Replacing the fullerenes by inorganic semiconductor nanostructures as electron acceptors is an alternative approach leading to so-called hybrid solar cells [76–80].

Nanostructures based on CdS, CdSe, CdTe, ZnO, SnO<sub>2</sub>, TiO<sub>2</sub>, Si, PbS and PbSe have been used so far as electron acceptors [60]. The idea is to create an extended heterojunction (often referred as bulk heterojunction in organic PV where a blend of two polymer is mixed at a nanometric scale) coupling inorganic nanostructured materials (electron acceptor) with a high surface / volume ratio (e.g. ZnO NR) and semiconductor polymer / molecules (electron donor) as schematically reported in Figure 2.27.

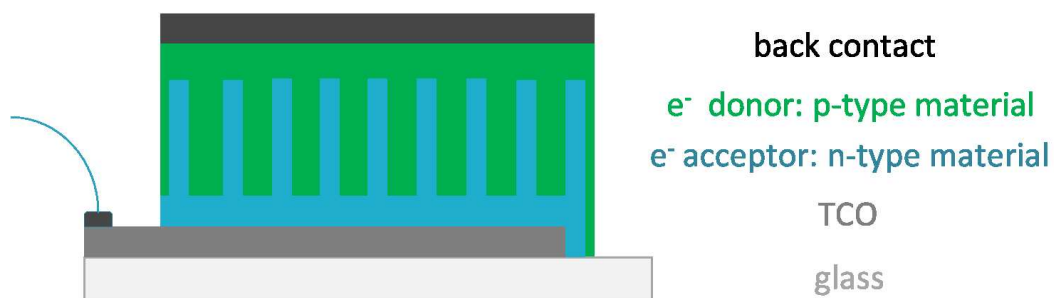


**Figure 2.27** XSC hybrid cell based on inorganic NR and organic polymer.

Upon illumination, the exciton is formed inside the organic absorbing material, it diffuses and dissociates at the interface transferring electrons and holes to n-type and p-type materials respectively. Electrons are collected at the TCO while holes at the metal counter-electrode. It must be noted that, in Figure 2.27, the organic materials acts as both light absorbing and hole carriers element. For most of hybrid inorganic / organic solar cells, two distinct materials are used, typically porphyrins and phthalocyanines are used to absorb visible light, while different conductive polymers are employed as donor materials [81–84].

Using nanostructured materials a n-type conductors has dramatic influence on PV device efficiency since it increases the exciton dissociation interface area. For example, in a PV cell based on CuPc-C<sub>60</sub>, the introduction of ZnO nanowires as electron donor layer has a more than fourfold increase in PV performance with respect to the device without nanowires [85]. NR shape present some interesting features: the NR have a single crystalline structure allowing a continuous path for

the electrons in the material. This minimizes the potential barriers such as grain borders and heterojunction barriers, improving electron conduction and reducing recombination. Moreover, NR present a high surface to volume that extends the possibility of exciton separation. Finally the NR make anode surface “rough” to induce scattering phenomena on incoming light and enables multiple trapping processes at the interface.

Bulk heterojunction hybrid solar cells containing inorganic nanostructures and semiconducting polymers are still lagging behind OSC in respect of device performance although they have theoretically the potential to exhibit better performances than devices containing solely organic compounds [60]. Research efforts have been done tailoring the anchoring groups of porphyrins and other dyes in order to provide a stronger binding to the inorganic materials and hence improve PV performances because of better electron injection [86–94].

Beside solar cells, there are ongoing researches to study phthalocyanines for gas sensing [95], in photodynamic therapy for cancer treatment [96,97], as semiconductor in field effect transistors [98–100] and as replacement for platinum in solid polymer fuel cells [101].

## References

- [1] L. R. Milgrom, *The Colours of Life: An Introduction to the Chemistry of Porphyrins and Related Compounds*, OUP, Oxford, 1997
- [2] X. Chen, Drain C. M., *Drug Des. ReV.*, 2004, **1** (3), 215
- [3] X. Chen, Hui L., Foster D. A., Drain C. M., *Biochemistry*, 2004, **43** (34), 10918
- [4] S. Hirohara, Obata M., Ogata S., Ohtsuki C., Higashida S., Ogura S., Okura I., Takenaka M., Ono H., Sugai Y., *J. Photochem. Photobiol. B*, 2005, **78** (1), 7
- [5] C. M. Drain, C. Kirmaier, C.J. Medforth, D.J. Nurco, K.M. Smith. D. Holten, *J. Phys. Chem.*, 1996, **100** (29), 11984
- [6] C. M. Drain, S. Gentemann, J.A. Roberts, N.Y. Nelson, C.J. Medforth, S. Jia, M.C. Simpson, K. M. Smith, J. Fajer, J.A. Shelnut, D. Holten, *J. Am. Chem. Soc.* 1998, **120** (15), 3781
- [7] J. L. Retsek et al., *J. Am. Chem. Soc.*, 2003, **125**, 9787
- [8] A. Varotto, G. Smeureanu, A. Aggarwal, C. M. Drain., *Fluorine-Related Nanoscience with Energy Applications*, Chapter 4
- [9] A. Marcelli, P. Foggi, L. Moroni, C. Gellini, P.R. Salvi, I.J. Badovinac, *J. Phys. Chem. A*, 2007, **111**, 2276
- [10] Y. Kurabayashi, K. Kikuchi, H. Kokubun, Y. Kaizu, H. Kobayashi, *J. Phys. Chem.*, 1984, **88**, 1308

- [11] M. Gouterman, *J. Mol. Spec.*, 1961, **6**, 138
- [12] M. Gouterman, G.H. Wagnière, L.C. Snyder, *J. Mol. Spec.*, 1963, **11**, 108
- [13] J. J. Weaver, *Corroles*, PhD Thesis, CALTEC, 2005
- [14] J. P. Collman et al., *Metal Ions in Biology*, Vol. 2, 1980, T.G. Spiro Ed., Wiley, New York
- [15] M. A. Schiavon et al., *J. Molecular Catalysis A*, 2001, **174**, 213
- [16] T. H. Richardson et al., *Thin Solid Films*, 2001, **393**, 259
- [17] K. S. Suslick, et al., Shape Selective Oxidation Catalysis, in *Comprehensive Supramolecular Chemistry*, Vol. 5, 1996, Elsevier, Oxford, p. 141
- [18] P. Bhyrappa et al., *J. Am. Chem. Soc.*, 1996, **118**, 5708
- [19] A. Goldoni, *Porphyrins: Fascinating Molecules with Biological Significance*, Elettra highlights, Trieste (2001–2002)
- [20] K. Sakaguchi, Chikamatsu M., Yoshida Y., Azumi R., Yase K., *Jpn. J. Appl. Phys.*, 2007, **46**, 345
- [21] G. Guillaud, Simon J., Germain J. P., *Coord. Chem. Rev.*, 1998, **178-180**, 1433
- [22] Z. Li, B. Li, J. Yang, J. G. Hou, *Acc. Chem. Res.*, 2010, **43** (7), 954
- [23] J. D. Wright, *Prog. Surf. Sci.*, 1989, **31**, 1
- [24] R. Zhou, F. Josse, W. Goepel, Z. Oeztuerk, O. Bekaroglu, *Appl. Organomet. Chem.* 1996, **10**, 557
- [25] H. Fukagawa, H. Yamane, S. Kera, K.K. Okudaira, N. Ueno, *Phys. Rev. B*, 2006, **73**, 041302
- [26] H. A. Abdeldayem, D.O. Frazier, B.G. Penn, D.D. Smith, C.E. Banks, *Thin Solid Films*, 1999, **350**, 245
- [27] X. Q. Zhou, M. Wang, S.L. Yang, *Mater. Chem. Phys.* 2002, **73**, 70
- [28] W. B. Wang, X. Li, S. Wang, W. Hou, *Dyes Pigm.* 2007, **72**, 38
- [29] Q. Zhang, Wang D., Xu J., Cao J., Sun J., Wang M., *Mater. Chem. Phys.* 2003, **82**, 525
- [30] S. Yamaguchi, Y. Sasaki, *Chem. Phys. Lett.* 2000, **323**, 35
- [31] T. Nishi, K. Kanai, Y. Ouchi, M.R. Willis, K. Seki, *Chem. Phys.*, 2006, **325**, 121
- [32] J. Mizuguchi, G. Rihs, H.R. Karfunkel, *J. Phys. Chem.* 1995, **99**, 16217
- [33] A. Yamashita, T. Maruno, T. Hayashi, *J. Phys. Chem.*, 1994, **98**, 12695
- [34] T. Saito, Sisk W., Kobayashi T., Suzuki S., Iwayanagi T., *J. Phys. Chem.*, 1993, **97**, 8026
- [35] N. Coppedè, T. Toccoli, A. Pallaoro, F. Siviero, K. Walzer, M. Castriota, E. Cazzanelli, and S. Iannotta, *J. Phys. Chem. A*, 2007, **111** (49), 12550
- [36] M. Brumbach, D. Placencia, and N. R. Armstrong, *J. Phys. Chem. C*, 2008, **112** (8), 3142
- [37] B. A. Gregg, *J. Phys. Chem. B*, 2003, **107** (20), 4688
- [38] C. W Tang, *Appl. Phys. Lett.*, 1986, **48**, 183
- [39] J. Simon, J. Andre, *Molecular Semiconductors*; Springer-Verlag: Berlin, 1985
- [40] B. A. Gregg, *Chem. Phys. Lett.*, 1996, **258**, 376
- [41] P. Peumans, V. Bulovic, S.R. Forrest, *Appl. Phys. Lett.*, 2000, **76**, 2650
- [42] G. Yu, J. Gao, J.C. Hummelen, F. Wudl, A.J. Heeger, *Science*, 1995, **270**, 1789
- [43] J. J. M. Halls, C.A. Walsh, N.C. Greenham, E.A. Marseglia, R.H. Friend, S.C. Moratti, A.B. Holmes, *Nature*, 1995, **376**, 498

- [44] A. J. Heeger, *J. Phys. Chem. B*, 2001, **105**, 8475
- [45] S. E. Shaheen, Brabec C. J., Sariciftci N. S., Padinger F., Fromherz T., *Appl. Phys. Lett.*, 2001, **78**, 841
- [46] M. Granstroem, K. Petritsch, A.C. Arias, A. Lux, M.R. Anderson, R.H. Friend, *Nature*, 1998, **395**, 257
- [47] W. U. Huynh, J.J. Dittmer, A.P. Alivisatos, *Science*, 2002, **295**, 2425
- [48] S. A. Jenekhe, S. Yi, *Appl. Phys. Lett.*, 2000, **77**, 2635
- [49] C. J. Brabec et al, *Adv. Funct. Mater.*, 2001, **11**, 374
- [50] A. C. Arango, L.R. Johnson, V.N. Bliznyuk, Z. Schlesinger, S.A. Carter, H.H. Hoerhold, *Adv. Mater.* 2000, **12**, 1689
- [51] G. G. Malliaras, J.R. Salem, P.J. Brock, J.C. Scott, *J. Appl. Phys.*, 1998, **84**, 1583
- [52] A. Hagfeldt, M. Graetzel, *Acc. Chem. Res.*, 2000, **33**, 269
- [53] B. O'Regan, M. Graetzel, *Nature*, 1991, **353**, 737
- [54] B. A. Gregg, In *Semiconductor Photochemistry and Photophysics*; Marcel Dekker: New York, 2003; Vol. 10, pp 51-88
- [55] M. K. Nazeeruddin et al., *J. Am. Chem. Soc.*, 1993, **115**, 6382
- [56] G. Schlichthoerl, H.Y. Huang, J. Sprague, A.J. Frank, *J. Phys. Chem. B*, 1997, **101**, 8141
- [57] A. Soedergren, A. Hagfeldt, J. Olsson, S.E. Lindquist, *J. Phys. Chem.*, 1994, **98**, 5552
- [58] A. Nozik, *J. Physica E*, 2002, **14**, 115
- [59] S. Ruehle, M. Shalom, and A. Zaban, *ChemPhysChem*, 2010, **11**, 2290
- [60] Y. Zhou, M. Ecka and M. Krueger, *Energy Environ. Sci.*, 2010, **3**, 1851
- [61] C. N. Hoth, P. Schilinsky, S. A. Choulis and C. J. Brabec, *Nano Lett.*, 2008, **8**, 2806
- [62] A. Troisi, *Adv. Mater.*, 2007, **19**, 2000
- [63] E. A. Silinsh, V. Capek, *Organic Molecular Crystals*, 1994, AIP Press, New York
- [64] S. Verlaak, D. Beljonne, D. Cheyns, C. Rolin, M. Linares, J. Cornil, and P. Heremans, *Adv. Funct. Mater.* 2009, **19**, 3809
- [65] P. Peumans, S. Uchida, and S. R. Forrest, *Nature*, 2003, **425**, 158
- [66] Q. L. Song, F. Y. Li, H. Yang, H. R. Wu, X. Z. Wang, W. Zhou, J. M. Zhao, X. M. Ding, C. H. Huang, and X. Y. Hou, *Chem. Phys. Lett.* 2005, **42**, 416
- [67] B. A. Gregg and M. C. Hanna, *J. Appl. Phys.* 2003, **93**, 3605
- [68] C. Rothe, S. M. King, and A. P. Monkman, *Phys. Rev. B*, 2005, **72**, 085220
- [69] H. R. Kerp, E.E. Van Faassen, *Chemical Physics Letters*, 2000, **332**, 5
- [70] J. J. M. Halls, K. Pichler, R.H. Friend, S.C. Moratti and A.B. Holmes, *Appl. Phys. Lett.*, 1996, **68**, 3120
- [71] D. E. Markov, E. Amsterdam, P.W.M. Blom, A.B. Sieval and J.C. Hummelen, *J. Phys. Chem. A*, 2005, **109**, 5266
- [72] D. E. Markov, C. Tanase, P. W. M. Blom and J. Wildeman, *Phys. Rev.B*, 2005, **72**, 045217
- [73] M. Y. Chan, S. L. Lai, M. K. Fung, C. S. Lee, and S. T. Lee, *Appl. Phys. Lett.*, 2007, **90**, 023504

- [74] W. B. Chen, H. F. Xiang, Z. X. Xu, B.-P. Yan, V. A. L. Roy, and C. M. Che, *Appl. Phys. Lett.*, 2007, **91**, 191109
- [75] J. Xue, S. Uchida, B. P. Rand, and S. R. Forrest, *Appl. Phys. Lett.*, 2004, **85**, 5757
- [76] E. Holder, N. Tessler and A. L. Rogach, *J. Mater. Chem.*, 2008, **18**, 1064
- [77] B. R. Saunders and M. L. Turner, *Adv. Colloid Interface Sci.*, 2008, **138**, 1
- [78] M. Skompska, *Synth. Met.*, 2010, **160**, 1
- [79] D. V. Talapin, J. S. Lee, M. V. Kovalenko and E. V. Shevchenko, *Chem. Rev.*, 2010, **110**, 389
- [80] N. C. Greenham, in *Organic Photovoltaics: Materials, Device Physics, and Manufacturing Technologies*, ed. V. D. C. Brabec and U. Scherf, Wiley-VCH, 2008, ch. 6, p. 179
- [81] W. Cheng, Y. Shen, G. Wu, F. Gu, J. Zhang and L. Wang, *Semicond. Sci. Technol.* 2010, **25**, 125014
- [82] P. Balrajua, Manish Kumarb, M.S. Royb, G.D. Sharmaa, *Synthetic Metals*, 2009, **159** (13), 1325
- [83] N. F. Atta, H.M.A. Amin, M. W. Khalil, A. Galal, *Int. J. Electrochem. Sci.*, 2011, **6**, 3316
- [84] D. Walker, S. Chappel, A. Mahammed, B. S. Brunshwig, J. R. Winklera, H. B. Graya, A. Zaban and Z. Gross, *J. Porphyrins Phthalocyanines*, 2006, **10**, 1259-1262
- [85] J. Liu, S. Wang, Z. Bian, M. Shan, and C. Huang, *Appl. Phys. Lett.* 2009, **94**, 173107
- [86] M. G. Walter, A. B. Rudine and C. C. Wamser, *J. Porphyrins Phthalocyanines*, 2010, **14**, 759
- [87] I. Aviv and Z. Gross, *Chem. Commun.*, 2007, 1987
- [88] M. Garcia-Iglesias, J. J. Cid, J. H. Yum, A. Forneli, P. Vazquez, M. K. Nazeeruddin, E. Palomares, M. Graetzel and T. Torres, *Energy Environ. Sci.*, 2011, **4**, 189
- [89] M. Garcia-Iglesias et al., *Chem. Sci.*, 2011, **2**, 1145
- [90] X. Li, H. Wang and H. Wu, *Functional Phthalocyanine Molecular Materials, Structure & Bonding*, 2010, **135**, 229
- [91] I. Lopez-Duarte, M. Wang, R. Humphry-Baker, M. Ince, M. V. Martinez-Diaz, M. K. Nazeeruddin, T. Torres, and M. Graetzel, *Angew. Chem. Int. Ed.*, 2011, **50**, 1
- [92] L. Zhang, Z. Cheng, Q. Huan, X. He, X. Lin, L. Gao, Z. Deng, N. Jiang, Q. Liu, S. Du, H. Guo, and H. Gao, *J. Phys. Chem. C*, 2011, **115**, 10791
- [93] G. Baffou, A. J. Mayne, G. Comtet, G. Dujardin, Ph. Sonnet, *Appl. Phys. Lett.*, 2007, **91**, 073101
- [94] A. Morandeira et al., *J. Am. Chem. Soc.* 2007, **129**, 9250
- [95] M. Bouvet, *Anal Bioanal Chem*, 2006, **384**, 366
- [96] D. Samaroo, M. Vinodu, X. Chen, and C. M. Drain, *J. Comb. Chem.*, 2007, **9**, 998
- [97] C. M. Whitacre, D. K. Feyes, T. Satoh, J. Grossmann, J. W. Mulvihill, H. Mukhtar, and N. L. Oleinick, *Clin Cancer Res*, 2000, **6**, 2021
- [98] R. Zeis, T. Siegrist, and C. Kloc, *Appl. Phys. Lett.* 2005, **86**, 022103
- [99] R. W. I. de Boer, A. F. Stassen, M. F. Craciun, C. L. Mulder, A. Molinari, S. Rogge, A. F. Morpurgo, *Appl. Phys. Lett.* 2005, **86**, 262109
- [100] Y. Zhang, X. Cai, Y. Bian and J. Jiang, *Structure & Bonding*, 2010, **135**, 275
- [101] K. K. Tintula, S. Pitchumani, P. Sridhar and A. K. Shukla, *Bull. Mater. Sci.*, 2010, **33** (2), 157

# 3 Experimental

---

## 3.1 Synthetic procedures

### 3.1.1 Growth of ZnO nanostructures

ZnO nanostructures with different morphologies (nanowires, nanorods, nanotapes, nanocombs, nanotetrapods, etc.) can be obtained by vapour phase growth techniques (Figure 3.1). As the nanocrystal nucleation and growth requires high supersaturation and synthesis parameters for the different morphologies are similar, even small fluctuations in the local growth conditions may lead to growth of mixed nanostructures. Therefore specific synthesis processes are required for selective growths of nanostructures with *single* morphology. Different experimental approaches have to be used in order to stabilize these growth processes on large-scale production. The most and widely employed expedient for growing ZnO nanowires or nanorods is the use of metal catalyst particles (*e.g.* Au) on the substrate to obtain size-controlled VLS (vapour-liquid-solid) growths. On the contrary, no precursor or catalyst has been used in our optimized growth processes to avoid inclusion of undesired impurities or dopants, which may have detrimental effects on material properties. Our research group defined three different catalyst-free optimized growth processes for three different ZnO morphologies:

- nanotetrapods (TP)
- vertically aligned nanorods (NR)
- nanowires (NW)

Since 2005 significant efforts have been made to optimize the growth process in order to obtain reproducible and large-scale growths of the desired nanostructures. As a simplified overview, growth process is similar for the three kind of nanostructures and is based on the evaporation of 5N Zn precursor followed by a controlled oxidation by means of 5N O<sub>2</sub> so that high purity material is obtained. Herein are reported the details about the growth of TP and NR, two interesting ZnO morphologies which have been functionalized during the PhD in perspective of gas sensing, photocatalytic and photovoltaic applications.

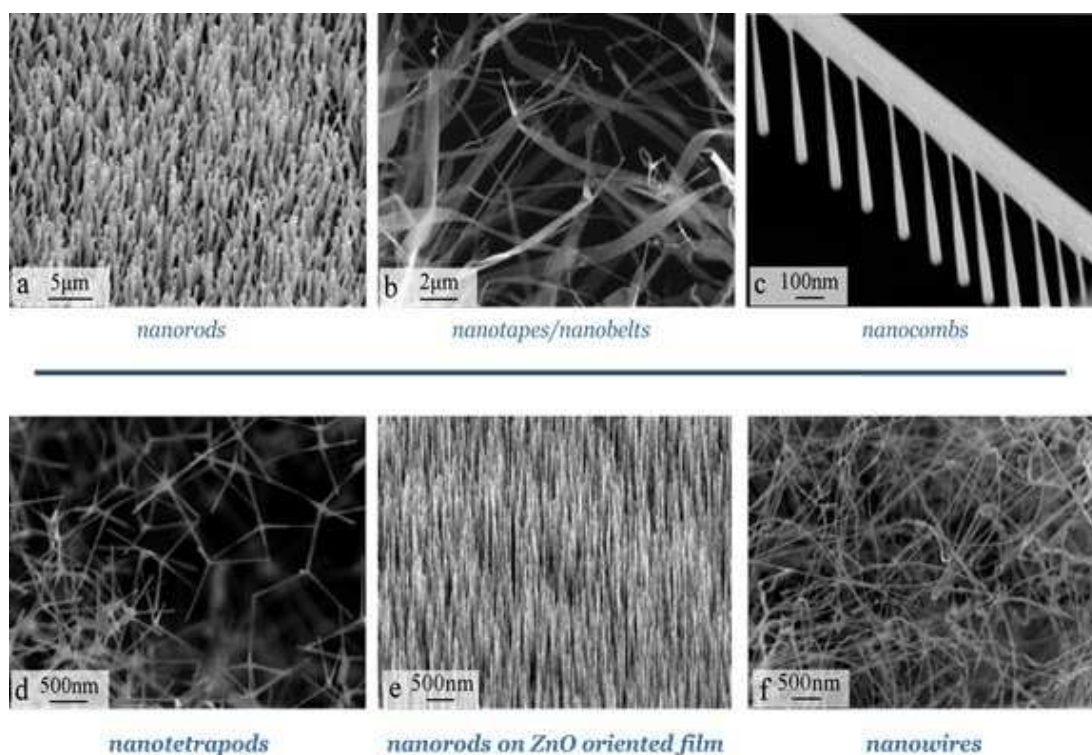


**Figure 3.1** Different ZnO morphologies grown by our group at IMEM institute. Adapted from [1].

### 3.1.1a Growth of ZnO tetrapods

Among different ZnO nanostructures, ZnO TP are the most suitable for large-scale integration since they can be obtained in large quantities (tens of milligrams per run in a small laboratory-scale reactor) by an optimized vapor-solid process. ZnO TP were grown by a combination of thermal evaporation and controlled oxidation, inside a tubular furnace with two independent heating elements and where different gases can be fluxed (Figure 3.2). No catalyst or precursor was used in order to reduce as much as possible unwanted contaminations. A metallic Zn foil (99.999% pure) was used as source material after a fast etching in diluted acid to remove oxide traces, which might reduce the evaporation rate. Source material was placed in the first zone of the furnace (labelled “Zn evaporation zone” in Fig. 1) and then heated up to 700 °C in an inert gas flow (Ar, 100 sccm). In this configuration Zn source was protected from oxidation by the inert gas flow, the whole synthesis process can run up to complete source evaporation. Zn vapor generated by heated source was carried by the Ar flow along the reactor up to the furnace region where it matched a 10 sccm oxygen flow (labeled “nucleation and growth zone” in Figure 3.2), which enter the reactor through a separate inlet tube. In this “matching-region”, where temperature was set in the range 600-500 °C, TP nucleation and growth started.

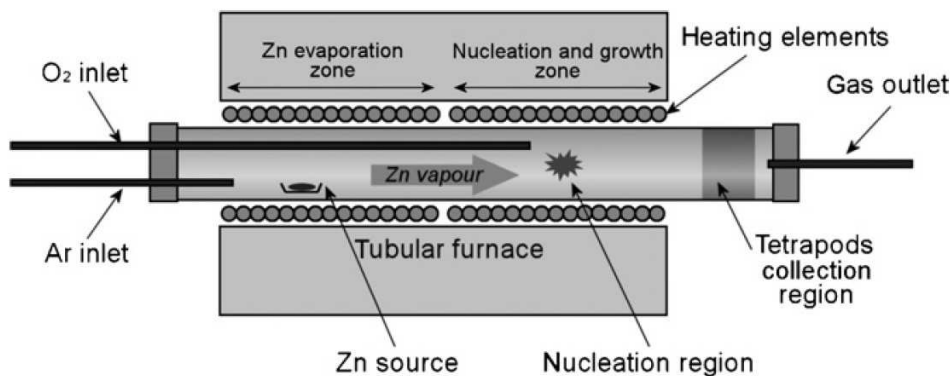


**Figure 3.2** Simplified sketch of the synthesis reactor [2].

While floating in the gas stream, TP grew until they reached the cold zone at the end of the furnace. Floating TP came out of the heated zone in form of a continuous white smoke and there they deposited on the walls of reactor's quartz tube, forming a thick and fluffy layer. This kind of thick "film" can be easily removed from the reactor at the end of the growth. The study of morphology by SEM imaging showed that the TP "legs" generally are 50-200nm thick (cross-section) and a few microns in length (Figure 3.3 (a) and (b)). Average TP dimension can be generally controlled by correctly tuning the growth parameters. In the described growth reactor different temperatures can be chosen for the region of source material and for the region of oxygen introduction. Growth dynamics in this system is rather complex and different parameters must be carefully balanced, but general observations can be done, *i.e.* TP thickness increases generally with higher source temperature, lower carrier gas flow and higher oxidation temperature.

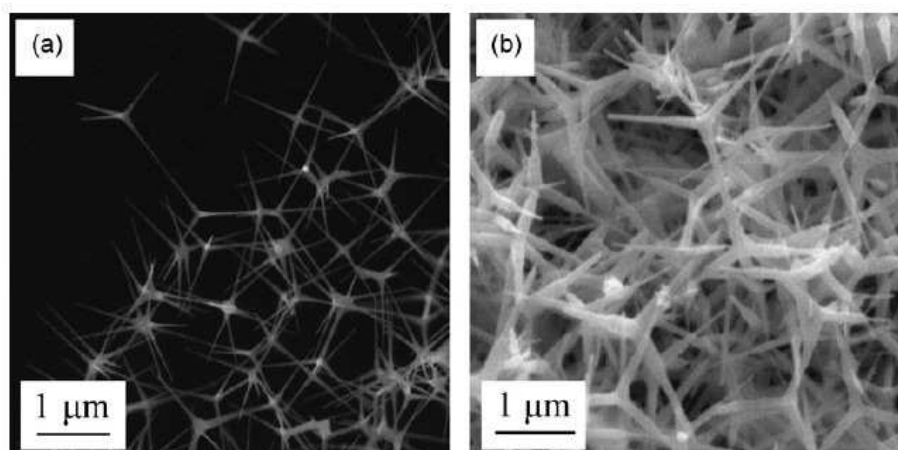


**Figure 3.3** SEM images of different TP growths reflecting different dimensions. Adapted from [2].

Collected TP can be dispersed in organic solvents (isopropyl alcohol (IPA), n-butyl alcohol, dimethylformamide (DMF), methylethylketone (MEK), chloroform) and precipitated from the suspension through a mechanical mask onto the desired substrate. This is particularly interesting for large scale integration, where substrate as large as 1 inch can be prepared. Moreover, the



possibility to obtain stable suspension with these nanostructures, makes them potentially compatible with the preparation of screen-printing “inks”.

### 3.1.1b Growth of ZnO nanorods

Recently our group have obtained on ZnO films by vapor phase at relatively low temperature ( 500 °C ) on different substrates (glass, ITO, AZO, Si). In this temperature range, which is for example interesting for glass-compatible processes for solar cell production, it is generally impossible to obtain a standard vapor–solid growth of these ordered nanostructures without the use of metal-organic precursors or metal catalysts [3]. The growth of ZnO NR was carried out inside a laboratory scale reactor (a tubular furnace), through which it is possible to flow different gasses (Ar, O<sub>2</sub> with regards to the NR growth). The used source material was pure metallic Zn powders (5N purity, 300 mg) that were softly etched before use in 1 : 100 diluted HNO<sub>3</sub> for 1 min. This etching process is fundamental in order to remove the native oxide and to make possible a maximized and reproducible Zn evaporation from source material. The source and substrate were placed one next to the other, with the substrate in a downstream position, at the center of the furnace. Source material was partially covered so that generated vapor could exit only through a small window.

According to Figure 3.4, the growth procedure consisted of three main steps: at first (0) a partially closed Zn source container and a substrate with seeding ZnO layer are put in the reactor (Figure 3.5a); during the first step (1) Zn vapors accumulate inside the source container and during the second step (2) Zn nanoclusters form inside Zn-rich vapors and are transported onto the substrate (Figure 3.5b). At the third step (3) NR grow from the nuclei created by the Zn clusters (Figure 3.5c) [3].

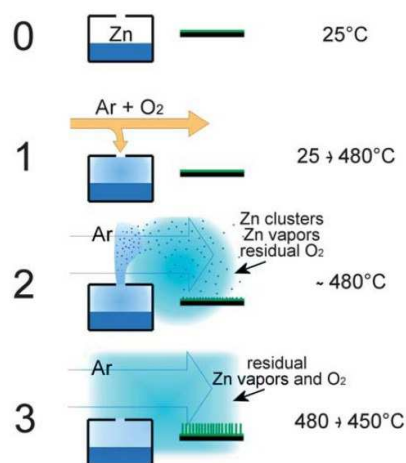


**Figure 3.4** Scheme of the main reaction steps to grow ZnO NR [3].

(1) The first step is devoted to the accumulation of Zn vapors in the source material container and takes place during heating and the 5 min temperature plateau at 480 °C. During this first step, oxygen is mixed with Ar in the gas flowing at the top of the source container and, in that position, Zn vapors escaping from the small container window are locally oxidized, preventing any premature growth on the substrate. At the same time, the small window size prevents any strong oxidation of source material that, by continuous evaporation, fills the empty container volume with a pressure that approaches the equilibrium value for Zn vapor at this temperature.

(2) The second step is very fast and allows Zn nanoclusters to form. It starts when the Ar/O<sub>2</sub> mixture is substituted by a larger Ar flow. The decrease in oxygen content in the reactor let Zn vapor spread in the reactor from the container window, where it gets in contact with the colder Ar flow. The sudden temperature gradient promotes the formation of Zn clusters (Figure 3.5b) that are brought by the flow in the nearby substrate region. This second step takes place in less than 1 min and then stops because further Zn condensation is rapidly inhibited by the decrease in Zn vapor pressure.

(3) The third and last step, then, takes place during the first minutes of cooling (generally from 480 °C to 450 °C), during which Zn nanoclusters, on the substrate, oxidize and act as nuclei and preferential growth sites for NR. It is indeed the step in which NR nucleate and grow on the substrate by consuming most of the neighboring residual Zn vapor and O<sub>2</sub> (Figure 3.5c). The NR growth takes place homogeneously over a large area (Figure 3.5d) [3].

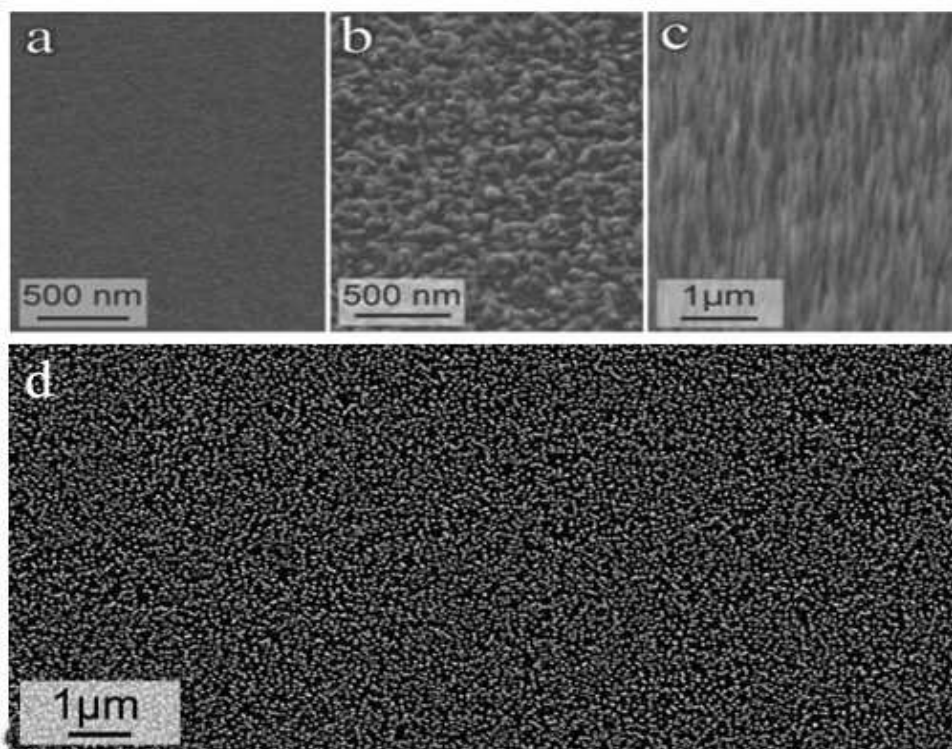


**Figure 3.5** SEM images of: **(A)** the starting ZnO seeding film; **(B)** the oriented nuclei obtained by nanoclusters oxidation; **(C)** the resulting ZnO NR **(D)** NR seen from above [3].

### 3.1.2 Solution growth of nanoparticles

Experimental setup for the solution-based synthesis of semiconductor NP is standard and simple (Figure 3.6). A *home-brew* Schlenk line is placed under the lab hood and allow to work under vacuum (water pump) or inert gases (Ar, N<sub>2</sub>) atmosphere. Three (or four) necks round flasks are used in order to have inlet for vacuum / gas, temperature controller, eventually a neck with rubber membrane for the hot-injection of precursors, and an outlet neck to fit a reflux condenser. Traps are used both in and out of the reaction room: zeolites are inline to the reaction flask to limit humidity contamination and a bubbler is placed to trap solvent vapors eventually escaping the reflux condenser.

The heating / stirring plate allows to work as high as 350 °C with 200ml of high boiling solvent (*e.g.* oleylamine) when fireclays are used to limit heat dissipation. When the reaction is complete, a centrifuge (Hettich RotoSilenta III, 8000 r.m.p. max) is used to wash and collect the solid phase.

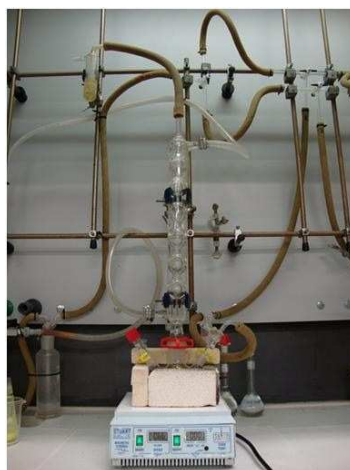


**Figure 3.6** The synthetic apparatus used for the synthesis of semiconductor nanoparticles.

### 3.1.3 Supersonic Molecular Beam Deposition (SuMBD)

The growth of thin organic thin films has been performed by Dr. Nicola Coppedè in a tailor-made SuMBD apparatus (Figure 3.8) [4] developed at the IMEM-CNR institute in Trento. It is based on the supersonic expansion in vacuum of a carrier noble gas, seeded by the organic molecules through thermal sublimation. Although in a classical beam, or Knudsen cell, the vapor formed will effuse in a molecular regime, in a supersonic beam, it is seeded in a much higher pressure of a lighter gas (*e.g.*, H<sub>2</sub>, He, or Ar), so that an isentropic expansion into vacuum occurs. The velocity and internal energy distributions of the molecules follow a Maxwell–Boltzmann distribution function, with kinetic energy one or two order of magnitude higher respect to thermal regimes. The angular distribution is typically cosine-like with a higher directionality in the beam. A well-defined beam is then obtained by the skimming of the expansion with a sharp-edged collimator, with a

conical profile. The major characteristics of supersonic beams are narrow velocity and angular distributions, an average velocity that, in the limit of very low seeding, can reach that of the much lighter carrier gas, and fast cooling of the internal degrees of freedom. The SuMBD apparatus basically consists of a differentially pumped supersonic beam, a TOF mass spectrometer, and a deposition chamber (Figure 3.7).

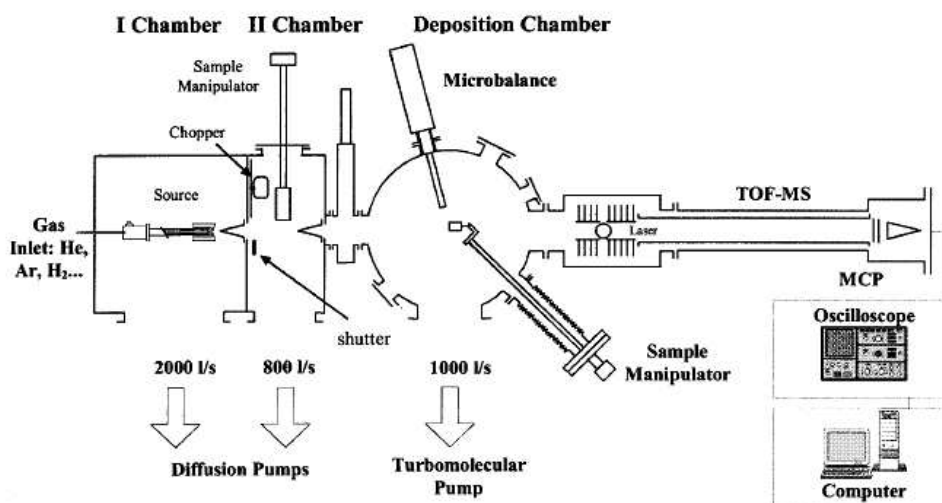


Figure 3.7 SuMBD experimental apparatus [5].

The supersonic beam source, placed in a high vacuum chamber, is made of a quartz tube with a micrometric nozzle at the front end (typically 50–130  $\mu\text{m}$  in diameter). An inert carrier gas (helium in this experiment) is injected in the quartz tube at a controlled pressure (2–3 bar). Inside the tube, a vessel with the organic material powder is used to sublimate by Joule heating the molecules, dispersing them at very low concentrations into the gas, and expanding both through the source nozzle into the deposition chamber. A conical skimmer selects the central part of the beam, which proceed to the sample in a ultra-high vacuum chamber (Figure 3.8).

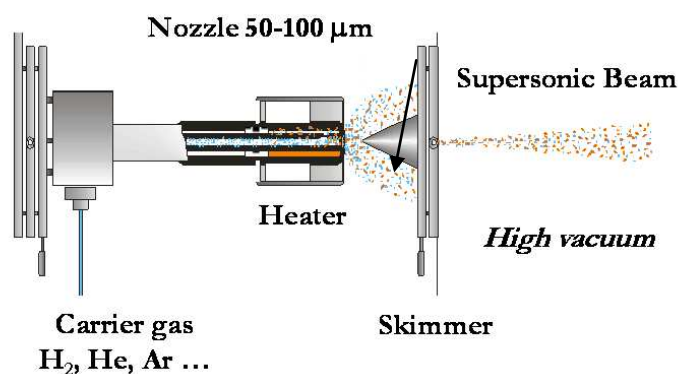
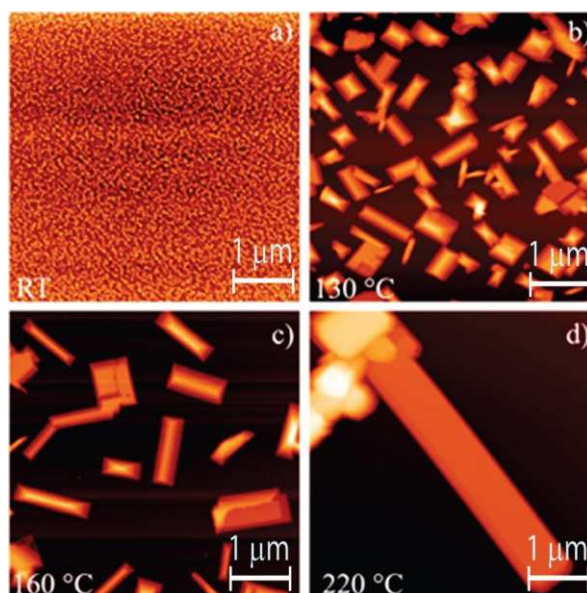


Figure 3.8 Sketch of the SuMBD source [6].

By changing the working parameters (nature and pressure of the carrier gas, sublimation temperature, nozzle diameter, and temperature), it is possible to finely control key properties of molecules in the supersonic beam such as kinetic energy, momentum, and cooling of the internal degrees of freedom typically induced by expansion. The source is typically operated using a He carrier gas pressure in the range of 100–200 kPa. The central part of the beam is selected by skimming the free jet expansion via a sharp edged conical collimator, which separates the source from the deposition chambers (base pressure  $10^{-8}$  mbar). Here, the molecular beam is intercepted by the substrate, the temperature of which can be varied from -115 up to 350 °C, with a stability of about 1 °C. SuMBD deposition allows the tuning of the kinetic energy of the molecules during the deposition in order to control the growth process, resulting in an improved quality of the organic semiconducting thin films, reaching growth regimes that are not accessible to thermodynamic equilibrium techniques [5,6]. An example of films and ordered crystals grown by SuMBD technique is illustrated in Figure 3.9.



**Figure 3.9** AFM micrographs ( $5 \mu\text{m} \times 5 \mu\text{m}$ ) of TiOPc thin films deposited on  $\text{SiO}_2$  by SuMBD at different substrate temperatures: (A) 25 °C, (B) 165 °C, (C) 160, and (D) 220 °C [7].

## 3.2 Characterization techniques

### 3.2.1 Optical Properties

The optical properties of a semiconductor have their genesis in both intrinsic and extrinsic effects. Intrinsic optical transitions take place between the electrons in the conduction band and holes in the valence band, including excitonic effects due to the Coulomb interaction. Excitons are classified into free and bound excitons. In high quality samples with low impurity concentrations, the free excitons can also exhibit excited states, in addition to their ground-state transitions. Extrinsic properties are related to dopants/impurities or point defects and complexes, which usually create electronic states in the bandgap, and therefore influence both optical absorption and emission processes. The electronic states of the bound excitons, which may be bound to neutral or charged donors and acceptors, depend strongly on the semiconductor material, in particular the band structure. ZnO is a direct gap semiconductor ( $E_g \sim 3.2$  eV) with the global extremes of the upmost valence and the lowest conduction bands (VB and CB, respectively) at the same point in the Brillouin zone, namely at  $\mathbf{k} = 0$ , *i.e.* at the  $\Gamma$ -point. The lowest CB is formed, from the empty 4s states of  $\text{Zn}^{2+}$  or the antibinding  $sp^3$  hybrid states, while the VB originates from the occupied 2p orbitals of  $\text{O}_2^-$  or the binding  $sp^3$  orbitals.

#### 3.2.1a Absorbance

The simplest way to describe the expected absorption spectrum in a direct-gap semiconductor, like ZnO, is in terms of this band-to-band transition as shown in Figure 3.10. In an optical transition, both energy and momentum must be conserved. Because the momentum of a photon,  $h/\lambda$  ( $\lambda$  is the wavelength of light which is typically thousands of angstroms), is very small compared to the crystal momentum  $h/a$  ( $a$  is the lattice constant, typically a few Angstroms), the photon absorption process should conserve the electron momentum. Thus, the absorption coefficient  $\alpha(h\nu)$  for a given photon energy  $h\nu$  is proportional to the probability,  $P_{if}$ , for the transition from the initial state to the final state (governed also by the conservation of momentum), the density of electrons in the initial state,  $n_i$ , and also the density of electrons in the final states,  $n_f$ . This process must be summed for all possible transitions between states separated by an energy difference equal to  $h\nu$ :

$$\alpha(\hbar\omega) = A \sum P_{if} n_i n_f$$

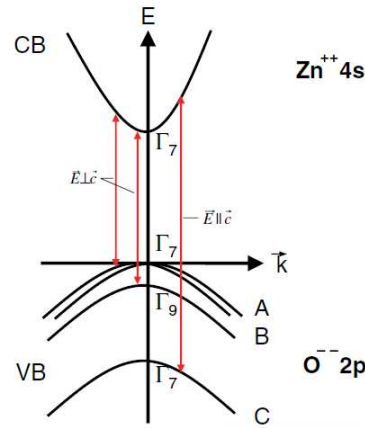


**Figure 3.10** Valence and conduction bands of ZnO in the vicinity of the fundamental bandgap [8].

Depending upon the relationship between the momentum in the initial and final states (which depend on the profile of the “parabolic energy valley”) direct or indirect transitions can occur, and this affects all the three terms  $P_{if}$ ,  $n_i$  and  $n_f$ . It must be noted that in transitions between indirect valleys (Figure 3.11) momentum is conserved via interaction with a phonon (*i.e.* a quantum lattice vibration), which can be either emitted or adsorbed.

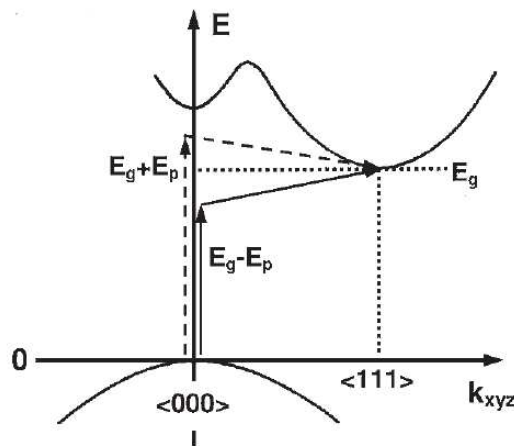


**Figure 3.11** Indirect band gap semiconductor with conduction band valleys at  $k = \langle 000 \rangle$  and  $k = \langle 111 \rangle$  [9].

By using the parabolic valley model, an expression of  $\alpha(h\nu)$  for each type of transition (allowed or forbidden in dependence on selection rules) can be obtained [9–11]. As a common feature, for crystalline solids,  $\alpha(h\nu)$  appeared expressed in all cases in the form:

$$\alpha(h\nu) = B(h\nu - E_g)^n$$

where  $B$  contains the dependence on  $P_{if}$ ,  $n_i$  and  $n_f$  specific for each type of transition (that essentially rules the transition edge width),  $E_g$  is the interband energy gap and  $n$  can take values 1/2, 3/2, 2, 3 for direct allowed, direct forbidden, indirect allowed and indirect forbidden

transitions, respectively. As semiconductor dimensions decreases, quantum confinement plays an important role in their electronic and optical properties. The quantum confinement effect for SC NP can be qualitatively explained using the effective mass approximation [12–15]. For a spherical particle with radius  $R$ , the effective band gap,  $E_g(r)$ , is given by:

$$E_g(r) = E_g(\infty) + \frac{\hbar^2}{8r^2} \left( \frac{1}{m_e} + \frac{1}{m_h} \right) - \frac{1.8e^2}{\epsilon r}$$

where  $r$  is the NP radius,  $E_g(r)$  and  $E_g(\infty)$  is the effective band gap and the bulk band gap, respectively. The  $m_e$  and  $m_h$  are the effective mass of electron and hole, and  $\epsilon$  is the bulk dielectric constant. The second term on the right-hand side shows that the effective band gap is inversely proportional to  $R^2$ , it increases as size decreases. On the other hand, the third term shows that the band gap energy decreases with decreasing  $R$  due to the increased Coulombic interaction. The second term becomes dominant with small  $R$ , thus the effective band gap is expected to increase with decreasing  $R$  [16]. In semiconductors, confinement effects are strong for particles whose radius is significantly smaller than the exciton Bohr radius,  $a_B$ , ( $r \ll a_B$ ), intermediate for  $r \sim a_B$  and negligible for larger particles with radius a few times larger than  $a_B$ . The Bohr exciton radius,  $a_B$ , is given by:

$$a_B = \frac{\epsilon_0 \epsilon \hbar^2}{\pi \mu e^2}$$

where  $\epsilon_0$  and  $\epsilon$  are the permittivity of vacuum and relative permittivity of the semiconductor,  $\mu$  is the reduced mass of the electron and hole,  $\frac{m_e m_h}{m_e + m_h}$ , and  $e$  is the electron charge. For example, the Bohr radius of CdS is around 2.4 nm [17], and particles with radius smaller or comparable to 2.4 nm show strong quantum confinement effects as indicated by a significant blue shift of their optical absorption relative to that of bulk [18–20].

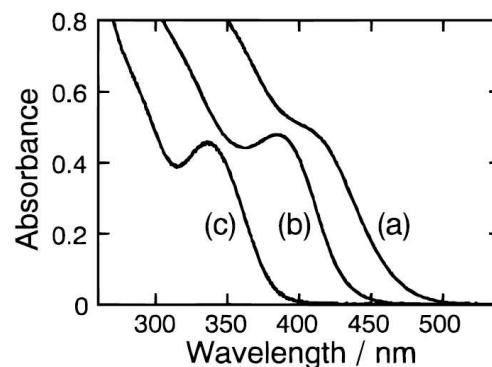


**Figure 3.12** Absorption spectra of CdS nanoparticles in heptanes, curves correspond to different CdS NP dimensions: a) 1 nm, b) 3 nm, c) 5 nm. Adapted from [21].



Absorbance spectroscopy is also used to determine the optical properties of a solution. Light is sent through the sample and the amount of absorbed light is measured. When the wavelength is varied and the absorbance is measured at each wavelength, a (wavelength vs absorbance) graph can be drawn using computer software. The applications of absorbance spectroscopy for solutions are extensive. For example, the absorbance can be used to measure the concentration of a solution by using Beer-Lamberts Law. However, when dealing with encapsulated nanoparticles as well “rough” thin films (*e.g.* ZnO NR, TP), the optical properties are much more complicated and the interpretation may not be straightforward because the measured absorbance spectrum does not necessarily show the actual absorbance but the extinction of the light. The extinction is both the absorbed and the scattered light from the particles / film. The absorption measurements were taken by Jasco V-530 spectrophotometer, typically operating in the 200–1100 nm spectral range, with 100 nm/min scanning speed and 1 nm data pitch.

### 3.2.1b Photoluminescence (PL)

Photoluminescence is a result of incident-photon absorption that generates electron-hole pairs and produces emission of a photon at different wavelength. The incident photons, when absorbed, excite electrons usually from the valence band into the conduction band through momentum-conserving processes because the photon momentum is negligible. The electrons and holes thermalize to the lowest energy state of their respective bands via phonon emission before recombining across the fundamental bandgap or the defect levels within the bandgap and emitting photons of the corresponding energies. A photon with an energy larger than the bandgap excites an electron from the VB to the CB. Since the density of states varies in three dimensions for a parabolic  $E(\mathbf{k})$  relation as the square-root of the energy, one would expect on this level, the onset of the absorption spectrum  $\alpha(h\nu)$  according to

$$\alpha(h\nu) \simeq \sqrt{h\nu - E_g}$$

for  $h\nu \geq E_g$ , equals to zero otherwise. Indeed, this picture is too simple to be compatible with reality. Absorption process is a two-particle transition, *i.e.* by the absorption of a photon simultaneously an electron in the CB and a hole in the VB are created. Similarly, two particles are annihilated in a radiative or non-radiative recombination process. The point is now that the electron and hole interact via their attractive Coulomb potential, forming a series of hydrogen-like states below the gap, Figure 3.13. These states are called excitons.

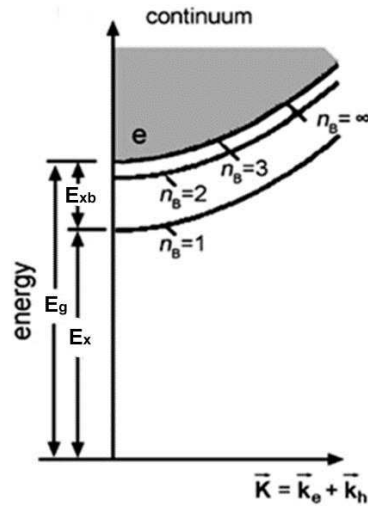


**Figure 3.13** Schematic drawing of the excitonic states. Adapted from [22].

The excitons are the quanta of the excitation in the electronic system of semiconductors or insulators. The ground state is a semiconductor with completely filled VB and empty CB. It has energy  $E = 0$  and total momentum  $\hbar\mathbf{k} = 0$ . The series of hydrogen-like exciton states with main quantum number  $n_B = 1, 2, 3, \dots$  is followed by the ionization continuum, starting at  $E_g$ . In photoluminescence, the observed transition with highest energy corresponds to the exciton energy  $E_x = E_g - E_{xb}$  (Figure 3.13). The ZnO excitonic binding energy ( $E_{xb}$ ) is roughly equal  $E_{xb} \approx 60$  meV while the excitonic Bohr radius is  $a_B = 18 \text{ \AA}$  [23–31]. The huge deviations from the energy of hydrogen ( $R_y(\text{H}) = 13.6$  eV,  $a_B(\text{H}) = 0.53 \text{ \AA}$ ) are caused by the effective and reduced electron and hole masses (band diagram curvature) and the dielectric constant of the material (*screening*). However, the optical properties of free, intrinsic excitons, which are characterized by a  $\mathbf{k}$  vector and a dispersion relation  $E(\mathbf{k})$ , are just a first order assumption. In fact electrons doesn't move freely through the crystal and are subject to scattering processes, *e.g.* with phonons or structural defects. Furthermore, excitons can be bound to some center or defect, like ionized or neutral donors ( $D^+$ ,  $D^0$ ) or neutral acceptors ( $A^0$ ) forming  $D^+X$ ,  $D^0X$  or  $A^0X$  bound-exciton complexes (BXC) [32–36]. Usually there are no  $A^-X$  complexes because it is energetically more favorable to have a neutral acceptor  $A^0$  and a free electron ( $A^0e$ ). These BXC have no translational degree of freedom, therefore they form – at low temperatures and defect concentrations – very narrow luminescence and absorption bands. In Figure 3.14 is reported a low temperature spectrum of ZnO TP grown by our group at IMEM (refer to Ch. 3.1 for growth details). Free (FX) and bound ( $D^0X$ ,  $A^0X$ ) exciton emissions are observed.

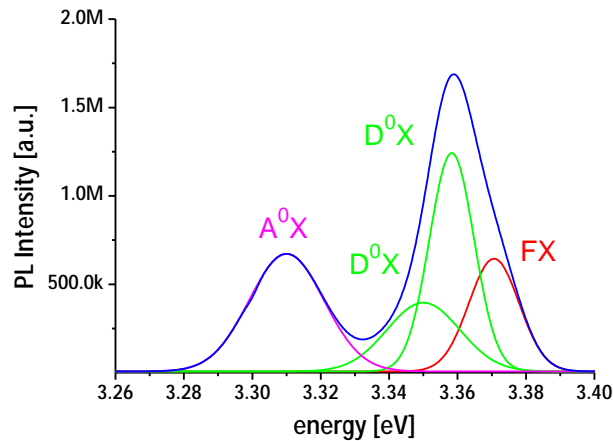


**Figure 3.14** ZnO PL spectra at low temperature (10K). NBE luminescence due to different BXC recombinations.

The PL setup is straightforward and a schematic view is pictured in Figure 3.15. Exciting laser is a 325 nm He-Cd produced by Kimmon Electronics and rated for 200 mW. Laser beam passes through a mechanical chopper (32 Hz frequency) controlled by a power supply allowing precise adjustments of the chopper frequency. The periodic interruptions of the light was required in order to provide the reference signal for the lock-in amplifier, which operates on the base of a phase-locked loop (PLL) device. Two optical mirrors set the beam height and a convergent lens focuses the spot on the sample mounted on the cryostat. Luminescence light is collected through two condenser lenses and focused on monochromator's input slits. PMT is used as photon to electron conversion element, the signal is amplified by a lock-in amplifier (Princeton Applied Research mod. 5209) and a RS-232 pc based interface (SPEX 1702/04) is used to program the spectrum acquisition. The actual setup is pictured in Figure 3.15.

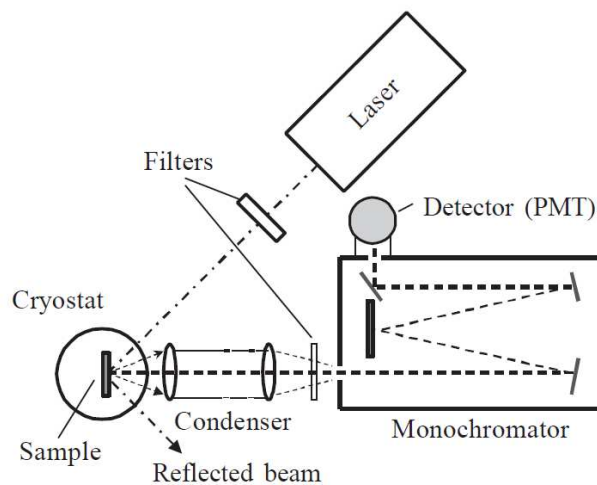


**Figure 3.15** Schematic representation of the PL setup.

User-defined parameters are:

- wavelength range (330 ÷ 800 nm)
- scanning speed (0.1 ÷ 15 Å / s)
- Integration time (3 ms ÷ 3 s)

The low temperature setup is made by a rotary pump ( $10^{-3}$  mbar), a compressor and the cryostat. Rotary pump is used to make vacuum inside the cryostat chamber, while the compressor employs a closed loop circulation of helium gas, used for sample cooling. The gas flows from the compressor to the refrigerator cryostat through a stainless steel high pressure hoses. Helium is heated when cooling the cryostat cold head, that is thermally coupled to the cold finger where the sample is mounted on. Two diodes control the temperature: one just above the cold head and the other is mounted on the cold finger itself, 5 mm away from the sample.

## 3.2.2 Structural Characterizations

### 3.2.2a X-Ray Diffraction (XRD)

XRD is a versatile, non-destructive analytical method for identification and quantitative determination of various crystalline forms, known as ‘phases’ of compound present in powder and solid samples. Diffraction occurs as waves interact with a regular structure whose repeat distance is about the same as the wavelength. The phenomenon is common in the natural world, and occurs across a broad range of scales. For example, light can be diffracted by a grating having scribed lines spaced on the order of a few thousand angstroms, about the wavelength of light. It happens that X-rays have wavelengths on the order of a few angstroms, the same as typical inter-atomic distances in crystalline solids. When certain geometric requirements are met, X-rays scattered from a crystalline solid can constructively interfere, producing a diffracted beam. In 1912, W. L. Bragg recognized a predictable relationship among several factors summed in the well-known Bragg equation:

$$n\lambda = 2d \cos \theta$$

Bragg's law states the condition for a sharp diffraction peak from an infinite crystal with perfect 3D order. Typically the diffraction peak has a finite width which is associated with imperfection in some of the Bragg parameters. These imperfections can be associated with beam divergence, a somewhat polychromatic source, or defects in the crystals. The latter can be a basis for quantitative measurement of the deviation from the Bragg requirement for perfect crystal which is infinite in all

spatial directions. Deviations from the latter requirement have been explained in terms of 3 features: (1) finite crystallite size (Scherrer equation [45–47]), (2) distortions of the first kind, which are random motion of atoms in a crystalline lattice (Debye thermal broadening) or other local randomization of lattice sites which do not disturb the 3D repetition or crystalline motif, and (3) distortions of the second kind, which involve destructive of long range order in the crystal, *i.e.* at long distances the lattice does not repeat perfectly. These usually lead to preferential broadening of high order peaks. The Scherrer equation can be written as:

$$D = \frac{\kappa\lambda}{\beta \cos \theta}$$

where  $D$  = mean diameter,  $k$  = shape factor,  $\lambda$  = wavelength,  $\beta$  = the full-width at half maximum, and  $\theta$  = Bragg angle for studied reflection. Since small angular differences in angle are associated with large spatial distances (inverse space), broadening of a diffraction peak is expected to reflect some large scale feature in the crystal. The simplest way to obtain the Scherrer equation is to take the derivative of Bragg's law holding the wavelength constant and allowing the diffraction angle and the Bragg spacing to vary,  $2d\sin\theta = \lambda$ . Take derivative in  $d$  and  $\theta$  yields  $2\Delta d\cos\theta\Delta\theta = \lambda$  since  $\Delta\theta$  can be positive or negative the absolute value must be taken and it reflects the half width of the peak (really half-width at half-height) so  $2\Delta\theta$  is the peak full-width at half-height ( $\beta$ ). The shape factor provides information about the “roundness” of the particle. For a spherical particle the shape factor is 1, for all other particles it is smaller than 1. The formula for this calculation is:

$$\kappa = 4\pi \frac{\text{area}}{\text{perimeter}^2}$$

If a Gaussian function is used to describe the peak a pre-factor of 0.9 occurs so the Scherrer equation is given as [48]:

$$\Delta D = \frac{0.9\lambda}{\beta \cos \theta}$$

XRD patterns were recorded using a Thermo Scientific (Thermo ARL X'tra) diffractometer at Laboratorio di Strutturistica “M. Nardelli” (Università di Parma), thanks to Prof. Gianluca Calestani for allowing me to use the instrumentation. The diffractometer has a Bragg-Brentano  $\theta$ – $\theta$  configuration (Figure 3.16) with a maximum  $2\theta$  excursion ranging from  $-8^\circ$  and  $180^\circ$ . X-Ray source is Cu  $K\alpha$  ( $\lambda = 1.542 \text{ \AA}$ ) and the accelerating voltage can be set in the range  $20 \div 40 \text{ KV}$ . Diffracted rays are collected through a solid state Si:Li detector cooled by Peltier element.

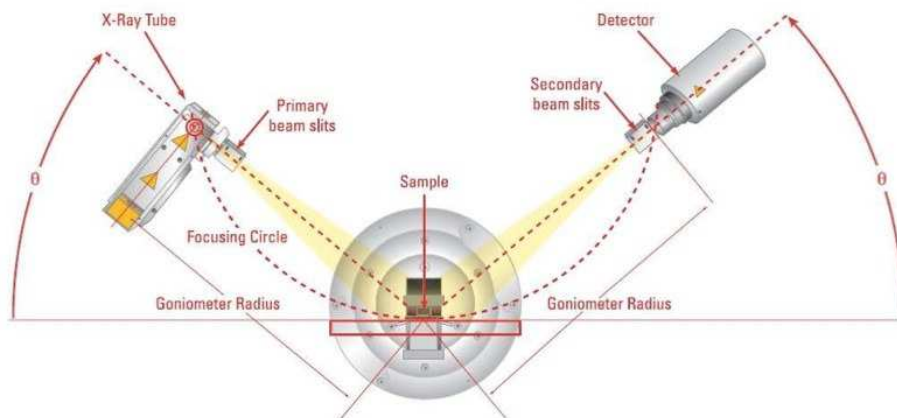


**Figure 3.16** The Bragg-Brentano  $\theta$ - $\theta$  geometry.

A typical ZnO wurtzite XRD pattern (Cu  $K\alpha$  radiation) is showed in Figure 3.17. The measure is about ZnO TP grown by our group at the IMEM institute (refer to Ch. 3.1.1a for growth details).

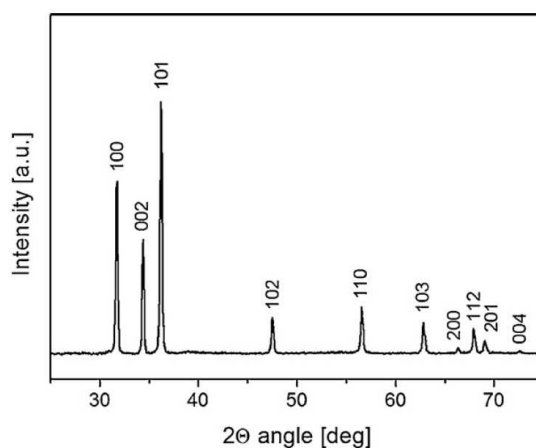


**Figure 3.17** Powder XRD pattern of ZnO TP with a typical wurtzite structure (PDF 36-1451) [2].

### 3.2.2b Transmission Electron Microscopy (TEM)

TEM analysis were performed by Dr. Laura Lazzarini in the IMEM institute, using a JEOL JEM-2200FS. The primary electrons are emitted by a field-emission gun (with accelerating working voltage is 200 eV), consisting in an extraordinary thin tungsten tip, covered by zirconium coating. Electro-magnetic condenser lenses collect the electrons coming from the source and send them to the specimen in a parallel and coherent beam. Just beyond the sample, several magnetic lenses (objective, intermediate and projector) collect the transmitted beam, in order to compose a magnified sample image and send it to a CCD camera. TEM equipment allows a wide range of analytical methods. In particular, the sample imaging can be obtained by TEM, High resolution

(HREM) and in scanning (STEM) mode. The first two methods allow to display the material crystalline lattice (see Figure 3.18), by using the transmitted and the low-angle (Bragg) diffracted electrons while STEM mode generates high-angle and incoherent diffracted electrons, whose intensity depends on the atomic number  $Z$ . This method, called  $Z$ -contrast, gives also chemical information about the material. Moreover, purely chemical information about sample composition can be extracted by Energy Dispersive X-Ray Spectrometry (EDX). To operate the TEM in diffraction mode (ED), and obtain a reciprocal lattice image, the objective aperture is removed from the beam path and the scope is adjusted to focus an image of the back focal plane of the objective lens, not the image plane. The obtained pattern is completely dependent on the  $d$ -spacing and composition of the crystal that is being analyzed.

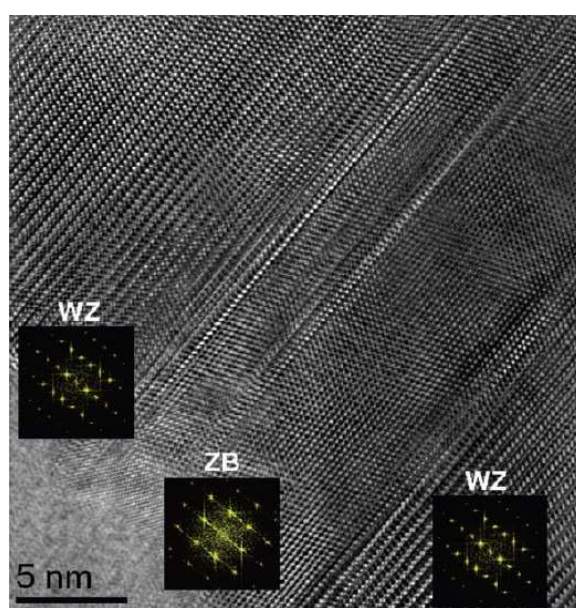


**Figure 3.18** HREM image of ZnO TP nanostructure. A zinc blend phase is observed between two wurtzite regions (as shown by FT insets). Adapted from [39].

### 3.2.3 Magnetic Characterizations

Magnetic materials encompass a wide variety of materials and are classified in terms of their magnetic properties and their uses. They are classified by their susceptibility to magnetic fields into diamagnetic materials with weak repulsion from an external magnetic field (negative susceptibility), paramagnetic materials showing small and positive susceptibility, and ferromagnetic (FM) materials which exhibit a large and positive susceptibility to magnetic fields. In the first two categories the magnetic properties do not persist if the external magnetic field is removed, while for ferromagnetic materials, which exhibit strong attraction to magnetic fields,

these properties are stable even after removal of the external field. If a sufficiently large magnetic field is applied, the spins within the material align with the field. The maximum value of magnetization achieved in this state is called the saturation magnetization,  $M_S$ . As the magnitude of the field decreases, spins cease to be aligned with the field and the total magnetization decreases. In FM materials, a residual magnetic moment remains at zero field. The value of the magnetization at zero field is called the remanent magnetization ( $M_R$ ). The magnitude of the field that must be applied in the negative direction to bring the magnetization of the sample back to zero is called the coercive field ( $H_C$ ).

It is known that the magnetic properties of nanostructures are quite different from corresponding bulk. The key difference between the magnetic behavior of a bulk magnetic material and a collection of single domain FM NP arises from the mechanism by which the magnetization is cycled through the hysteresis loop. In a bulk material, the magnetization increases in response to the field via domain wall nucleation and rotation as well as the rotation of the magnetization vector away from the easy axis of magnetization. In a single domain nanoparticle, domain wall movement is not possible and changes in magnetization of a material occur via activation over an energy barrier. These barriers arise from magnetocrystalline, magnetoelastic and/or shape anisotropy, all of which are energy densities and depends on grain volume ( $V$ ). The critical diameter for a magnetic particle to reach the single domain limit is equal to:

$$R_{sd} = \frac{36\sqrt{AK}}{\mu_0 M_S^2}$$

where  $A$  is the exchange constant,  $K$  is the effective anisotropy constant and  $M_S$  is the saturation magnetization. For most magnetic materials, this diameter is in the range 10–100 nm, though for some high-anisotropy materials the single domain limit can be several hundred nanometers [49].

If the number of atoms per particles is decreasing, the interaction energy (exchange energy) could reach values as low as the thermal energy  $k_B T$  at room temperature. This leads to a spontaneous random orientation of the magnetic spin inside the particles, or in other words, the remanence magnetisation as well as the coercivity will be zero. This means that the system reached the thermodynamic equilibrium and no hysteresis is present (on the contrary, ferromagnetism is a metastable state): this corresponds to the SPM state. Ferromagnetic and superparamagnetic behavior are compared in Figure 3.19: SPM describes the state of a single-domain-sized grain when thermal energy is sufficient to overcome barriers to a reversal of magnetization. When the energy barriers are large with respect to thermal energy, the magnetization is “blocked” and the probability of spontaneous reversal becomes negligible. When the barriers are relatively low, thermal excitations can result in reversal of the magnetization over very short time scales, and the grain is in a superparamagnetic state.



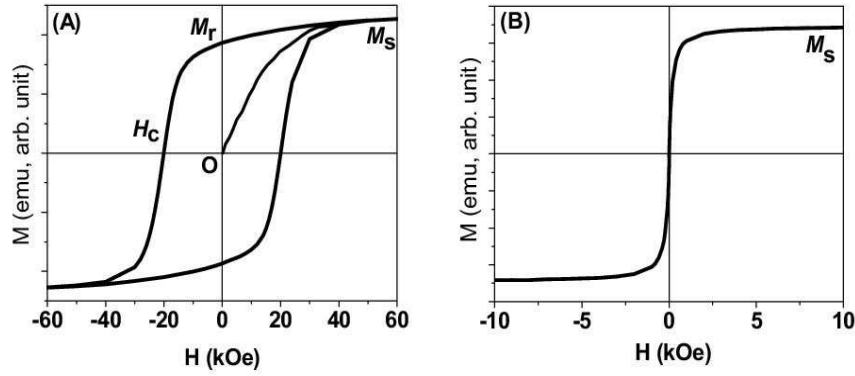


**Figure 3.19** Magnetization as function of the external applied field for (A) ferromagnetic material, (B) superparamagnetic material

SPM can be understood by considering the behavior of a well-isolated single-domain particle. The magnetic anisotropy energy per particle which is responsible for holding the magnetic moments along a certain direction can be expressed as follows:

$$E(\theta) = K'V \sin \theta$$

where  $V$  is the particle volume,  $K'$  anisotropy constant and  $\theta$  is the angle between the magnetization and the easy axis. The energy barrier  $K'V$  separates the two energetically equivalent easy directions of magnetization. With decreasing particle size, the thermal energy,  $k_B T$ , exceeds the energy barrier  $K'V$  and the magnetization is easily flipped. For  $k_B T > K'V$  the system behaves like a paramagnet, instead of atomic magnetic moments, there is now a giant (super) moment inside each particle. This system is named superparamagnetic. Such a system has no hysteresis and the data of different temperatures superimpose onto a universal curve of  $M$  versus  $H$ . The relaxation time of the moment of a particle,  $\tau$ , is given by the Néel-Brown expression [50] where  $k_B$  is the Boltzmann constant, and  $\tau_0 \sim 10^{-9}$  s.

$$\tau = \tau_0 \exp\left(\frac{K'V}{k_B T}\right)$$

If the particle magnetic moment reverses at times shorter than the experimental time scales, the system is in a SPM state, if not, it is in the so-called blocked state (ferromagnetic behavior).

The temperature, which separates these two regimes, the so-called blocking temperature,  $T_B$ , can be calculated by considering the time window of the measurement.

The blocking temperature depends on the effective anisotropy constant, the size of the particles, the applied magnetic field, and the experimental measuring time. For example, if the blocking temperature is determined using a technique with a shorter time window, such as ferromagnetic resonance which has a  $\tau \sim 10^{-9}$  s, a larger value of  $T_B$  is obtained than the value obtained from dc magnetization measurements. Moreover, a factor of two in particle diameter can change the reversal time from 100 years to 100 nanoseconds. While in the first case the magnetism of the particles is stable, in the latter case the assembly of the particles has no remanence and is SPM.

SPM behavior could be observed at sizes  $< 20$  nm for iron oxide  $\gamma\text{-Fe}_2\text{O}_3$ ; (magnetically soft material, relatively small anisotropy  $\sim 10^3$  J/m<sup>3</sup>) or at 3 nm for FePt alloy (magnetically hard material, huge anisotropy  $\sim 10^6$  J/m<sup>3</sup>).

### 3.2.3a AGFM

Iron oxide magnetic nanoparticles were characterized by using two different techniques depending on the mass of the magnetic material, hence, in first assumption, the total magnetic momentum to be measured. AGFM (alternate gradient field magnetometry) is a high sensitivity technique for the measurement of magnetic moments as a function of an applied magnetic field. The technique is based on the application of an alternated field-gradient, in order to produce a periodic force onto a sample set in a uniform field [51].

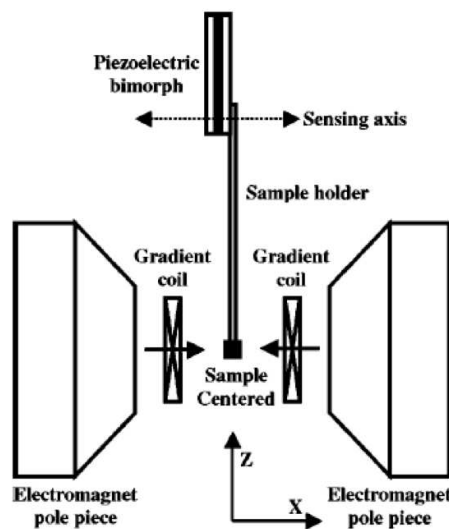


**Figure 3.20** Schematic view of a AGF magnetometer.

The sample is mounted on a quartz probe that transmits the deflection due to the field-gradient to a piezoelectric sensor. The sensor produces a voltage proportional to the force, and hence to the magnetic moment of the sample (Figure 3.20). The piezoelectric signal is processed by a lock-in system, thus eliminating most of the noise. Moreover, the measurements are performed at the mechanical resonance of the probe ( $10^2 - 10^3$  Hz) with a consequent amplification of the signal. The high sensitivity ( $10^{-8}$  emu) makes this technique ideal for the characterization of small quantity of magnetite nanoparticles (in the order of micrograms). The magnetometer employed during this thesis (Micromag 2900) works at room temperature with a maximum magnetic field of 20 kOe.

### 3.2.3b VSM

On the other hand, VSM is one of the most utilized techniques to measure basic magnetic properties as a function of the applied magnetic field in a wide range of temperatures, with a sensitivity of about  $1 \cdot 10^{-3}$  emu (or equivalently  $10^{-7}$  A m<sup>2</sup>).

The sample is placed in a constant magnetic field created by an electromagnet and moved up and down at a frequency of 75 Hz perpendicularly to the magnetic field direction. As the sample is moved, the magnetization changes as a function of time producing an induced *e.m.f.* in a set of pick-up coils according to Faraday's Law of induction, preamplified by lock-in integrated in the VSM detection module. When the sample moves in a direction, the magnetic flux increases in one of the coils while decreases for the other overriding the variations due to the homogeneous field. Therefore, only the changes due to the magnetization from the sample are registered.

VSM technique firstly developed by Simon Foner in the late 50s [52], and nowadays is a low cost alternative to other magnetometry techniques, as the magnetic field is provided by a water-cooled electromagnet, avoiding the use of liquid He or N<sub>2</sub>, which is required in SQUID magnetometry. The VSM equipment used in this thesis is a custom-built setup, located at the IMEM institute in Parma, the maximum applied magnetic field is 1.8 T, although it can be increased up to 2 T by decreasing the distance between the electromagnet pole pieces. Both AGFM and VSM measurement were performed, at IMEM, by our colleagues Dr. Francesca Casoli and Dr. Valentina Chiesi.

## 3.2.4 Functional Characterization

### 3.2.4a Gas sensing

ZnO nanostructures have been widely used for sensing applications because of their high sensitivity to the chemical environment. Nanostructures have the advantage of a high surface area, and electronic processes are strongly influenced by surface processes. The sensing process is governed by oxygen vacancies on the surface that influence the electronic properties of ZnO.

At the working temperature (~400 °C) oxygen species in the air are adsorbed on the nanostructures surfaces and ionized to O<sup>-</sup><sub>ads</sub> and O<sup>2-</sup><sub>ads</sub> by capturing free electrons of the particles. This leads to the formation of a thick space-charge layer which increases the potential barrier (Figure 3.21A). As a consequence, the resistance of the sensor is high. On the other hand, when a reducing gas or volatile organic compound is allowed to enter the sensor, it reacts with the adsorbed oxygen to form CO<sub>2</sub> and H<sub>2</sub>O with the release of electrons.

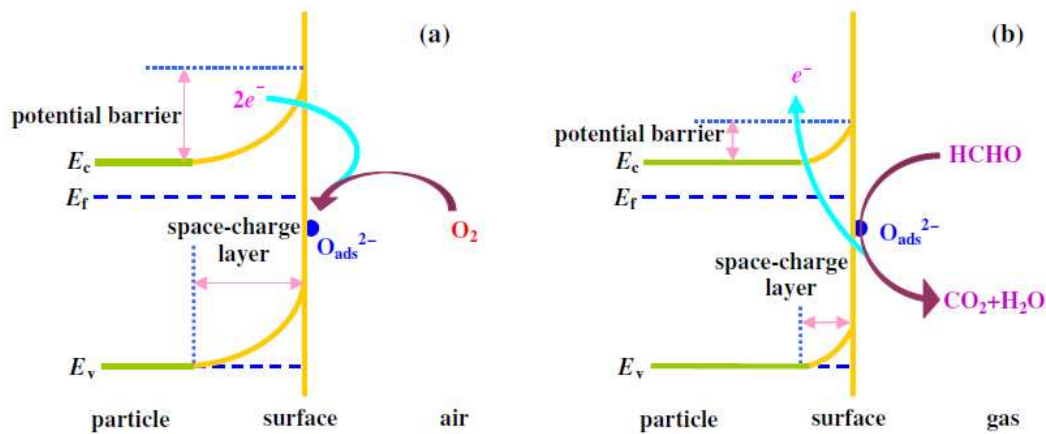
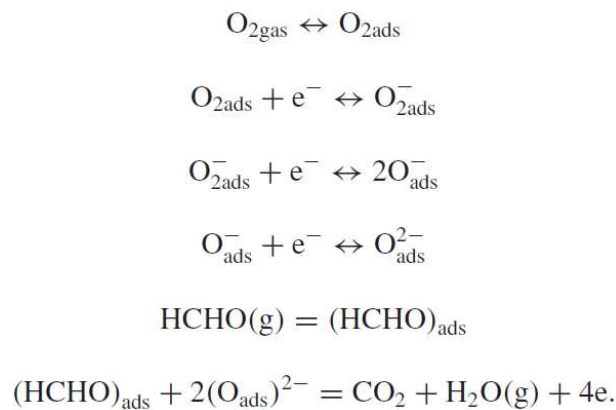


**Figure 3.21** Schematic drawing of the working principle of a chemoresistive gas sensor. (A) Adsorption of oxygen on semiconductor surface and depletion of the nanostructure. (B) Oxidation of a reducing gas (formaldehyde) and release of one electron to the semiconductor CB [53].

This process results in the thinning of the space-charge layer, thus decreasing the potential barrier and increasing the current. In this case, the resistance of the sensor is low. On the contrary, oxidizing gases captures further electrons from the semiconductor CB resulting in a resistance increase. In Figure 3.21B a schematic sketch for the oxidation of formaldehyde is represented. According to Wolkenstein's model [54] the sensing mechanism for formaldehyde can be expressed as follows:



In Figure 3.22 a schematic draw of the gas sensor is provided. Gold contacts and platinum heater are evaporated on alumina substrate, then ZnO TP are deposit on the substrate by means of a mechanical mask to form a stripe across the gold contacts. Finally the alumina is wire-bonded into a TO-8 package taking care to let the substrate float to avoid thermal dissipation through the TO-8.

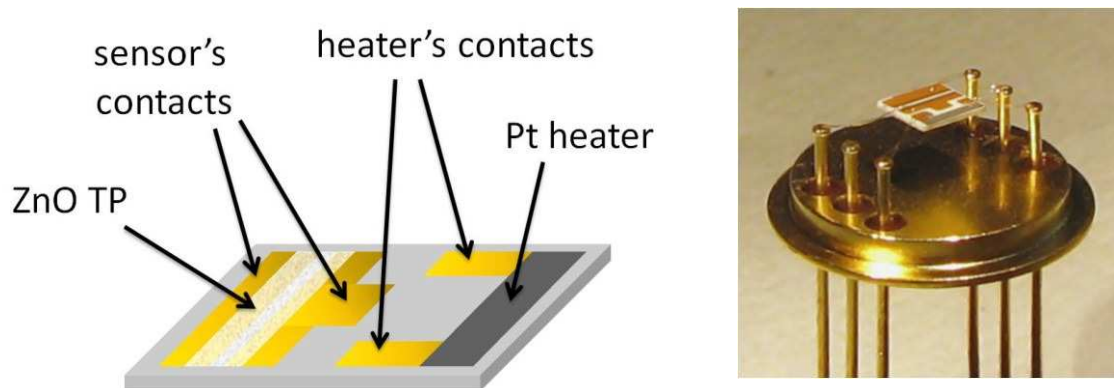


**Figure 3.22** Simplified sketch of the gas sensor device (left), the actual device bonded into a TO-8 (right).

To correctly measure the conductance variation due to electrons release/injection into the semiconductor CB, it is necessary to fix all the environmental conditions which may affect the material conductance, *i.e.* temperature, relative humidity (RH) and gases flows. Therefore, the test system must be provided with an appropriate apparatus to create the different gas mixtures, with known and reproducible concentration of gases, RH values and flow (Figure 3.23). Moreover, instruments to measure the sensor electrical properties are required (*i.e.* a current meter with at least 5 digit accuracy). Finally, a power supply is needed to heat the sensor up to the desired temperature.

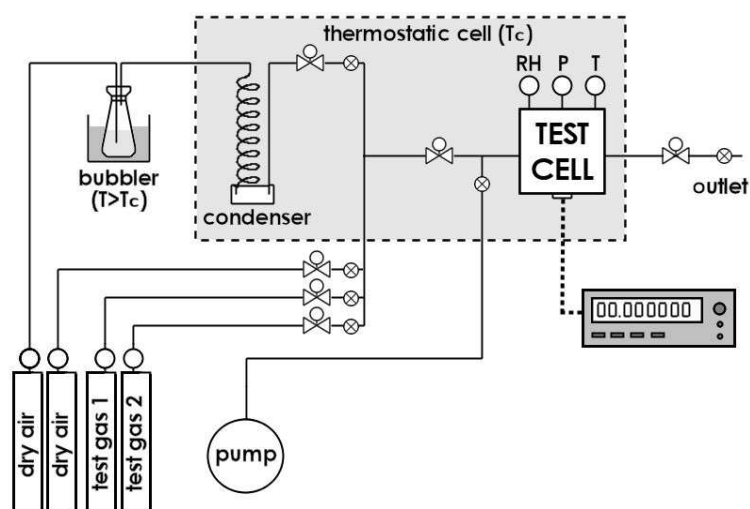


**Figure 3.23** Schematic representation of the gas sensing measuring equipment.

When the gas is introduced in the test cell ( $t_0$ ), the conductance ( $G_{air}$ ) of the sensor may change. This variation takes place in a time that is mainly dependent on the reaction mechanism at the sensor surface. At last, the equilibrium value ( $G_{gas}$ ) is asymptotically reached. If the interaction with the surface is a reversible reaction, when the gas introduction is stopped ( $t_2$ ), the conductance decreases to the initial value ( $G_{air}$ ). The times requested to change from  $G_{air}$  to  $G_{gas}$  (when the gas is introduced) and from  $G_{gas}$  to  $G_{air}$  (when it is removed from the test cell), are typical of the peculiar

sensor-gas interaction. Due to the asymptotic behaviour, it is a well adopted convention to report the time corresponding to 63% of  $\Delta G$  ( $t_1 - t_0$  and  $t_3 - t_2$  in Figure 3.24).

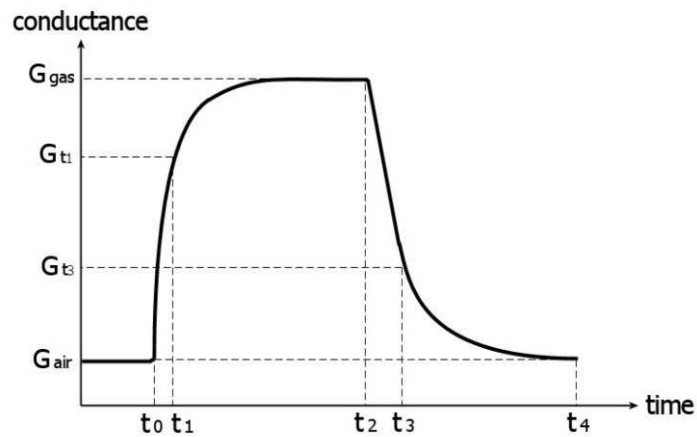


**Figure 3.24** A generic conductance vs. time curve of a gas sensor. The gas is introduced in the test cell at  $t_0$  and removed at  $t_2$ .

The gas response  $R$  to a specific gas concentration is generally defined as:

$$R = \frac{G_{gas} - G_{air}}{G_{air}} = \frac{\Delta G}{G_{air}}$$

By varying the gas concentration, it is possible to define the conductance ( $G$ ) vs. concentration ( $C$ ) curve and define the sensor sensitivity  $S_C$  to that gas (as shown in Figure 3.25).

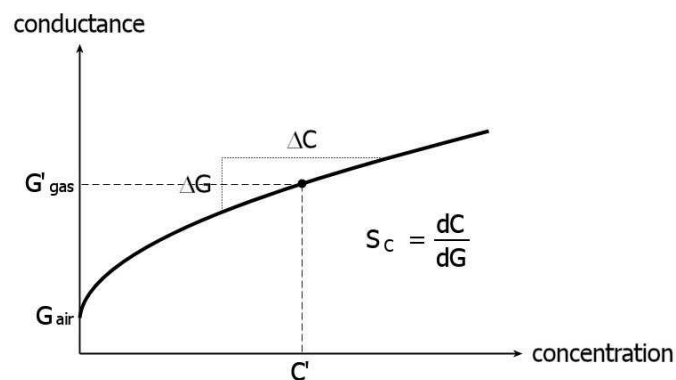


**Figure 3.25** Definition of “sensitivity” ( $S$ ) of a sensor to a concentration  $C$  of a gas.

The response and the sensitivity, are temperature-dependent. So, repeating the electrical characterization at different temperatures, it is possible to define the maximum response (or sensitivity) temperature, *i.e.* the temperature at which the response (or the sensitivity) to a specific gas is maximum. At the same time it could be possible to locate temperature ranges in which the selectivity to a gas of interest is maximized. This is possible when, in that temperature range, the

response to the “interfering” gas is negligible. In this way it could be possible to partially overcome the problem of the low selectivity that generally affects this kind of sensors.

### 3.2.4b Photocatalytic activity

The term photocatalysis in general, refers to any chemical process in which the external energy source is derived from radiation in the ultraviolet - visible range [55]. The basic mechanisms of heterogeneous photocatalysis have been investigated by many researchers [56-60] and can be represented schematically by the band gap model (Figure 3.26). When energy greater than  $E_g$  is applied to the semiconductor surface, valence band electrons are promoted to the conduction band, creating electron – hole pairs (1). Migration of the pairs to the semiconductor surface (2) allows the occurrence of redox reactions with adsorbates with suitable redox potentials (3). Thermodynamically, oxidation will occur if the redox potential of the valence band is more positive than that of the adsorbates.

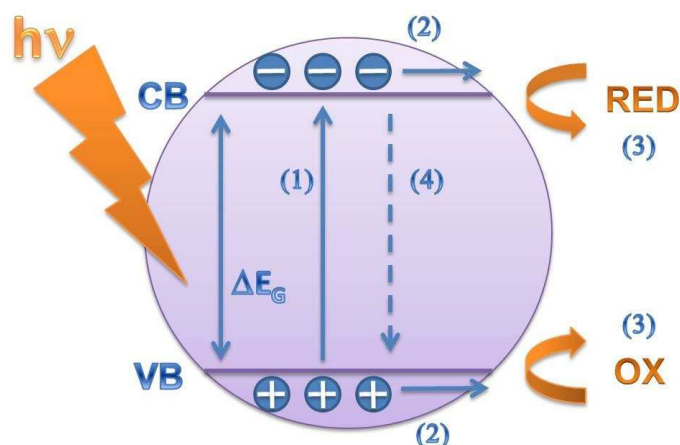


**Figure 3.26** Schematic view of the photocatalytic process.

Similarly, conduction band electrons can reduce adsorbed species if their redox potential is more negative than that of the adsorbates. Clearly, the most likely outcome of the formation of electron-hole pairs is their simple recombination, with subsequent release of thermal energy and/or light (4). Electron-hole recombination typically takes place within a few nanoseconds, while the redox processes may require microseconds (even ms) and this reduces photocatalytic activity considerably. Therefore, efficient carrier *separation* is a vital parameter when determining activity [61]. Before any reaction or recombination step can take place the charge carriers must be trapped a/o separated. Defects play an important role in this process. Defects can be either intrinsic, (i.e. oxygen vacancies in nanostructured reducible oxides), or extrinsic, such as dopants or impurities.

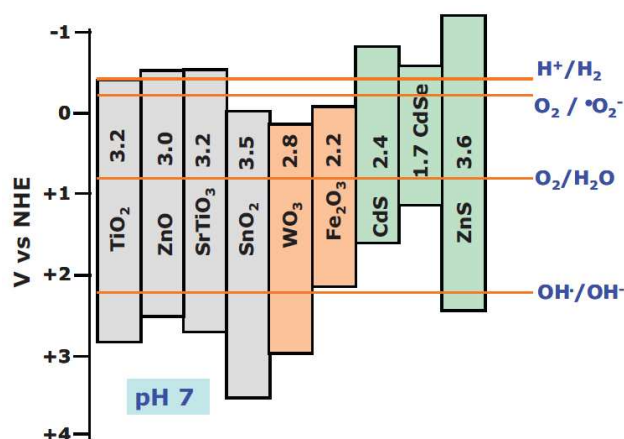
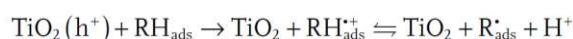
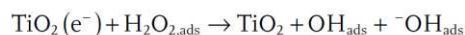
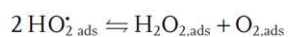
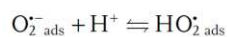


**Figure 3.27** Band alignment of common semiconductors and standard redox potentials at pH=7 (versus normal hydrogen electrode) [62].

As shown in Figure 3.27, the valence band redox potential of TiO<sub>2</sub> (and ZnO) is more positive than that of the OH•/OH<sup>-</sup> redox couple, resulting in the oxidation of adsorbed water and hydroxyl groups to highly reactive hydroxyl radicals on both irradiated forms of the oxide. This reaction is the basis behind the immense research effort into TiO<sub>2</sub> (and secondly ZnO) for the oxidation of organic contaminants in aqueous waste streams [56,57, 63–65]. Two oxidation reactions can take place at the TiO<sub>2</sub> (ZnO) valence band. Firstly, adsorbed organic material (RH) can be directly oxidized by semiconductor holes (h<sup>+</sup>) producing cationic radicals RH<sup>+</sup>. Secondly, the oxidation of water and/or hydroxyl groups can give rise to the formation of highly reactive hydroxyl radicals, OH• that can subsequently initiate further compound oxidation [63].



The main reaction occurring at the TiO<sub>2</sub> (ZnO) conduction band is the reduction of adsorbed molecular oxygen, resulting in the formation of superoxide radicals O<sub>2</sub><sup>•-</sup>. Such superoxide radicals, can give rise to the formation of additional OH• radicals through the following reactions:





Although both ZnO and TiO<sub>2</sub> are excellent photocatalysts upon UV illumination, they are wide band gap semiconductors (3.2 eV) thus only 5% of the solar energy can be harvested. For this reason, considerable research effort has been invested into increasing their photocatalytic activity, particularly by enhancing its ability to be activated by visible light. To improve photocatalytic activities, composite semiconductor photocatalyst systems have received a great deal of attention because of two important reasons. First, in the composite semiconductor systems with different energy levels, wide band-gap semiconductors can harvest visible light by coupling narrow band-gap semiconductor photosensitizers [70,71]. Second, charge injection from one semiconductor into another can lead to efficient and longer charge separation by reducing the electron-hole pair recombinations [72,73]. Various types of ZnO micro / nanomaterials have been studied for photocatalyst applications [74]. However, there are difficulties in collecting and recycling powder-type photocatalysts after use. Recently, 1-D ZnO nanostructure arrays, such as nanowires [75,76] and nanobelts [77] have been tested as immobilized photocatalysts due to their expected high photocatalytic activity resulting from large surface-to-volume ratio, and recyclable characteristics [78]. Considerable research effort has been invested in the combination of photocatalysts with organic and inorganic dyes too, such as erythrosin B [79] and *cis*-di(thiocyanato-*N,N*-bis(2,2'-bipyridyl-dicarboxylate)Ru(II) [80]. A huge number of potential dye / sensitizers have been reported in the literature, but the ones with optimum performance appear to be transition metal complexes derived from polypyridines ( Ru(II) ), porphyrins, or phthalocyanines ( Zn(II), Mg(II) or Al(III) ) as ligands [81,82]. The principle behind these systems is that the dyes absorb the visible radiation and form excited states. From these states, electrons are injected into the conduction band of the semiconductor oxide, thereby inducing a visible response in the oxide. For effective function, the adsorbed dye needs to have an excited state located above the bottom of the semiconductor band [16] and to have a strong interaction with the oxide such that a fast and efficient electron junction is produced. Assuming these considerations are met, the results of such sensitization are (1) an increased efficiency of the excitation process, and (2) an expansion of the absorption spectrum of the semiconductor via excitation through the sensitizer. However, such dyes are complex molecules and are not a low cost option. This, together with the fact that their thermal and/or photochemical stability is poor, can lead to poor lifetimes for photocatalysts prepared in this way [83]. However, if oxygen is excluded from the system and the oxidation state of the dye is quenched with an appropriate electrolyte, such a strategy has been demonstrated to be successful [84] but probably not suitable for real life applications where photocatalytic systems often operate in free air or water based environment [63]. Although there are many procedures reported for the measurement of heterogeneous photocatalytic activity in liquid [56,85], the conceptual basic setup is common and very simple. Two samples are typically prepared. A first one, in which the photocatalyst is dispersed in the liquid phase containing the organic pollutant whose degradation has to be measured; and a second sample (a reference) without the catalyst. The

samples are kept at a constant temperature while illuminated with an appropriate light source (monochromatic UV radiation, halogen lamp or solar simulator are the most used) in order to photo-generate carriers in the photocatalyst and promote redox reactions at the surface to form the active species (typically superoxide and hydroxyl radicals) that degrade the organic molecule. The illumination is stopped after a fixed time, the photocatalyst is then removed from the liquid phase (by means of sedimentation, centrifugation, filtration) and an aliquot of liquid is collected. A UV-VIS absorbance measurement is acquired and the comparison between the sample and reference gives informations about the photocatalytic activity. Typically a dye is used as pollutant for laboratory tests, for example methylene blue (MB). The degradation rate ( $D$ ) of MB in isopropyl alcohol (IPA) is related to the intensity of MB main peak (665 nm) and is expressed as:

$$D = \frac{A_0 - A_t}{A_0}$$

Where  $A_0$  is the absorbance maximum of the reference and  $A_t$  is referred to the sample. In Figure 3.28 is shown a typical absorbance spectrum of a solution of  $10^{-5}$  M MB in isopropyl alcohol (blue line) used as a reference and a sample using ZnO TP as catalyst illuminated for 1 hour at 325 nm. In this case, the degradation rate is  $D \approx 0,6$ , about the 60%.

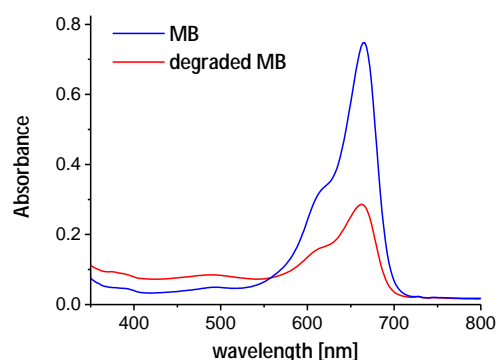


**Figure 3.28** Absorbance spectra of reference MB (blue line) and photo-degraded MB (red).

Photocatalytic activity of ZnO is attributed both to the donor states caused by the large number of defect sites such as oxygen vacancies and interstitial zinc atom and to the acceptor states which arise from zinc vacancies and interstitial oxygen atoms [86]. A reasonable assumption is that interfacial electron transfer takes place predominantly between these donor states ( $V_O$  and  $Zn_i$ ) and MB, instead of radiative charge recombination which causes green emission in ZnO. Being a cationic dye, MB, acquires electron from excited donor states and decomposes.

## References

- [1] M. Zha, D. Calestani, A. Zappettini, R. Mosca, M. Mazzer, L. Lazzarini and L. Zanotti, *Nanotechnology*, 2008, **19**, 325603
- [2] D. Calestani et al. *Sensors and Actuators B*, 2010, **144**, 472
- [3] D. Calestani, M. Z. Zha, L. Zanotti, M. Villani and A. Zappettini, *CrystEngComm*, 2011, **13**, 1707
- [4] P. Milani, S. Iannotta, *Cluster Beam Synthesis of Nanostructured Materials*, 1999, Springer-Verlag, Berlin
- [5] S. Iannotta and T. Toccoli, *Journal of Polymer Science: Part B: Polymer Physics*, 2003, **41**, 2501
- [6] K. Walzer, T. Toccoli, A. Pallaoro, S. Iannotta, C. Wagner, T. Fritz, K. Leo, *Surface Science*, 2006, **600** (10), 2064
- [7] N. Coppedè, M. Castriota, E. Cazzanelli, S. Forti, G. Tarabella, T. Toccoli, K. Walzer and S. Iannotta, *J. Phys. Chem. C*, 2010, **114**, 7038
- [8] C. Klingshirn, *phys. stat. sol. (b)*, 2007, **244** (9), 3027
- [9] J. I. Pankove, *Optical Processes in Semiconductors*, 1971, Ch.3, Dover Publications, New York
- [10] G. A. Khan and C.A. Hogarth, *Journal of Materials Science*, 1991 **26** , 412
- [11] J. Tauc, in *Optical Properties of Solids*, 1972, North – Holland Publisher, Amsterdam, p. 277
- [12] A. L. Efros, *Fizika i Tekhnika Poluprovodnikov* , 1982, **16**, 1209 (*Sov. Phys. Semicond.* 1982, **16**, 772)
- [13] L. E. Brus, *J. Chem. Phys.* 1984, **80**, 4403
- [14] A. I. Ekimov, A.L. Efros, M.G. Ivanov, A.A. Onushchenko, S.K. Shumilov, *Solid State Commun.*, 1985, **56**, 921
- [15] M. G. Bawendi, W.L. Wilson, L. Rothberg, P.J. Carroll, T.M. Jedju, M.L. Steigerwald, L.E. Brus, *Phys. Rev. Lett.*, 1990, **65**, 1623
- [16] J. Z. Zhang, *J. Phys. Chem. B*, 2000, **104**, 7239
- [17] M. Gratzel, *Heterogeneous Photochemical Electron Transfer*; CRC Press, Boca Raton, 1989
- [18] V. L. Colvin, A.N. Goldstein, A.P. Alivisatos, *J. Am. Chem. Soc.*, 1992, **114**, 5221
- [19] D. Duonghong, J.J. Ramsden, M.J. Gratzel, *J. Am. Chem. Soc.*, 1982, **104**, 2977
- [20] J. Z. Zhang, R.H. O’Neil, T.W. Roberti, *J. Phys. Chem.*, 1994, **98**, 3859
- [21] T. Nakanishi, B. Ohtani, and K. Uosaki, *J. Phys. Chem. B*, 1998, **102** (9), 1571
- [22] C. Klingshirn, *Semiconductor Optics*, 2007, Springer, Heidelberg, Berlin
- [23] R. Helbig, *Freie und gebundene Exzitonen in ZnO*, 1975, Habilitation Thesis, Erlangen
- [24] K. Hümmer, *Exzitonische Polaritonen in einachsigen Kristallen*, 1978, Habilitation Thesis, Erlangen
- [25] T. Skettrup, *phys. stat. sol. (b)*, 1982, **109**, 663
- [26] K. Hümmer, *phys. stat. sol. (b)*, 1973, **56**, 249
- [27] J. Lagois and K. Hümmer, *phys. stat. sol. (b)*, 1975, **72**, 393
- [28] K. Hümmer and P. Gebhardt, *phys. stat. sol. (b)*, 1978, **85**, 271
- [29] K. Hümmer, R. Helbig, and M. Baumgärtner, *phys. stat. sol. (b)*, 1978, **86**, 527

- [30] R. Kuhnert, R. Helbig, and K. Hümmer, *phys. stat. sol. (b)*, 1981, **107** 83
- [31] J. Lagois, *Phys. Rev. B*, 1981, **23**, 5511
- [32] D. C. Reynolds and T. C. Collins, *Phys. Rev.* 1969, **185**, 1099
- [33] E. Tomzig and R. Helbig, *J. Lumin.* 1976, **14**, 403
- [34] G. Blattner, C. Klingshirn, R. Helbig and R. Meinl, *phys. stat. sol. (b)*, 1981, **107**, 105
- [35] R. Thonke and K. Sauer, in: *Optics of Semiconductors and Their Nanostructures*, Springer Series in Solid State Sciences, Vol. 146, edited by H. Kalt and M. Hetterich (Springer, Berlin, 2004), p. 73
- [36] B. K. Meyer et al., *phys. stat. sol. (b)*, 2004, **241**, 231
- [37] S. K. Kim, S.Y. Jeong, C. R. Cho, *Appl. Phys. Lett.*, 2003, **82**, 562
- [38] M. C. Newton, P.A. Warburton, *Mater. Today*, 2007, **10**, 50
- [39] L. Lazzarini, G. Salviati, F. Fabbri, M. Zha, D. Calestani, A. Zappettini, T. Sekiguchi and B. Dierre, *ACS Nano*, 2009, **3** (10), 3158
- [40] N. E. Hsu, W. K. Hung, and Y. F. Chen, *J. Appl. Phys.*, 2004, **96**, 4671
- [41] I. Shalish, H. Temkin, and V. Narayanamurti, *Phys. Rev. B*, 2004, **69**, 245401
- [42] D. Li, Y. H. Leung, A. B. Djuriscic, Z. T. Liu, M. H. Xie, S. L. Shi, S. J. Xu, and W. K. Chan, *Appl. Phys. Lett.*, 2004, **85**, 1601
- [43] A. B. Djuriscic, Y. H. Leung, W. C. H. Choy, K. W. Cheah, and W. K. Chan, *Appl. Phys. Lett.* 2004, **84**, 2635
- [44] J. V. Foreman, *Photoexcited Emission Efficiencies of Zinc Oxide*, PhD Thesis, 2009, Department of Physics Duke University
- [45] B. D. Cullity, *Elements of X-ray Diffraction*, 1978, 2nd Edition
- [46] J. Fang, K. L. Stokes, W. Zhou, J. A. Wiemann, J. Dai, and C. J. O'Connor, *Colloidal Bismuth Nanoparticles*, 2000, ISCANI, World Scientific Publishing, p. 91–96
- [47] H. P. Klug and L. E. Alexander, *X-ray Diffraction Procedures for Polycrystalline and Amorphous Materials*, Wiley, New York (1954)
- [48] V. Ciupinã, S. Zamfirescu and G. Prodan, *NATO Security through Science Series*, 2007, 231-237
- [49] R. Skomski and J. M. D. Coey, *Permanent Magnetism*, Institute of Physics Publishing, Bristol and Philadelphia, 199
- [50] C. M. Sorensen, *Magnetism in Nanoscale Materials in Chemistry*, (Ed.: K. J. Klabunde), Wiley-Interscience Publication, New York, 2001
- [51] P. J. Flanders, *J. Appl. Phys.*, 1988, **63**, 3940
- [52] S. Foner, *Rev. Sci. Instrum.*, 1959 **30**, 548
- [53] T. Chen, Q. J. Liu, Z. L. Zhou and Y. D. Wang, *Nanotechnology*, 2008, **19**, 095506
- [54] T. Wolkenstein, *Electronic Processes on Semiconductor Surfaces during Chemisorption*, 1991, New York Consultants Bureau, pp 35
- [55] G. Colon-Ibanez, C. Belder-Coldeira and M. Fernandez-Garcia, *Synthesis, Properties and Applications of Oxide Nanomaterials*, 2007 John Wiley & Sons, Inc., Hoboken, NJ, p. 491
- [56] M. R. Hoffmann, S. T. Martin, W. Choi and D. W. Bahnemann, *Chem. Rev.*, 1995, **95**, 69

- [57] D. S. Bhatkhande, V. G. Pangarkar and C. M. Breenackers, *Journal of Chemical Technology and Biotechnology*, 2001, **77**, 102
- [58] M. A. Fox and M. T. Dulay, *Chem. Rev.*, 1993, **93**, 341
- [59] J. Zhao and X. Yang, *Building and Environment*, 2003, **38**, 645
- [60] J. Peral and D. F. Ollis, *J. Mol. Catal. A: Chem.*, 1997, **115**, 347
- [61] L. Cao, A. Huang, F. Spiess and S. L. Suib, *Journal of Catalysis*, 1999, **188**, 48
- [62] P. Lianos, *Journal of Hazardous Materials*, 2011, **185**, 575–590
- [63] R. P. K. Wells, Oxide Materials in Photocatalytic Processes, in *Metal Oxide Catalysis*, J. S. David, H. Justin, 2008, Wiley-VCH, Weinheim, pp. 776
- [64] J. C. D'Oliveira, G. Al Sayyed, P. Pcihat, *Environ. Sci. Technol.*, 1990, **24**, 990,
- [65] M. Janus and A. W. Morawski, *Appl. Cat. B – Environmental*, 2007, **75**, 118
- [66] A. Sclafini and J. M. Herrmann, *J. Phys. Chem.*, 1996, **100**, 13655
- [67] O. Carp, C.L. Huisman and A. Rellr, *Progress in Solid State Chemistry*, 2004, **32**, 33
- [68] M. A. Fox and M. T. Dulay, *Chem. Rev.*, 1993, **93**, 341
- [69] Y. Yamaguchi, M. Yamazaki, S. Yoshihara, T. Shirakashi, *Journal of Electroanalytical Chemistry*, 1998, **442**, 1
- [70] H. Fujii, M. Ohtaki, K. Eguchi and H. Arai, *J. Mol. Catal. A: Chem.*, 1998, **129**, 61
- [71] P. V. Kamat, *Chem. Rev.*, 1993, **93**, 267
- [72] K. R. Gopidas, M. Bohorquez and P. V. Kamat, *J. Phys. Chem.*, 1990, 94, 6435
- [73] J. E. Evans, K. W. Springer and J. Z. Zhang, *J. Phys. Chem.*, 1994, **101**, 6222
- [74] F. Lu, W. Cai and Y. Zhang, *Adv. Funct. Mater.*, 2008, **18**, 1
- [75] J. Yang, S. An, W. Park and G. Yi, *Adv. Mater.*, 2004, **16**, 1661
- [76] T. Kuo, C. Lin, C. Kuo and M. H. Huang, *Chem.Mater.*, 2007, **19**, 5143
- [77] T. Sun, J. Qiu and C. Liang, *J. Phys. Chem. C*, 2008, **112**, 715.
- [78] Y. Tak, H. Kim, D. Lee, K. Yong. *Chem. Commun.*, 2008, 4585
- [79] P. V. Kamat and M. A. Fox, *Chem. Phys. Lett.*, 1983, **102**, 379
- [80] B. O'Regan and M. Graetzel, *Nature*, 1991, **353**, 737
- [81] Y. M. Choi, W.U. Choi, C.H. Lee, T. Hyeon and H.I. Lee, *Env.Sci.Tec*, 2001, **35**, 966
- [82] S. Cheung, A. Fung and M. Lam, *Chemosphere*, 1998, **36**, 2461
- [83] M. Anpo, *Bulletin of the Chemical Society of Japans*, 2004, **77**, 1427
- [84] Z. Jin, X. Zhang, G. Lu and S. Li, *J. Mol. Catal. A: Chem.*, 2006, **259**, 275
- [85] C. H. Wu, *J. M. Chem, Ind. Eng. Chem. Res.*, 2006, **45**, 6450
- [86] F. Tuomisto, K. Saarinen, *Phys. Rev.*, 2005, **72**, 085206

# 4 Results: functionalized materials

---

## 4.1 Cadmium Sulphide

Hybrid nanostructures consisting of two or more different functional units display new and enriched properties for optical, catalytic, photovoltaic and even biomedical applications. It is well known that an interface in hybrid nanostructures facilitates transport of electrons across both sides [1] and entirely novel properties may arise because of the coupling between the different materials: typically the increase of photocatalytic activity and photo-generated carriers. In particular heterostructures of ZnO NR / NW and CdS have been widely investigated for photoenergy conversion applications, ranging from catalysis [2–4] to solar cell [5–9] and hydrogen production through photo-induced water splitting [10–14].

This chapter is dedicated to the study of CdS–ZnO coupled compound. The sensitization of ZnO TP with CdS has been carried out through a modified non-aqueous chemical bath deposition (CBD) process, which allows the control of CdS thickness and morphology, without the need of any surface passivating agents – thus providing a clean interface between CdS and ZnO – in order to obtain a type-II heterojunction to be used in the aforementioned applicative fields.

Although different approaches for the synthesis of CdS NP are reported in literature (refer to Ch. 2.2.2), none of them can be considered fully suitable for the functionalization of ZnO nanostructures. In fact, CBD depositions are mainly aqueous-based methods and require alkaline or acidic environment that invariably affects the ZnO surface: ZnO is a well-known amphoteric material, which dissolves in alkaline environment to produce water soluble zincate anions ( $\text{Zn(OH)}_4^{2-}$ ), while at low pH values,  $\text{Zn}^{2+}$  ions are present. These remarks exclude definitely traditional CBD techniques as a possible strategy to functionalize ZnO nanostructures without affecting their surface. High temperature syntheses (*e.g. hot-injection* method, refer to Ch. 2.2.2a) require the presence of surface passivating agents or ligands, to limit the extremely high surface reactivity of small NP. These molecules, typically consisting of a coordinating head group and a long alkyl chain, are very useful reactants in high temperature synthesis since adsorb to the surfaces of the growing NP providing a capping layer that stabilizes the NP in solution. In addition ligands also mediate NP growth creating a diffusion barrier, hence resulting in a diffusion-limited growth.

Despite of these advantages, it is preferable to avoid such complexing or capping agents that would likely be trapped at the boundary between CdS nanoparticles and ZnO degrading interface performance (*i.e.* charge separation and injection in a PV cell or photocatalytic system) [15–19].

#### 4.1.1 Synthesis of CdS nanoparticles

A new approach in the synthesis of CdS NP is desirable and different solvents were tested (Table 4.1.1), firstly towards the ability to effectively suspend semiconductor nanostructures (ZnO TP and CdS NP), then as a solvent themselves (*i.e.* dissolve CdS precursors). Solvents with high dielectric constant and high dipole moment resulted the best as dispersive media, among the tested bunch. This could be due to the affinity (electrostatic shield) with negative charged hydroxyl and oxygen groups located at the ZnO nanostructures' surface. In particular, *N,N*-Dimethylformamide (DMF) showed very good response as both, dispersive media and solvent. It effectively shields polar solutes and nanostructures (both CdS and ZnO), keeping them floating without visible aggregation / precipitation, so that ligands or surfactants are not needed.

##### Polar aprotic solvents

Name	Formula	$\epsilon$	Boiling Point [°C]	Viscosity [cP] @ 20°C	Dipole moment [D]
Dimethyl sulfoxide	$\text{CH}_3\text{-S(=O)-CH}_3$	47	189	2.00	3.96
Dimethylformamide	$\text{H-C(=O)N(CH}_3)_2$	38	153	0.92	3.86
Acetonitrile	$\text{CH}_3\text{-C}\equiv\text{N}$	37	82	0.34	3.84
Methyl ethyl ketone	$\text{CH}_3\text{-C(=O)-CH}_2\text{-CH}_3$	19	79	0.43	2.76
Tetrahydrofuran	$\text{-CH}_2\text{-CH}_2\text{-O-CH}_2\text{-CH}_2\text{-}$	7.5	66	0.48	1.63
Acetone	$\text{CH}_3\text{-C(=O)-CH}_3$	21	56	0.32	2.91

##### Polar protic solvents

Name	Formula	$\epsilon$	Boiling Point [°C]	Viscosity [cP] @ 20°C	Dipole moment [D]
Water	$\text{H-O-H}$	80	100	0.001	1.85
Methanol	$\text{CH}_3\text{-OH}$	33	65	0.59	1.69
Ethanol	$\text{CH}_3\text{-CH}_2\text{-OH}$	30	78	1.200	1.69
Iso-propanol	$\text{CH}_3\text{-CH(OH)-CH}_3$	18	82	2.05	1.55
n-Butanol	$\text{CH}_3\text{-CH}_2\text{-CH}_2\text{-CH}_2\text{-OH}$	18	118	3	1.52

**Table 4.1.1** List of solvents tested against the dispersion of ZnO nanostructures.

In a typical reaction, 266 mg of cadmium acetate dehydrate (Sigma–Aldrich 98%, PM = 266.5) are added to a beaker containing 50 ml of DMF. The beaker is placed on the heating/stirring plate and the temperature is raised to 120 °C. Then 152 mg of thiourea (ACS grade > 99%, Sigma–Aldrich, PM = 76.1) dissolved in 10 ml of DMF are quickly added to the solution (final Cd<sup>2+</sup>/S<sup>2-</sup> molar ratio 1:2) which turns immediately pale yellow. Reaction was carried on for 5 minutes then cooled down spontaneously. The solid phase was separated by centrifugation at 5000 rpm for 15 minutes and washed with distilled water to remove unreacted precursors. The “hot injection” (130 °C is not that hot compared to the temperature reached with high boiling solvents in the so–called *hot–injection* method, see Ch. 2.2.2a) promotes a quick nucleation but since no complexing or passivating agents are used, settling time is crucial. The kinetic requirement is simple: the less is the settling time, the smaller the NP are. But this is true for a diffusion limited growth, where the kinetic limiting stage is the flow of nutrient phase to the growing embryos, this requirement is typical achieved using polymer as surfacting agents, or strong ligands, that slow down the growth kinetic. When just a solvent is used (DMF in this case), it is difficult to separate the nucleation stage and the growth process in time and obtain nearly monodisperse particles. When a small nucleus or embryo is close to a larger crystal, the ions formed by (partial) dissolution of the smaller, can be incorporated into the larger crystal. As the smaller crystal becomes even smaller, its dissolution will become ever more favorable and eventually it will disappear. The result is that the larger crystals grow at the expense of the smaller ones and no dimensional control is achieved. Finally, if the particles concentration is sufficiently high, then the probability of collisions between these particles becomes high. This can result in either aggregation or coalescence.

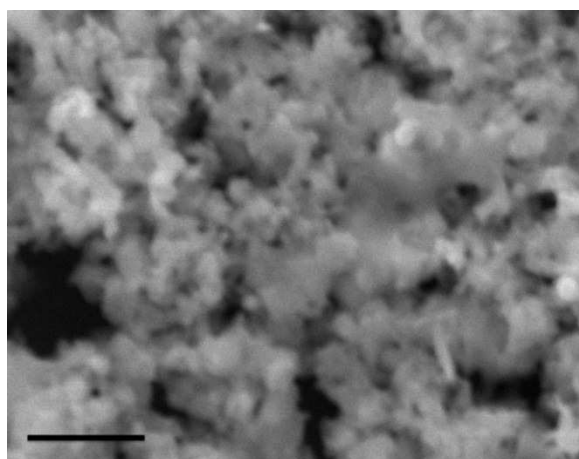


**Figure 4.1.1** SEM image of highly polydispersed CdS NP (sample CdS1). Scale bar is 1  $\mu\text{m}$ .

All of these considerations can explain the results of the sample CdS1 as shown in the SEM analysis reported in Figure 4.1.1. XRD diffractogram is depicted in Figure 4.1.2: the different peaks FWHM and peaks shape (lorentzian) suggest different grain sizes for CdS NP (dimensional



polydispersed NP). The observed crystalline phase is hexagonal wurtzite, according to ICDD database (JCPDS #80–0006).

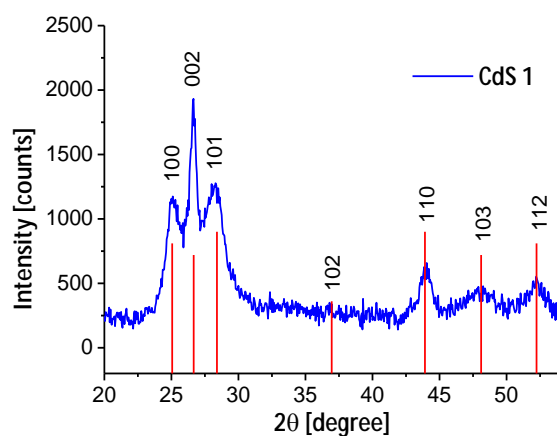


**Figure 4.1.2** XRD analysis on the sample CdS1. CdS NP crystallize in wurtzite phase (JCPDS #80–0006), peaks shape suggest a wide dimensional range of NP.

Different syntheses were performed in order to understand the chemical / physical parameters that influence the nucleation–growth process of CdS NP in DMF. Here’s a brief description:

1. Precursor concentration has to be high enough to promote a high number of critical nuclei but not too high in order to avoid coalescence and aggregation.
2. Temperature is *very* important when dealing with thiourea, CdS precipitation can take place in seconds or hours depending on the working temperature.
3. Lowering the solution temperature after injection of thiourea helps to slow and kinetically limits growth.
4. Adding a small amount of thiourea *after* the nucleation phase (*i.e.* when the solution turns yellow) helps to avoid Ostwald ripening (it *focuses* NP dimensions) [20].

Further syntheses were performed and finally, in Figure 4.1.3 A and B, rather monodispersed CdS nanoparticles (sample CdS2) are shown. The synthesis was carried out as follows: 132 mg of cadmium acetate were loaded into 50 ml DMF and thiourea was added when the system reached the working temperature (70 °C). 144 mg of thiourea were dissolved into 50 ml DMF but only 30 ml were quickly added at one time. The remaining 20 ml were slowly added during a couple of minutes after the typical yellow color appeared. Conversely to the previous synthesis, where the growth started at the same time that nucleation occurs, temperature lowering helps to separate the two events. In fact solution changed color slowly, the growth of CdS NP is likely limited by surface processes because of the temperature drop caused by thiourea addition. Reaction was stopped after 15 minutes and the solution cooled down spontaneously. Although NP looks quite

large (about 50 nm), there is no evidence that NP are single grains. On the contrary, their shape suggests they are likely regular aggregates of smaller NP and XRD analysis confirms the hypothesis (Figure 4.1.4). Scherrer analysis on the (100), (002) and (101) reflection shows a mean diameter of 10 nm. The improved dimensional control with respect to the sample CdS1 can be due to the rapid temperature drop caused by the addition of a big volume (30 ml to 50 ml) of cold thiourea solution. Thus, not only growth kinetic has been slowed down, but also thiourea dissociation is limited. Moreover, the following slow addition of thiourea helped to stabilize growing nuclei and to reduce dimensional polydispersity.

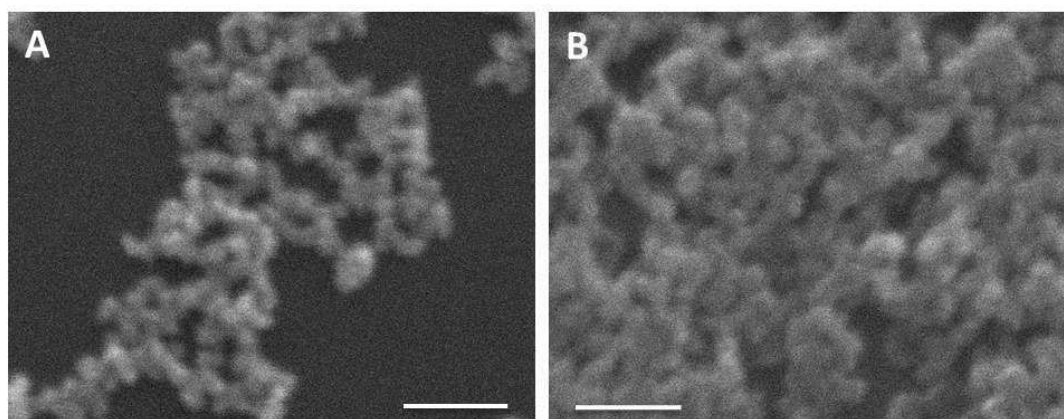


**Figure 4.1.3** CdS nanoparticles aggregates (sample CdS2). Scale bars are 500 nm.

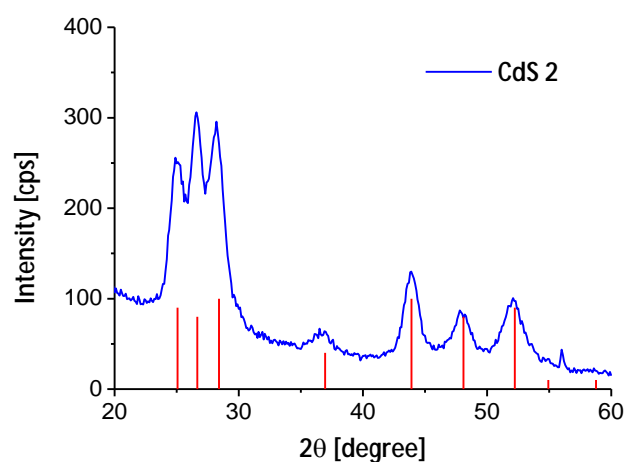


**Figure 4.1.4** XRD analysis on the sample CdS2. CdS NP present a wurtzite structure and peaks shape is almost gaussian reflecting a good dimensional control.

A third example about how to further reduce NP dimensions, is reported in Figure 4.1.5 (sample CdS3). This synthesis was performed at an intermediate temperature (90 °C) which was found to be a good compromise between a rather burst nucleation (dissociation rate of thiourea at 90 °C is significantly higher than that at 70 °C in DMF) and a delayed / slow growth. Moreover a rapid quench of the solution in a cold water bath was chosen to avoid further particles enlargement.

According to SEM images (Figure 4.1.5), aggregation is observed. It is likely that particles minimize their surface energy by forming bigger “particles” with rather spherical shape. XRD analysis confirms the hypothesis of aggregation: mean grains dimension, estimated by peaks FWHM, is significantly lower than tens of nanometers, as observed in SEM images.

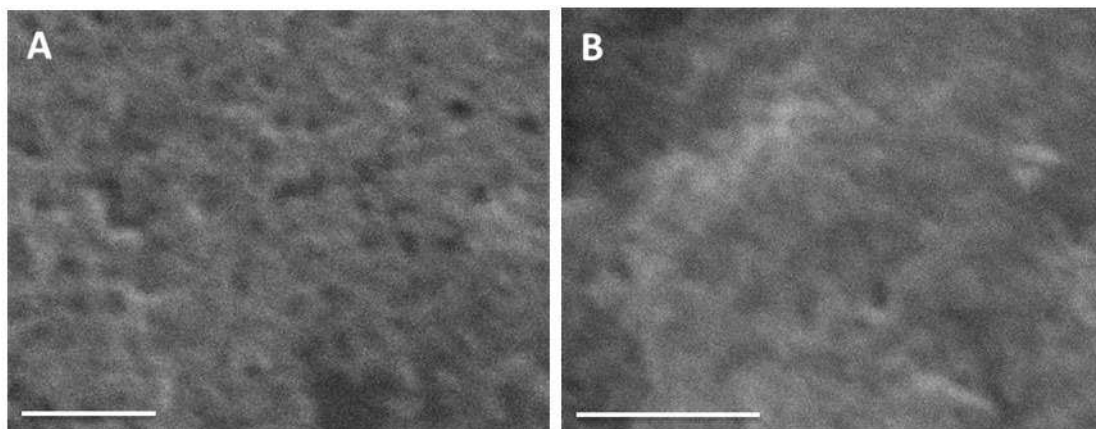


**Figure 4.1.5** Small grains CdS NP achieved through thiourea dissociation rate control and burst growth stop achieved by thermal quench (sample CdS3). Scale bars are 500 nm.

Considering the low angle reflections (between  $25^\circ$  and  $28^\circ$ ) a peaks convolution is evident due to particles dimension decrease and resulting increase in FWHM. Calculation based on Scherrer formula for (100), (002) and (101) peaks gives a mean diameter of 4.1 nm. The peaks broadening is noticeable in high order reflection too: (103) peak is masked under the more intense (110) and (112) reflections. Scherrer analysis on these peaks reported 3.7 nm which is consistent with the previous analysis based on high d-spacing reflections.

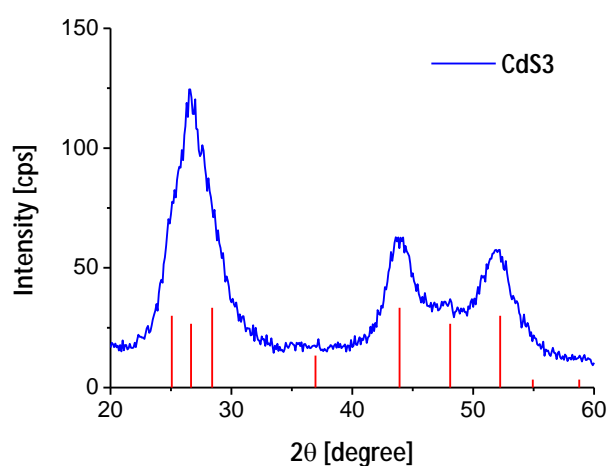


**Figure 4.1.6** XRD spectrum of small CdS NP (sample CdS3), mean grains dimension is about 4 nm.

TEM investigation was performed on this sample even though it was not easy to prepare the copper grid properly: in fact the free-standing NP tend to aggregate, particularly upon solvent

evaporation. The HREM image of a “thin” aggregate is reported in Figure 4.1.7A, crystal fringes are evident and NP mean diameter is in the order of 5 nm. The Fourier transform (FT) is also reported (B): the first evidence is the broad ring, centered at  $3.25 \pm 0.1 \text{ \AA}$ . The FWHM of this peak corresponds to a mean dimensions in the order of 1 nm but this value is inconsistent with both HREM observations and XRD mean dimensions calculated by the Scherrer formula. Moreover the spot at lower  $d$ -spacing ( $2.05 \text{ \AA}$ ) corresponding to the wurtzite (110) reflections has a different width. In fact CdS wurtzite (100), (002) and (101) peaks overlap and the observed ring is the convolution of the three distinct peaks with  $d$ -spacing respectively of  $3.57 \text{ \AA}$ ,  $3.34 \text{ \AA}$  and  $3.15 \text{ \AA}$ . This results in NP dimensions of 4 nm and is in agreement with both HREM observation and XRD–Scherrer mean dimension, indicating that each individual CdS NP is a single crystal. The (102) reflection has not been observed in both XRD and TEM analysis and this can be due to the low intensity and the relative high background (in the XRD spectrum) / noise (in the FT image).

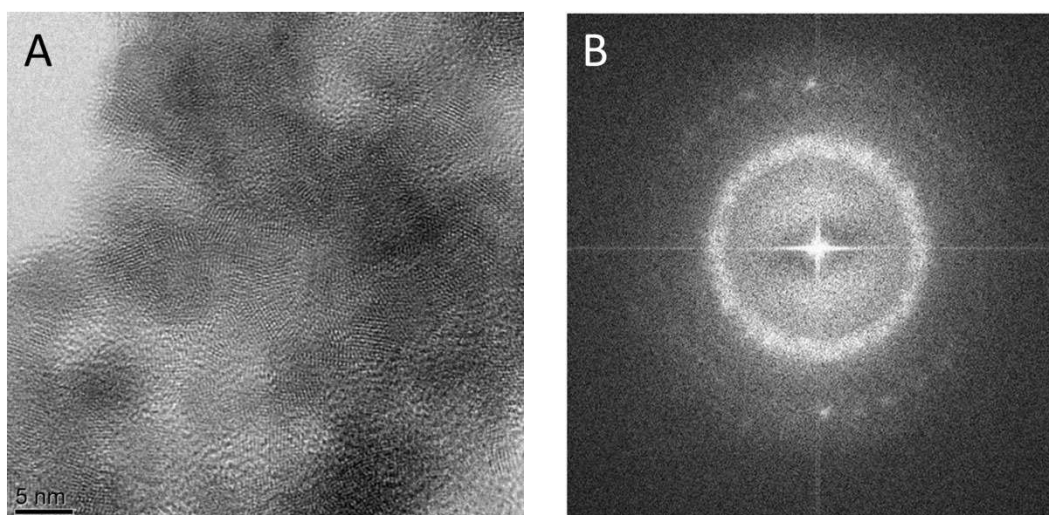


**Figure 4.1.7** (A) HREM image of CdS NP in sample CdS3. (B) reports the FT pattern. HREM image marker is 5 nm.

The new approach at the CdS synthesis looks promising: in this way it is possible to control the CdS NP dimensions *rather* effectively without the need of surface passivating agents, ligands or surfactants. The bottom line is that aggregation occurs inevitably: however it is not supposed to take place during the synthesis, but because of centrifugation or drying. It is worth noting that this synthetic approach is specific for the functionalization of ZnO and it is not intended to replace “conventional” methods, (*hot-injection* in particular) that allow far superior dimensional control and the possibility to obtain *single* NP or ordered 2D, 3D superstructures because of the role of capping agents.

The present challenge is indeed the ability to synthesize *small* CdS nanoparticles ( $2 \div 10 \text{ nm}$ ) without any surface passivating agents and create an effective type-II heterojunction between CdS and ZnO nanostructures.

## 4.1.2 CdS functionalization of ZnO tetrapods

### 4.1.2a Synthesis and structural characterization

CdS@ZnO heterostructure has been synthesized through a modified CBD process using DMF, without the need of any passivating agents. In a typical reaction 3 mg ( $\sim 37 \mu\text{mol}$ ) of ZnO TP are dispersed into a 100 ml beaker together with 50 ml of DMF keeping a vigorous stirring for 10 minutes and sonicated for 5 minutes. 3 ml of  $10^{-5}$  M solution of cadmium acetate (99.99%, Sigma–Aldrich, CAS: 89759–80–8) in DMF is added to the suspension and stirred for 30 min, then temperature is quickly raised to  $90 \text{ }^\circ\text{C}$  and 3 ml of  $10^{-5}$  M solution of thiourea (99%, Sigma–Aldrich, CAS: 62–56–6) in DMF is added. The suspension is then cooled down to room temperature and rinsed with distilled water. The solid phase is collected by centrifugation and washed again with water to remove the excess of unreacted precursors (sample CdS@ZnO). SEM analysis on the coupled compound is unable to reveal nano–sized structures attributable to CdS (Figure 4.1.8, left), the sample morphology reminds that of bare ZnO TP. To reveal the presence of CdS, an EDX spectrum is acquired and the analysis shows (Figure 4.1.8, right) an atomic ratio Cd/Zn = 1:13. Silicon peak is due to the substrate.

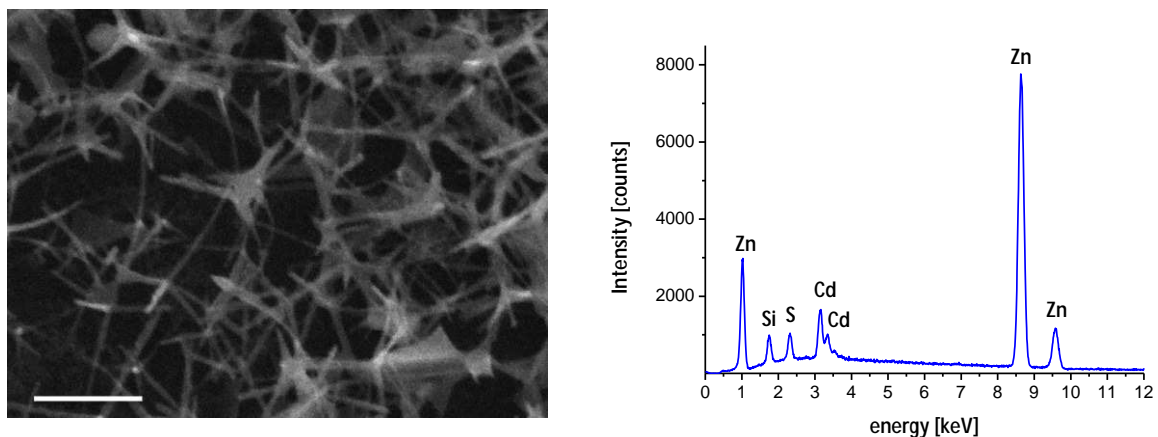


**Figure 4.1.8** SEM image of as synthesized sample CdS@ZnO (left). Scale bar is 1  $\mu\text{m}$ . EDX analysis on CdS@ZnO TP coupled material (right).

To understand the EDX spectrum, one can consider the hypothesis of heterogeneous nucleation: a core–shell structure *i.e.* a ZnO TP core and a thin, uniform CdS layer surrounding it. In fact, the ZnO surface can be considered a catalyst for cadmium sulphide nucleation. Heterogeneous nucleation is energetically preferred to the homogeneous one and can occur near equilibrium saturation conditions while homogeneous nucleation requires a (highly) supersaturated solution. In heterogeneous nucleation, subcritical nuclei or even individual ions can adsorb onto the substrate

because of both VdW and electrostatic interactions, and minimize their free energy by sticking (*i.e.* incorporate) to the surface.

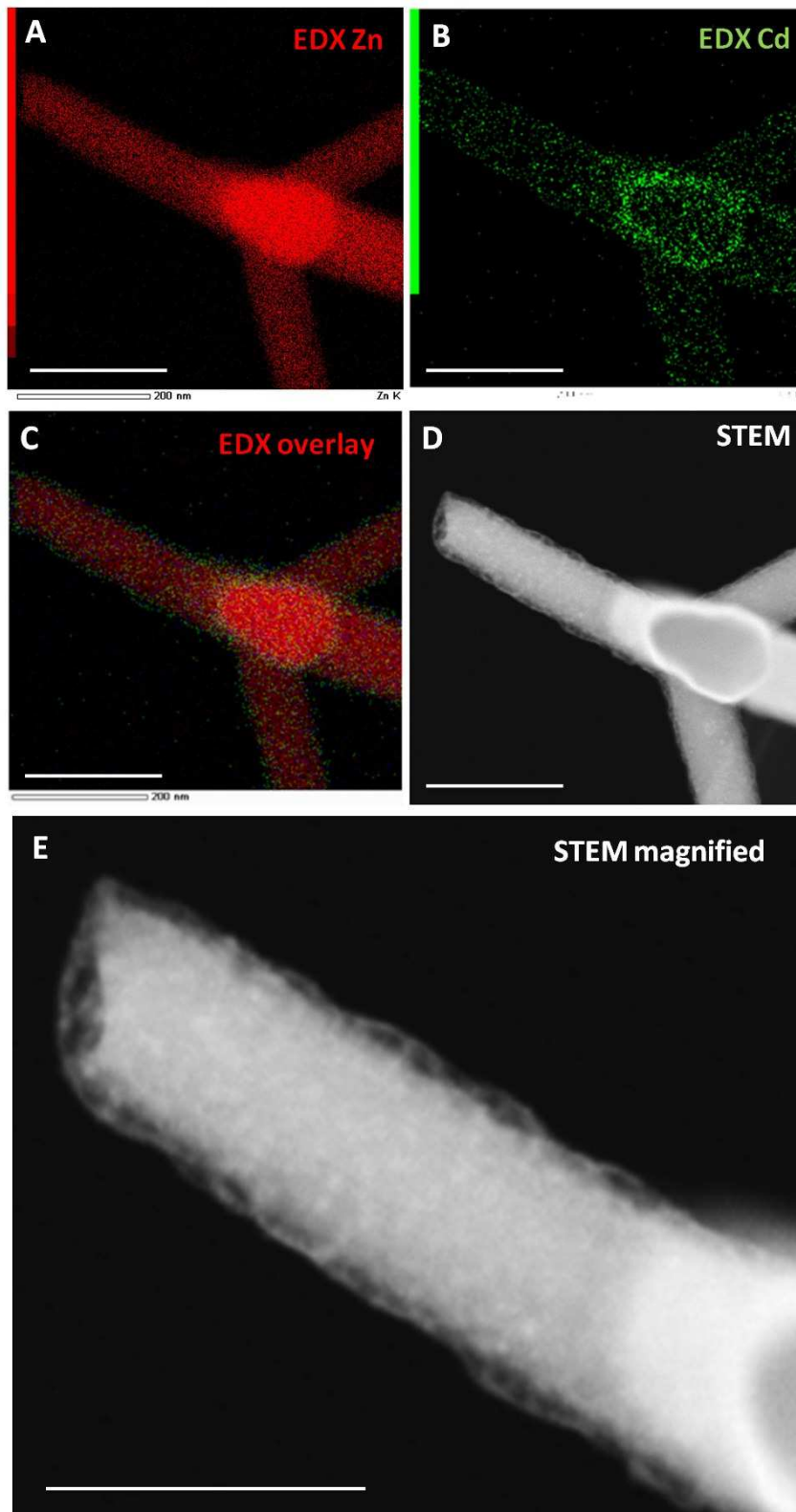


**Figure 4.1.9** TEM analysis of the sample  $\text{CdS@ZnO}$ . EDX mapping of Zn (A), Cd (B) and Zn + Cd (C) forming the  $\text{CdS@ZnO}$  core-shell heterostructure. STEM image (D) and a magnify view of CdS grains surrounding the ZnO core (E). Scale bars are 200 nm in all images.

It is known (refer to Ch. 2.2.2), that CdS nucleation / growth can take place through two different mechanisms: ion-by-ion and hydroxide cluster. The former is more likely to be the dominant in our system because of pH and solvent used. In ion-by-ion mechanism, controlling the dissociation rate of sulphur precursors is crucial to promote heterogeneous nucleation instead of the homogeneous one. A rapid release of  $S^{2-}$  ions would invariably lead to CdS bulk precipitation ( $K_{ps} = 10^{-28}$ ). But since the pH is neutral and DMF, instead of water, is used, thiourea dissociation rate is significantly lowered so that it is possible to control the  $S^{2-}$  concentration simply by means of temperature setting. It was found that 90 °C still keeps low values of local supersaturation to promote heterogeneous nucleation (*in situ* nucleation and growth on TP surface) over homogeneous one. TEM analyses performed on the functionalized TP demonstrate that a thin grainy layer of cadmium sulphide, about 10 nm thick, surrounds the ZnO TP (Figure 4.1.9 D and E).

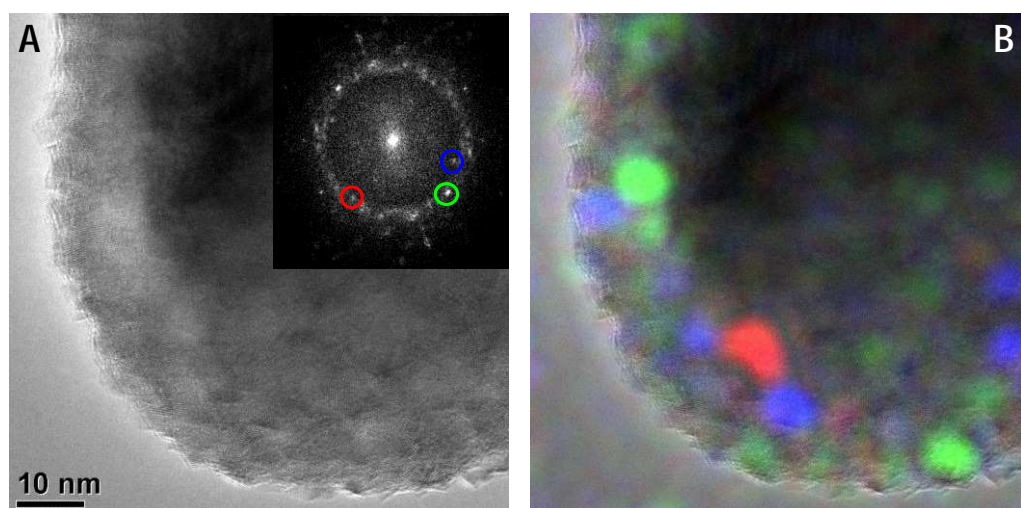


**Figure 4.1.10** (A) HREM image of the dense arrangement of CdS crystallites on a TP arm tip. In the inset its FT. (B) Intensity map obtained with the spatial frequencies circled in the FT.

The STEM EDS mapping analysis confirms that the cadmium sulphide coats the ZnO core, as shown in Figure 4.1.9 A and B that reports the X-ray maps obtained with the Zn  $K\alpha$  and Cd  $L\alpha$  respectively, while Figure 4.1.9C is the superposition of the two. The CdS crystallites completely cover the ZnO as it is shown in STEM images (Figure 4.1.9 D and E) and in the HREM image reported in Figure 4.1.10A. Its Fourier Transform (FT) in the inset, reports the typical ring feature coming from the random orientation of the CdS crystallites. The intensity distribution of the spatial frequencies present in the FT can be analyzed, in order to display which region has given rise to a particular frequency, as done in Figure 4.1.10B using the three much intense reflections (100, 002 and 101) for the wurtzite structure. An estimation of the average grain dimension has been done on different images and it has been found to be in the range of 2 ÷ 5 nm, taking into account the error inherent to this procedure. This is in good agreement with the value obtained from XRD data (Figure 4.1.11). Scherrer analysis on the three main broad peaks at 24.09°, 26.6° and 28.3°,

corresponding respectively to (100), (002) and (101) reflections of wurtzite structure ( $P6_3mc$ ) (JCPDS No. 80–0006), shows an average size of about 3 nm. No other peaks arising from possible impurity phases were observed.

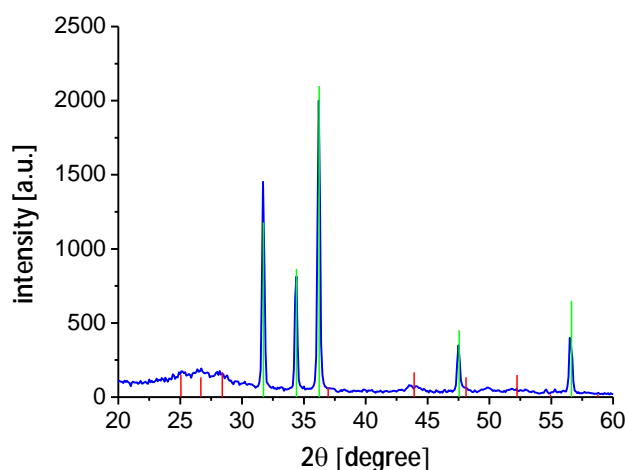


**Figure 4.1.11** XRD analysis on the  $CdS@ZnO$  TP core–shell structure. Reflections in red belong to CdS (JCPDS No. 80–0006) and green to ZnO (JCPDS No. 79–0205)

Dimensional control is good since grains dimensions appear to be uniform throughout the sample: it is likely that  $Cd^{2+}$  ions are adsorbed on zinc oxide surface and act as ‘nucleation seed’ for cadmium sulphide formation following the ion–by–ion mechanism. Slow dissociation of thiourea and consequent low concentration of  $S^{2-}$  ions in the solution avoids bulk precipitation and promotes in situ growth on TP surface.

#### 4.1.2b Photoluminescence

Since TEM observations show an average CdS particle size of about 3 nm, a blue shift in the photoluminescence spectra of cadmium sulfide is expected. While the absorption and scattering of incident light in larger colloidal particles is described by Mie’s theory, the optical spectra of nanocrystalline compound semiconductors [21–27], which show blue shifts in their absorption edge as the size of the particle decreases, cannot be explained by classical theory [28–31]. Similar size dependent optical properties are examples of the size quantization effect which occurs when the size of the nanoparticle is smaller than the bulk–exciton Bohr radius of the semiconductor. For nanoparticles the electron and hole are closer together than in the macrocrystalline material, and as such the Coulombic interaction between electron and hole cannot be neglected, they have higher kinetic energy than in the macrocrystalline material. Brus showed [29,30,32] for CdS and CdSe nanocrystallites that the size dependence on the energy of the first electronic transition of the exciton (or the band gap shift with respect to the typical bulk value) can be approximately calculated using the effective mass approximation [33]:



$$E_g(r) = E_g(\infty) + \frac{\hbar}{8r^2} \left( \frac{1}{m_e} + \frac{1}{m_h} \right) - \frac{1.8e^2}{\epsilon r}$$

where  $r$  is the radius of NPs,  $E_g(r)$  and  $E_g(\infty)$  are the effective band gap and the bulk band gap, respectively. The  $m_e$  (0.21) and  $m_h$  (0.80) are the effective mass of electron and hole, and  $\epsilon$  (8.9) is the bulk dielectric constant.

To evaluate cadmium sulphide optical properties, CdS nanoparticles were prepared using DMF as solvent as described in the previous chapter (sample CdS3) and a room temperature luminescence spectrum was collected (Figure 4.1.12A). As expected [29–33] the effect of quantum confinement is huge: bulk cadmium sulphide has a band gap of 2.4 eV (corresponding to 516 nm), while the luminescence of the sample shows a nearly 0.6 eV blue shift.

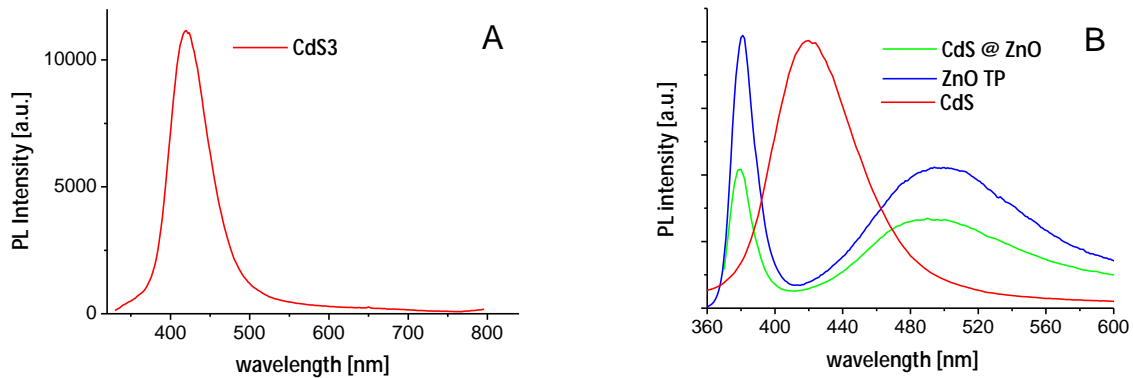


**Figure 4.1.12** (A) PL spectra of CdS NP. (B) PL spectra of the coupled compound CdS@ZnO TP (green line) showing a quench of CdS luminescence (red line). Bare ZnO TP are shown as reference (blue line).

The luminescence of CdS NP is very intense and the peak is quite large, with tails on both sides. Comparing the FWHM and spectral barycenter of the curve with those reported in literature [34,35], the luminescence of the observed sample is due to NP with dimensions ranging from 2.5 nm to 5 nm which is consistent with TEM and XRD analysis. Emission spectrum of ZnO TP is reported in figure 4.1.12B, blue line. TP are the same used for the functionalization with CdS and measured in the same experimental conditions, thus directly comparable. The ZnO TP PL spectra shows a common behavior [36,37] with a UV peak centered at 380nm (3.26 eV) caused by interband transition and a wide emission band, which covers almost the visible range, centered at 500 nm, corresponding to the green region (see Ch. 2.1.2). The green band is known to be associated to stoichiometry related defects such as zinc vacancies, interstitial zinc as well as surface defects [36]. It is worth to note that UV peak is stronger than green emission, this is a mark of a high quality vapor phase growth. As previously reported [38], green luminescence is often dominant in ZnO TP because of high surface to volume ratio.

The luminescence of the core–shell structure (Figure 4.1.12B, green line) clearly shows a quench of the CdS emission and a blue shift of the green band (all PL curves have the same vertical scale and are comparable). The latter can be due to CdS functionalization on ZnO TP, since the green band is strongly dependent on the ZnO surface. The former evidence is very interesting since this could be a proof of electron transfer from CdS to ZnO. ZnO nanostructures functionalized with an extremely thin layer of cadmium sulphide are widely used in ETA solar cells [6,7,39,40] and photocatalytic systems [2–4] because CdS and ZnO can form a type–II heterojunction, i.e. the conduction band edge of ZnO is located between the conduction band and the valence band of CdS (Figure 4.1.13).

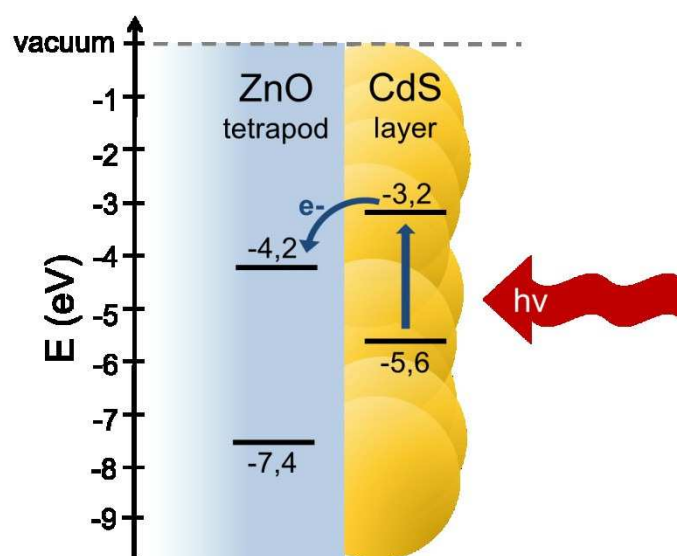


**Figure 4.1.13** Schematic sketch of a type–II heterojunction between CdS and ZnO.

In this band gap alignment, when the electron–hole pairs are generated (by visible light excitation) in CdS nanoparticles, the photoelectrons can be transferred to the conduction band of the ZnO TP, which assists the charge separation process of the electron–hole pairs before they recombine [39,40]. In a mono–crystals this holds true until CdS thickness does not exceed the CdS exciton diffusion length (from 100 nm up to several microns [41,42]), otherwise electron hole pairs can recombine and CdS stand–alone emission is observed. When dealing with nanostructures, such idealization is not observed because defects, impurities, grain boundaries and surface states may promote the exciton recombination.

For comparison purpose, in Figure 4.1.14 the TEM analysis of a coupled compound CdS on ZnO TP sample grown with an excessive concentration of precursors ( $Cd / Zn = 1:5$ ) is reported, *i.e.* sample CdS@ZnO–2, in which heterogeneous nucleation occurs only partially, and some homogeneous nucleation takes place. This causes the formation of large CdS aggregates (some in excess of 100 nm) formed by small NP (Figure 4.1.14).

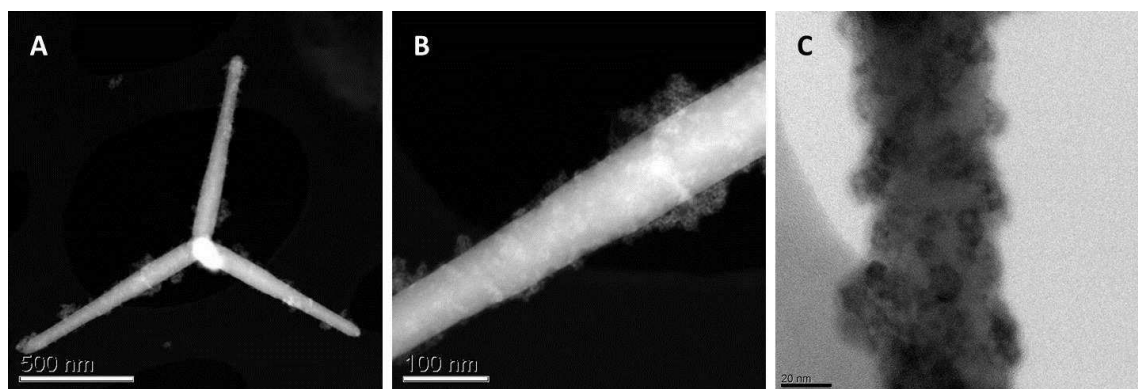


**Figure 4.1.14** TEM analysis on a sample  $\text{CdS@ZnO-2}$  grown with excess of precursors ( $\text{Cd} / \text{Zn} = 1:5$ ): homogeneous nucleation takes place together with heterogeneous one. (A) STEM image of the sample  $\text{CdS@ZnO-2}$ , (B) is a magnified view of A, (C) shows the spot-like CdS coverage. Scale bars are respectively 500, 100 and 20 nm.

Since such large agglomerates don't allow an efficient charge separation (only a fraction of CdS NP are close to ZnO surface and allow electron transfer), the CdS emission is observed. Figure 4.1.15A reports a comparison of the luminescence spectra of the two samples grown with different Cd / Zn ratio: blue line is about sample  $\text{CdS@ZnO-2}$ , green line is the same shown in Figure 4.1.12 ( $\text{Cd} / \text{Zn} = 1:13$ ), about the sample  $\text{CdS@ZnO}$ , and it is reported for comparison. It is worth noting that CdS NP grains dimensions (Figure 4.1.14C) appear to be not as uniform as those represented in Figure 4.1.9 and 4.1.10: increasing the concentration of precursor doesn't allow an accurate dimensional control. This consideration could provide a possible explanation for the PL spectrum reported in Figure 4.1.15A.

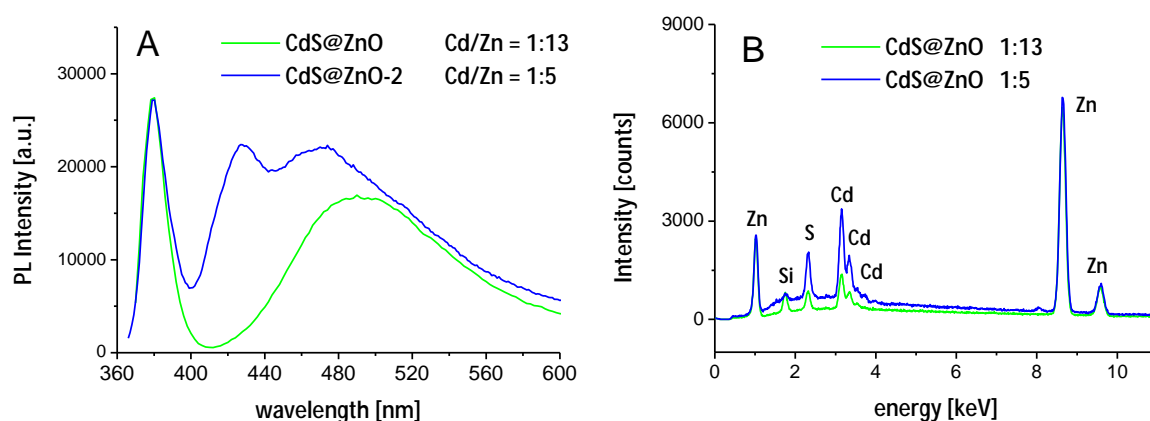


**Figure 4.1.15** Comparison between different CdS “layers”: core-shell (green) and spot-like (blue) (A) PL spectra showing the CdS emission quench in the case of core-shell, whereas the sample grown with excess Cd (spot-like) emits, (B) SEM-EDX analysis: Cd/Zn is 1:13 in the core-shell, 1:5 in the spot-like.

The blue line refers to the sample grown with excess of precursor salts ( $\text{CdS@ZnO-2}$ ): the CdS emission peak is visible at 430 nm and the part of the spectrum at lower wavelengths is likely to reflect the dimensional dispersion of CdS NP: particles with higher dimensions emit in the green region where ZnO point defects have their own characteristic luminescence. The superposition of

the two contributions shifts the resulting band at higher energy. Figure 4.1.15B shows the EDX analysis of CdS@ZnO-2 (blue line), the green line refers to the core-shell sample (CdS@ZnO), and is reported for sake of clarity.

#### 4.1.2c Photocurrent measurement

PL measurement *suggests* a charge transfer between CdS layer and ZnO (in the sample CdS@ZnO, Cd / ZnO = 1:13 sample) but that's not the ultimate proof, because the quench in CdS luminescence may be also due, for example, to non-radiative recombination at the ZnO-CdS interface.

Hence further experiments were needed to cast light on this aspect. The collected nanostructures were suspended in isopropyl alcohol (magnetic stirring + sonication) and then deposited through centrifugation on a glass substrate with Au interdigitated contacts and a photocurrent spectrum was recorded. Samples were illuminated at different wavelength (from UV to NIR) while collecting a current measurement at a fixed voltage bias (1V). As shown in Figure 4.1.16 bare ZnO TP and CdS@ZnO TP behaves differently. Please note that the graph has 2 vertical scales for better scaling the curves into the graph itself: the one on the left is about the coupled compound while on the right is reported the photocurrent of bare ZnO TP. The first evidence is that photocurrent maximum has different values in the two samples: the current in the coupled compound is about 5 times higher than that on bare ZnO TP. This non linear effect can be possibly ascribed to the heterojunction which is formed between CdS and ZnO: when a photon is absorbed inside the CdS layer an exciton is created and separated at the interface, transferring the electron to the ZnO CB. Moreover the absorption shoulder centered at 400 nm in the coupled compound is consistent with the emission spectra of CdS NP reported in Figure 4.1.12 and centered at 420 nm.

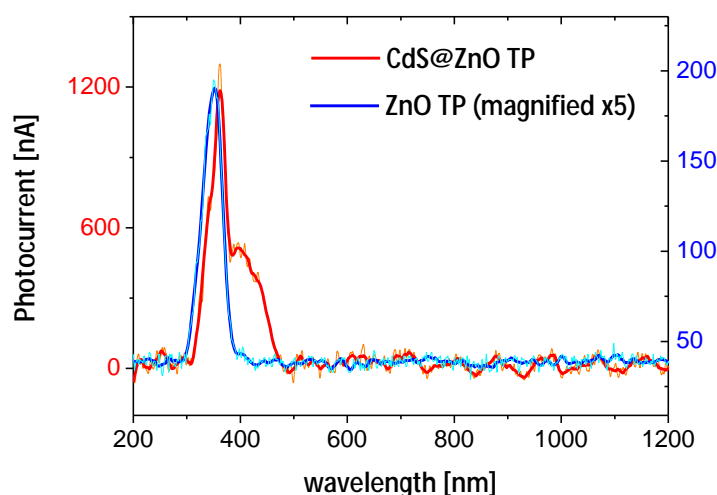


**Figure 4.1.16** Photocurrent spectrum of CdS@ZnO TP core-shell compared to bare ZnO TP.

The wavelength corresponding to the photocurrent maximum is nearly the same (about 380 nm). The red shift in the coupled compound can be explained considering the wavelength overlap between CdS and ZnO absorptions curves: the resulting curve is the sum of the two individual absorptions and the contribution at lower energy moves the spectral barycentre of the curve towards lower energy. Interestingly, at wavelength corresponding to the bulk CdS band gap (515 nm), no enhancement in photocurrent is measured. Finally it must be noted that, in the core-shell structure, the ZnO surface is “passivated” with the CdS layer, while CdS surface is exposed to air. It is known from previous works [43,44] that photo-desorption of chemical species attached on CdS surface (*i.e.*  $O_2^-$  or  $O^-$ ) results in an electron-depleted surface layer due to the electron transfer from CdS to oxygen, this lowers the CdS photocurrent value.

#### 4.1.2d Photocatalytic activity

According to literature [2,6,7,39,40], visible-light photocatalytic measurements are also used to prove charge transfer between coupled compounds forming a type-II heterojunction. The photocatalytic activity of the sample CdS@ZnO is evaluated by the decomposition rate of methylene blue (MB) in isopropyl alcohol (IPA) solution. For calibration purpose a  $10^{-5}$  M solution MB has been illuminated for an hour with a He-Cd laser (15mW at 442nm) while keeping a vigorous stirring. The absorbance spectrum is shown in Figure 4.1.17 (grey line).

Besides reference, three samples have been prepared:

- a) 4.8 mg (60  $\mu$ mol) of ZnO TP dispersion in 50ml IPA.
- b) 8.6 mg (60  $\mu$ mol) of CdS nanoparticles (3 nm average diameter); synthesized in the way of sample CdS3, described in the previous chapter, and dispersed in 50 ml IPA.
- c) 5.1 mg of coupled compound CdS@ZnO as previously described (1:13 molar ratio, 56 + 4  $\mu$ mol total), dispersed in 50 ml IPA.

Similarly, the three samples were illuminated for an hour keeping a vigorous stirring which helps the dispersion of the nanostructures into the IPA and allows atmospheric oxygen to diffuse into the liquid phase. The solid phase is then separate by centrifugation and an absorption spectrum of the liquid is then measured.

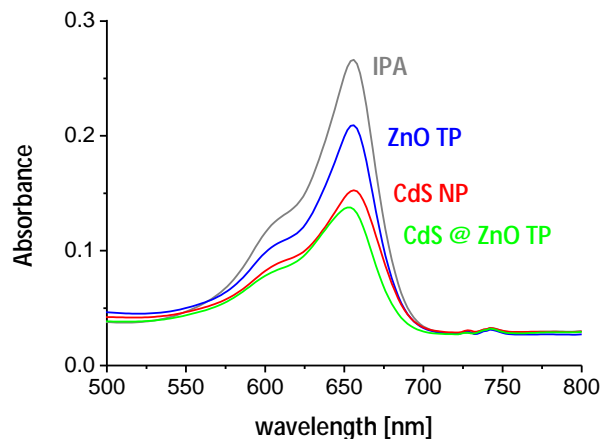
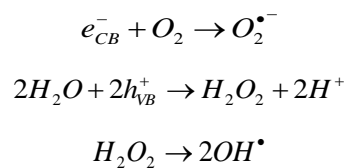


**Figure 4.1.17** Absorbance spectra after 1 hour illumination at 442 nm: a) grey line: MB in IPA solution; b) blue line: 60 μmol of ZnO TP; c) red line: 60 μmol of CdS NP; d) green line: the coupled compound 4 μmol CdS surrounding 56 μmol ZnO TP

Even though a 442 nm excitation is not able to produce direct inter-band transition in ZnO, it has sufficient energy to excite surface states and a small amount of photocatalytic activity have been measured for 60 μmol of ZnO TP (Figure 4.1.17, blue line), compared to our reference sample consisting of MB in IPA (Figure 4.1.17, grey line).

The same molar quantity (60 μmol) of cadmium sulphide shows an enhanced photocatalytic activity (Figure 4.1.17, red line). This can be explained considering both the larger surface area of CdS nanoparticles and the lower energy gap with respect to ZnO TP. Electron-hole pairs are formed inside the CdS upon illumination at 442 nm, and both carriers can be transferred to the absorbed species and promote photocatalytic activity: CB electrons react with oxygen to form superoxide radical, VB holes react with water to produce hydrogen peroxide and hence hydroxyl radicals as follows:



For a comprehensive analysis of the photocatalytic process in semiconductor oxides the reader could refer to Fox [43], Sobczykński [44] and, in particular, Hoffmann [45]; while kinetic mechanism for MB degradation is described in detail by Wu *et al.* [46]. However, without any loss of rigorousness, the photocatalytic activity of the core-shell CdS-ZnO (1:10 molar ratio) is expected to be lower than that of CdS because of both lower quantity (4 μmol vs 60 μmol) and lower active surface (CdS@ZnO TP vs 3 nm CdS3 NP). To the contrary absorption spectrum (Figure 4.1.17, green line) shows an enhancement of photocatalytic activity, which cannot be

justified by a simple addition of the two separated CdS and ZnO contributions. Since it is consistent to assume that ZnO surface is almost fully covered by CdS, it is worth to note that the photocatalytic enhancement is due to cadmium sulphide valence band holes only. If one considers the photocatalytic activity per mole of CdS, the coupled compound shows a 15x enhancement compared to CdS NP. The observed enhancement can be reasonably explained only considering that charge transfer in type-II heterostructure slows electron-hole recombination and hence extends carriers lifetime [47,48].

The kinetically slow stage in a photocatalytic reaction, which takes place on SC surface, is the interfacial charge transfer which involves the release of a trapped carrier at the surface (hole or electron, depending on the material) and transfer to the photocatalytic “active” species adsorbed on the surface ( $-OH$ ,  $O_2$ ,  $O_2^-$ ,  $O^-$ ) [45]. In our case, the charge separation is efficient, so that holes lifetime is sufficiently high to promote the formation of hydroxyl radicals that degrade MB molecules. On the contrary, with regard to CdS NP, the rate of recombination is higher (there is no electron transfer to another material) and even if both carriers take part in the redox process, to create both hydrogen peroxide and superoxide radicals, the measured photocatalytic activity is lower.

#### 4.1.2e Gas sensing

Semiconductor metal oxide gas sensors (MOX) are considered one of the basic technologies to identify and measure the concentrations of gas in the atmosphere. These microelectronic devices offer a wide variety of advantages over traditional analytical instruments such as low cost, short response time, easy manufacturing, and small size. Our group focused his research attention to gas sensors a few years ago and the results of bare ZnO TP-based chemo-resistive gas sensors have been previously reported [49,50]. Herein is reported the effect of CdS functionalization on ZnO TP, evaluated through the measurement of gas sensing properties. For this purpose the sample with irregular CdS deposition (CdS@ZnO-2) is far more interesting than the core-shell one (CdS@ZnO). In fact the core-shell structure ideally has no ZnO free surface: the study is aimed to tailor the ZnO TP surface properties – and hence the gas sensor response – not to investigate the CdS stand-alone response. A brief description of the gas sensor preparation is reported in Chapter 3.2.4a. Being ZnO a n-type semiconducting oxide, it is generally subject to a positive conductivity variation when exposed to reducing gases or volatile compounds (*e.g.* carbon monoxide, ethanol), while a negative variation is observed when the sensor is exposed to oxidizing gases and volatile compounds (*e.g.* nitrogen dioxide, ozone). Although this kind of sensors is generally extremely sensitive [49,50], they are also not-selective and a chemo-resistive response is observed towards a very large number of compounds. The best way to enhance their selectivity is usually based on the

functionalization of their surface by different materials, as other oxides and semiconductors, noble metals or organic molecules.

In the case of CdS-functionalized ZnO TP, among the tested gases, we have observed an unexpected behavior towards NO<sub>2</sub>: the typical decrease in sensor conductivity when detecting an oxidizing gas (ZnO n-type response) is observed only below 350 °C, while above this temperature sensor conductivity increases (p-type response), as reported in Figure 4.1.18. Measurements have been performed by the volt-ampereometric technique at constant voltage (DC) of 5V, under a 500 ml / min constant flow with 30% relative humidity. This peculiar behavior can be exploited in order to distinguish NO<sub>2</sub> from other interfering gases, adding selectivity to the ZnO TP-based gas sensors. The simplest hypothesis to explain the observed sensor response consists in the assumption that CdS NP have p-type conductivity. What is actually observed could be the superposition of two distinct sensing mechanisms, at lower temperatures ZnO n-type response prevails while at higher temperature CdS p-type conductivity is observed. Unfortunately there are no reports of CdS based gas sensors showing a p-type response, so it's not possible to compare the present results. Moreover p-type CdS is usually obtained only through intentional doping with copper [51–55] or bismuth [56,57], hence a deeper study of the heterojunction and of the NP electrical properties is required to fully understand the sensing mechanism.

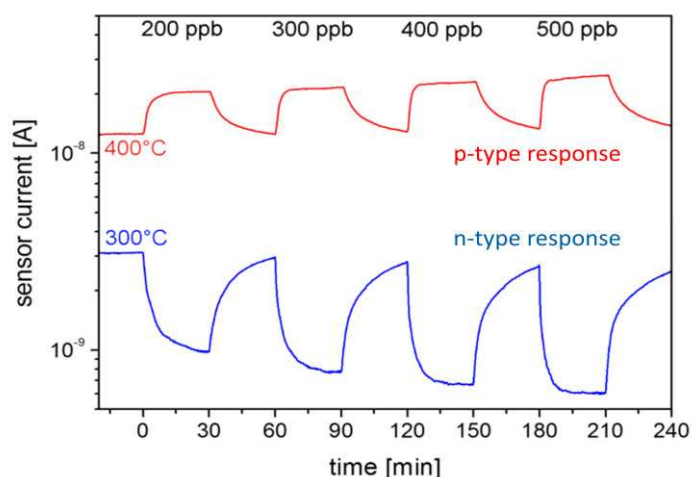


**Figure 4.1.18** Dynamic response of CdS@ZnO-2 gas-sensor towards different concentration of NO<sub>2</sub> at 300 °C (blue) and 400 °C (red). The inversion of the chemo-resistive response is clearly visible.

#### 4.1.2f Final remarks

In conclusion, a novel heterostructure based on ZnO TP core surrounded with an extremely thin CdS shell (10nm) has been synthesized with a modified CBD deposition without the need of any surfactants / ligands. The heterostructure has been studied by functional characterizations, such as photocurrent and photocatalytic activity measurements, which point out the formation of a type-II



heterojunction between CdS and ZnO TP, allowing efficient photoelectron transfer. The CdS / ZnO interface shows good optical properties (exciton separation, quench of CdS luminescence and extended photocurrent range) and enhanced photocatalytic activity. That's why we expect the realized heterostructure will offer promising applications not only as active material in the degradation of organic pollutants, but also as solar energy harvesting material (i.e. photoanode in photo electrochemical or photovoltaic cells).

Moreover varying synthetic parameters, the CdS morphology can be changed from homogeneous layer to spot-like. The spot-like CdS / ZnO TP heterostructure presents both CdS and ZnO TP surface exposed to air and this conformation has shown unexpected NO<sub>2</sub> gas-sensing behavior. In fact, the inversion of chemo-resistive response (with respect to bare ZnO TP) adds *selectivity* to the sensor and can be useful to distinguish between different interfering gases.

### 4.1.3 CdS functionalization of ZnO nanorods

Taking advantage from the previously described CdS functionalization of ZnO TP, which has been shown to form a type-II heterojunction with interesting properties, this small section briefly describes the CdS sensitization of ZnO NR. NR morphology was chosen because it presents some interesting features: NR have a single crystalline structure so that the structural homogeneity and crystalline properties are maintained over the whole NR length, allowing a continuous path for the electrons inside the material. With energy harvesting applications in mind, NR have been grown on c-axis oriented AZO layer (refer to Ch. 3.1.1b for growth details) which minimizes the potential barriers improving electron mobility and hence reducing recombination (AZO and ZnO NR share the same lattice parameters and grows along the (001) direction perpendicular to the substrate). Moreover, NR present a high surface to volume ratio and a "rough" surface that helps scattering phenomena on incoming light and enables multiple trapping processes at the interface.

Unfortunately, when dealing with ZnO NR, the synthetic procedures described in Ch. 2.2.2, are not directly applicable. Vertically aligned NR, indeed, are not dispersed in the liquid but lie to a glass substrate, as described in Ch. 3.1.1b. In this case, the formation of a thick stagnant layer limits the diffusion of CdS precursors towards the ZnO NR surface, hence the supersaturation at the interface is generally so low, that is not possible to promote heterogeneous nucleation without triggering the homogeneous one, at the same time. Therefore an alternative approach to the functionalization has been explored. According to literature, Pathan and Lokhande [58] gathered informations about a smart technique used since 1980s to deposit thin films on different substrates: the successive ionic layer adsorption and reaction (SILAR) method. The term adsorption can be defined as the

interfacial layer between two phases of a system. Adsorption may be expected when two heterogeneous phases are brought into contact with each other. Hence, gas–solid, liquid–solid and gas–liquid are three possible adsorption systems, however SILAR method concerns with adsorption in liquid–solid system only. The adsorption is a surface phenomenon between ions and the substrate surface, it is possible due to attractive forces (VdW or electrostatic forces). Experimentally the SILAR method consists of 4 steps [58]:

- 1) Adsorption: In this first step of SILAR process, the cations present in the precursor solution are adsorbed on the surface of the substrate and form the Helmholtz electric double layer *i.e.* composed of two layers: the inner (positively charged) and outer (negatively charged) layers.
- 2) Rinsing (I): In this step, excess adsorbed ions, are rinsed away from the diffusion layer. This results into saturated electrical double layer.
- 3) Reaction: In the reaction step, the anions from anionic precursor solution are introduced to the system and a new solid phase is formed on the interface. This process involves the reaction of adsorbed cations with the anionic precursor. The reaction in pre–adsorbed (cations) and newly adsorbed (anions) forms the thin films of desired material.
- 4) Rinsing (II): In the last step of a SILAR cycle, the excess and unreacted species, and the reaction byproduct are removed from the diffusion layer.

It must be noted that SILAR technique, like CBD, requires an aqueous alkaline environment and hence it is not compatible with ZnO nanostructures, on one hand because  $[\text{Zn}(\text{OH})_4]^{2-}$  ions are formed so that ZnO surface is invariably degraded / etched [59,60], on the other, when a dense array of ZnO NR is used, the wettability is poor. Oppositely to what is reported in literature, it was not possible to tailor properties of hydrophobicity or hydrophilicity of ZnO NR under different conditions of UV illumination [61], so that finally water was not considered as a good solvent for the reaction. Taking into account the previous research on ZnO TP, DMF was chosen as solvent for cadmium and sulphur precursors. In fact, when heterogeneous nucleation is considered, ZnO TP and NR are very similar nanostructures from the crystallographic point of view, since they have the same orientation (both grows along the 0001 direction) and display the same lateral faces, typically (01-10) or (2-1-10) [62], thus they may show the same surface reactivity. It is worth mentioning that thiourea is not a good choice for SILAR deposition because it requires relatively high temperature (80 °C) to dissociate and release  $\text{S}^{2-}$  ions (when an alkaline bath is not used) and the mechanism of atomic adsorption onto a surface – at the base of SILAR method – is an exothermic process.

In a typical reaction, the ZnO NR substrate is immersed in a 0.1 M solutions of cadmium acetate (99.99%, Sigma–Aldrich, CAS: 89759–80–8) in DMF for 30 seconds, rinsed in 1:1 (v/v) DMF:H<sub>2</sub>O then immersed 0.1 M solution of Na<sub>2</sub>S (Sigma–Aldrich, CAS: 1313–82–2) in DMF and rinsed again. This coating cycle was repeated 50 times and the sample is then characterized morphologically by SEM. Images are reported in Figure 4.1.19.

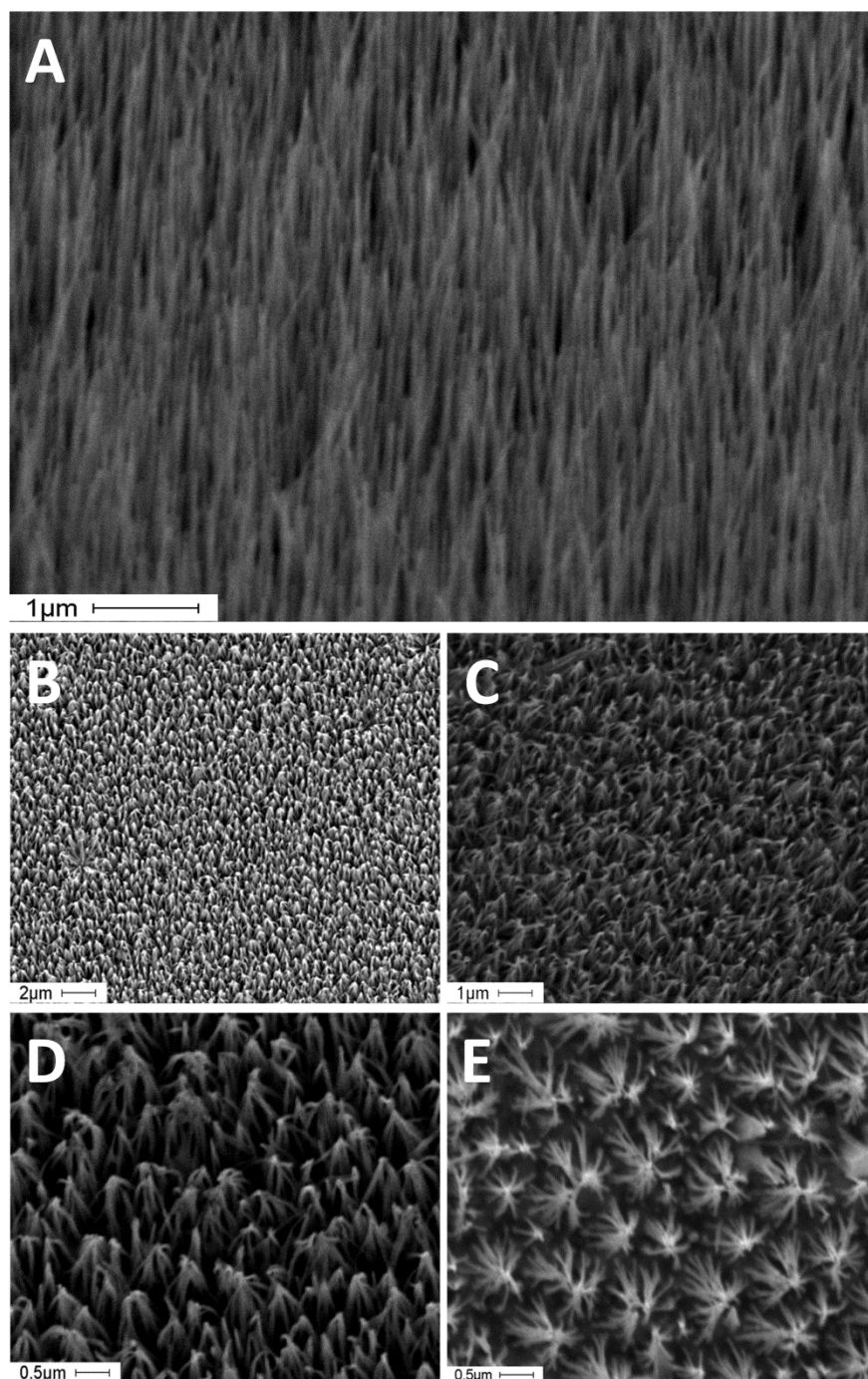


**Figure 4.1.19** SEM view of as-grown NR (A) and CdS functionalized NR (B–E) at different tilt / magnification.

Interestingly, there is no evidence of CdS bulk precipitation (at least aggregates larger than a hundred of nanometers) but a bending is observed and the top of the adjacent NR coalesced to form “volcano-like” structures. According to our experience, this is not due to CdS functionalization itself [63], or high-pH value [64] but it’s rather caused by capillarity forces as a consequence of wetting. Similar morphologies have been observed simply immersing NR in different solvents: *e.g.* water, chloroform, methylethylketone, dimethylformamide and isopropyl alcohol. TEM analyses of the CdS functionalized ZnO NR are reported in Figure 4.1.20. Contrary

to what was expected for the SILAR deposition [65,66] a core–shell structure is not observed (Figure 4.1.20 A and B) although a sufficient dimensional control is achieved so that CdS aggregates are not in excess of 20 nm. The control of CdS thickness is a necessary (although not sufficient) condition for efficient exciton separation and electron transfer to attached ZnO NR: this is crucial for future applications such as photovoltaic or photo–electrochemical cells (PEC).

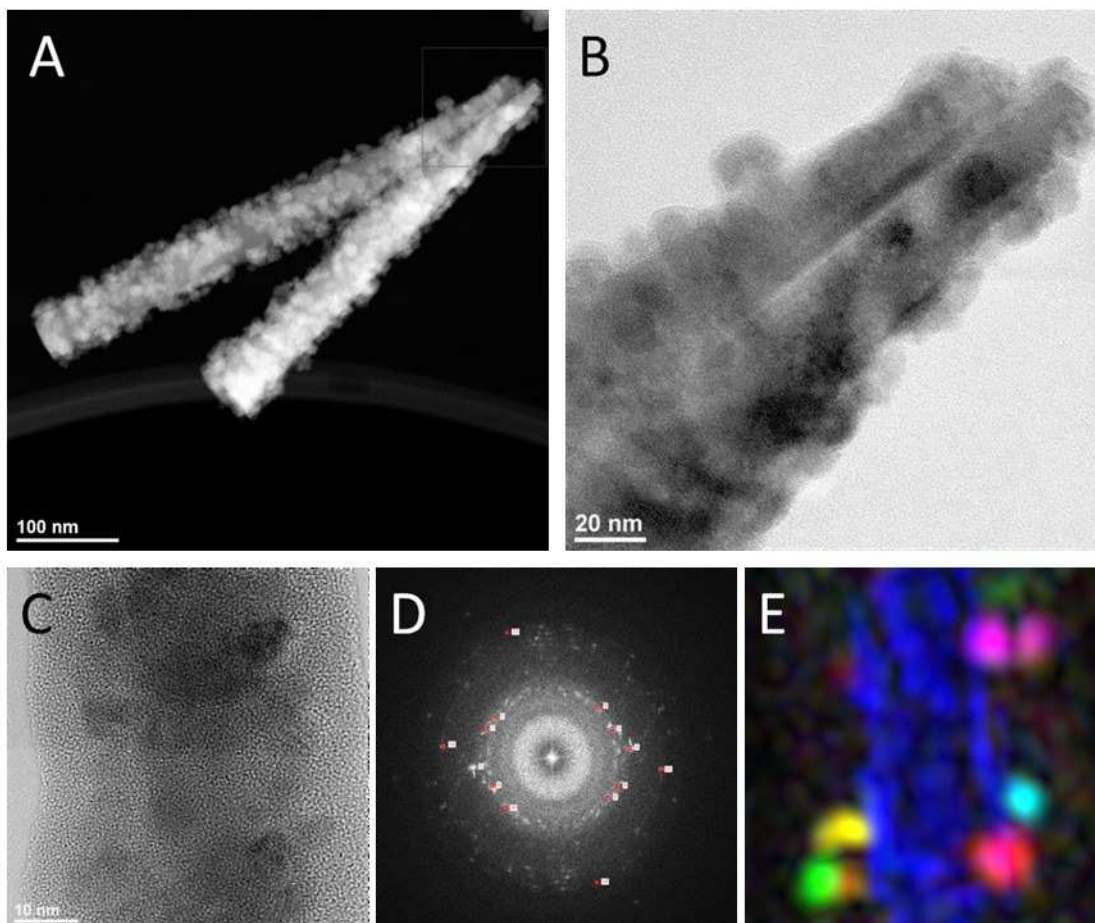


**Figure 4.1.20** TEM analysis of CdS functionalized ZnO NR.

According to HREM image reported in (C), it is difficult to evaluate CdS grain dimensions because of image poor SNR and low contrast. However the corresponding FT (D) reports the typical ring feature coming from the random orientation of the CdS crystallites. It is possible to obtain the intensity distribution of the spatial frequencies present in the FT, in order to display what region has given rise to a particular frequency, which has been done in (E). Average CdS grain dimension has been estimated to be in the range of a few nanometers ( $\sim 10$  nm), taking into account the error inherent to this procedure.

As future work perspective, achieving a continuous CdS layer that surrounds the ZnO NR entirely, is highly desirable. In fact, on the one hand, it enhances the fraction of visible light collected by the composite photoanode (CdS–ZnO), on the other, it reduces recombination between ZnO and the hole transporting material and hence improves the device efficiency.

## References

- [1] C. Yang, J. Wub and Y. Hou, *Chem. Commun.*, 2011, **47**, 5130
- [2] Y. Tak, H. Kim, D. Lee and K. Yong, *Chem. Commun.*, 2008, 4585
- [3] J. Nayak, S.N. Sahu, J. Kasuya, S. Nozaki, *Applied Surface Science*, 2008, **254** (22), 7215
- [4] P. Kundu, P. A. Deshpande, G. Madras and N. Ravishankar, *J. Mater. Chem.*, 2011, **21**, 4209
- [5] Y. Zang, T. Xie, T. Jiang, X. Wei, S. Pang, X. Wang, D.Wang, *Nanotechnology*, 2009, **20**, 155707
- [6] Y. Tak, S.J. Hong, J.S. Lee, *Cryst. Growth Des.*, 2009, **9** (6), 2627
- [7] Y. Tak, S. J. Hong, J. S. Lee, and K. Yong, *J. Mater. Chem.*, 2009, **19**, 5945
- [8] G. Guerguerian, F. Elhordoy, C. J. Pereyra, R. E. Marotti, F. Martin, D. Leinen, J. R. Ramos-Barrado and E. A. Dalchiale, *Nanotechnology*, 2011, **22**, 505401
- [9] C. Luan *et al.*, *Nanoscale Res Lett.*, 2011, **6** (1), 340
- [10] X. Wang, G. Liu, G. Q. Lu, H. M. Cheng, *International journal of hydrogen energy*, 2010, **35**, 8199
- [11] S. Wei, Z. Shao, X. Lu, Y. Liu, L. Cao, Y. He, *J. Environ. Sci.*, 2009, **21** (7), 991
- [12] X. Wang *et al.*, *Energy Environ. Sci.*, 2011, **4**, 3976
- [13] G. Wang, X. Yang, F. Qian, J. Z. Zhang and Y. Li, *Nano Lett.*, 2010, **10** (3), 1088
- [14] C. A. Grimes, *Light, Water, Hydrogen*, New York, 2008, Springer Science Business Media
- [15] S. Ruehle, M. Shalom, and A. Zaban, *ChemPhysChem*, 2010, **11**, 2290
- [16] Y. J. Shen, Y. L. Lee, *Nanotechnology*, 2008, **19**, 045602
- [17] I. Mora-Serò, S. Giménez, T. Moehl, F. Fabregat-Santiago, T. Lana-Villareal, R. Gòmez, J. Bisquert, *Nanotechnology*, 2008, **19**, 424007
- [18] J. Chen, J. L. Song, X. W. Sun, W. Q. Deng, C. Y. Jiang, W. Lei, J. H. Huang, R. S. Liu, *Appl. Phys. Lett.*, 2009, **94**, 153115
- [19] I. Robel, V. Subramanian, M. Kuno, P. V. Kamat, *J. Am. Chem. Soc.*, 2006, **128**, 2385
- [20] X. Peng, J. Wickham, and A. P. Alivisatos, *J. Am. Chem. Soc.* **1998**, *120*, 5343
- [21] M. L. Steigerwald, L.E. Brus, *Acc. Chem. Res.* 1990, **23**, 183
- [22] M. G. Bawendi, M.L. Steigerwald, L.E. Brus, *Annu. Rev. Phys.Chem.* 1990, **41**, 477
- [23] H. Weller, *Angew. Chem., Int. Ed.* 1993, **32**, 41
- [24] H. Weller, *Adv. Mater.*, 1993, **5**, 88
- [25] A. Hagfeldt, M. Graetzel, *Chem. Rev.*, 1995, **95**, 49
- [26] J. H. Fendler, F.C. Meldrum, *Adv. Mater.*, 1995, **7**, 607
- [27] A. P. Alivisatos, *J. Phys. Chem.*, 1996, **100**, 13226
- [28] H. Haug, S.W. Koch, *Quantum theory of the optical and electronic properties of semiconductors*, 1990, World Scientific Publishing Co., London, p 333
- [29] L. E. Brus, *J. Chem. Phys.* 1983, **79**, 5566
- [30] L. E. Brus, *J. Chem. Phys.*, 1984, **80**, 4403
- [31] L. E. Brus, *J. Phys. Chem.*, 1986, **90**, 2555
- [32] M. L. Steigerwald, L.E. Brus, *Acc. Chem. Res.*, 1990, **23**, 183

- [33] R. Rossetti, J.L. Ellison, J.M. Gibson, *J. Chem. Phys.*, 1984, **80** (9), 4464
- [34] W. W. Yu and X. Peng, *Angew. Chem. Int. Ed.*, 2002, **41** (13), 2368
- [35] J. Ouyang *et al.*, *J. Phys. Chem. C*, 2009, **113**, 7579
- [36] M. C. Newton, S. Firth, T. Matsuura, *JPCS*, 2006, **26**, 251
- [37] L. Lazzarini, G. Salviati, F. Fabbri, M. Zha, D. Calestani, A. Zappettini, T. Sekiguchi and B. Dierre, *ACS Nano*, 2009, **3** (10), 3158
- [38] C. Zollfrank, C.R. Rambo, M. Batentschuk, *J. Mater. Sci.*, 2007, **42**, 6325
- [39] Y. Zhang, T. Xie, T. Jiang, *Nanotechnology*, 2009, **20**, 155707
- [40] S. Hotchandani, P.V. Kamat, *J. Phys. Chem.*, 1992, **96** (16), 6834
- [41] G. Diemer, G.J. Van Gurp, W. Hoogenstraaten, *Journal of Physics and Chemistry of Solids*, 1959, **8**, 182
- [42] B. V. Novikov, A. V. Ilinskii, K. F. Lieder, N. S. Sokolov, *physica status solidi (b)*, 1971, **48** (2), 473
- [43] M. A. Fox, M.T. Dulay, *Chem. Rev.* 1993, **93**, 341
- [44] A. Sobczykński, A. Dobosz, *Polish Journal of Environmental Studies*, 2001, **10** (4), 195
- [45] M. R. Hoffmann, S.T. Martin, W. Choi, *Chem. Rev.* 1995, **95**, 69
- [46] C. H. Wu, J.M. Chern, *Ind. Eng. Chem. Res.* 2006, **45**, 6450
- [47] K. R. Gopidas, M. Bohorquez and P. V. Kamat, *J. Phys. Chem.*, 1990, **94**, 6435
- [48] J. E. Evans, K. W. Springer and J. Z. Zhang, *J. Phys. Chem.*, 1994, **101**, 6222
- [49] M.C. Carotta *et al.*, *Sensors and Actuators B*, 2009, **137**, 164
- [50] D. Calestani, M. Z. Zha, R. Mosca, A. Zappettini, M. C. Carotta, V. Di Natale, and L. Zanotti, *Sensors and Actuators B*, 2010, **144**, 472
- [51] T. D. Dzhafarov, M. Altunbas, A. I. Kopya, V. Novruzovgif and E. Bacaksiz, *J. Phys. D: Appl. Phys.*, 1999, **32** (24), L125
- [52] T. Abe, Y. Kashiwaba, M. Baba, J. Imai, H. Sasaki, *Applied Surface Science*, 2001, **175-176**, 549
- [53] N. A. Zeenath, K.P. Varkey and K.P. Vijayakumar, *J. Phys.: Condens. Matter*, 1998, **10**, 2053
- [54] H. Kato, J. Sato, T. Abe, and Y. Kashiwaba, *phys. stat. sol. (c)* 2004, **1** (4), 653
- [55] P. J. Sebastian, *Applied Physics Letters*, 1993, **62** (23), 2956
- [56] F. Chernow, G. Eldridge, G. Ruse, and L. Wählin, *Appl. Phys. Lett.*, 1968, **12**, 339
- [57] G. Eldridge, F. Chernow, and G. Ruse, *J. Appl. Phys.*, 1973, **44**, 3858
- [58] H. M. Pathan and C.D. Lokhande, *Bull. Mater. Sci.*, 2004, **27** (2), 85
- [59] M. Willander, P. Klason, L.L. Yang, *phys. stat. sol. (c)*, 2008, **5** (9), 3076
- [60] Y. Tak, S. J. Hong, J. S. Lee, and K. Yong, *Crystal Growth & Design*, 2009, **9** (6), 2627
- [61] I. Gonzalez-Valls and M. Lira-Cantu, *Energy Environ. Sci.*, 2009, **2**, 19
- [62] Z. L. Wang, *J. Phys.: Condens. Matter*, 2004, **16**, R829
- [63] Y. Zhang, T. Xie, T. Jiang, X. Wei, S. Pang, X. Wang and D. Wang, *Nanotechnology*, 2009, **20**, 155707
- [64] A. Dev and S. Chaudhuri, *Nanotechnology*, 2007, **18**, 175607
- [65] M. Seol, H. Kim, Y. Tak and K. Yong, *Chem. Commun.*, 2010, **46**, 5521
- [66] J. Joo *et al.*, *Nanotechnology*, 2010, **21**, 325604

## 4.2 Iron oxides

Magnetic nanoparticles are of great interest for researchers from a wide range of disciplines and their wide applications range includes magnetic fluids [1–3], catalysis [4–12], biotechnology and biomedicine [13–19], magnetic resonance imaging and medical diagnostic [20–25], data storage [26–35] as well as environmental remediation [36–43]. In most of the above mentioned applications, the particles perform best when their size is below a critical value, related to the blocking temperature, which is dependent on the material, but is typically around 20 nm. Unfortunately, as already discussed in Chapter 2.2.1, such small particles tend to form aggregates to reduce the energy associated with the high surface to volume ratio of the nano-sized particles. For many applications it is thus crucial to develop protection strategies to chemically stabilize the naked magnetic nanoparticles against degradation during or after the synthesis. It is noteworthy that in many cases the protecting shells not only stabilize the nanoparticles, but can also be used to promote the adhesion of as-grown NP on the desirable substrate, for instance on ZnO TP.

The results presented in this chapter deal with the functionalization of ZnO TP with iron oxide (magnetite) NP, in order to extrinsically *add* magnetic properties to ZnO TP. This paves the way to future applications in energy harvesting (photocatalytic systems, water splitting) and sensing applications (both ZnO and iron oxides are used as MOX gas sensors).

In fact, a major issue in photocatalytic systems concerns with the removal of these catalysts by filtration: up to now, recycling and efficient re-use of supported NP catalysts remains a challenging issue. Along this line, magnetic separation of magnetic NP catalysts appears as a possible solution [44–47]. On the other side, in gas sensing applications, the main drawback associated with the use of MOX sensors is the poor selectivity. As discussed for CdS functionalization, coupling different materials can be an effective way to add selectivity, moreover the use of iron oxide nanoparticles, ensures the same thermally activated adsorption / desorption mechanisms of the surface oxygen-related species (*e.g.*  $O^-$ ,  $O^{2-}$  and  $OH^-$ ) observed in ZnO. As concerns solar hydrogen generation, nowadays, despite several decades of research, the only systems that allows a large scale hydrogen generation is the use of expensive photovoltaic cells to power water electrolysis. Direct photocatalytic water splitting is still a challenging problem albeit extensive efforts have been made to investigate iron oxide (hematite in particular) for hydrogen production [48–50]. Hematite is a promising material for inexpensive solar energy conversion via water splitting but has been limited by the large overpotential (0.5 ÷ 0.6 V) that must be applied to afford high water oxidation photocurrent. A wide adopted strategy to overcome this limitation is to couple it with a catalyst to increase the kinetics of the oxygen evolution reaction (AZO, ZnO,  $TiO_2$ ,  $Al_2O_3$ ) [51,52]. Moreover, ZnO nanostructures themselves (functionalized with

semiconductor QD) have been recently demonstrated to provide a stable photoelectrochemical platform for the photolysis of water [53–55]. With these possible applications in mind, the first part of this chapter is devoted to the synthesis of Fe<sub>3</sub>O<sub>4</sub> in both aqueous and organic environment, the second deals with Fe<sub>3</sub>O<sub>4</sub> functionalization of ZnO TP.

## 4.2.1 Synthesis of Fe<sub>3</sub>O<sub>4</sub> nanoparticles

Chemical methods for preparing magnetic iron oxide NPs are mainly divided into two routes: (1) thermal decomposition of iron organo–metallic compounds in a higher boiling point organic (often coordinating) solvent and (2) co–precipitation in aqueous solution using polymer or charged molecules as surfactants. The synthesis of magnetite NP in organic solvent are energy–intensive, employ toxic chemicals, and yield NPs in non–polar solutions [31]. Co–precipitation is a facile and convenient way to synthesize MNPs (metal oxides and ferrites) from aqueous salt solutions. This is typically performed by the addition of a base at room temperature (or relatively low temperature) in air (or inert atmosphere).

### 4.2.1a Synthesis by co–precipitation

The research on Fe<sub>3</sub>O<sub>4</sub> NP started from the work made by Hui and co–workers [56]: the authors reported a synthetic protocol for the large–scale production of hydrophilic Fe<sub>3</sub>O<sub>4</sub> NP using a Fe(II) precursor, citrate and sodium nitrate via a facile method. This approach is interesting because authors obtained magnetite NP through a controlled oxidation of Fe(II) precursor and not by the usual co–precipitation method.

A typical synthesis developed as follows: 1 mmol of citric salt (C<sub>6</sub>H<sub>5</sub>Na<sub>3</sub>O<sub>7</sub> · 2H<sub>2</sub>O), 4 mmol of NaOH, and 0.2 mol of NaNO<sub>3</sub> are mixed in 20 mL of deionized water. The mixture was then heated to 100 °C and 1 mL of 2 M FeSO<sub>4</sub>·4H<sub>2</sub>O (2 mmol) solution was added into the mixture rapidly (equivalent to 0.10 M Fe<sup>2+</sup> in the alkali solution), the mixed solution was kept at 90 °C for 30 min. The solution was finally cooled down to room temperature naturally. On the contrary to what is reported, the collected solid phase was brownish–red (an indication for the presence of maghemite). Shen *et al.* observed that this can be due to insufficient addition of the base [57].

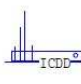
Basing on Hui work [56], the protocol for the synthesis was revised as follows (sample NPH): 10 mmol of citric salt (C<sub>6</sub>H<sub>5</sub>NaO<sub>7</sub> · 2H<sub>2</sub>O), 20 mmol of FeSO<sub>4</sub>, and 0.2 mol of NaNO<sub>3</sub> are mixed in 20 mL of deionized water, the solution is the heated to 100 °C and an excess of NaOH 10M (3 ml) is



quickly added to the beaker. The solution turned immediately black and the reaction is stopped after 10 minutes. Rinsing with deionized water follows to remove unreacted precursors and byproducts. The XRD spectrum is reported in Figure 4.2.1 and XRD reflection for both  $P4_132$   $\gamma$ - $\text{Fe}_2\text{O}_3$  (maghemite, JCPDS 39–1346) and  $F3dm$   $\text{Fe}_3\text{O}_4$  (magnetite, JCPDS 86–1362) are reported in Table 4.2.1. The spectrum has a mediocre signal-to-noise ratio, but it is reported as is, since it contains all informations to unambiguously identify the collected solid phase as magnetite (JCPDS 86–1362) or maghemite (JCPDS 39–1346) with space group  $P4_132$ . To distinguish between these two structures using XRD on nano-crystalline systems is quite a hard task (refer to Chapter 2.2.3 to delve into). If maghemite cation vacancies are completely disordered, then maghemite crystallize in a *fcc*  $F3dm$  and there is no way to distinguish it from magnetite, using structural analyses (e.g. XRD, TEM-ED). On the contrary, if some ( $P4_132$ ) – or complete ( $P4_12_12$ ) – vacancies order is present, (*theoretically*) there are small differences that may help to identify the maghemite phase instead of magnetite. For example, (110) and (111) reflections in maghemite are weak but comparable, while the (110) reflection is absent in magnetite due to symmetry restrictions (a *fcc* lattice presents only all odd or all even reflections), so that the presence of the (110) peak allow to qualitatively determine the presence of *ordered* maghemite. The estimation of the eventually concurred presence of magnetite is a more difficult task because most of the other intense peaks overlap and because of intrinsic FWHM broadening in nanostructures. On the contrary, it is reasonable to assume that since (110) and (111) peaks intensities are comparable, if no preferential orientation is observed *and* maghemite show some vacancy ordering, the absence of the (110) may indicate the presence of magnetite.

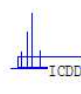
Since complete ordering of maghemite nanocrystals is unlikely, we assume that, if *partial* cation vacancy order is present, the structure is  $P4_132$ . However, it must be noted that the phenomenon of vacancy ordering in the lattice is not yet fully understood. It is not clear, for example, under which conditions, if any, vacancy disorder occurs. It has been suggested that the degree of ordering depends on crystal size, and that very small particles of maghemite do not show *complete* vacancy ordering ( $P4_12_12$ ) [58,59], although a *partial* order ( $P4_132$ ) was observed even in 5 nm particles [60] (refer to Ch. 2.2.3 for in-depth review).

39-1346		Wavelength= 1.54178						*		
Fe203	2 $\theta$	Int	h	k	l	2 $\theta$	Int	h	k	l
Iron Oxide	14.969	5	1	1	0	81.498	1	7	1	
	18.399	4	1	1	1	85.422	<1	[	7	2
	23.790	5	2	1	0	87.391	2	6	4	
Maghemite-C, syn	26.124	5	2	1	1	89.334	<1	[	7	3
Rad.: CuK $\alpha$ $\lambda$ : 1.54178 Filter: Graph Mono d-sp: Diff.	30.265	35	2	2	0	90.317	7	7	3	
Cut off: 15.0 Int.: Diffract. I/ICor.: 1.4	32.151	2	2	2	1	95.203	3	[	8	0
Ref: Schulz, D., McCarthy, G., North Dakota State University, Fargo, North Dakota, USA, ICDD Grant-in-Aid, (1987)	33.910	2	3	1	0					
	35.659	100	3	1	1					
	37.280	3	2	2	2					
	38.879	1	[	3	2	0]				
	40.410	1	[	3	2	1]				
Sys.: Cubic S.G.: P4 $_1$ 32 (213)	43.320	16	4	0	0					
a: 8.3515(22) b: c: A: C:	44.741	1	4	1	0					
$\alpha$ : $\beta$ : $\gamma$ : Z: 10.667 mp:	46.110	<1	[	3	3	0]				
Ref: Lindsley, D., Min. Soc. of America, Short Course Notes (Wash., D.C.), 3, L-18 (1976)	50.049	2	4	2	1					
	53.779	10	4	2	2					
	54.972	1	4	3	0					
Dx: 4.856 Dm: 4.900 SS/FOM: F $_{30}$ = 95(.0090 , 35)	56.154	1	[	5	1	0]				
$\epsilon\alpha$ : $\eta\omega\beta$ : 2.74 $\epsilon\gamma$ : Sign: 2V:	57.321	24	5	1	1					
Ref: Deer, W., Howie, R., Zussman, J., Rock Forming Minerals, 5, 73 (1961)	59.620	1	5	2	0					
	60.738	2	5	2	1					
	62.981	34	4	4	0					
	64.051	1	4	4	1					
	65.130	1	5	3	0					
	67.262	<1	[	4	4	2]				
Color: Light brown	68.314	1	[	6	1	0]				
Peak height intensity. Sample from Control Data as used in hard disks. Space group dependent upon preparation (Bernal et al.).	69.368	1	6	1	1					
Optical data on specimen from Iron Mountain, Shasta County, California, USA. Pattern reviewed by Syvinski, W., McCarthy, G., North Dakota State University, Fargo, North Dakota, USA, ICDD Grant-in-Aid (1990). Agrees well with experimental pattern.	71.441	3	6	2	0					
Additional weak reflections [indicated by brackets] were observed.	72.468	1	5	4	0					
$\sigma(I_{obs}) = \pm 0.067$ . Spinel group, spinel subgroup. Silicon used as an internal stand. Single-crystal data used. PSC: cP53.33.	74.540	5	5	3	3					
To replace 4-755 and 24-81. Mwt: 159.69. Volume[CD]: 582.50.	75.513	2	6	2	2					
	76.514	<1	[	6	3	0]				
	77.515	<1	[	6	3	1]				
	79.522	1	4	4	4					
	80.500	<1	[	6	3	2]				

 © 1999 JCPDS-International Centre for Diffraction Data. All rights reserved  
PCPDFWIN v. 2.02

86-1362		Wavelength= 1.54060					
Fe2.92904	2 $\theta$	Int	h	k	l		
Iron Oxide	18.285	105	1	1	1		
	30.077	292	2	2	0		
	35.427	999*	3	1	1		
Magnetite - from Nagatoro, Saitama Pref., Japan	37.058	74	2	2	2		
Rad.: CuK $\alpha$ $\lambda$ : 1.54060 Filter: d-sp: Calculated	43.055	208	4	0	0		
Cut off: 17.7 Int.: Calculated I/ICor.: 4.91	47.140	6	3	3	1		
Ref: Calculated from ICSD using POWD-12++, (1997)	53.412	84	4	2	2		
Ref: Okudera, H., Kihara, K., Matsumoto, T., Acta Crystallogr., Sec. B: Structural Science, 52, 450 (1996)	56.937	275	5	1	1		
	62.522	362	4	4	0		
	65.738	8	5	3	1		
	70.928	27	6	2	0		
Sys.: Cubic S.G.: Fd3m (227)	73.962	66	5	3	3		
a: 8.3969(5) b: c: A: C:	74.964	27	6	2	2		
$\alpha$ : $\beta$ : $\gamma$ : Z: 8 mp:	78.924	21	4	4	4		
Ref: Ibid.	81.859	4	7	1	1		
	86.706	27	6	4	2		
	89.601	96	7	3	1		
Dx: 5.107 Dm: ICSD # : 082456							

Peak height intensity. R-factor: 0.013. Al $_2$  Mg O $_4$  type. PSC: cF55.44. Mwt: 227.63. Volume[CD]: 592.05.

 © 1999 JCPDS-International Centre for Diffraction Data. All rights reserved  
PCPDFWIN v. 2.02

**Table 4.2.1** XRD reflections for maghemite (top, JCPDS 39-1346) and magnetite (bottom, JCPDS 86-1362)

Looking at the XRD spectrum reported in Figure 4.2.1, the (111) peak is clearly visible at 18.2° while the (110) is not observed, this means that magnetite *and / or* maghemite – without vacancy ordering – is present. However, the identification of the phase is not a crucial point in this work because both magnetite and maghemite (whether vacancy-ordered or not) show comparable magnetic response. The shape of the peaks reveal a high dimensional dispersion and Scherrer analysis on the main peak provides a 9.8 nm NP mean dimension.

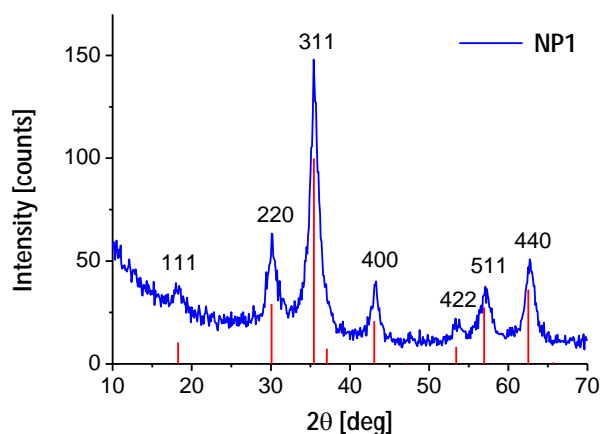
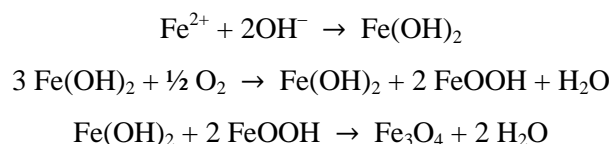


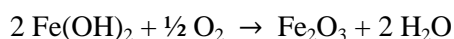
**Figure 4.2.1** XRD spectrum of sample NP1 synthesized via controlled oxidation of Fe(II) precursor.

To better understand the nucleation / growth process of Fe<sub>3</sub>O<sub>4</sub> NP in solution, Hui investigated the influence of experimental parameters that affect the size of Fe<sub>3</sub>O<sub>4</sub> NPs. These were found to be: (1) the reacting time; (2) the concentration of Fe<sup>2+</sup> ions, and (3) the amount of NaNO<sub>3</sub>. With respect to Hui synthesis, the one reported here was performed lowering the reaction time, increasing the Fe(II) concentration and the ionic strength of the solution (NaNO<sub>3</sub> concentration). All these parameters concur to lower the NP mean dimensions (20 nm in the Hui’s work). Increasing the concentration of NaOH helps to promote a quick nucleation and leads to the formation of magnetite instead of maghemite. The alkalization reaction of iron (II) ions to form iron hydroxide as intermediate to the formation of Fe<sub>3</sub>O<sub>4</sub> NP is reported [61,62]:



Thus, it is concluded that in the synthesis with iron (II) ions alone, Fe<sub>3</sub>O<sub>4</sub> is formed as a result of the dehydration reaction of iron (II) hydroxide and iron (III) oxhydroxide, in which the latter compound is produced by the partial oxidation of iron (II) hydroxide by molecular oxygen dissolved in water [56]. Adding an excess of NaOH moves the equilibrium to the (rapid) formation of hydroxide and then to magnetite.

If the NaOH results to be less than expected (i.e. for the presence of citric acid), maghemite formation can occur:



Although magnetite and maghemite are metastable structures (magnetite oxidizes to maghemite at RT and both form hematite at high temperature) with similar ferrimagnetic behavior and almost identical unit cell dimensions, their identification is possible, for example, through the investigation of optical properties. In fact, magnetite is a  $\text{Fe}^{2+}\text{-Fe}^{3+}$  mixed-valence metal, appears black and presents intervalence charge transfer (IVCT) transitions in the visible and near-IR region. Maghemite, by contrast, is a semiconductor with  $\sim 2$  eV optical absorption threshold and thus shows almost no absorption beyond  $\sim 650$  nm.

Tang *et al.* [63] reported UV-vis-NIR spectra of as-grown magnetite and oxidized maghemite NP (obtained through heat treatment in air of the as-grown NP). While magnetite NP absorbs light in the NIR region (800  $\div$  1200 nm), the absorption of oxidized NP (maghemite) decreases until almost no absorption is observed. The absorption spectrum reported in Figure 4.2.2A is in excellent agreement with Tang observation: magnetite (red line) absorption in the NIR region is observed, while maghemite (blue line) doesn't absorb in the NIR but present an absorption threshold around 650 nm. In Figure 4.2.2B is the reported a picture of maghemite (left) and magnetite (right).

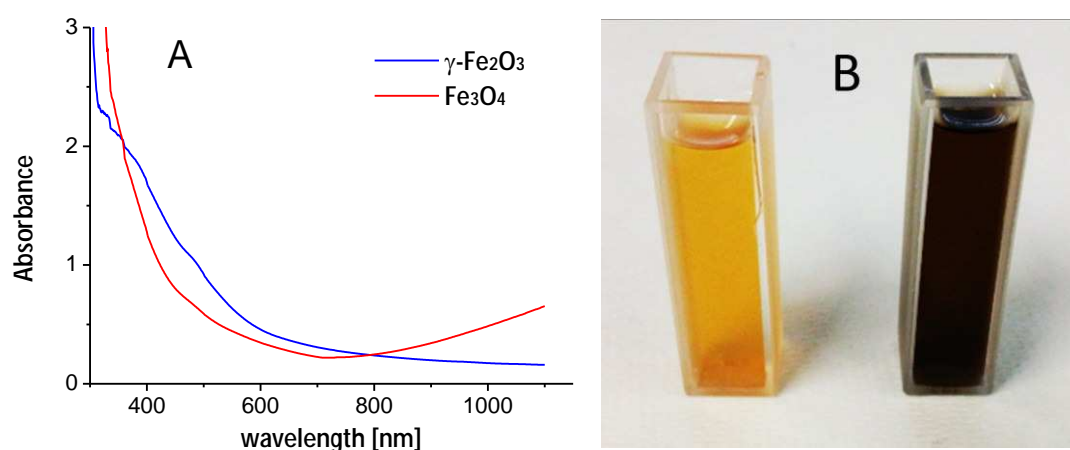
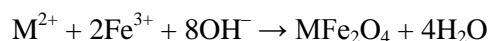


**Figure 4.2.2** (A) Absorption spectrum of both magnetite (red) and maghemite (blue) NP. (B) Picture of the samples measured in (A).

However, even if magnetite NP were finally obtained, it was not possible to reduce dimensional dispersion with this synthetic approach. Possibly the high ionic strength of the solution shields the charge of citric acid and the electrostatic stabilization of iron oxide NP is less effective.

Hence a different approach was used, and it is based on the more traditional co-precipitation method. According to literature, iron oxide nanoparticles (either Fe<sub>3</sub>O<sub>4</sub> or γ-Fe<sub>2</sub>O<sub>3</sub>), as well as ferrites, are usually prepared in an aqueous medium [64], and the chemical reaction of formation may be written as:



Where M can be Fe<sup>2+</sup>, Mn<sup>2+</sup>, Co<sup>2+</sup>, Cu<sup>2+</sup>, Mg<sup>2+</sup>, Zn<sup>2+</sup> and Ni<sup>2+</sup>. Complete precipitation should be expected at a pH level between 8 and 14, with a stoichiometric ratio of 2:1 (Fe<sup>3+</sup>/M<sup>2+</sup>). The proposed aqueous based synthesis of magnetite NP is a scalable and “green” strategy to produce Fe<sub>3</sub>O<sub>4</sub> NP on large scale, in ambient atmosphere and low temperatures, since it avoids the use of polluting / toxic solvents and metallorganic precursors. Moreover, the possibility to use ionic surfactants, or polymer with polar moieties (i.e. –OH, O), should in theory assure the *affinity* with the of ZnO nanostructures, whose surface will be later functionalized with. In Table 4.2.2 three syntheses are reported, these are performed under the same conditions, with the exception of the chosen surfactant. Synthetic parameters, XRD and magnetic measurement data are herein summarized (see text for discussion).

Sample NP1		Sample NP2		Sample NP3	
FeCl <sub>3</sub>	307 mg	FeCl <sub>3</sub>	307.5 mg	FeCl <sub>3</sub>	302 mg
FeSO <sub>4</sub>	152 mg	FeSO <sub>4</sub>	151.4 mg	FeSO <sub>4</sub>	152 mg
Citric acid	210 mg	PEG-400	500 μl	PVP-10000	206 mg
NaOH (10M)	1 mL	NaOH (10M)	1 mL	NaOH (10M)	1 mL
H <sub>2</sub> O	10 mL	H <sub>2</sub> O	10 mL	H <sub>2</sub> O	10 mL
Working Temp	RT	Working Temp	RT	Working Temp	RT
Reaction time	5 min	Reaction time	5 min	Reaction time	5 min
Mean diameter	5.4 nm	Mean diameter	7.5 nm	Mean diameter	7.3 nm
M <sub>s</sub> (at 1.7 T)	52±1.6		59±2		54±1.6
	[Am <sup>2</sup> /Kg]		[Am <sup>2</sup> /Kg]		[Am <sup>2</sup> /Kg]

**Table 4.2.2** Summary of magnetite NP produced via co-precipitation method.

As a general consideration, contrary to what was reported [65,66], it was not necessary to drive the reaction at high temperature (above 80 °C) to obtain crystalline Fe<sub>3</sub>O<sub>4</sub> NP. Looking at the XRD spectrum reported in Figure 4.2.3 (left), all three samples, regardless of the surfactant agent used, present Fd3m structure peaks (the positions of the calculated peaks according to JCPDS 86-1362 are reported out of scale in gray dotted lines) while no spurious phases are observed. Mean

dimensions, as calculated with Scherrer formula, are reported in Table 4.2.2. Opposite to what was noticed for the precipitation from iron (II) precursor only (NPH), the analysis of XRD peaks shape reveals a better dimensional control (almost gaussian peaks) and smaller diameter (larger FWHM). Samples synthesized with steric surfactants (PEG for the sample NP2 and PVP for NP3), despite of their different molecular weight, lead to NP with almost the same dimensions, and about 30% bigger compared to NP1, passivated with citric acid (Figure 4.2.3, right). Electrostatic stabilization seems to be more efficient in high dielectric medium, *i.e.* water, and chelating ligands are known to act as strong ligands thus create an extra energy barrier against the growth on NP.

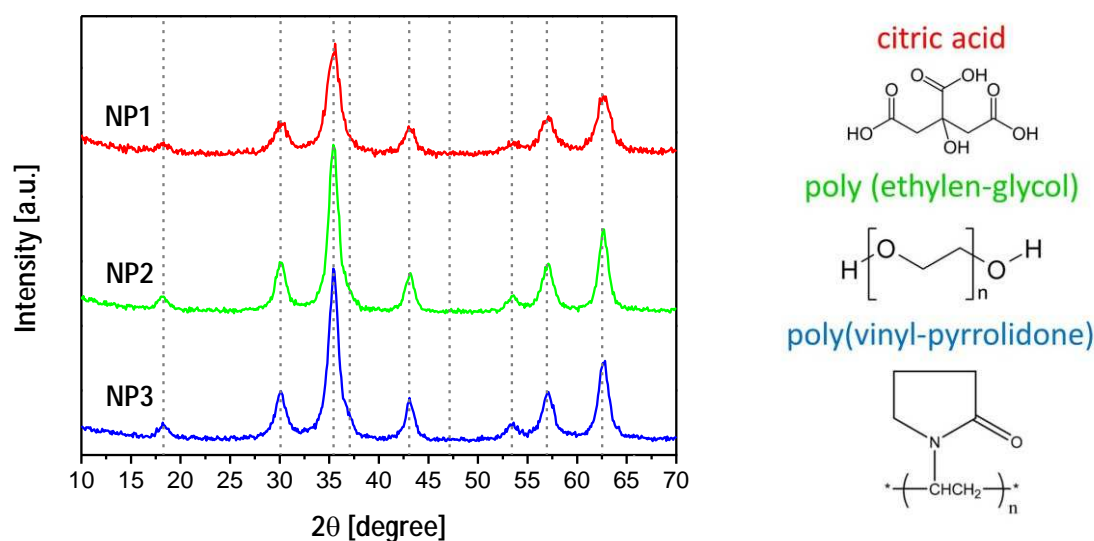


**Figure 4.2.3 Left:** XRD spectrum of magnetite NP obtained with the co-precipitation method, dotted gray vertical lines are the magnetite reflections according to JCPDS 86-1362.  
**Right:** Surfactants adopted for the synthesis: citric acid (NP1), PEG-400 (NP2) and PVP-10000 (NP3)

The magnetic properties of the  $\text{Fe}_3\text{O}_4$  NP were studied using a vibrating sample magnetometer (VSM) at room temperature. All the NP samples exhibited SPM properties with only slight differences in saturation magnetization, *i.e.* magnetic properties are absolutely comparable among the three samples.  $M(H)$  curves are reported in Figure 4.2.4. Saturation magnetization is in the order of  $50 \div 60 \text{ A m}^2 \text{ Kg}^{-1}$  (for an external applied field of 1.5 T) for all the three samples. It must be noted that these values are under-estimated since the weight used to rescale the magnetic momentum considers both the weight of magnetite NP and the weight of the surfactant. It is difficult to estimate the difference between the measured value and the *intrinsic* momentum of NP (per unity of mass), but the weight of capping agents is reasonably estimated in the order of a few percents. Thus the values are comparable to those reported in literature for SPM NP obtained with both co-precipitation [67,68] and hot injection method [69,70].

Moreover values are close to the magnetite bulk magnetization ( $84 \text{ A m}^2 \text{ Kg}^{-1}$ ) too: this is a fingerprint of the good crystalline quality of the prepared NP samples. More in detail, NP1 presents a saturation magnetization slightly lower than NP2 and NP3; this could be related to the lower NP dimensions: this can imply spin disorder at the surface and crystalline strains that are known to cause a decrease of the magnetization. The reduction of the particle size results in a large amount of magnetic atoms on the surface of the particle. These atoms have fewer nearest neighbors to which they can interact. Therefore, it is more likely that their magnetic moment becomes randomly oriented at the surface (spin-canting) and that higher applied fields are needed to align them parallel to it [71].

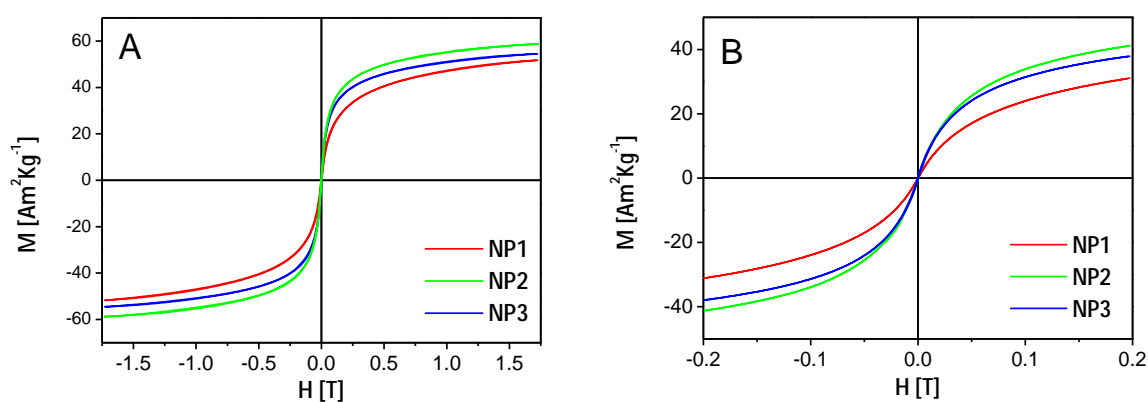


**Figure 4.2.4** (A)  $M(H)$  VSM measurement for samples synthesized via co-precipitation method. (B) is a low-field enlargement of (A).

In summary, magnetite NP with controlled dimensions (under 10 nm), good crystallinity and superparamagnetic behavior, are synthesized regardless of the surfactant utilized. The synthesis of water-dispersible NP paves the way to future applications in aqueous environments, such as photocatalysis and biomedical applications. In fact small superparamagnetic iron oxide NP encapsulated with PVP [14–17] and PEG [18,19] are known to be widely used in MRI as contrast agents and in drug delivery applications. The as-synthesized NP can be dispersed in isopropyl alcohol and used as *building blocks* to functionalize ZnO nanostructures, as described later, albeit surfactants with high molecular weight (PEG-400 and PVP-10000) are not the best choice for surface functionalization.

### 4.1.2b Synthesis in organic solvents

Among all the synthetic procedures reported in literature, the thermal decomposition of iron acetylacetonate,  $\text{Fe}(\text{acac})_3$ , in a high boiling point organic solvent (diphenyl ether), in the presence of reducing reagent (1,2-hexadecandiol) and co-surfactants (oleic acid and OA), was first demonstrated to be an effective way to synthesize monodisperse  $\text{Fe}_3\text{O}_4$  NP [69]. Further studies [72] showed that the thermal decomposition of iron-oleate complex can produce monodisperse  $\text{Fe}_3\text{O}_4$  NP on a relatively large scale (refer to Ch. 2.2.3b for further details). Although this thermal decomposition method has become the main synthetic approach to high quality  $\text{Fe}_3\text{O}_4$  NP, the mechanism leading to the chemical conversions to  $\text{Fe}_3\text{O}_4$  is complicated by the multi-component reactants present in the reaction mixture. To meet a demand beyond the laboratory-scale production, a more reliable and simplified synthetic technique to  $\text{Fe}_3\text{O}_4$  NP, with a better stoichiometric control, is still desired. Successive studies by Sun and co-workers [73] show that the presence of excess amount of OA (and oleic acid as co-surfactant) is the key to provide a proper reductive environment for the thermal decomposition of  $\text{Fe}(\text{acac})_3$  and synthesis of FeO nanoparticles. Authors indicate that OA acts as an alternative reducing agent, which is inexpensive and even stronger than the 1,2-hexadecandiol that was used previously in the  $\text{Fe}_3\text{O}_4$  NP synthesis [69].

Since iron (III) acetylacetonate is not soluble in OA at RT, in a typical synthesis, OA is chosen as reaction media but the iron precursor is dissolved in a small amount of diphenyl ether and quickly added to the reaction flask when OA reached the working temperature. More in details, 15 mL of oleylamine were heated at 280 °C under nitrogen atmosphere. 700 mg of  $\text{Fe}(\text{acac})_3$ , dissolved in 15 ml diphenyl ether were quickly added to OA and the solution turned immediately black. The mixture was kept refluxing at this temperature for 1 h then allowed to cool down to room temperature. The  $\text{Fe}_3\text{O}_4$  NP were extracted upon the addition of 50 mL of ethanol, followed by centrifuging. Collected NP can be later dispersed in non-polar solvents, such as hexane or toluene, resulting in liquid suspensions stable for months (sample NP4).

The XRD study on the as-synthesized NP reveals the presence of  $\text{Fe}_3\text{O}_4$  (Figure 4.2.5). Relative peaks intensity follows the spectrum reported in the ICDD database (JCPDS 86-1362) and show excellent agreement with it, *i.e.* even the very weak (222) reflection is visible, at 37°. Peaks shape, on the other hand, shows an almost lorentzian trend: Scherrer analysis on different peaks estimate mean dimensions varying from 6 to 18 nm. Beside the polydispersity, the *mean* diameter is in agreement with similar synthesis reported in literature [74].



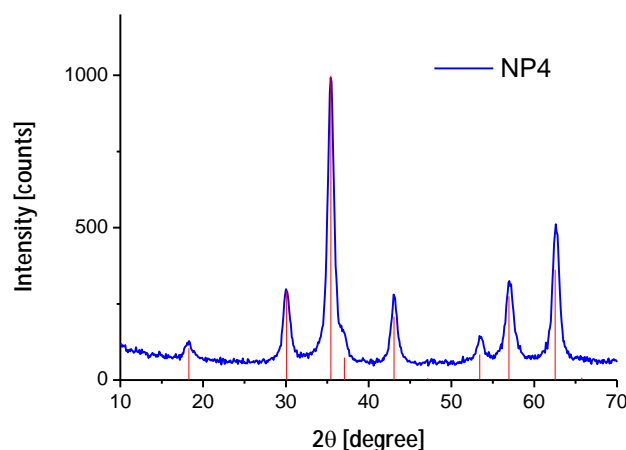


**Figure 4.2.5** XRD pattern of NP4 synthesized through the hot injection method. NP show good crystallinity. Red lines refer to magnetite simulated spectrum according to JCPDS 86–1362.

What is currently observed is in agreement to what Xu and co-workers reported [74]. The higher is the ratio between oleylamine and diphenyl ether, the smaller the  $\text{Fe}_3\text{O}_4$  NP are. For example, 7 nm  $\text{Fe}_3\text{O}_4$  NP were obtained when only OA was used. NP with dimensions of 8 and 10 nm were produced with the volume ratio of OA to diphenyl ether of 2:1 and 3:2, respectively. If the volume ratio of OA to benzyl ether was less than 1:1, bigger  $\text{Fe}_3\text{O}_4$  NP, with a broad size distribution were produced. This is probably due to the insufficiency of capping during the particle growth.

Figure 4.2.6 shows TEM images of representative  $\text{Fe}_3\text{O}_4$  nanoparticles. According to STEM images (A and B) NP look aggregated and the dimensional control is not very good. It is hard to say if NP aggregate because of solvent evaporation or during the synthesis. HREM analysis (C) reveals facet NP with irregular shape and dimensions in excess of 10 nm. Electronic diffraction pattern is reported in (D): the sharp diffraction spots reveal a good degree of crystallinity, in fact the (111) peak of the magnetite is clearly visible ( $d = 4.85 \text{ \AA}$ ) while no reflections are present at higher atomic distance, *i.e.* the (110) peak of partially-ordered maghemite at  $5.92 \text{ \AA}$ . The indexing of the intensity radial distribution is showed in (E) and it is consistent with the XRD pattern reported in Figure 4.2.5. It is worth repeating that is not possible to distinguish between  $\text{Fe}_3\text{O}_4$  and F3dm  $\gamma\text{-Fe}_2\text{O}_3$  (maghemite without cation vacancy ordering), since they share the same cell parameters. A simple but effective aid for phase identification is given by a visual analysis: but the black color of the obtained NP (even in hexane suspension) indicates magnetite as dominant phase. VSM measurement (Figure 4.2.7) reports a SPM behavior at RT and the saturation magnetization is  $57 \pm 1.6 \text{ Am}^2/\text{Kg}$ .

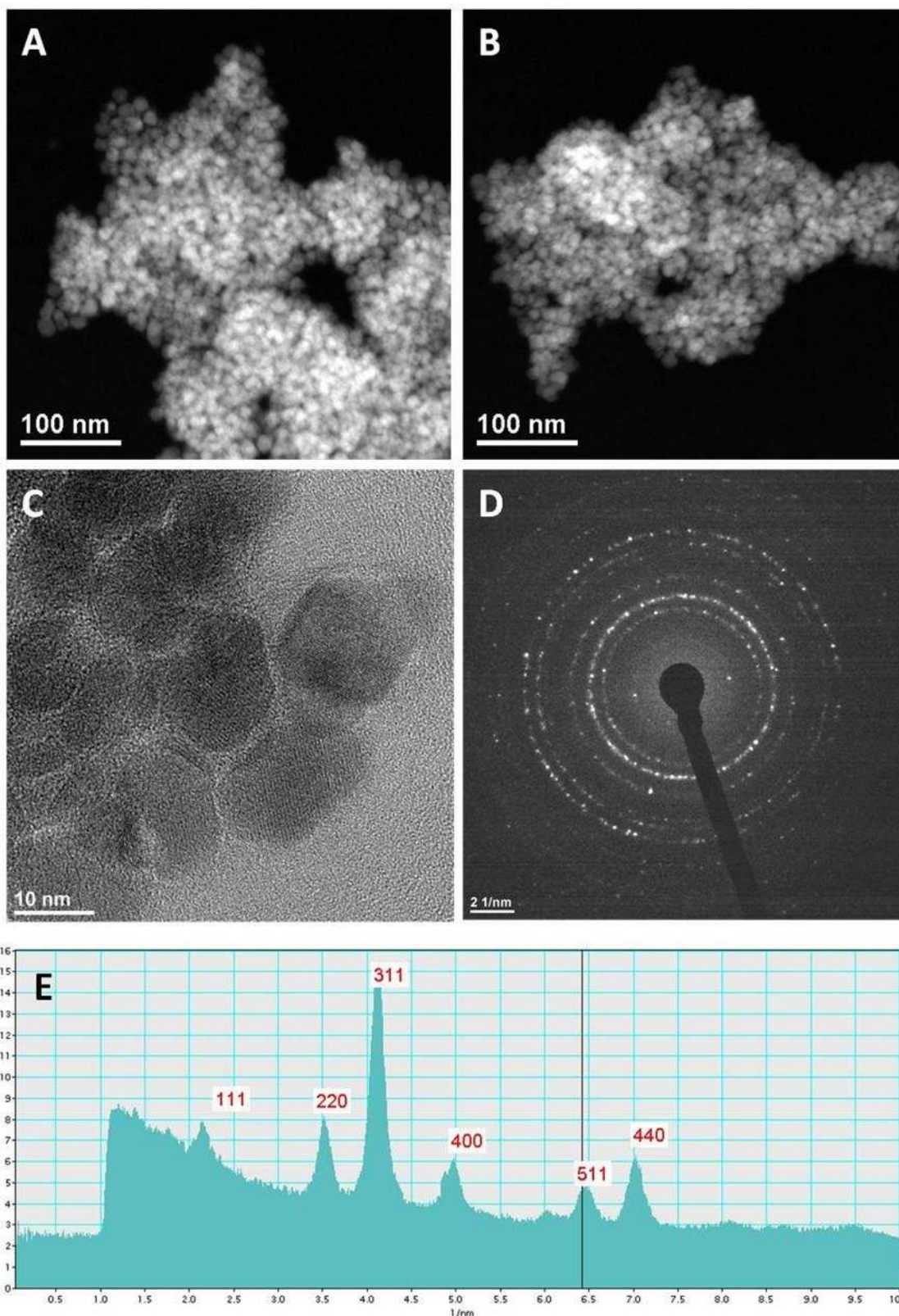


**Figure 4.2.6** TEM analysis on the sample NP4. (A) and (B) are low magnification STEM images. (C) and (D) are HREM images. The inset in (D) is the FT. (E) is the angular integration of (D).

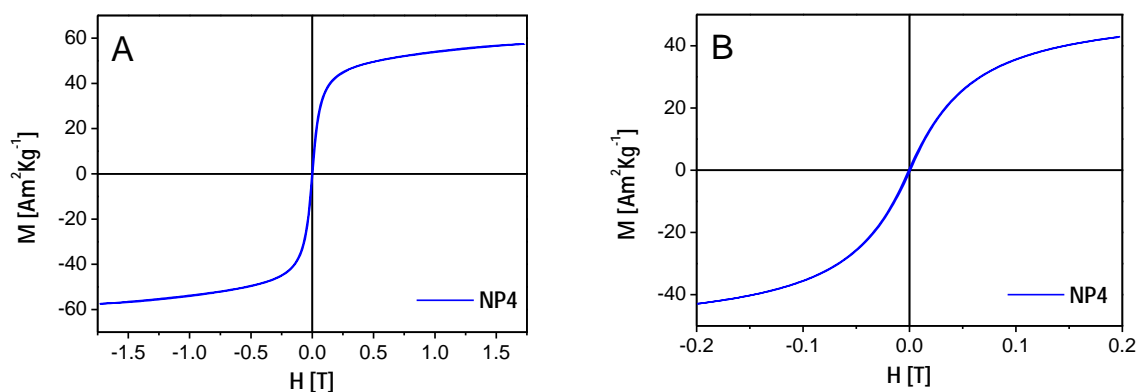


**Figure 4.2.7** VSM measurement on the sample NP4. SPM behavior is observed. **(B)** is a low-field enlargement of **(A)**.

In order to obtain NP with more controlled shape and dimensions, OA was chosen as both solvent and ligand. OA has a higher boiling point with respect to benzyl ether (350 °C) but is not able to dissolve  $\text{Fe}(\text{acac})_3$  at room temperature. The chosen synthetic route follows the so called *heating-up* method albeit without the need to use a multistep reaction and separately synthesize the metal-oleate complex (refer to Ch. 2.2.3b for an introduction to *heating-up*).

Iron (III) precursor and solvent quantity are kept the same with respect to the synthesis performed via *hot-injection* (NP4). Sample NP5 was prepared as follows: 700 mg of  $\text{Fe}(\text{acac})_3$  are mixed together with 15 ml oleylamine at RT, under nitrogen inert gas flux. The reaction flask is rapidly heated at 350 °C and kept at this temperature (refluxing OA) for 1 hour, then cooled down spontaneously. The particles are washed in isopropyl alcohol and re-dispersed in hexane. The black suspension results completely stable for over 6 months.

XRD was used to record the crystal information of  $\text{Fe}_3\text{O}_4$  NP: the spectrum is reported in Figure 4.2.8. Interestingly, comparing the aforementioned synthesis protocol (using OA), with the one reported by Sun and co-workers (using OA and oleic acid) [73], results in an unexpected observation. Sun reported the formation of wüstite ( $\text{FeO}$ ) NP and addressed the observed reduction of iron (III) precursor, to the use of OA. On the contrary, the actual synthesis – which is identical to the one reported by Sun, but oleic acid was not used this time – lead to the formation of magnetite NP. The evidence is that oleic acid – rather than OA – plays a major role in the *reduction* of  $\text{Fe}(\text{acac})_3$ . Incidentally, no  $\alpha$ -Fe is observed (*i.e.*  $\alpha$ -Fe may result from the possible wüstite disproportionation to magnetite). The pattern presents all the magnetite reflections and the relative intensity of the peaks are in excellent agreement with the data reported in the ICDD database (JCPDS 86-1362). Moreover this time the peak shape is noticeably more Gaussian and FWHM is larger than NP synthesized via hot injection (NP4), this reflect a better dimensional control and NP with smaller diameter. Scherrer analysis reports 7.5 nm mean dimensions.

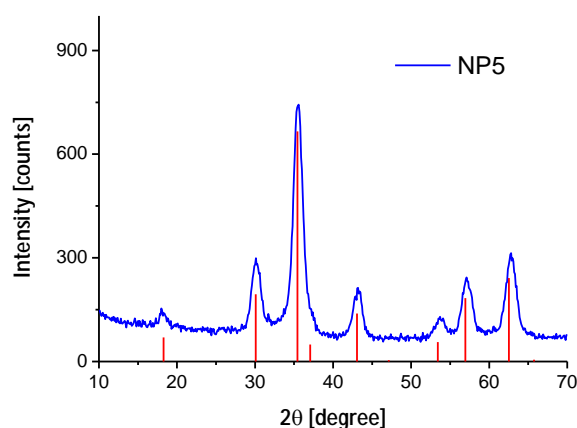


**Figure 4.2.8** XRD pattern of NP5, prepared via *heating-up* method. Red lines refer to magnetite spectrum according to JCPDS 86-1362

The good dimensional control achieved via *heating-up* method is testified by TEM analysis reported in Figure 4.2.9. Low magnification STEM images (A and B) reveal little “aggregates” of small NP (about 10 nm) randomly dispersed on the TEM copper grid. These “aggregates” are due to the interactions between the OA hydrophobic tails that interdigit themselves and provide some 2D order to the NP on the copper grid. High magnification STEM images (C and D) confirm the hypothesis on the role of OA.  $\text{Fe}_3\text{O}_4$  NP are not in contact each other, but look separate: it is clearly visible a dark spacing between different particles (caused by OA surface passivation), *i.e.* OA looks black with respect to iron in the Z-contrast image.

Moreover, OA seems to play a role into determining NP shape: this is not surprising since many research groups worldwide addressed the shape control of different nanostructures to the influence of this surfactant. Literature studies on OA-capped synthesized nanocrystals is huge: materials range from semiconductors (CdS [75],  $\text{Bi}_2\text{S}_3$  [76]), metals (iron [77], cobalt [78]), intermetallic alloys (FePt [79–81]) to oxides (magnetite [82],  $\text{MnFe}_2\text{O}_4$  [83],  $\text{CoFe}_2\text{O}_4$  [84]), and more. According to STEM images reported in (C) and (D), the observed NP shapes vary from round particles to truncated octahedrons. This is not surprising, since it is reported that the growth of faces lateral can be slowed down by the addition of a ligand. In fact, it is known that oleate-Fe(III) complexes (derived from either OA or oleic acid) lead to the formation of facet nanocrystals, cubes [85] and octahedrons [86] in particular. Moreover, one should consider that according to Wulff’s theorem, the equilibrium shape of a *fcc* single crystal is indeed a truncated octahedron.

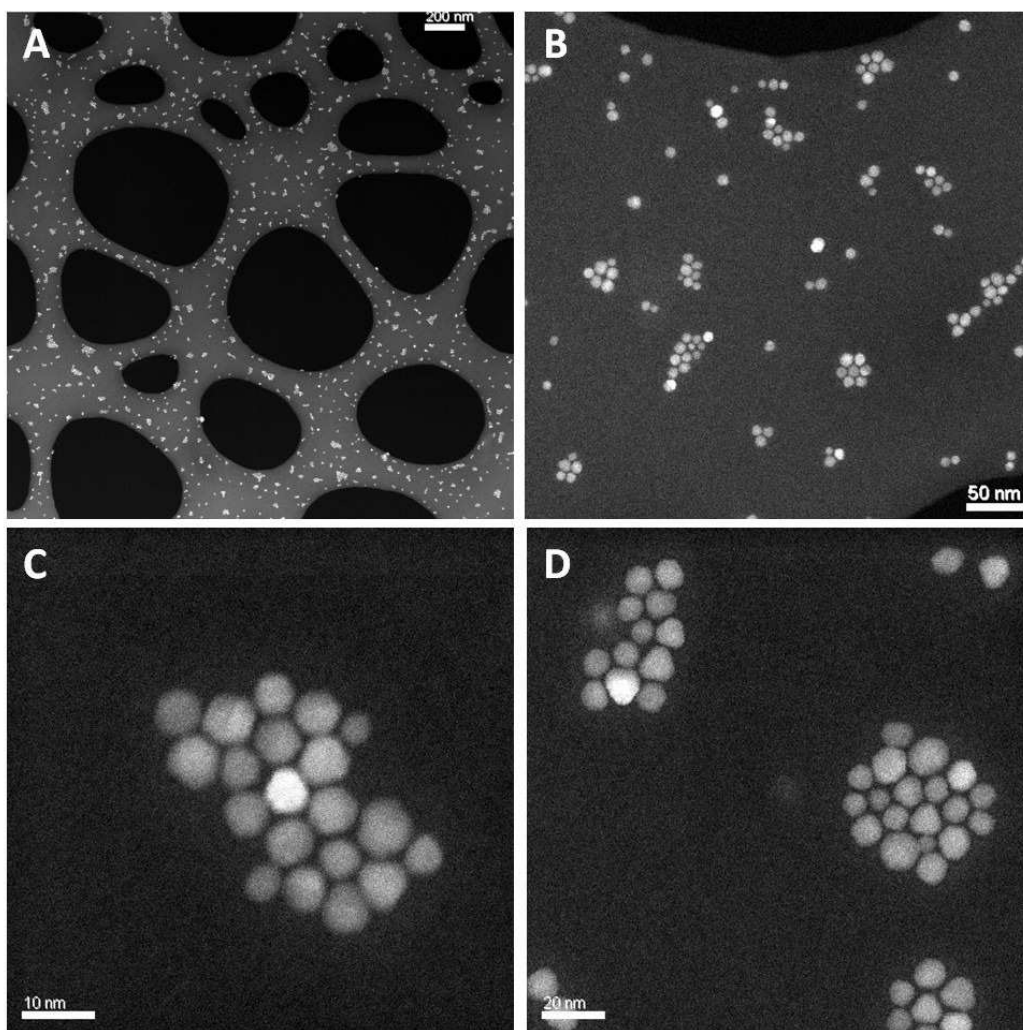


**Figure 4.2.9** STEM analysis on the sample obtained by heating-up method (NP5). Single nanoparticles “aggregate” because of hydrophobic OA interactions.

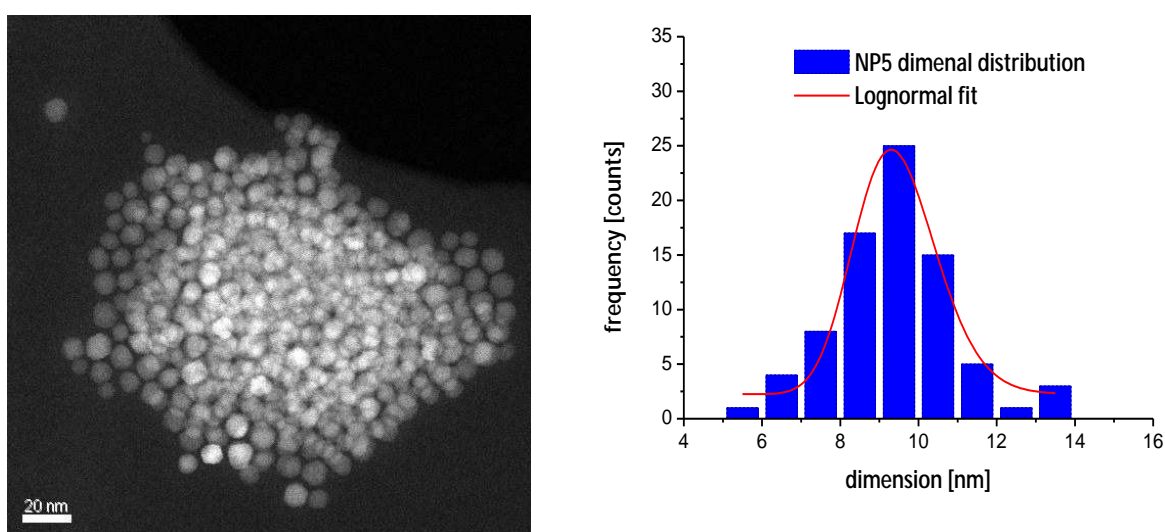


**Figure 4.2.10** STEM image of magnetite NP (left) and the statistic on NP dimensions (right).

Compared to STEM observation, Scherrer analysis seems to underestimate the NP mean dimensions. Mean NP diameter obtained by the statistic on NP5 dimensional distribution is calculated to be  $9.4 \pm 1$  nm (Figure 4.2.10). However, considering the relatively low number of particles used to perform the statistical analysis and the intrinsic error in Scherrer calculation, the two results are not conflicting. Taking advantage of the big aggregate, electronic diffraction was performed on the sample and is reported, together with the angular integration, in Figure 4.2.11. Once again, magnetite *a/o* maghemite without vacancy ordering (F3dm) is the only phase observed. Rigidly speaking, the small ripples between  $2.5$  and  $3 \text{ nm}^{-1}$  can be possibly due to maghemite  $P4_132$  (210) and (211) reflections, however relative intensities are so small that we can assume  $P4_132$  maghemite contribution almost unimportant. In addition, considering the black color of the hexane suspension, the F3dm maghemite phase, if present, is negligible. Of course other techniques (i.e. Mössbauer or Raman spectroscopy) will definitely help the (quantitative) identification of the magnetic phase but, to the aim of this thesis, to distinguish between magnetite and maghemite is almost unimportant, since both phases have similar magnetic behavior.

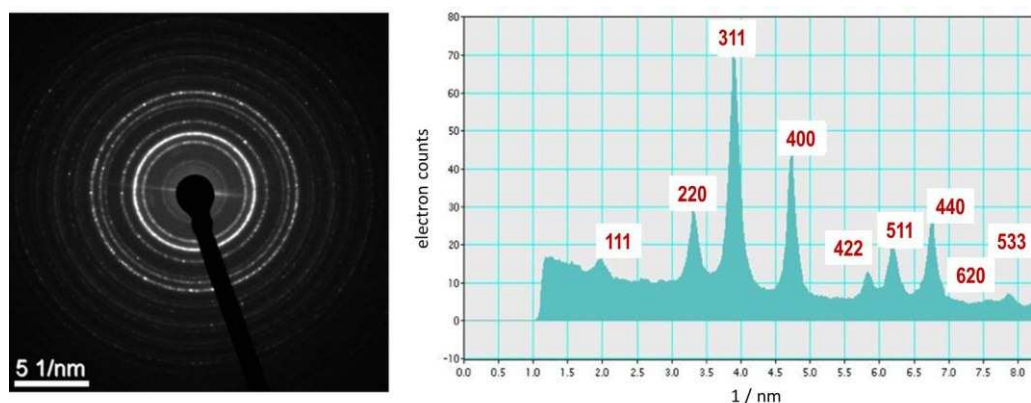


**Figure 4.2.11** ED of NP5 (left) and angular integration (right) showing magnetite peaks indexed according to JCPDS 86–1362.

Finally magnetic measurements (VSM) were performed on the sample NP5, these are reported in Figure 4.2.12. The NP set behaves like a superparamagnet at room temperature and the saturation magnetic moment reaches  $53 \pm 1.6 \text{ A m}^2/\text{Kg}$ . While the synthesis with either OA and benzyl ether (NP4) led to the formation of bigger NP with irregular shape that aggregate (maybe sinterize during the synthesis), the use of OA, as both ligand and surfactant, brings to rather monodispersed NP with smaller overall diameter. Morphological differences do not translate in different magnetic properties: curve shape, saturation magnetization and behavior with small applied field, are very close for both samples.

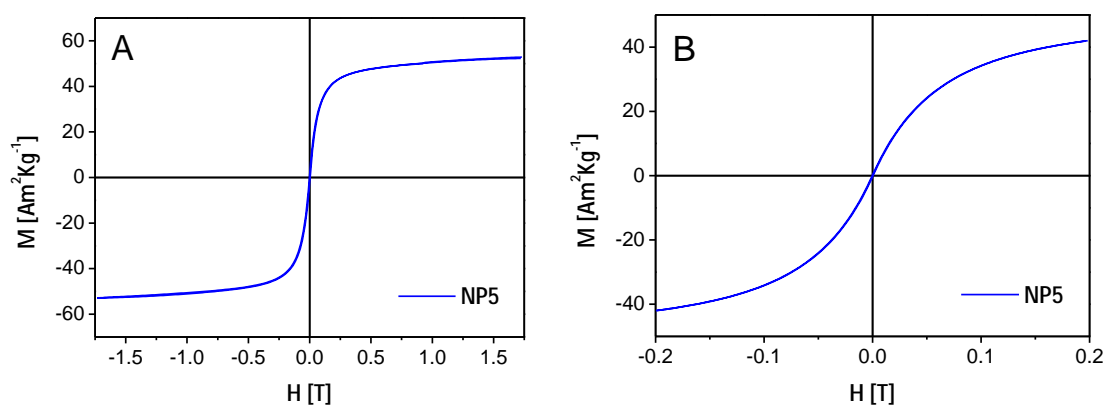


**Figure 4.2.12** Hysteresis loop of NP5 showing a SPM behavior. **(B)** is a low field magnification of **(A)**.

In summary, magnetite NP have been synthesized in both aqueous (via partial oxidation of Fe(II) precursor and co-precipitation of Fe(II) and Fe(III) salts) and organic environment (via *hot-injection* and *heating-up* methods). Despite of the different synthetic approaches, the NP dimensions and magnetic properties are comparable among all samples prepared, as shown in Figure 4.2.13. Saturation magnetizations are comparable with the best reported in literature [56,64,87,88], and about 30% lower than the value of bulk magnetite (it is worth noting that surfactant weight is not subtracted).

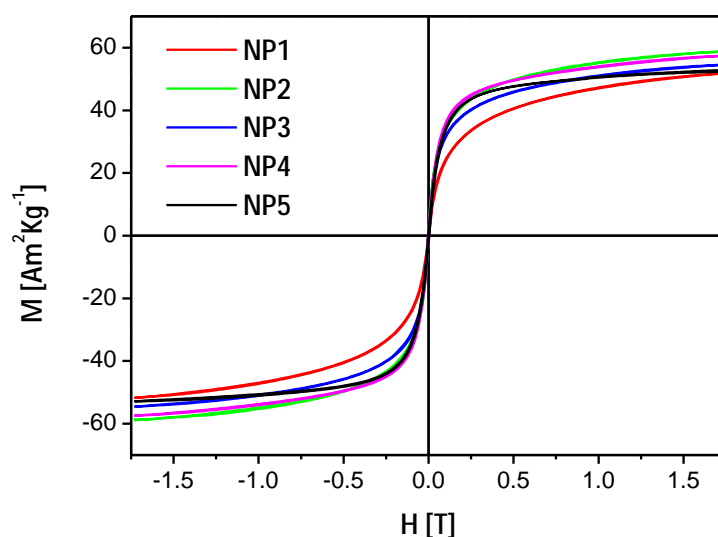


**Figure 4.2.13** Resuming  $M(H)$  graph for all different NP synthesized. Interestingly, magnetic behavior is almost comparable among all measured samples.

## 4.2.2 Fe<sub>3</sub>O<sub>4</sub> functionalization of ZnO tetrapods

ZnO is a unique material that exhibits semiconducting, piezoelectric, and pyroelectric multiple properties. Conductivity can be tuned from metallic to insulating (including *n*-type and *p*-type conductivity), it is highly transparent and possesses magneto-optic and chemical-sensing characteristics. It can be grown in many different nanoscale forms, thus allowing various novel devices to be achieved. Unfortunately undoped ZnO is not ferromagnetic.

One approach to produce ferromagnetic semiconductors is to introduce small amounts of magnetic ions (Mn, Co, Ni, or Fe) into non-magnetic semiconductors creating diluted magnetic semiconductors (DMS). ZnO-based DMS have attracted a great deal of research attention and controversy over the past decade. DMS are mainly used as building blocks for spintronic devices such as spin valves, spin transistors, spin light-emitting diodes, non-volatile memory, and ultra-fast optical switches. Besides ZnO, a significant amount of research efforts have been focused on discovering different materials suitable for these applications [89].

Although there are many papers reporting DMS and related applications, our main goal is different. The basic idea is to *add* magnetism to ZnO nanostructures, keeping as many ZnO intrinsic properties as possible. The way to go is the functionalization of ZnO surface, by coupling it with iron oxide NP. There is no need to deposit NP *in situ* (as previously described for the core-shell structure made by CdS on ZnO): surfactants or ligands trapped at the interface are not a significant issue (oppositely to the case of CdS for photovoltaic applications). On the contrary, it is important to keep the fraction of ZnO *free* surface, as high as possible. This turns out particularly interesting, for example, in (photo)catalytic systems, where the added magnetism allows to separate the catalyst by the application of an external magnetic field. Besides catalysis, the multifunctional nanostructure could be used as gas-sensor: a large number of studies have been focused on iron oxides, which, especially in the maghemite phase, exhibits good sensing characteristics towards hydrocarbon gases, carbon monoxide and alcohol [90–96]. Finally, the possibility to drive the ZnO nanostructures by the application of an external magnetic field paves the way to nanomedical applications as described later on.

This chapter presents a simple and reproducible procedure to functionalize ZnO nanostructures with iron oxide nanoparticles through a controlled annealing in inert atmosphere. Since ZnO and magnetite / maghemite are both oxides, they have a similar surface chemistry and a heat treatment can be an effective way to stick NP on ZnO surface. Obviously, performing an annealing on a partially oxidized nanomaterials (Fe<sub>3</sub>O<sub>4</sub> NP) in a close contact to an oxide (ZnO) is not a simple task since the ZnO surface is known to be covered with physisorbed reactive oxygen species (–OH, O<sup>2–</sup>, O<sup>–</sup>). Different preliminary annealing conditions have been explored in order to avoid (or control) oxidation, to obtain Fe<sub>3</sub>O<sub>4</sub> (or  $\gamma$ -Fe<sub>2</sub>O<sub>3</sub>) magnetic nanoparticles. Moreover the dispersion



of magnetic NP inside the TP “film” has been studied. This is a crucial point since ideally no significant aggregation between NP should occur, so that *single* SPM NP are scattered on the ZnO TP, leaving the most part of ZnO surface free, to be used for example as sensor, catalyst or UV emitter. Thus it is crucial to study the molar ratio ZnO / Fe<sub>3</sub>O<sub>4</sub> and the possible influence of surfactants in the sticking of magnetic NP on ZnO TP. We focused on the production of magnetite NP as described in the previous section (samples NP1, NP2, NP3) and three different passivating agents have been tested: citric acid, PVP and PEG (see Table 4.2.3 for a summary of the synthesis conditions). Part of the three as-prepared NP batch were mixed in 1:10 weight ratio together with ZnO TP in IPA solution. The mixture was stirred and sonicated alternatively for 1 hour to homogeneously disperse iron oxide NP in the liquid phase. An aliquot of each sample is collected and dried under vacuum (rotative pump) at 60 °C. The dispersion of NP1, NP2 and NP3 together with ZnO TP are herein referred as samples TPM1, TPM2 and TPM3 respectively. An annealing under N<sub>2</sub> inert gas is then performed to promote the sticking of iron oxide NP on ZnO TP: samples are placed inside a tubular furnace at 500 °C, kept inside for 10 minutes and then quenched to RT.

	Sample TPM1	Sample TPM2	Sample TPM3
NP sample	NP1	NP2	NP3
Capping agent	Citric acid	PEG-400	PVP-10000
Mean diameter	5.4 nm	7.5 nm	7.3 nm
Fe <sub>3</sub> O <sub>4</sub> / ZnO (w/w)	1:10	1:10	1:10
Annealing details:			
- Temperature	500 °C	500 °C	500 °C
- Holding time	10 min	10 min	10 min
Mean diameter after annealing	24 nm	16 nm	23 nm

**Table 4.2.3** Summary of coupled compounds magnetite NP – ZnO TP.

XRD analyses were performed (Figure 4.2.14) to study crystallographic structure and dimensions of the annealed samples. The inert atmosphere worked effectively preventing NP from oxidation (no  $\alpha$ -Fe<sub>2</sub>O<sub>3</sub> hematite peaks were found). Reflection marked with star (\*) belongs to wurtzite ZnO (JCPDS 80-0075) and grey vertical dotted lines belongs to magnetite (JCPDS 86-1362) and are reported for clarity. According to Figure 4.2.14, TPM2 and TPM3 spectra are nearly identical, the relative intensity of the main magnetite peak (111) at 35.4° is far less intense than that belonging to ZnO wurtzite main peak (101) at 36.2°. This is reasonable because small NP have FWHM larger than ZnO microcrystalline TP and only a fraction of iron oxide NP is expected to be attached on ZnO surface. TPM1 on the other hand present a slightly different spectrum. The magnetite (111) reflection is higher than ZnO (002) and comparable with (101): this means that there are more NP

per unit of ZnO TP. The reason of this maybe lies in the chosen surfactant: both PEG (used for NP2 sample) and PVP (used for NP3) are steric surfactants with relatively high molecular weight with respect to citric acid (NP1). Since the mass of NP and surfactant is constant along the three samples, NP2 and NP3 contain less iron per unit of mass. Secondly, citric acid is known to be a chelating agent and could bind the ZnO TP surface, promoting a more efficient sticking of magnetite NP on TP.

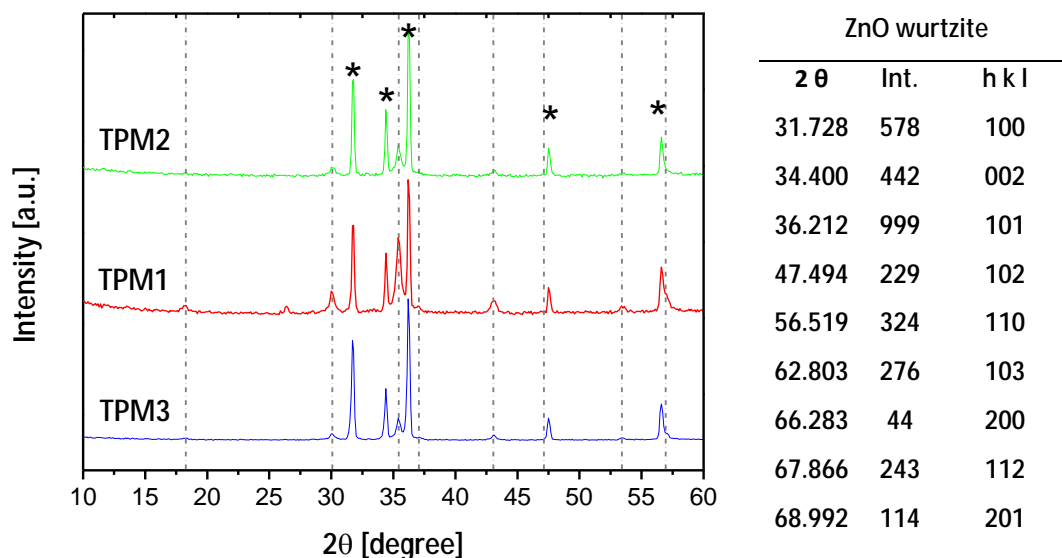


**Figure 4.2.14** XRD samples of coupled nanostructures magnetite NP on ZnO TP. ZnO wurtzite reflections are marked with a star and reported in the table on the left (according to JCPDS 80–0075).

Figure 4.2.15 reports a compared XRD analyses between as-grown and annealed NP for the sample NP1 and TPM1. Samples NP2–TPM2, NP3–TPM3 showed a comparable behavior and are omitted. NP dimensions are significantly increased by the thermal annealing (cfr. Table 4.2.3). It is necessary to decrease the number of NP per ZnO unit to avoid the coalescence / sinterization process and reducing heating time could help too. FE–SEM analysis was performed to study the morphology of the coupled compound and verify the eventual sticking of NP on ZnO TP surface (Figure 4.2.16). Citric acid (TPM1) seemed to perform better than PEG (TPM2) and PVP (TPM3): the observed roughness on TP legs is due to magnetite NP aggregates. On the contrary, TPM2 and TPM3 show only a minor fraction of NP stuck on TP legs and a uniform layer covering the TP legs: this is supposed to be caused by the polymer (partial) decomposition that takes place during the thermal annealing.

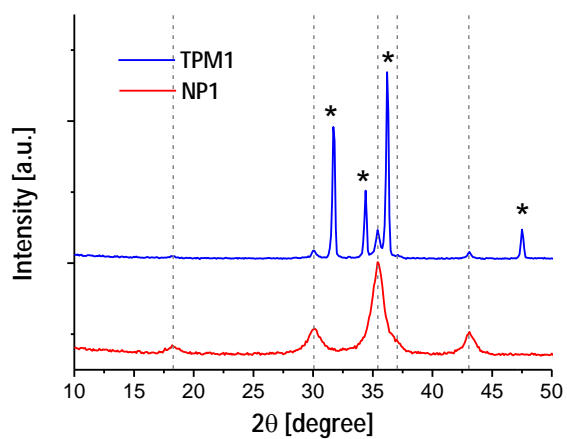


**Figure 4.2.15** XRD spectrum of as-grown NP (NP1, red line) and the corresponding magnetite – ZnO TP coupled compound after the thermal annealing (TPM1, blue line).

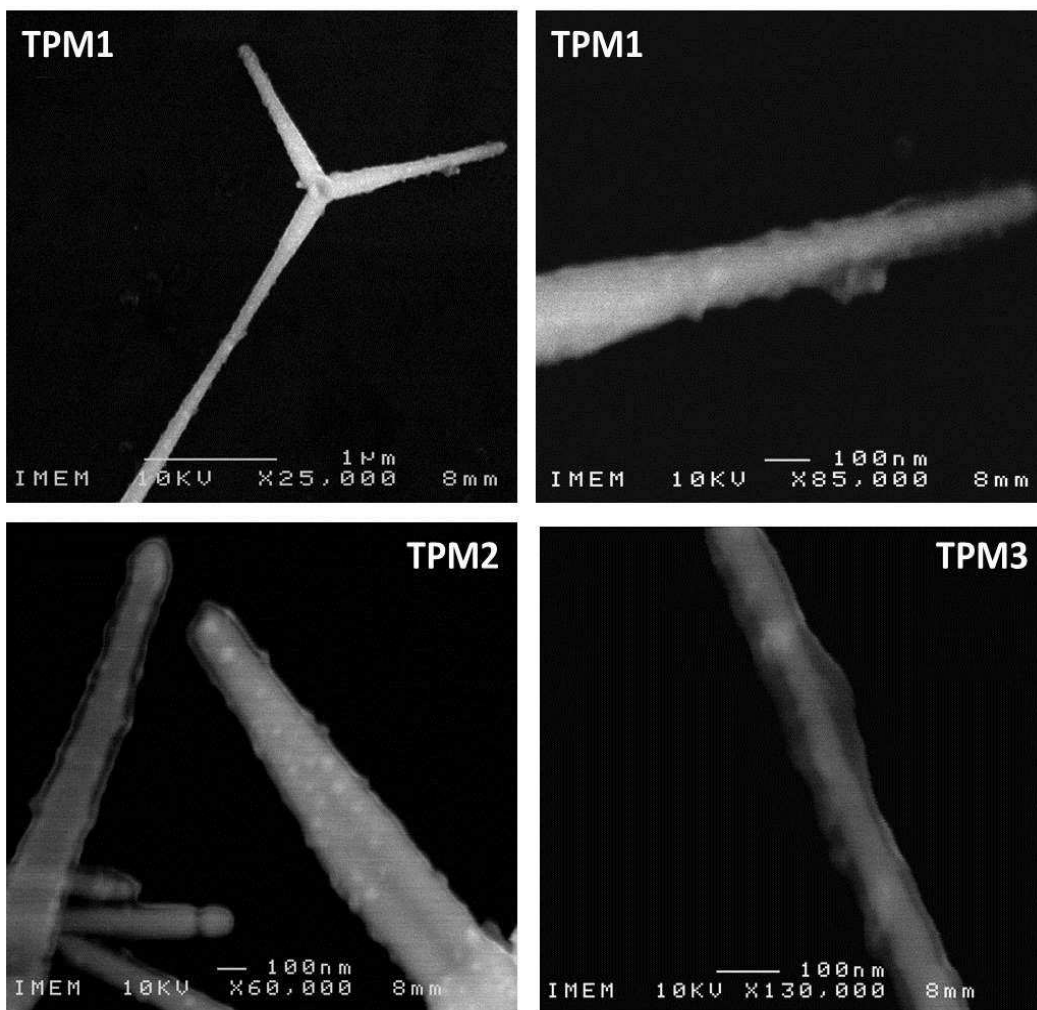


**Figure 4.2.16** FE-SEM analysis of coupled compound magnetite / ZnO TP. Refer text for discussion.

TEM investigation on the sample TPM1 confirms the presence of NP aggregates randomly distributed on TP legs (Figure 4.2.17A). The EDX map in (B) confirms the presence of iron (green) around the ZnO TP leg (blue). Thermal annealing does not completely eliminate the organic shell surrounding NP, leaving an amorphous layer surrounding TP legs as evidenced by HREM images in (C) and (D). Even if the residual contamination of citric acid resulted in a thinner shell compared to PEG or PVP, one of the surfactant used leaved the ZnO TP surface free of traces.

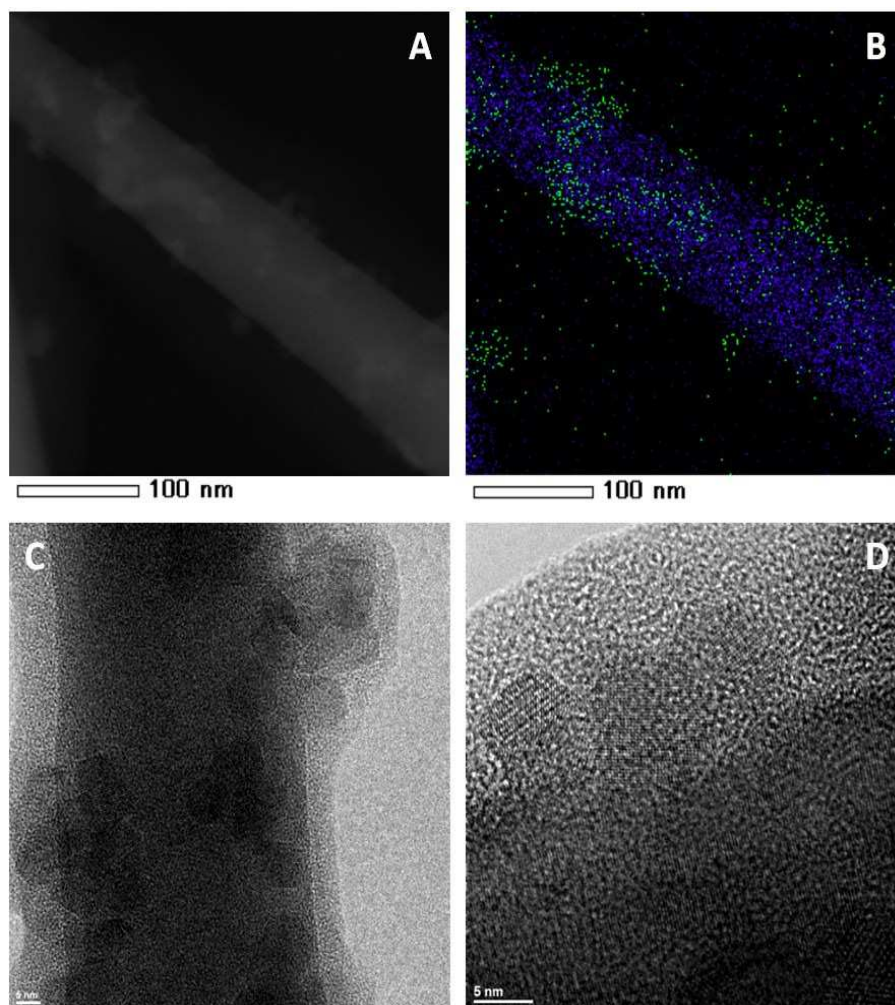


**Figure 4.2.17** TEM analysis on sample TPM1. (A) STEM image of aggregate NP on TP leg, (B) EDX of iron distribution (green) on ZnO (blue). (C) and (D) HREM images of iron oxide NP surrounded by amorphous shell probably caused by surfactant partial decomposition (scale bars are 5 nm).

Moreover, aggregate dimensions vary from a few nanometers up to almost 100 nm. If NP gets close during the annealing, due to surfactant loss, some of them may coalesce / sinterize. If the distance between two NP is in the order of the exchange interaction length (a few nanometers), upon application of an external magnetic field, the resulting particle acts like a bigger particle. If the SPM critical dimension is exceeded (20 nm), particles perform as a ferromagnet. This is what was observed in the AGFM measurement reported in Figure 4.2.18. The coercive field is small but

not unimportant ( $H_C = 0.0017 \pm 0.0002$  T) and the ratio  $M_R / M_S$  is about 2%. This means that a small fraction of NP reached the SPM limit and became ferromagnetic. Besides, the measured saturation magnetization for the coupled material (both ZnO TP and magnetite NP) is  $0.41 \pm 0.08$  Am<sup>2</sup>/Kg. This is roughly about 50% less than expected, but this could be explained by systematic error on the estimation of NP weight. The main reasons include the error of NP mass (no surfactant contribution is subtracted) and the estimation of the attached NP (it is assumed that all NP are attached to the TP surface). This lead to an overestimation of NP mass used for the normalization, hence to a lower value of magnetization is reported. It is worth mentioning that coercive field and remanence magnetization values for the coupled compound are very small, hence no significant aggregation between different nanostructures – due to magnetic dipolar interactions – is expected. On the contrary, upon application of an external field, one can *trigger* aggregation *a/o* drive, transport or collect these nanostructures.

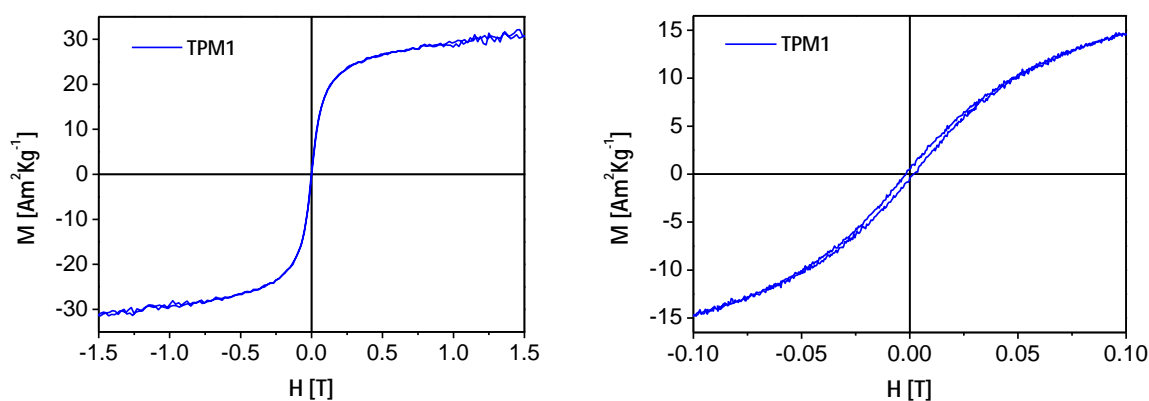


**Figure 4.2.18** Hysteresis loop for the sample TPM1 showing a ferromagnetic behavior. On the right is reported a low field enlargement of the curve on the left.

To overcome the problem of surfactant decomposition, OA was chosen as both ligand and solvent, in the synthesis of magnetic NP, as reported in the previous section (sample NP5). OA is an high boiling solvent (350 °C) and, according to our experience, it is expected to be thermally stable, refluxing in inert atmosphere. A fraction of magnetite NP dispersed in hexane were mixed to the ZnO TP suspension in IPA (Fe / Zn = 1:20), stirred and sonicated for 3 hours, then an aliquote is collected and dried under vacuum at 60 °C, as for the previous samples. The mixed compound was then quickly annealed under nitrogen atmosphere: the sample was inserted in the tubular furnace when the temperature reached 400 °C, kept inside for 10 min, extracted from the furnace, cooled down and then dispersed in IPA (sample TPM5). A representative TEM analysis is shown in Figure 4.2.19. A first evidence is the expected absence of any surfactant contamination, ZnO (and Fe<sub>3</sub>O<sub>4</sub>) surface looks clean from organic contamination, oppositely to what was observed in previous samples, encapsulated with PEG-400, PVP-10000 and, to a small degree, with citric acid. Nevertheless NP aggregation is not completely avoided, but aggregation itself is not crucial

for future application (*e.g.* gas sensing or photocatalytic systems) until aggregation does not lead to ferromagnetic behavior. In such case, the magnetic (dipolar) interaction may drive the ZnO TP aggregation, *i.e.* an unwanted lowering of the photocatalytic performance.

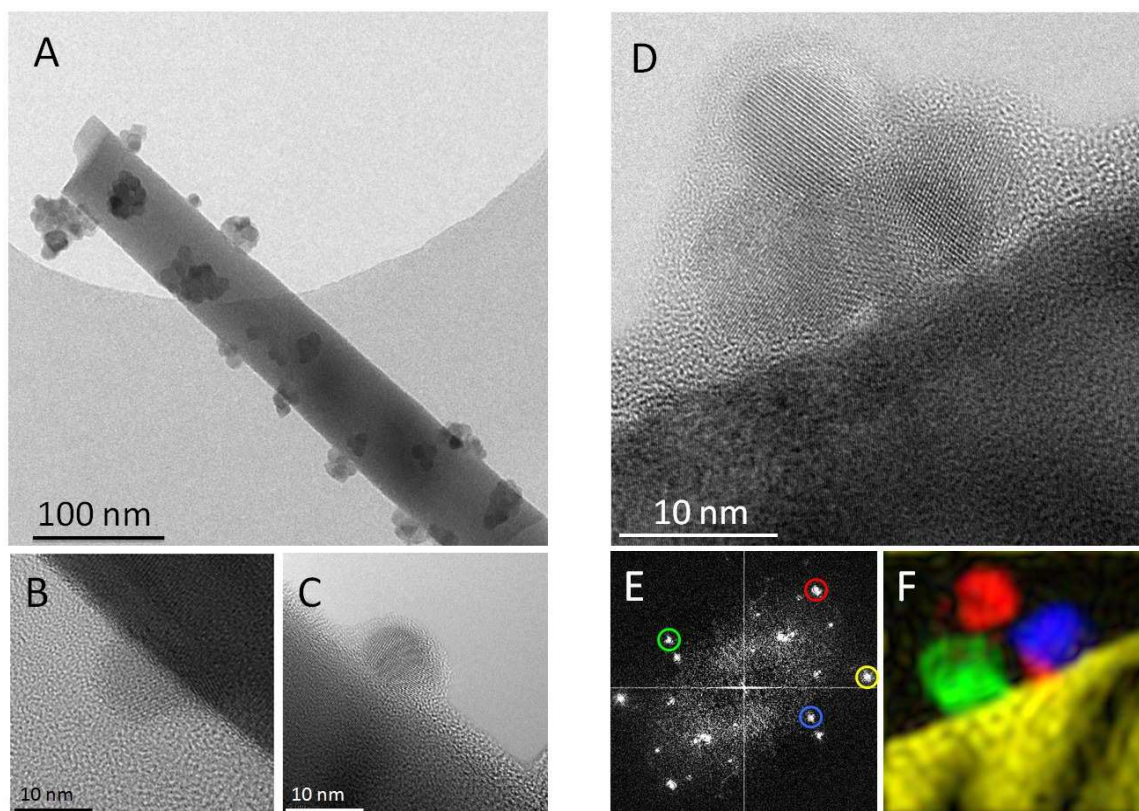


**Figure 4.2.19** TEM analyses on the  $\text{Fe}_3\text{O}_4$  functionalized ZnO TP (sample TPM5). Refer to text for discussion.

From our experience, aggregation it is likely to take place before the heat treatment. No matter how much the ZnO TP to  $\text{Fe}_3\text{O}_4$  ratio is increased, (minor) NP aggregation is still observable. This is ascribable to the low “affinity” between OA hydrophobic tails and ZnO surface: it is very likely that, upon drying / solvent evaporation, NP aggregation takes place because of VdW interaction between intermingled OA chains. The following heat treatment leads to coalescence / sinterization. On the other hand, the sticking of iron oxide NP on ZnO TP seems to be effective. The two HREM images in Figure 4.2.19B and C pick out a large contact area between NP and ZnO TP, this is confirmed by another HREM image reported in (D).

The FT shows (220), (311) and (400)  $\text{Fe}_3\text{O}_4$  reflections together with (002) ZnO wurtzite (E). The intensity map obtained with the spatial frequencies, marked with circles in the FT, is reported with the same color in (F) and displays the different orientations of magnetite NP. Magnetic properties were investigated through AGFM measurement and the results are shown in Figure 4.2.20. According to the  $M(H)$  curve presented in (A), an apparent SPM behavior is observed. However a closer view reveals a small, but measurable, coercive field ( $H_c = 0.0037 \pm$

0.0004 T) proving that a fraction of NP reached their magnetically blocked state (B). This is likely ascribable to the increase in NP dimensions, resulting from the annealing process. It is worth noting that the annealing was performed under the same conditions (temperature, time, atmosphere) in both TPM1 (citric acid capped NP on ZnO TP) and TPM5 (OA-capped) sample and, as expected, magnetic properties are comparable.

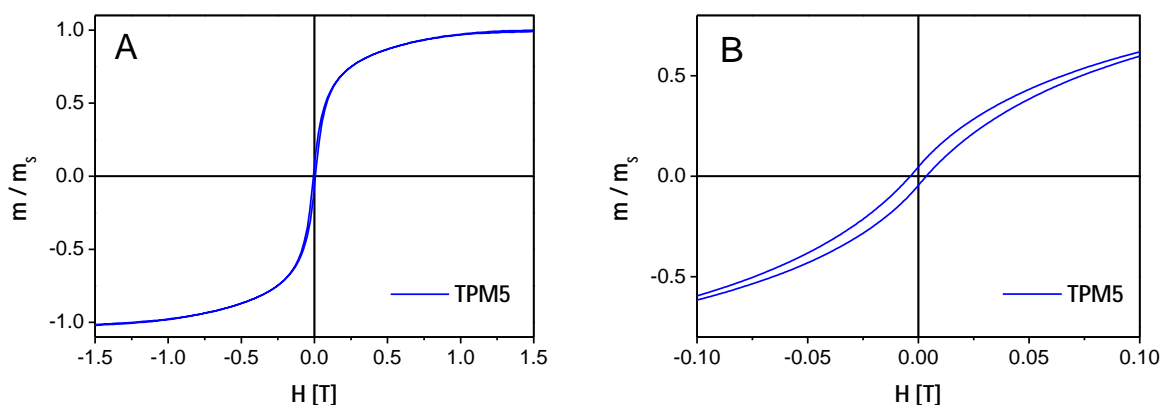


**Figure 4.2.20** (A) Magnetization curve of the sample TPM5. (B) low field magnification.

Contrary to what one may expect, it was not possible to reduce particles aggregation (and hence obtain a complete SPM behavior) varying the synthetic parameters (*i.e.* lowering the annealing time or temperature, as well as NP to ZnO weight ratio). This fact suggests that NP aggregation takes place *before* the annealing process, probably because of solvent evaporation (and subsequent VdW interaction between different OA-capped NP). This underlies an intrinsic limit for the proposed functionalization method, that's why alternative and more sophisticated procedures, like chemical-driven self-assembly of iron oxide NP onto ZnO TP will be explored in the future. However, the measured coercive field and magnetization remanence are almost unimportant for most of the envisaged applications (*e.g.* gas sensing, photocatalysis), so that the synthesis of a *perfect* superparamagnetic coupled material (coercive field approaching zero *i.e.* comparable with the instrumental error), at present, is not a nodal point.

Room temperature PL spectra (Figure 4.2.21A) reveals a NBE emission, for the coupled compound  $\text{Fe}_3\text{O}_4 - \text{ZnO}$  TP (red line), similar to what is observed for the bare ZnO TP (blue line). This is not surprisingly since magnetite shows no emission in the measured range. No significant shift of NBE emission is observed at RT, just a slightly lower intensity (about 10%) ascribable to the surface functionalization. On the other hand, the visible defect emission ( $\sim 500$  nm) is blue-shifted. The chemical origin of the green luminescence in ZnO is still under debate, there is still no agreement on which point defect contribute (most) to the luminescence, but scientific community agrees on the fact that surface defects play an important role in the defect band emission (refer to Ch. 2.1). A similar blue-shift was observed in CdS functionalized ZnO TP too (as reported in Ch.

4.1) and it is likely that surface functionalization (irrespective of the nature of the functionalizing material) passivates some of the radiative defects on ZnO surface responsible for the green emission, but a deeper study should be required since, as mentioned early, a general agreement on the nature of the green emission still lacks.

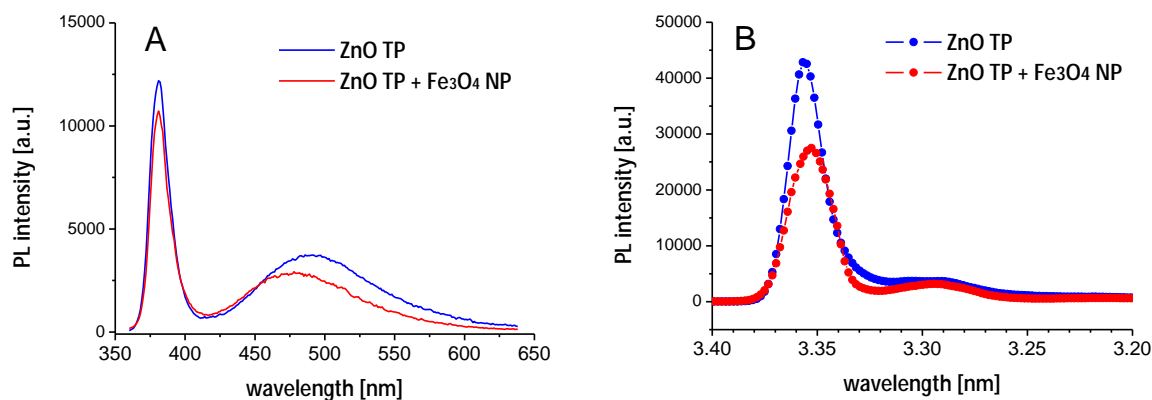


**Figure 4.2.21** PL spectra of bare ZnO TP (blue line) and functionalized ZnO TP (red line) at RT (A) and 20 K (B).

Low temperature ( $\sim 20$  K) PL measurement is reported in Figure 4.2.21B. The emission spectra of the coupled compound (red line) is still qualitatively similar to that of bare ZnO TP (blue line). A small red shift in the NBE emission is observed from 3.355 eV, to 3.353 eV. The observed luminescence is consistent to what previously reported for ZnO TP and is due to FX and D<sup>0</sup>X recombinations [97,98]. A less intense emission is present at 3.290 eV, according to what is reported in literature, this is ascribable to A<sup>0</sup>X and ZB NBE recombinations [97,98].

Finally, no substantial modification of ZnO TP emission is observed due to functionalization with magnetite nanoparticles, this was both expected and desirable. The goal of our research focused in the *addition* of extrinsic magnetism to ZnO TP preserving ZnO own properties, like defective surface states and NBE photoluminescence. The functionalization approach was chosen to be as simple as possible and potentially portable to different ZnO nanostructures. Super-paramagnetic magnetite (Fe<sub>3</sub>O<sub>4</sub>) nanoparticles are physically coupled to vapor-phase grown ZnO TP and then undergo an optimized thermal treatment to sinter in form of strongly coupled composite nanostructures, without affecting the crystalline phase and the properties of each material. Such functionalized nanostructures can be readily used in photocatalytic systems or gas sensing devices, moreover it would be very interesting to study the Fe<sub>3</sub>O<sub>4</sub>-ZnO coupled compound in water splitting and biomedical applications (i.e. drug delivery, PDT).

At present, most photocatalysts suffer from low efficiency *a/o* serious instability for hydrogen evolution from water splitting under the irradiation of solar light. To solve the above issues, different hybrid semiconductor heterostructures have been explored due to their great flexibility in



extending light response range and promoting the separation of photo-induced charge carriers, in contrast to single phase photocatalysts [99–103].

As concerns possible biomedical applications, it must be noted that ZnO nanostructures are known to produce singlet oxygen upon UV [104,105] and X-Ray irradiation [106]. In this regard, recent studies have shown that ZnO nanoparticles exhibit a high degree of cancer cell selectivity with the ability surpass the therapeutic indices of some commonly used chemotherapeutic agents in similar *ex vivo* studies [107–109]. Obviously the possibility to use an external magnetic field to selectively drive the nanostructure into a localized area, as well transport drugs to a specific target, constitutes a high intrinsic value of the proposed coupled nanostructure, for biomedical applications.

## References

- [1] S. Chikazumi, S. Taketomi, M. Ukita, M. Mizukami, H. Miyajima, M. Setogawa, Y. Kurihara, *J. Magn. Magn. Mater.* 1987, **65**, 245
- [2] P. H. Lihn et al., *Journal of Physics: Conference Series*, 2009, **187**, 012069
- [3] A. P. Khandhar, R. M. Ferguson, and K. M. Krishnan, *J. Appl. Phys.*, 2011, **109**, 07B310
- [4] A. H. Lu, W. Schmidt, N. Matoussevitch, H. B. Pinnermann, B. Spliethoff, B. Tesche, E. Bill, W. Kiefer, F. Schueth,; *Angew. Chem. Int. Ed.* 2004, **43**, 4303
- [5] S. C. Tsang, V. Caps, I. Paraskevas, D. Chadwick, D. Thompson, *Angew. Chem. Int. Ed.*, 2004, **43**, 5645
- [6] A. Idris, N. Hassan, R. Rashid, *Journal of Hazardous Materials*, 2011, **186** (1), 629
- [7] C. Liu, F. Li, X. Li, G. Zhang, Y. Kuang, *Journal of Molecular Catalysis A: Chemical*, 2006, **252**, 40
- [8] S. Q. Liu, *Environmental Chemistry for a Sustainable World*, 2012, **1**, 99
- [9] S. H. S. Chan, Y. Wu, J. C. Juan and C. Y. Teh, *J Chem Technol Biotechnol*, 2011, **86**, 1130
- [10] W. Du, Y. Xu, Y. Wang, *Langmuir*, 2008, **24** (1), 175
- [11] N. Zhao, W. Ma, Z. Cui, W. Song, C. Xu, and M. Gao, *ACS Nano*, 2009, **3**(7), 1775
- [12] C. R. F. Lund, J. E. Kubsh, J. A. Dumesic, *Solid State Chemistry in Catalysis*, ACS Symposium Series, Vol. 279, Ch. 19, pp 313
- [13] A. K. Gupta, M. Gupta, *Biomaterials* 2005, **26**, 3995
- [14] Y. Zhang, J. Y. Liu, S. Ma, Y. J. Zhang, X. Zhao, X. D. Zhang, Z. D. Zhang, *J Mater Sci: Mater Med.*, 2010, **21**, 1205
- [15] C. K. Nair and D. Chandrasekharan, *Cancer Prevention Research*, 2008, **1** (7), Supplement
- [16] H. Y. Lee, N. H. Lim, J. A. Seo, S. H. Yuk, B. K. Kwak, G. Khang, H. Bang Lee, S. H. Cho, *J Biomed Mater Res Part B: Appl Biomater* 2006, **79B**, 142
- [17] J. Neamtu, N. Verga, *Digest Journal of Nanomaterials and Biostructures*, 2011, **6** (3), 969

- [18] N. Tomašovičová, M.Koneracká, P.Kopčanský, M.Timko, V. Závašová, *Measurement Science Review*, 2006, **6** (2-3), 32
- [19] M. M. Yallapu, S.P. Foy, T.K. Jain, V. Labetwar, *Pharmaceutical Research*, 2010, **27** (11), 2283
- [20] M. Bradford et al., *Molecular imaging*, 2003, **2** (4), 324
- [21] C. Beata et al., *Biomaterials*, **29** (4), 487
- [22] L. X. Tiefenauer, A. Tschirky, G. Kuhne, R.Y. Andres, *Magnetic Resonance Imaging*, 1996, **14** (4), 391
- [23] D. B. Shieh et al., *Biomaterials*, 2005, **26** (34), 7183
- [24] S. Mornet, S. Vasseur, F. Grasset, P. Verveka, G. Goglio, A. Demourgues, J. Portier, E. Pollert, E. Duguet, *Prog. Solid State Chem.* 2006, **34**, 237
- [25] Z. Li, L. Wei, M. Y. Gao, H. Lei, *Adv. Mater.* 2005, **17**, 1001
- [26] S. Sun, *Adv. Mater.*, 2006, **18**, 393
- [27] M. Chen, J. P. Liu, and S. Sun, *J. Am. Chem. Soc.*, 2004, **126** (27), 8394
- [28] M. A. Tarascon, L.K. Kurihara, E.E. Carpenter, S. Calvin, V.G. Harri, *Inter. Mater. Rev.*, 2004, **49**, 125
- [29] B. D. Terris and T. Thomson, *J. Phys. D: Appl. Phys.* 2005, **38**, R199
- [30] S. Singamaneni, V. N. Bliznyuk, C. Binek and E. Y. Tsymbal, *J. Mater. Chem.*, 2011, **21**, 16819
- [31] T. Hyeon, *Chem. Commun.*, 2003, 927
- [32] S. Sun et al., *J. Phys. Chem. B*, 2003, **107** (23), 5419
- [33] B. Rellinghaus, S. Stappert, M. Acet, E. F. Wassermann, *Journal of Magnetism and Magnetic Materials*, 2003, **266** (1-2), 142
- [34] C. Liu, X. Wu, T. Klemmer, N. Shukla, X. Yang, and D. Weller, *J. Phys. Chem. B*, 2004, **108** (20), 6121
- [35] C. Liu, X. Wu, T. Klemmer, N. Shukla, and D. Weller, *Chem. Mater.*, 2005, **17** (3), 620
- [36] D. W. Elliott, W. X. Zhang, *Environ. Sci. Technol.*, 2001, **35**, 4922
- [37] M. Takafuji, S. Ide, H. Ihara, Z. Xu, *Chem. Mater.*, 2004, **16**, 1977
- [38] L. Cumbal and A. K. SenGupta, *Environ. Sci. Technol.*, 2005, **39** (17), 6508
- [39] X. Li and W. X. Zhang, *Langmuir*, 2006, **22** (10), 4638
- [40] S. M. Ponder et al., *Chem. Mater.*, 2001, **13** (2), 479
- [41] W. X. Zhang, D. W. Elliott, *Remediation*, 2006, **16** (2), 7
- [42] C. Su, R.W. Puls, *Environ. Sci. Technol.*, 2001, **35** (7), 1487
- [43] L. Li et al., *Critical Reviews in Environmental Science and Technology*, 2006, **36**, 405
- [44] S. Xu, W. Shangguan, J. Yuan, M. Chen, J. Shi and Z. Jiang, *Nanotechnology*, 2008, **19**, 095606
- [45] M. Ye, Q. Zhang, Y. Hu, J. Ge, Z. Lu, L. He, Z. Chen, Y. Yin, *Chem. Eur. J.*, 2010, **16**, 6243
- [46] F. Chen, Y. Xie, J. Zhao, G.Lu, *Chemosphere*, **44**, 2001, 1159
- [47] A. Lu, W. Schmidt, N. Matoussevitch, B. Spliethoff, B. Tesche, E. Bill, W. Kiefer, F. Schüth, *Angew. Chem. Int. Ed.*, 2004, **43**, 4303
- [48] K. Sivula, R. Zboril, F. Le Formal, R. Robert, A. Weidenkaff, J. Tucek, J. Frydrych and M. Gratzel, *J. Am. Chem. Soc.*, 2010, **132** (21), 7436
- [49] K. Sivula, F. Le Formal, and M. Gratzel, *ChemSusChem*, 2011, **4**, 432

- [50] S. D. Tilley, M. Cornuz, K. Sivula, and M. Graetzel, *Angew. Chem. Int. Ed.*, 2010, **49**, 6405
- [51] F. Le Formal, N. Taetreault, M. Cornuz, T. Moehl, M. Graetzel and K. Sivula, *Chem. Sci.*, 2011, **2**, 737
- [52] Y. Lin, G. Yuan, S. Sheehan, S. Zhou and D. Wang, *Energy Environ. Sci.*, 2011, **4**, 4862
- [53] H. Ming Chen, C.K. Chen, C.C. Lin, R.S. Liu, H. Yang, W.S. Chang, K.H. Chen, T.S. Chan, J.F. Lee, and D.P. Tsai, *J. Phys. Chem. C*, 2011, **115**, 21971
- [54] H. M. Chen, C.K. Chen, Y.C. Chang, C.W. Tsai, R.S. Liu, S.F. Hu, W.S. Chang, K.H. Chen, *Angew. Chem., Int. Ed.*, 2010, **49** (34), 5966
- [55] G. M. Wang, X.Y. Yang, F. Qian, J.Z. Zhang, Y. Li, *Nano Lett.*, 2010, **10** (3), 1088
- [56] C. Hui, C. Shen, T. Yang, L. Bao, J. Tian, H. Ding, C. Li, and H. J. Gao, *J. Phys. Chem. C*, 2008, **112**, 11336–11339
- [57] L. Shen, P.E. Laibinis, T.A. Hatton, *Langmuir*, 1999, **15** 447
- [58] R. M. Cornell and U. Schwertman, *The Iron Oxides, Structure, Properties, Reactions, Occurrences and Uses*, 2003, Weinheim: Wiley-VCH
- [59] T. J. Bastow, A. Trinchi, M.R. Hill, R. Harris, and T.H. Muster, *J. Magn. Magn. Mater.*, 2009, **321**, 2677
- [60] M. P. Morales, S. Veintemillas-Verdaguer, M. I. Montero, and C. J. Serna, *Chem. Mater.* 1999, **11**, 3058
- [61] P. H. Refait, *J. Mater. Res.*, 1993, **34**, 797
- [62] A. A. Olowe, *J. Mater. Res.*, 1991, **32**, 965
- [63] J. Tang, M. Myers, K. A. Bosnick, and L. E. Brus, *J. Phys. Chem. B*, 2003, **107**, 7501
- [64] H. Iida, K. Takayanagi, T. Nakanishi, T. Osaka, *J. Colloid Interface Sci.*, 2007, **314**, 274
- [65] R. F. Ziolo, E.P. Giannelis, B.A. Weinstein, M.P. O’Horo, B.N. Ganguly, V. Mehrotra, M.W. Russell, D.R. Huffman, *Science*, 1992, **257**, 219
- [66] L. Zhang, G.C. Papaefthymiou, J.Y.J. Ying, *Appl. Phys.*, 1997, **81**, 6892
- [67] Y. Zhu and Q. Wu, *Journal of Nanoparticle Research*, 1999, **1**, 393
- [68] H. S. Lee, W. C. Lee, and T. Furubayashi, *J. Appl. Phys.*, 1999, **85** (8), 5231
- [69] S. Sun and H. Zeng, *J. Am. Chem. Soc.* 2002, **124**, 8204
- [70] A. G. Roca, M. P. Morales, K. O’Grady and C. J. Serna, *Nanotechnology*, 2006, **17**, 2783
- [71] M. Niederberger, N. Pinna, *Metal Oxide Nanoparticles in Organic Solvents*, Springer-Verlag London Limited, 2009
- [72] J. Park et al, *Nat. Mater.*, 2004, **3**, 891
- [73] Y. Hou, Z. Xu, and S. Sun, *Angew. Chem. Int. Ed.* 2007, **46**, 6329
- [74] Z. Xu, C. Shen, Y. Hou, H. Gao, and S. Sun, *Chem. Mater.*, 2009, **21**, 1778
- [75] K. T. Yong, Y. Sahoo, M.T. Swihart, and P.N. Prasad, *J. Phys. Chem. C*, 2007, **111**, 2447
- [76] L. Cademartiri, R. Malakooti, P. G. O’Brien, A. Migliori, S. Petrov, N.P. Kherani, and G. A. Ozin, *Angew. Chem. Int. Ed.*, 2008, **47**, 3814
- [77] H. Shao, H. Lee, Y. Huang, I. Ko, and C. Kim, *IEEE Trans. Magn.*, 2005, **41** (10), 3388
- [78] S. I. Cha, C.B. Mo, K.T. Kim, and S.H. Honga, *J. Mater. Res.*, 2005, **20** (8), 2148
- [79] S. Sun et al., *J. Phys. Chem. B*, 2003, **107**, 5419

- [80] N. Shukla M.M. Nigra, T. Nuhfer, M.A. Bartel, A.J. Gellman, *Nanotechnology*, 2009, **20**, 065602
- [81] N. Poudyal, G. S. Chaubey, C. B. Rong, and J. Ping Liu, *J. Appl. Phys.* 2009, **105**, 07A749
- [82] G. Gao, X. Liu, R. Shi, K. Zhou, Y. Shi, R. Ma, E. T. Muromachi, G. Qiu, *Crystal Growth & Design*, 2010, **10** (7), 2888
- [83] H. Zeng, P. M. Rice, S. X. Wang, and S. Sun, *J. Am. Chem. Soc.*, 2004, **126**, 11458
- [84] Q. Song and Z. J. Zhang, *J. Am. Chem. Soc.*, 2004, **126** (19), 6164
- [85] D. Kim, N. Lee, M. Park, B. H. Kim, K. An, and T. Hyeon, *J. Am. Chem. Soc.*, 2009, **131**, 454
- [86] L. Zhang, J. Wu, H Liao, Y. Hou and S. Gao, *Chem. Commun.*, 2009, 4378
- [87] J. Sun, Shaobing Zhou, Peng Hou, Yuan Yang, Jie Weng, Xiaohong Li, Mingyuan Li, *Journal of Biomedical Materials Research Part A*, 2006, 333
- [88] S. Peng, S. Sun, *Angew. Chem.*, 2007, **46** (22), 4155
- [89] M. Snure, D. Kumar, and A. Tiwari, *Spintronic Materials and Devices*, JOM, June 2009
- [90] L. Duk-Dong, and C. Dong-Han, *Sensor Actuat. B*, **1**(1-6), 231
- [91] J. Peng and C.C. Chai, *Sensor Actuat. B*, 1993, **14** (1-3), 591
- [92] K. Siroky, J. Jiresova, L. Hudec, *Thin Solid Films*, 1994, **245**, 211
- [93] Z. Tianshu, Hongmei L., Huanxing Z., Ruifang Z., and Yusheng S., *Sensor Actuat. B*. **32** (3), 181
- [94] S. Tao, X.Q. Liu, X. Chu, and Y. Shen, *Sensor Actuat. B*, 1999, **61** (1-3), 33
- [95] I. S. Lim, G.E. Jang, C.K. Kim, and D.H. Yoon, *Sensor Actuat. B*, 2001, **77** (1-2), 215
- [96] G. Neri, A. Bonavita, S. Galvagno, P. Siciliano, and S. Capone, *Sensor Actuat. B* 2002, **82** (1), 40
- [97] L. Lazzarini, G. Salviati, F. Fabbri, M. Zha, D. Calestani, A. Zappettini, T. Sekiguchi and B. Dierre, *ACS Nano*, 2009, **3** (10), 3158
- [98] C. Klingshirn, *ChemPhysChem* 2007, **8**, 782
- [99] X. Zong, *et al.*, *J. Am. Chem. Soc.*, 2008, **130** (23), 7176
- [100] X. W. Wang, G. Liu, Z.G. Chen, F. Li, L.Z. Wang and G.Q. Lu, *Chem Commun*, 2009, **23**, 3452
- [101] I. Tsuji, H. Kato and A. Kudo, *Angew Chem Int Ed*, 2005, **44** (23), 3565
- [102] J. Zhang, Q. Xu, Z. Feng, M. Li and C. Li, *Angew Chem Int Ed*, 2008, **47**, 9 1766
- [103] R. Abe, T. Takata, H. Sugihara and K. Domen, *Chem Commun*, 2005, **30**, 3829
- [104] Y. Yamamoto, N. Imai, R. Mashima, R. Konaka, M. Inoue, W. C. Dunlap, *Methods in Enzymology*, 2000, **319**, 29
- [105] M. C. DeRosa, R. J. Crutchley, *Coordination Chemistry Reviews*, 2002, **233-234**, 351
- [106] S. Kishwar, M. H. Asif, O. Nur, M. Willander, P.O. Larsson, *Nanoscale Res Lett.*, 2010, **5**, 1669
- [107] C. Hanley, J. Layne, A. Punnoose, K.M. Reddy, I. Coombs, A. Coombs, K. Feris, D. Wingett, *Nanotechnology*, 2008, **19** (29), 295103
- [108] H. Wang et al., *J Mater Sci Mater Med.*, 2009, **20** (1), 11
- [109] J. W. Rasmussen, E. Martinez, P. Louka, and D. G. Wingett, *Expert Opin Drug Deliv.*, 2010, **7** (9), 1063

## 4.3 Organics on ZnO nanorods

In recent years, organic photovoltaic devices have attracted considerable attention due to their low cost, ease of fabrication, and their flexibility [1]. Many research groups have reported on attempts to improve their performances in terms of efficiency and stability [2–8]. In particular, to overcome the weakness of organic materials, which includes short exciton diffusion length and air instability [9], organic–inorganic hybrid structures are generally considered to be promising alternatives [10–15]. In this respect, ZnO is the most widely used inorganic semiconductor, in this type of hybrid devices, because of its high transparency, non-toxicity and ease of fabrication of thin films and nanostructure [16–25]. Among organic molecules, the family of the phthalocyanines represents one of the most promising candidates for ordered organic thin films, as these systems possess attractive features such as chemical and temperature stability, together with the possibility to form thin films with good optical and electronic properties.

In this context, the present chapter shows part of the results obtained in the frame of “D.A.F.N.E.” project, devoted to the study of hybrid solar cells. The project involves, among the others, our group at IMEM Parma for the growth and optical characterization of ZnO nanostructures and IMEM Trento for the deposition of thin organic films (titanyl–phthalocyanines, free–base fluorinated porphyrin) on these nanostructures. More in details, the first part focuses on the directional deposition of titanyl–phthalocyanine (TiOPc) molecules in ZnO NR. The NR sensitization has been carried out using a supersonic molecular beam deposition (SuMBD) technique, which allows the deposition of organic molecules with an accurate control at the nanoscale. The directional–specific functionalization on a *single* side of ZnO NR array has been demonstrated for the first time as a viable process for future multiple functionalization on a single NR. A dual–functionalization, using TiOPc and 5,10,15,20–Tetrakis(pentafluorophenyl)-porphyrin (TPP) is herein reported, as well as a preliminary study on the deposition of a p–type (hole carrier) material.

### 4.3.1 TiOPc functionalization of ZnO nanorods

According to literature, dye–sensitized solar cells perform power conversion efficiencies over 11% under simulated standard solar emission (AM 1.5 G) [26,27]. Unfortunately, the use of liquid electrolytes in DSSC often results in leakage and sealing problems, and their scalability remains challenging. Many efforts to overcome these limitations have been performed by replacing the

liquid electrolyte by ionic liquids [28], or quasi-solid [29] and solid organic sensitizer and hole transporter [30]. Despite these efforts, different features in the preparation of these solid state devices need to be improved, from the permeation of the organic hole carrier material inside the metal oxide nanostructures [31], to the optimization of the solar spectra absorption [32,33]. The use of dyes with large absorption range [34] has improved the performances, but in order to efficiently harvest the whole solar spectrum, it would be useful to employ multiple dye molecules that maximize the absorption at specific and complementary frequencies. Unfortunately, because of the exciton diffusion length in most organic dyes (10 ÷ 20 nm) [1,61], the photoactive layer thickness has to be accurately tuned in order to efficiently separate the exciton at the interface with the nanostructured metal oxide, avoiding recombination and promoting electron injection to the semiconductor conduction band [35,64]. Combining these considerations with the ability to control the shape and the morphology of the metal oxide nanostructure, it is possible to design an improved hybrid structure with higher overall efficiency. Taking benefit from versatile synthesis procedures, different ZnO nanocrystals have been exploited in photovoltaic cells: nanoparticles [36], nanotetrapods [37] and nanorods [38,39] in particular. Among these, the latter, present some attractive features: first of all, the NR have a single crystalline structure and can be grown by vapor phase techniques at (relatively) low temperature, on a conductive transparent metal oxide (TCO) consisting of AZO deposited on commercial glass [40]. Moreover, because of their morphology, NR allow a continuous path for the electron, minimizing potential barriers (*i.e.* grain boundaries and heterojunction barriers) improving electron conduction and reducing recombination. Finally, NR present a high surface-to-volume ratio, and the surface “roughness” induces scattering phenomena of the incoming light that allow multiple trapping processes at the interface. Consequently, ZnO NR have been investigated in solid-state dye-sensitized solar cells [41–43].

In recent years SuMBD has been successfully employed in the growth of organic oligomer [44,46,47], with unique structural and morphological properties [48] and consequently improved device performances [45,49]. The technique is based on the controlled expansion of a carrier gas (He, Ar, Kr), seeded by the organic oligomer, in high vacuum. The molecular beam, properly selected and skimmed, presents specific characteristics in kinetic energy, alignment, and directionality, which produce unique properties in the grown organic films. In the Knudsen or traditional regime (molecular flow) molecules will not experience collisions, so the velocity and internal energy distributions of the molecules follow a Maxwell-Boltzmann distribution function, whereas the angular distribution is typically cosine-like. In SuMBD the presence of channeled openings could improve the directionality of the beam, giving rise to a  $\cos^n \theta$  ( $n \geq 2$ ) forward intensity, with a large number of collisions occurring in the free-jet expansion, determining a supersonic flow. In particular, considering the characteristic dimensions of the deposition apparatus, the supersonic beam presents an angular spread of about  $5^\circ$  on the sample substrate. The much sharper forward angular distribution of supersonic free jet, gives rise to an intensity, at the

beam target, that could be a factor up to 100 times larger than that for Knudsen cells. The result is that SuMBD technique allows the formation of a high directional beam, with narrow velocity and angular distributions, with high controlled kinetic energy (far outside the range of thermal evaporation), and with a fast cooling of the internal degrees of freedom [50].

Titanyl phthalocyanine (TiOPc), as organic dye molecule, exhibits a wide absorption spectrum in the visible range, it has been used as an active material in organic solar cells [51,52], it is used in organic light emitting diodes and has been investigated as conducting layer in organic field effect transistors [53–55]. Moreover it has been used as emitter in the NIR region and as photoconductive materials for printers and copying machines [56]. Among various TiOPc growth techniques, significant results are reported using Langmuir–Blodgett [57] and organic molecular beam (OMBD) deposition [58], while SuMBD technique has further improved the crystallinity and the phase control of TiOPc films [47,48].

Herein is reported the TiOPc sensitization of vertically aligned ZnO NR, using different angles between the molecular beam and the substrate, in order to investigate the effects of the beam directionality and achieve a directional deposition of TiOPc on a *single* side of ZnO NR.

The first step in the photoanode assembly is the growth of AZO film on glass substrate to be used as TCO. AZO films have been deposited by pulsed electron deposition (PED) technique at IMEM institute (thanks to Dr. Francesco Pattini and Francesco Bissoli), and are generally characterized by low roughness, high transparency and good electrical conductivity. The film shows preferential grain orientation with hexagonal wurtzite *c*-axis perpendicular to the substrate, as shown in Figure 4.3.1A.

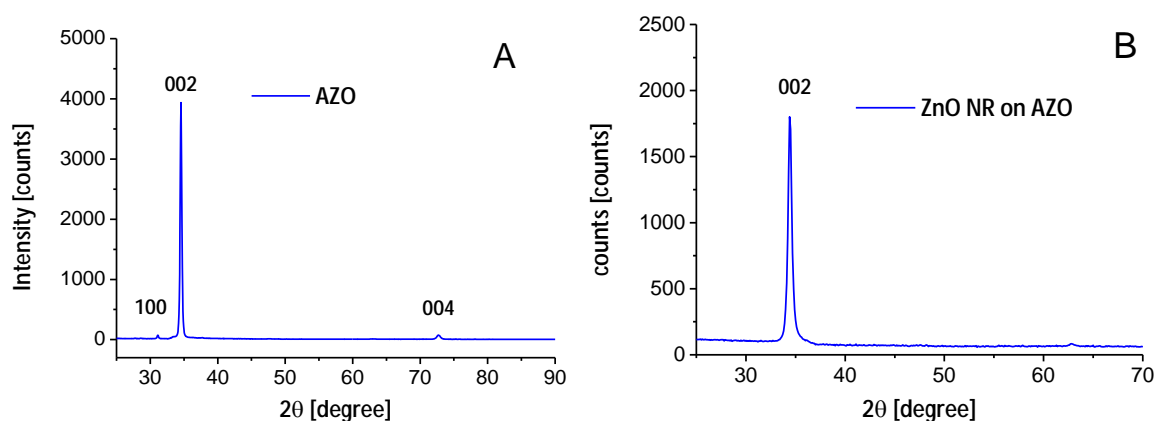


**Figure 4.3.1** XRD spectrum of *c*-axis oriented (A) AZO film, (B) ZnO NR grown on AZO. Reflections are indexed according to PDF 80–0075.

The ZnO NRs are grown on AZO films using a CVD technique at relatively low temperatures, compatible with glass substrates (typically 480 °C). For further informations refer to the Experimental section Ch. 3.1.1b and to Calestani *et al.* [40].

XRD spectrum of as-grown NR reported in Figure 4.3.1B, shows the same *c*-axis alignment observed in the AZO substrate. It is worth noting that the growth of NR has been limited only to a part of the substrate region covered with the AZO films (as shown in Figure 4.3.2) in order to extract electrons from the free AZO surface.

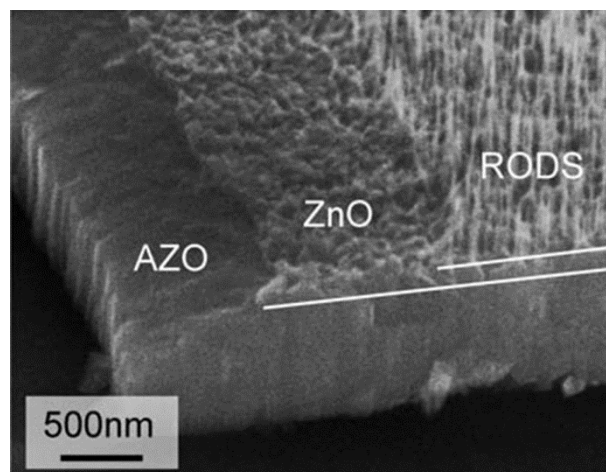


**Figure 4.3.2** SEM view of the different ZnO layer constituting the photoanode. Adapted from [40].

The growth of organic thin films has been performed at the IMEM institute in Trento by Dr. Nicola Coppedè in a tailor-made supersonic beam deposition apparatus [50], it basically consists of a differentially pumped supersonic beam, a TOF mass spectrometer, and a deposition chamber. The supersonic beam source, placed in a high vacuum chamber, is made of a quartz tube with a micrometric nozzle at the front end (typically  $50 \div 130 \mu\text{m}$  in diameter). An inert carrier gas (helium in this experiment) is injected in the quartz tube at a controlled pressure ( $2 \div 3 \text{ bar}$ ). Inside the tube, a vessel with the organic material powder is used to sublime by Joule heating the molecules, dispersing them at very low concentrations into the gas, and expanding both through the source nozzle into the deposition chamber. A conical skimmer selects the central part of the beam, which proceed to the sample in a ultra-high vacuum chamber. By changing the working parameters (nature and pressure of the carrier gas, sublimation temperature, nozzle diameter, and temperature), it is possible to finely control key properties of molecules in the supersonic beam such as kinetic energy, momentum, and cooling of the internal degrees of freedom typically induced by expansion. The source typically operates using a He gas carrier whose pressure is in the range of  $100 \div 200 \text{ kPa}$ . The central part of the beam is selected by skimming the free jet expansion via a sharp edged conical collimator, which separates the source from the deposition chambers (base pressure  $10^{-8} \text{ mbar}$ ). Here, the molecular beam is intercepted by the substrate, which temperature can be varied from  $-100$  up to  $350 \text{ }^\circ\text{C}$ , with a stability of about  $1 \text{ }^\circ\text{C}$ .



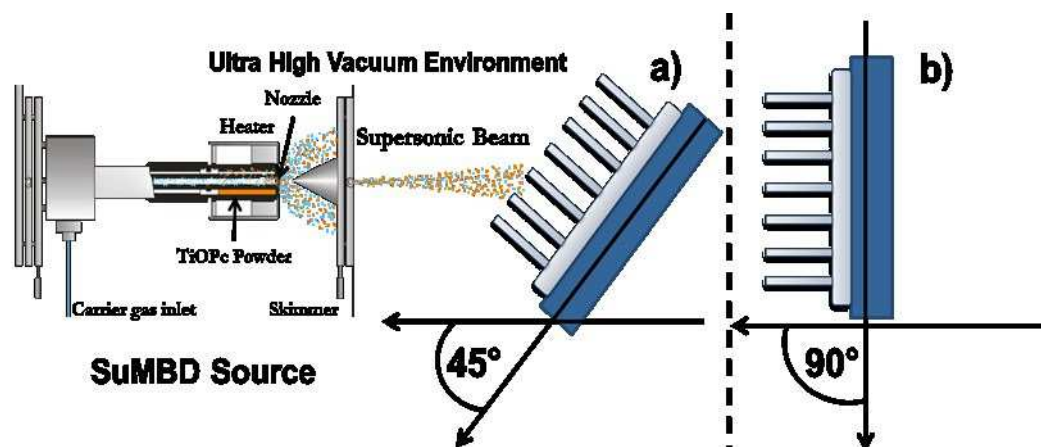


**Figure 4.3.3** Scheme of SuMBD deposition on two different samples of ZnO nanorods. Configuration (A) presents a 45° angle with respect to the beam direction, (B) is perpendicular (90°).

Figure 4.3.3 shows a schematics of the geometries used in the experiments. In particular, when the angle between the beam and the axis of nanorods is 45° (configuration a), only one side of the NR will be exposed to the beam and we expect that, if adsorption-activated kinetic processes will occur, the diffusion of molecules towards the other side of the NR will be avoided and a directional deposition will takes place. On the contrary, when the beam is parallel to the NR axis (configuration b) the whole NR array will be exposed to the arriving molecules, resulting in a homogeneous coverage. Comparing the results on the two directions with identical beam deposition parameters, it is possible to determine the role of directionality of the beam on the TiOPc growth.

TiOPc films have been grown at RT while a quartz microbalance was measuring the deposition rates, fixed at 0.5 nm/min. The source operating conditions have been tuned to keep the same high kinetic energy of 15 eV for all the deposited films. The in-line time-of-flight mass spectrometry (TOF-MS) coupled to laser (fourth harmonic of a Nd:YAG laser at 266 nm) multi-photon ionization has been used to monitor the intensity, purity, and stability of the beam. The duration of the deposition has been set to produce films of the same thickness (20 nm). The TiOPc starting material comes from the same batch (Syntec-Sensient GmbH) for all experiments. It has been purified by repeated vacuum-sublimation cycles, then measured by TOF mass spectrometer to exclude residual contamination. The TiOPc deposition was carried out as pictured in Figure 4.3.4. It is worth noting that the deposition on AZO, ZnO NR and glass substrate was performed at the same time, so that the organic layer thickness, is the same throughout the different zones of the sample.

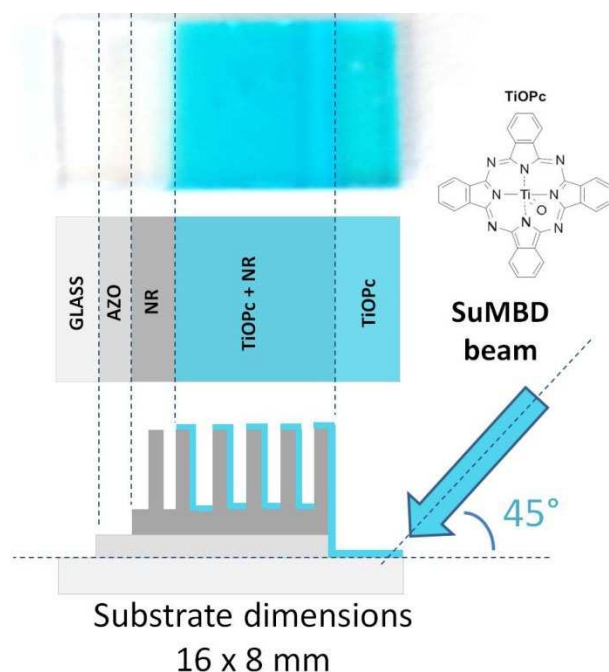


**Figure 4.3.4** Picture and sketch of ZnO NR sensitized with SuMBD deposited TiOPc. The beam direction is fixed at  $45^\circ$  with respect to the substrate.

Figure 4.3.5 reports the SEM analyses of as-grown ZnO NR, compared with those sensitized with TiOPc using an angle of  $90^\circ$  with respect to the sample surface. Figure (A) presents as-grown ZnO NR at 40.000x magnification: they show a regular shape and a uniform alignment over a wide area of the sample. A detailed image is shown in (B): NR length corresponds to  $2 \div 3 \mu\text{m}$ , while the average thickness is about 50 nm. Finally, (C) depicts the same sample, sensitized with 30 nm of TiOPc. The deposition of results to be regular and continuous, *i.e.* NR appear to be covered in a symmetric and homogenous way, and their overall thickness is increased to about 100 nm.

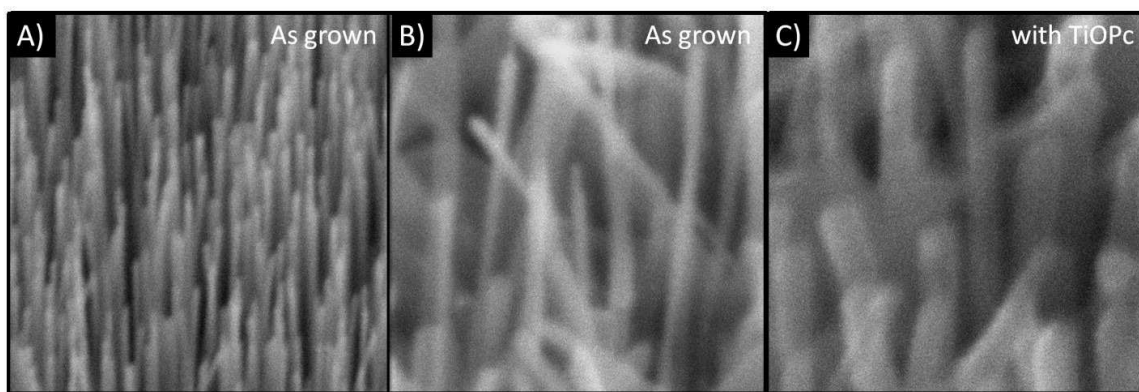


**Figure 4.3.5** SEM image of (A) as-grown ZnO NR, (40000x magnification). (B) as-grown ZnO NR, (80000x magnification). (C) TiOPc “perpendicular” deposition ( $90^\circ$ ) on ZnO NR, (80000x magnification).

In addition to the perpendicular deposition, a SuMBD growth was performed on a sample inclined at  $45^\circ$  respect to the beam. STEM analysis, with a high-angle annular dark-field (HAADF)

detector, was carried to obtain composition sensitive (Z contrast) images. The NRs have been removed from the substrate and dispersed over a holey carbon grid for TEM analysis. A STEM image of a bunch of ZnO NR is presented in Figure 4.3.6. As the intensity is directly related to the atomic number Z, the ZnO NR appear very bright with respect to the carbon background of the grid. The diameter at the base is in the range of  $40 \div 50$  nm while average length is about 1  $\mu\text{m}$ . A careful inspection of the image allows to distinguish a light halo, of intermediate gray, surrounding most NR only by one side: that suggests the directional TiOPc coverage.

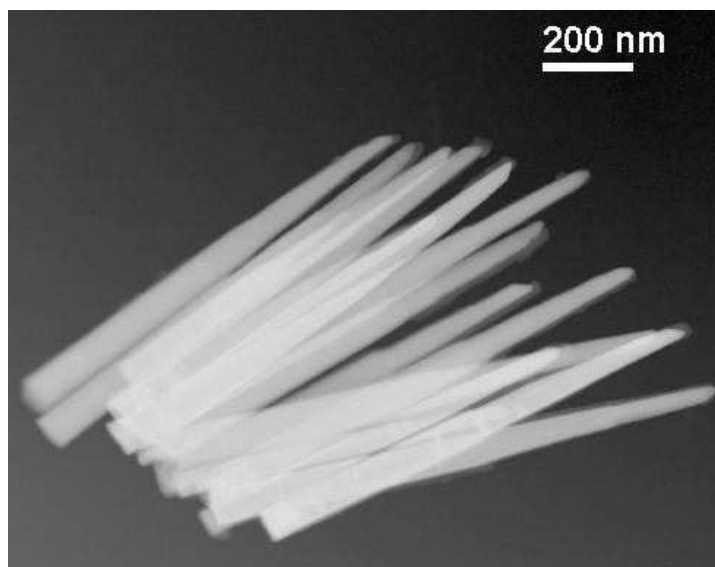


**Figure 4.3.6** STEM–HAADF image of a TiOPc–sensitized ZnO NR. The light halo surrounding NR only one side shows the directional deposition.

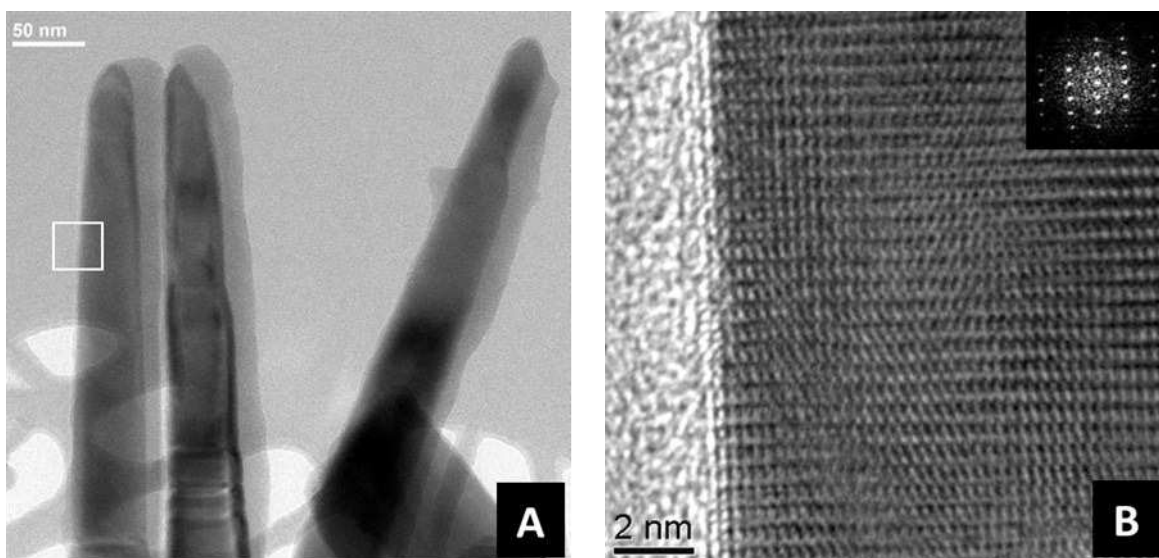


**Figure 4.3.7** (A) Zero–loss TEM image of ZnO NR (dark gray), displaying the directional deposition of TiOPc (light gray) only by the right side of NR. (B) HREM image of the portion squared in (A): no TiOPc is present on the left side of NR. ED pattern reported as inset shows the typical ZnO wurtzite lattice in the (2-1-10) projection.

A bright field, zero loss TEM image is reported in Figure 4.3.7A. The asymmetrical coverage is can be seen: ZnO NR appear dark gray, TiOPc layer looks intermediate gray (and surrounds the NR only on the right side), while the background carbon grid is bright. The deposited layer has a satisfactorily uniform thickness and covers the entire NR length. The HREM image in (B) is the enlargement of the white squared region in (A). The NR are single crystal with wurtzite structure and the lattice is in the (2-1-10) projection, as proved by the ED reported in the inset. It is worth noting that, according to HREM observation, there is no trace of organic deposition on the left side of the NR. To determine the composition and the spatial distribution of the chemical species, high resolution EDX has been performed ( $K\alpha$  lines are used, Zn in blue and Ti in green) and it is reported in Figure 4.3.8A. While zinc is homogeneously distributed across the whole NR, the Ti signal is mainly localized in the thin layer surrounding one side of the NR. Due to the very low quantity of Ti, the analysis has been difficult and required very long time to improve the statistic on counts. The asymmetric Ti distribution (B) has been confirmed over several different NR and it demonstrates the asymmetrical TiOPc coverage due to the  $45^\circ$  deposition.

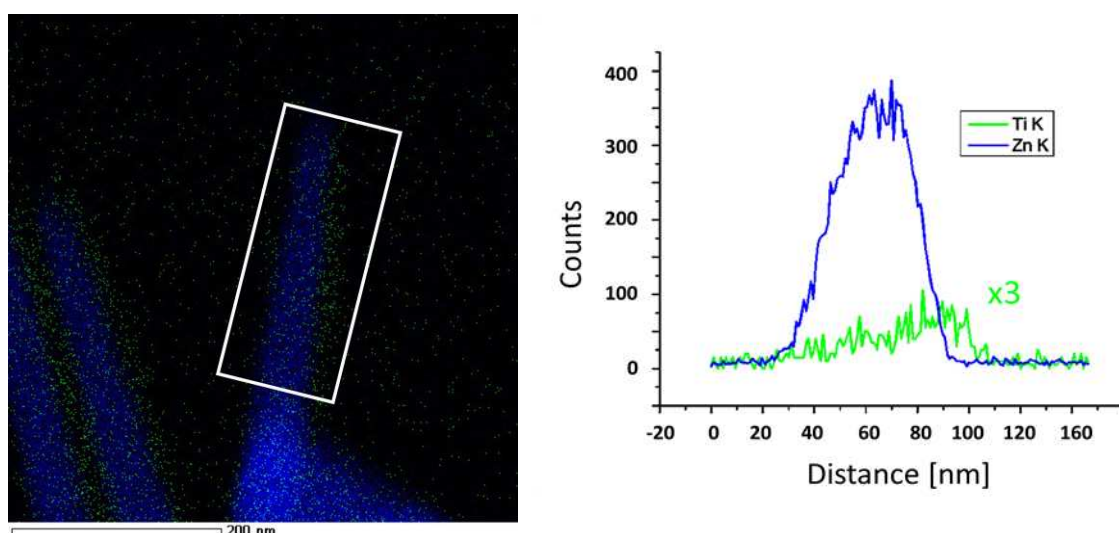


**Figure 4.3.8** (A) EDX map of the same NR reported in Figure 4.3.7A.  
 (B) Intensity profile of Zn and Ti signals, integrated in the area squared in (A).  
 The Ti distribution results asymmetric with respect to Zn.

Absorption and luminescence spectra of as-deposited TiOPc layer on glass substrate are reported in Figure 4.3.9A. What is currently observed is the typical absorption spectra of solid-state TiOPc [47,59] (blue line) consisting of two main broad bands: a B band (Soret) in the near-UV centered at 350 nm, due to the transition to the second excited state ( $S_0 \rightarrow S_2$ ), and a Q band, in the visible region, due to HOMO-LUMO transition ( $S_0 \rightarrow S_1$ ). Both of them include different components whose positions and intensities are known to be sensitive to the specific crystalline phase. Their energy, according to Mizuguchi *et al* [59] is strongly influenced by molecular distortion induced

by  $\pi$ - $\pi$  interactions between adjacent molecules along the  $c$ -axis. As a consequence, the optical properties in the visible range are very sensitive to the crystalline structure, which determines the degree of overlap between orbitals of neighboring molecules. Analyzing the shape of the Q band absorption, there is the presence of features reminiscent of an amorphous phase (shoulder at 650 nm and peak at 730 nm), combined with a component of phase II (the shoulder at 830 nm) [47]. PL measurement (red line) shows that HOMO-LUMO radiative recombination is not observed: this could imply that the lowest excited state ( $S_1$ ) is non-fluorescent, and fluorescence originates from a non-equilibrium excited state ( $S_2 \rightarrow S_0$ ). The PL emission of the samples grown at  $45^\circ$  and the emission of bare ZnO NR and TiOPc are compared in Figure 4.3.9B. The blue line is a typical RT luminescence spectrum of ZnO NR grown by vapor phase technique [60]: the near band edge emission is centered at 380 nm and is more intense than the defect band centered at 500 nm. The red line shows the emission band of TiOPc centered at 430 nm and finally the green line presents the complete system of TiOPc sensitized ZnO NR with  $45^\circ$  angle between the substrate and the beam. It is important to underline that the TiOPc deposited (for surface unit) is the same in the case of the green and red lines.

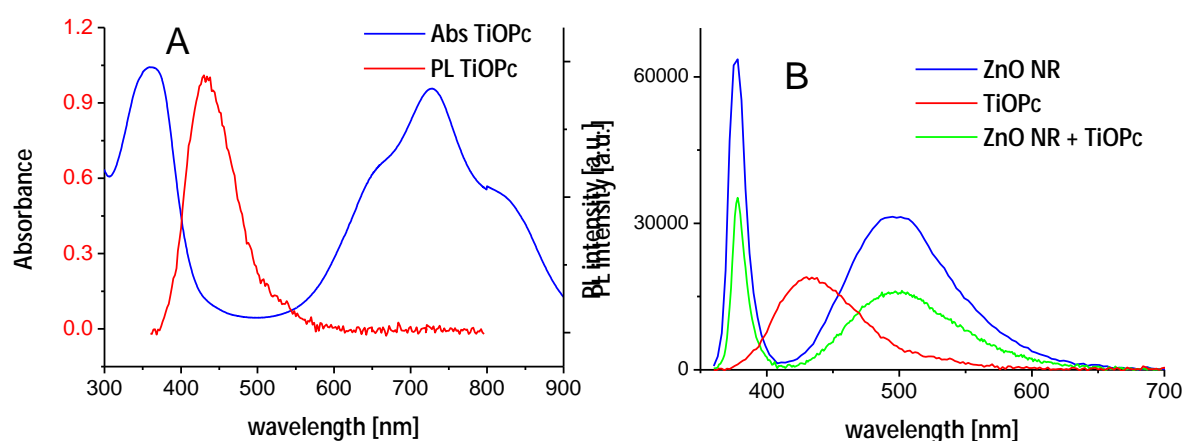


**Figure 4.3.9** (A) Absorption (blue) and emission (red) spectra of TiOPc. (B) PL spectra of ZnO NR (blue), TiOPc (red) and ZnO NR sensitized by directional deposition of TiOPc (green).

The comparison of the spectra in (B) suggests two main features: (1) the band at 430 of TiOPc has been completely quenched in the case of TiOPc-sensitized NR, (2) sensitized-NR have overall lower emission with respect to bare NR due to TiOPc absorption.

(1) As the thickness of the TiOPc layer, according to Figure 4.3.7, is about 10 nm (thus comparable with the typical exciton diffusion length in organic semiconductors [61]), considering ZnO and TiOPc band alignment, an injection of TiOPc photo excited charge in the oxide can take place and the exciton no longer recombines radiatively into the molecule [62]. This means that the sensitization is effective, the exciton is separated at the interface before recombination takes place and the charge is injected from organic molecule to the oxide nanostructure [65–70].

The band gap alignment of the coupled nanostructure forms a type-II heterojunction, in fact, the ZnO CB lies at 4.6 eV with respect to the vacuum [63], while the TiOPc LUMO is located at 4.0 eV [64] (*i.e.* 0.6 eV above). This is crucial for the photovoltaic applications of this organic–inorganic system as a hybrid photoanode.

(2) The emission of sensitized NR (Figure 4.3.9B, green line) is less intense than that of bare ZnO NR (blue line). According to Figure 4.3.9A (red line), the lower NBE emission is ascribed to the action of the TiOPc layer that firstly absorbs the laser incident radiation and secondly absorbs the ZnO UV emission. The lower intensity of the ZnO visible band (*green* luminescence) is likely due to TiOPc laser absorption, together with TiOPc surface functionalization. TiOPc deposition is likely to passivate surface states, which are usually addressed as the cause of ZnO visible emission (refer to Ch. 2.1 for in–depth review).

These results demonstrate that it is possible to selectively sensitize a single NR structure with a controlled and homogeneous deposition of TiOPc, choosing the side to be covered. This paved the way to different directional sensitizations, with two molecular species, each one covering selectively one side of the NR. This could be exploited in solar cell application to improve the absorption at different wavelengths: by choosing different molecules with different absorption peaks, it is possible to collect a wider fraction of the solar spectrum. Moreover the directional functionalization of the same NR with different molecules could be applied in gas sensing devices, to improve the selectivity of the device. Many other applications, including biomedicine, may benefit from a controlled directional and multiple functionalization of the nanostructures with different organic active materials, deposited side–by–side on each nanostructure.

### 4.3.2 Dual functionalization of ZnO NR

Taking advantage of the research on TiOPc deposition, a basic exploration in the direction of multiple functionalization on single NR was performed. Driven by the high directionality of SuMBD deposition, the key idea is to deposit two molecules with different absorption range into the single ZnO NR (Figure 4.3.10). Counting on the know–how acquired by the researchers at IMEM–Trento, a functionalization with TPP was chosen [71,72] since it is known to be stable under SuMBD sublimation and extends the absorption of the photoanode in the blue region (Figure 4.3.11A, red line).

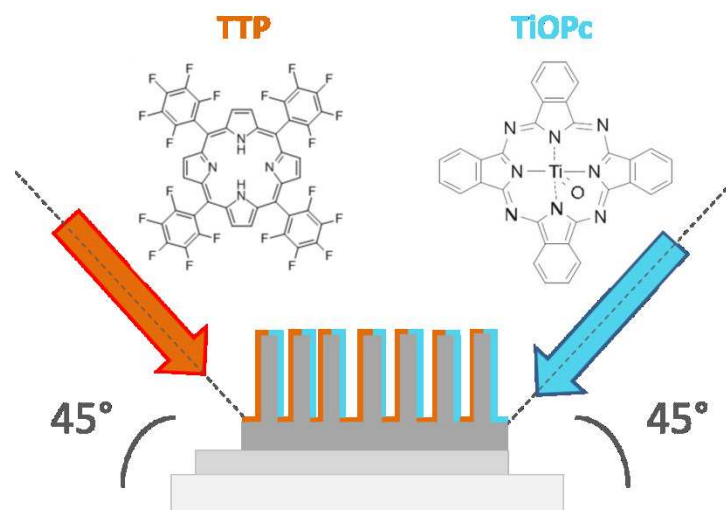


**Figure 4.3.10** Simplified sketch of double functionalized photoanode: two molecules are deposited on a single NR.

The SuMBD–deposited TPP on quartz (50 nm) shows a Soret band, with sharp absorption, that sweeps from 430 nm to the UV region and partially fills the gap between TiOPc Soret and Q bands (Figure 4.3.11A). Both samples are thin films (50 nm), grown using the SuMBD apparatus at IMEM–Trento.

A comparison between TPP absorption spectra in chloroform (blue) and in form of solid film (50 nm on quartz) is provided in (B). While the absorption spectra in liquid is in good agreement to what is reported in literature for TPP [73] and in general with those previously reported for fluorinated aryl porphyrins [74–78], the absorption spectra in solid phase presents plain differences, the peak structure of the Soret band results broadened and new peaks arise at 540 nm and 460 in the Q bands.

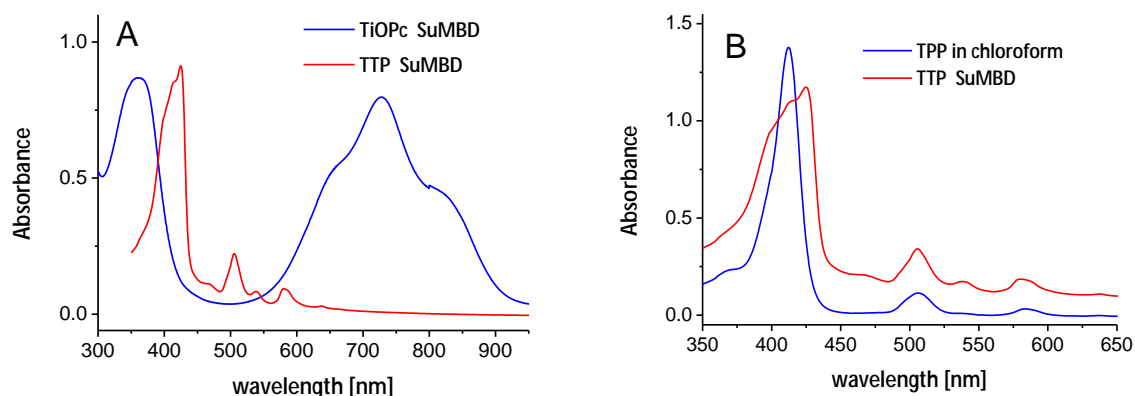


**Figure 4.3.11** (A) Absorption spectra of SuMBD–grown TiOPc and TPP thin films. The addition of TPP partially extends the absorption into the visible region. (B) Absorption spectra of TPP in liquid (blue) and 50 nm thin film (red).

As a general consideration, the position, appearance and intensity of bands depend on peripheral substitution, metallation, solvent, as well as aggregation of the molecules. SuMBD growth induces an improved degree of crystallization in organic oligomer due to the higher kinetic energy of the molecular precursor in the beam [47,79,80] a/o kinetically activates the formation of bonds at the interface. Molecular distortion and interplanar  $\pi$ - $\pi$  interactions arising from crystallization are known either in phthalocyanines [59] as well in porphyrins.

Di Magno and co-workers observed that sterically demanding groups at the porphyrin periphery lead to extensive nonplanar distortions in the relatively flexible porphyrin macrocycle [81], and a substantial alteration in the absorption spectra often accompany these structural changes [82–88]. The interaction in the solid state, induces a  $\pi$ - $\pi$  interaction between adjacent molecule that causes a distortion in the planar structure and lowers the symmetry of the molecule: for example, it is reported that when a distortion in the peripheral pentafluorophenyl rings is involved, the symmetry changes from  $D_{2h}$  to  $C_{2v}$  [73,89]. Perepogu and Bangal [90] observed a similar Q and B bands broadening in the study of TPP nanoparticles and possibly adduce the effect to hydrophobic interaction and  $\pi$ - $\pi$  stacking between adjacent molecules. Moreover, on the basis of DFT calculation, they suggest that pentafluorophenyl groups of TPP lie exactly in orthogonal direction (out-of-plane of porphyrin macrocycle) with respect to porphyrin macrocycle and this may cause a weak coupling that splits the B band in the region between 375 ÷ 450 nm.

The aforementioned considerations qualitatively explain the Q and Soret band splitting, of course a deeper study should be required for investigate the molecular distortion, the crystallization and the possible kinetically induced interaction (due to SuMBD deposition) with the substrate but this lays outside the purpose of this Thesis.

A side by side view of absorption and emission spectra of TPP thin films (50 nm) deposited by SuMBD technique is presented in Figure 4.3.12. Absorption spectra (red) is the same shown in Figure 4.3.11B and is reported for sake of clarity. The PL spectrum (blue) presents two major bands. The one centered at 460 nm related to the Soret absorption band (sometimes referred as B band), is attributed to the transition involving second excited singlet state ( $S_2 \rightarrow S_0$ ) due to optical transitions localized on the nitrogen atoms of the central macrocycle. The structured band ranging from 630 to 730 nm represents the luminescence related to the Q band absorption ( $S_1 \rightarrow S_0$ ) involving transitions from delocalized orbitals in the molecule and the observed Stoke-shift is in agreement to what is reported in literature [90–92]. It is worth noting that *typically* internal conversion from  $S_2$  to  $S_1$  is rapid so that fluorescence is only detected from  $S_1$  [93]. The phenomena of internal conversion were extensively studied in similar systems (*e.g.* Zn-tetraphenylporphyrin): the difference between characteristic lifetime of  $S_1$  (picoseconds) and  $S_2$  (femtoseconds) leads to the depopulation of  $S_2$  to  $S_1$  via vibrational states [94], hence no luminescence is observed in the blue-UV region. Besides this general observation, which can be



considered a sort of *rule of thumb* for porphyrins, other authors, since Bajema and Gouterman research [95], reported the  $S_2 \rightarrow S_0$  luminescence in the range 450 ÷ 500 nm as currently observed [96,97]. According to Marcelli *et al.* [96] the observed  $S_2$  luminescence is caused by the shortening of the  $S_1$  lifetimes due to macrocycle distortions.

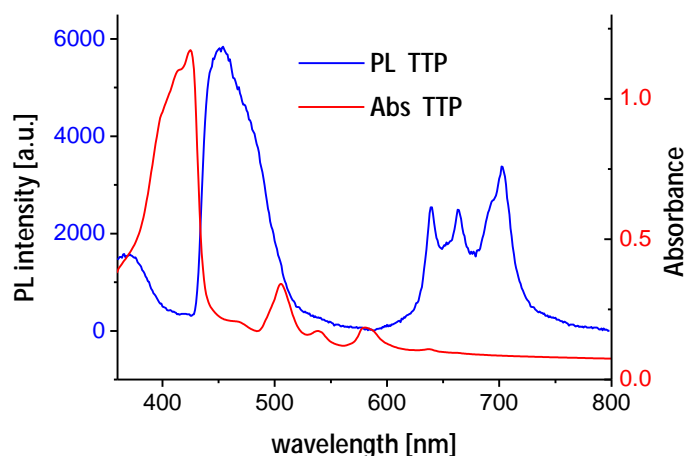


**Figure 4.3.12** Absorption (red, right vertical scale) and emission (blue, left vertical scale) spectrum of 50 nm TPP film deposit by SuMBD.

Possibly, in our case, the “solid–state effect” (crystallization, distortion,  $\pi$ – $\pi$  interaction) induced by SuMBD deposition is responsible for the intense  $S_2 \rightarrow S_0$  luminescence, but the full comprehension of the observed luminescence will require further studies.

The ZnO NR functionalization using a dual absorber was carried out by SuMBD technique: TiOPc and TPP are subsequently deposited on different directions on ZnO NR substrate as sketched in Figure 4.3.10. TEM analyses were performed on the sample by removing ZnO NR from the substrate and dispersing them on the TEM copper grid. STEM images are reported in Figure 4.3.13 and clearly point out that the deposition was not successful, compared to the previously reported deposition of TiOPc. The organic material didn’t form a regular layer on NR but looked rather crowded and the deposition is clearly observable on both sides of the NR. It is likely that the deposition of TiOPc, performed later than TPP deposition, suffers from porphyrin irregular coverage. An EDX analysis on a single NR is reported in Figure 4.3.14. According to it, TPP distribution (red) is symmetric with respect to ZnO NR length while TiOPc coverage (green) seems very low despite the higher atomic mass of titanium compared to fluorine. It is likely that TPP deposition covered on average the whole ZnO surface and subsequent adhesion of TiOPc results affected for the presence of porphyrin instead of bare ZnO.

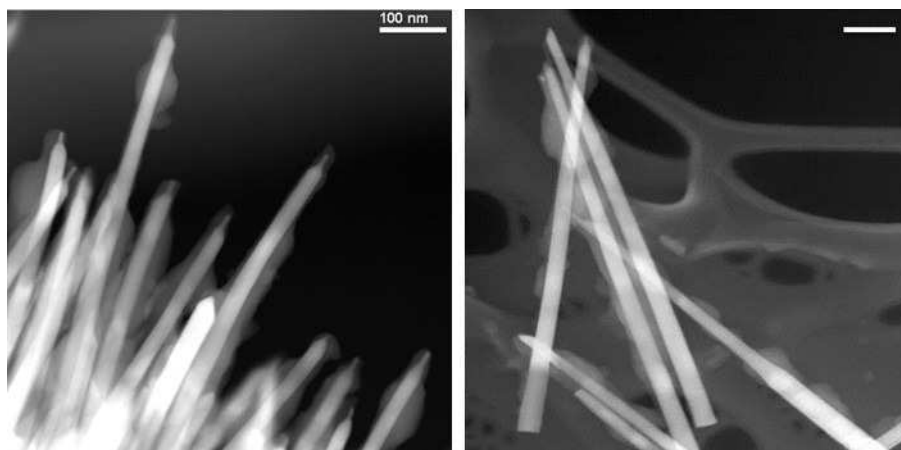


**Figure 4.3.13** STEM images on TiOPc + TPP dual sensitized ZnO NR. Scale bars are 100 nm.

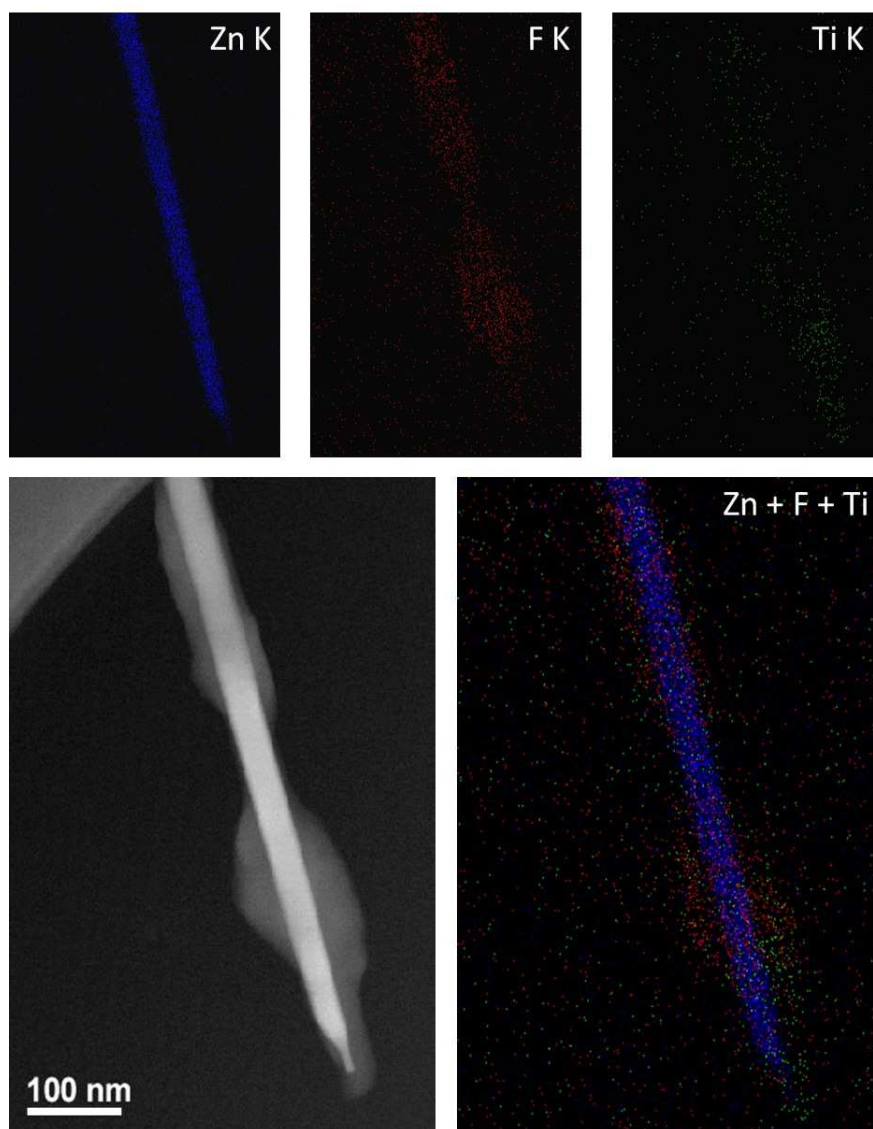


**Figure 4.3.14** EDX mapping and STEM image of irregular TPP layers around ZnO NR. According to EDX map, TiOPc content is very low.

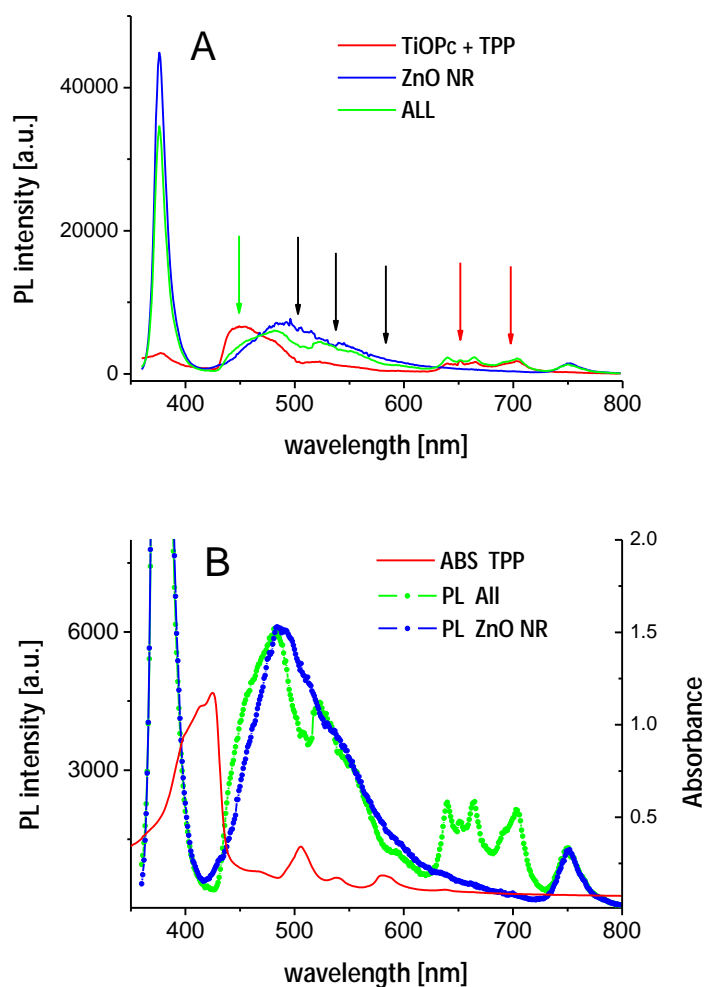
Moreover, large aggregates (in excess of 50 nm) are reported, this quite likely affects the efficiency of a future solar cell. In fact exciton, created upon light absorption in organic layer, has to be dissociated at the interface with ZnO, where the abrupt change of the potential energy creates a strong local electrical field that injects free carriers into the donor / acceptor material. Therefore, exciton diffusion length limits the thicknesses of the organic layer so that exciton diffusion length (typically 10 ÷ 20 nm) [1,9,61] should be comparable to the distance with ZnO NR interface. Otherwise, excitons decay via radiative or non-radiative pathways before reaching the interface, and their energy is lost for the power conversion.

Figure 4.3.15A reports the luminescence of three distinct zones of the sample: as-grown ZnO NR (blue), TPP (red) and TPP on ZnO NR (green). The NBE emission intensity of sensitized ZnO NR is lower compared to bare ZnO NR, however this is expectable since organic layer absorbs either part of the incident laser radiation and part of the ZnO NBE emission, as evidenced by the absorption spectrum reported in Figure 4.3.15B (red line). For sake of clarity, bare ZnO (blue) and sensitized-ZnO (green) luminescence spectra (normalized on ZnO NR defect band intensity) are reported together with the TPP absorption spectrum (red). In fact, the porphyrin absorption around 500 nm, partially explains the structured green emission of the sensitized ZnO NR: Q bands centered respectively about at 510, 540 and 580 nm (Figure 4.3.15B, red line) are responsible for the modulation of the ZnO visible emission band (black arrows). According to Figure 4.3.15A, the NBE emission profile is exactly the same while the green emission is modulated by TPP absorption.

What cannot be explained simply considering the porphyrin reabsorption, is the onset of the hybrid structure luminescence centered at about 450 nm (4.3.15A, green arrow). In fact, bare ZnO NR emission (blue line) present a lower slope at 450 nm while the TPP luminescence has a quick rise in this region. The luminescence of the hybrid structure is actually due to *both* ZnO and TPP luminescence.

Beside this, the plain difference between ZnO and TPP-ZnO luminescence emissions lies in the red region (600 – 750 nm) of the spectrum (Figure 4.3.15A, red arrows). This is caused by HOMO-LUMO recombination inside the porphyrin, due to ineffective charge injection into the ZnO. According to STEM images, the TPP layer thickness is irregular and largely exceeds the exciton diffusion length (10 ÷ 20 nm) so that radiative recombination is observed (green and red lines). The peak at 750 nm is the second order of ZnO NR NBE emission.

It is worth noting that TiOPc luminescence is not detected. This could be due to several factors: 1) according to EDX analysis, the contribution of TiOPc is just a fraction with respect to TPP, 2) TiOPc emission is centered at about 420 nm (Figure 4.3.9) where porphyrin has its absorption peak. Considering this, it is much more likely a TiOPc reabsorption due to TPP rather than a luminescence quench due to charge injection into ZnO.

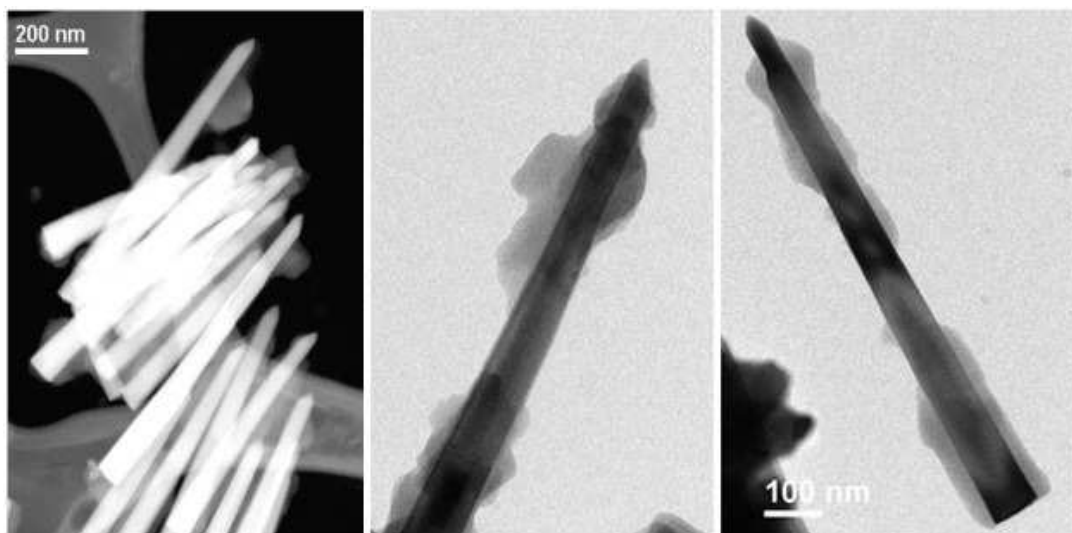


**Figure 4.3.15** (A) PL spectra of dual-sensitized photoanode measured in three different zones: on the dual organic layer (red), on bare ZnO NR (blue) and on sensitized ZnO NR (green). (B) normalized PL intensity of ZnO NR (blue) and sensitized ZnO NR (green), vertical scale is on the left. TPP absorbance (red) is also reported (vertical scale on the right), refer to text for discussion.

The sensitization with dual molecule has been reported, although not fully successful. This experiment was in the direction of dual functionalization on a single NR in order to use two absorber molecules and hence extend the fraction of visible spectrum collected by the photoanode. Unfortunately it was not possible to carefully control the morphology nor the thickness of the TPP absorbing layer, as in the case of the single TiOPc. It is crucial to investigate the causes of the non-uniform deposition, if it's due to TPP irregular coverage that invalidates the following TiOPc deposition, or simply the dual functionalization is not an effective way because of “interaction” among the two molecules. To understand from this failure, the TPP deposition on ZnO was investigated and the following section gives a brief overview to it.

### 4.3.3 TPP functionalization of ZnO NR

The deposition of TPP was carried out by SuMBD technique at IMEM–Trento, deposit porphyrin ( $E_k = 10$  eV on RT substrate) on ZnO NR – grown on AZO substrate – in analogy to what reported for TiOPc (according to the sketch reported in Figure 4.3.4). TEM analysis was performed on the sample by removing ZnO NR from the substrate and dispersing them on the TEM copper grid. STEM images are reported in Figure 4.3.16. What is actually observed is an irregular coverage, very similar to what was reported for the dual–functionalized TiOPc–TPP ZnO NR. TPP molecules are aggregated and the deposition is clearly observable on both sides of the ZnO NR. It is worth noting that aggregates dimensions are in excess of 100 nm, far larger than exciton diffusion length in most organic semiconductors.



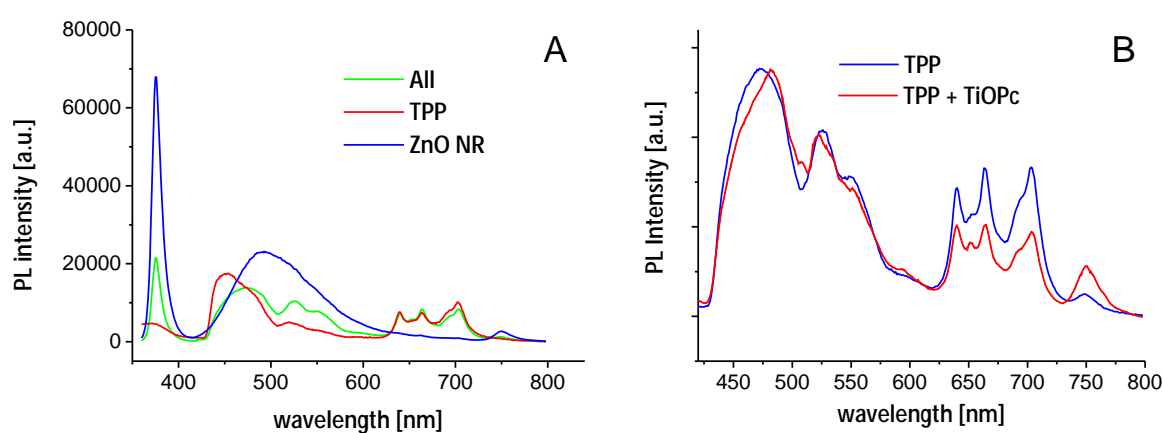
**Figure 4.3.16** STEM (left) and TEM (middle, right) images on TPP sensitized ZnO NR.

Figure 4.3.17A reports the luminescence of three distinct zones of the sample: as–grown ZnO NR (blue), mere TPP (red) and TPP deposited on ZnO NR (green). PL spectrum is qualitatively the exact copy of that reported for dual–functionalized (TPP and TiOPc) ZnO NR. More in details, the following common features are observed: (1) NBE emission intensity of TPP–sensitized ZnO NR is lower compared to bare ZnO NR. (2) The absorption spectra of TPP partially explains the structured green emission (around 500 nm) of the sensitized ZnO NR. (3) The luminescence shoulder of the hybrid structure centered at about 440 nm due to TPP recombination. (4) The emission in the red region of the spectrum (620 ÷ 720 nm) caused by HOMO–LUMO recombination inside the porphyrin due to ineffective charge injection into the ZnO. (5) The peak at 760 nm is due to the second order ZnO NBE emission.

Figure 4.3.17B reports a comparison between the PL emission of TPP functionalized ZnO NR and dual–sensitized TPP–TiOPc ZnO NR. Besides minor differences in the relative intensities, the two

spectra are identical. This means that the emission observed in the dual-sensitized photoanode (reported in the previous chapter) is only due to TPP aggregates, probably because TiOPc suffers from previously irregular deposited TPP and hence TiOPc adhesion is limited (EDX analysis in Figure 4.3.14 reveals just a minor Ti contribution). Moreover, and above all, the ineffective deposition of the sole TPP shows that the dual-deposition itself can be an effective way to create a composite photoanode on ZnO NR and the ineffectiveness of dual-sensitization can be totally ascribed to the TPP deposition.

The research in porphyrin deposition through SuMBD is still a hot research at IMEM Trento and different deposition parameters will be varied soon (beam kinetic energy and substrate temperature, above all) in order to improve the deposition.



**Figure 4.3.17** (A) PL spectra of porphyrin-sensitized photoanode measured in three different zones: TPP (red); bare ZnO NR (blue); and TPP on ZnO NR (green). (B) normalized PL intensity of TPP on ZnO NR (blue) and dual-deposition TPP+TiOPc on ZnO NR (red).

However, even if this configuration is not optimized for solar cell applications, it is instead interesting in photocatalytic [98], gas sensing devices [99]; and above all, in all those applications that benefit from photosensitized singlet oxygen production: *e.g.* environmental remediation (photo-oxidation of organic pollutants in wastewater treatment) and nanomedicine (PDT) [100].

Recently, Liu demonstrates that ZnO NR – porphyrin hybrid nanostructure is an effective anti-tumoral agent [102], thanks to the high yield of singlet oxygen generation, that appears to be the main cause of cytotoxicity inside the cell. When the coupled nanostructure is targeted to tumors and stimulated by X-Rays during radiotherapy, ZnO generates visible light that activates the porphyrin for PDT. ZnO nanostructures are one of the best candidates for this application, since they display very high quantum efficiency for  $^1\text{O}_2$  production [100,101] and their UV emission (380 nm) matches well the Soret band absorption of TPP (refer to Figure 4.3.12), and most porphyrin photosensitizers in general [103,104]. Therefore, the radiation and photodynamic therapies are combined and simultaneously occur, and the tumor destruction can be more efficient. More importantly, the ZnO-porphyrin complex could be used for deep tumor treatment as X-Rays

can penetrate through tissues (deeper than UV–Vis–NIR radiations) and strong X–Ray excited luminescence has been observed in ZnO nanoparticles [105,106]. Finally, porphyrin–functionalized ZnO NR have been recently used for the treatment of breast cancer [107].

#### 4.3.4 Preliminary study on hole conducting material

In order to study a future solar cell, a p–type material is needed to carry holes to the metal counter–electrode. In fact, in order to deposit the metallic contact (counter–electrode) on the top of organic–functionalized ZnO NR, and avoid recombination between the organic (or ZnO, if the organic coverage is very thin) and metal electrode, it is necessary to interpose a hole carrier material with sufficiently high mobility. PEDOT:PSS is chosen since it is nowadays a reference standard in “soft electronics” and is omnipresent, as electrode material; in antistatic coating agent, in pyroelectric sensors, light emitting diodes, field effect transistors, and photovoltaic cells [108–111]. Moreover it possesses a favorable band alignment to extract holes from TiOPc HOMO hence regenerating the molecule after exciton creation upon light absorption. A schematic sketch of the solar cell and band alignment of ZnO [112,113], TiOPc [113,114] and PEDOT:PSS [115,116] – with respect to the vacuum – are illustrated in Figure 4.3.18.

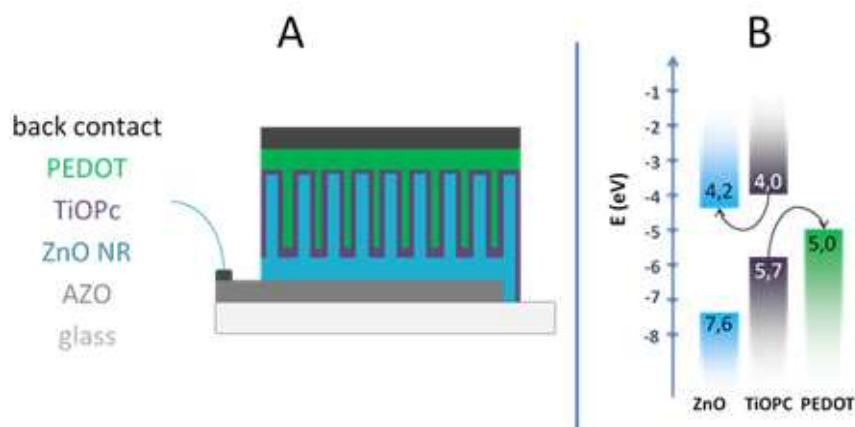


**Figure 4.3.18** (A) ZnO NR based hybrid solar cell: ZnO NR is used as n–type material, TiOPc as absorbing layer and doped–PEDOT as hole conducting material. (B) band alignment of ZnO, TiOPc and PEDOT:PSS.

PEDOT is built from ethylenedioxythiophene (EDOT) monomers. It is insoluble in many common solvents and unstable in its neutral state, as it oxidizes rapidly in air. To improve its processability, a polyelectrolyte solution (polystyrenesulfonate, PSS) can be added, and this results in an aqueous dispersion of PEDOT:PSS [poly 3,4–ethylenedioxythiophene : polystyrenesulfonate]), where PEDOT is its oxidized state. Each phenyl ring of the PSS monomer has one acidic sulfonate

(SO<sub>3</sub>H) group, refer to Figure 4.3.19 (left). It can be easily handled from aqueous solutions, exhibits high transparency in the visible range, and is remarkably stable under environmental, thermal, and mechanical stresses [117]. The aqueous dispersions of PEDOT:PSS used for this work is a commercial product known under the trade name Baytron–P from H.C. Starck. The PEDOT:PSS is then doped with ethylene glycol (20% v/v) and (0,001% v/v) dodecyl benzoic sulfonic acid (DBSA). The resulting PEDOT solution combines high conductivity (about 300 S cm<sup>-1</sup>), good transparency in the visible region, with excellent stability under ambient conditions and can be easily processed from aqueous dispersions by spin coating.

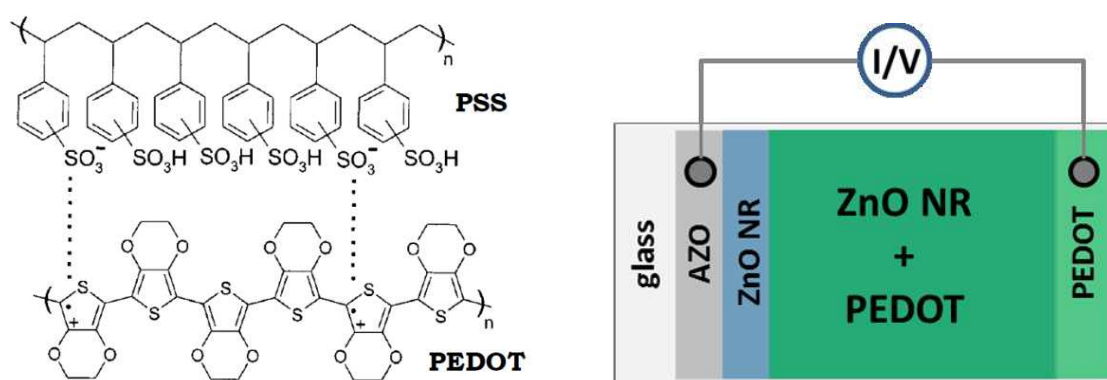


**Figure 4.3.19** Chemical structure of PEDOT:PSS (left), reproduced from [118]. Sketch of the ZnO NR – PEDOT solar cell (right).

As-grown ZnO NR were previously characterized by SEM analysis (Figure 4.3.21A) and exposed to UV light for 5 minutes to remove organic volatile compounds eventually attached to the surface. Then the aqueous suspension of PEDOT:PSS was spin-coated over NR at 3000 rpm for 60 seconds, taking care to mechanically mask the substrate for the deposition as schematized in figure 4.3.19 (right). The sample was then annealed on a hotplate (in air) at 140 °C for 1 hour and then characterized by SEM. The adhesion of the polymer on the ZnO NR results good: PEDOT covers ZnO NR surface in a uniform way, an enlargement of the mean ZnO NR dimensions is observed in Figure 4.3.20B. The polymer film corrugation reflects the underneath ZnO NR morphology and the layer thickness can be deduced from AFM images reported in Figure 4.3.21D to be in the order of hundreds nanometers (thanks to Dr. Paolo Ranzieri for AFM measurement). The deposition however is still not good to ensure a good contact plane for the future evaporated metal on the top. Lowering spin-coat rate to 1500 rpm and extending time up to 3 minutes, almost every ZnO NR results embedded in PEDOT as can be seen in Figure 4.3.20C.



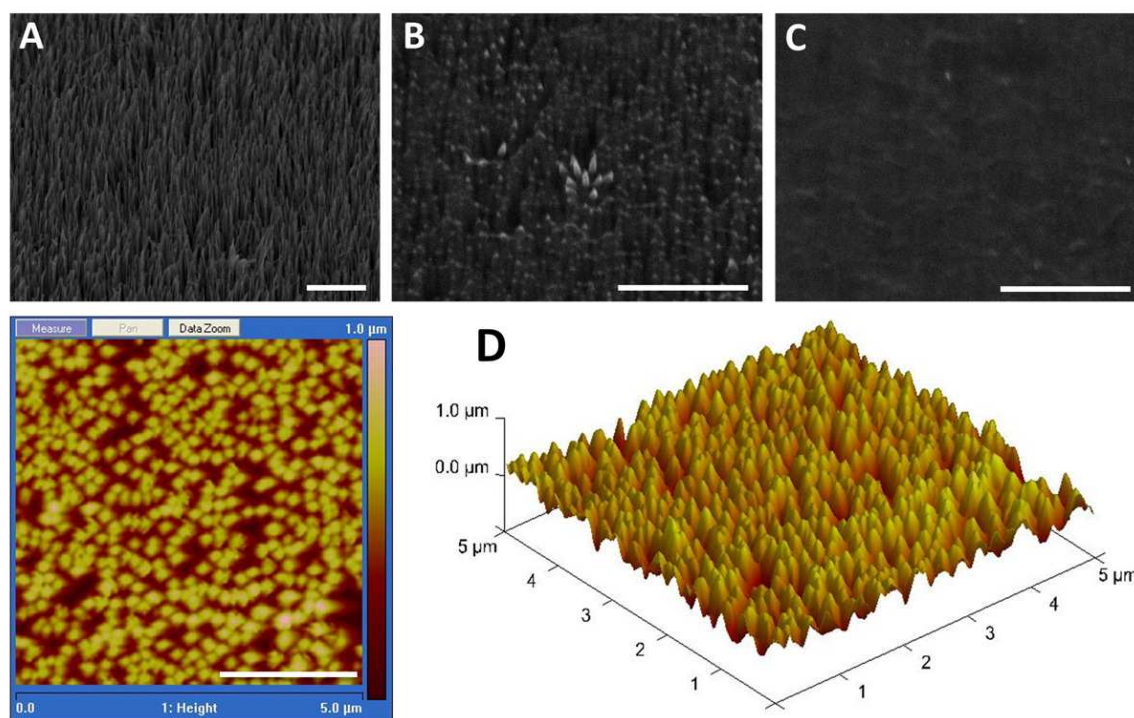


**Figure 4.3.20** (A) SEM image of as-grown ZnO NR, (B) PEDOT:PSS-coated ZnO NR, (C) PEDOT:PSS embedded ZnO NR. (D) AFM measurement on sample shown in (B). White scale bar on the right is 2  $\mu\text{m}$ .

In order to evaluate ZnO–PEDOT composite, electrical measurements were performed using gold tips as moving contacts. In Figure 4.3.21 is reported a preliminary  $I/V$  measurement performed under dark on three different zones of the sample (according to Figure 4.3.19 right) to verify the ohmic contacts, respectively between PEDOT–PEDOT (red), AZO–ZnO (green) and ZnO–ZnO (blue). These rough measurements serves just to ensure that contacts don't limit the current of the cell: since all the measured dark resistances are in the Kohm range, it is safe to assume that contact resistance is just a minor contribution.

$I/V$  characteristic of hybrid PEDOT–ZnO junction was recorded both in dark and under illumination (100W halogen lamp). It must be noted that these measurement were acquired and are shown hereby just to verify the effectiveness of PEDOT deposition. We are not interested to test the cell efficiency, in fact the simple structure pictured in Figure 4.3.19 is nowhere an optimized solar cell. First of all, a proper absorbing material is not used: 1 $\mu\text{m}$  thick PEDOT:PSS film is used as both absorber and hole carrier material. While PEDOT performances as p-type material has been widely investigated and reported in literature, the optical density of the PEDOT film is low and only a minor fraction of incident photons are collected. Moreover the contact geometry is all but optimized. As mentioned early, gold tips are used instead of large plane back contact. Using a tip placed outside the effective area of the cell, contacting PEDOT on glass (on the left of the cell, referring to Figure 4.3.19), tremendously limits the current of the cell because of huge series

resistance. Furthermore the use of gold tips on PEDOT, even if sometimes reported [119], is not optimized since gold work function is located 5.1 eV below the vacuum level while PEDOT HOMO at 5 eV, hence a lower work function metal (*e.g.* silver [120] or aluminum [121]) would be preferred.

With all these considerations in mind, finally Figure 4.3.22A shows the I/V characteristic of PEDOT–ZnO junction on linear scale. Under illumination, a photovoltaic effect is observed (red line) but short circuit current and open circuit voltage values are predictably low ( $I_{SC} = 194$  nA,  $V_{OC} = 0.4$  V). Dark current of the cell is very low too (blue line) and is reported on logarithmic scale in Figure 4.3.23B (blue line).

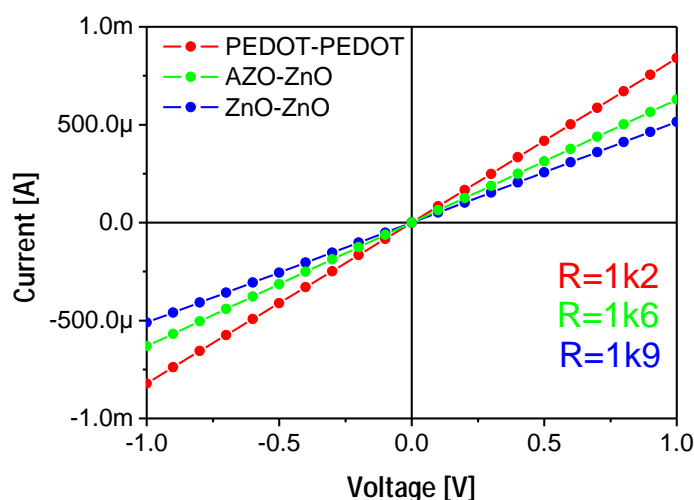


**Figure 4.3.21** I/V dark measurement to verify the ohmicity of gold tip moving contacts.

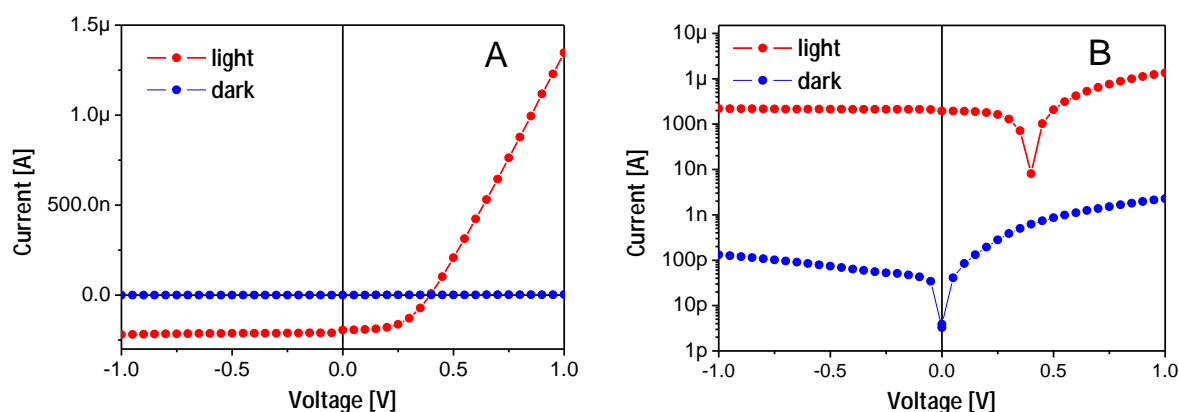


**Figure 4.3.22** Dark I/V characteristic (blue) and I/V under illumination (red) of the hybrid PEDOT:PSS / ZnO NR junction. Plots are reported in (A) linear and (B) logarithmic scale, for sake of clarity.

A photovoltaic effect was roughly proved, this demonstrates that a hybrid heterojunction is formed between PEDOT and ZnO NR and, consequently, the spin coating is a simple but effective way to deposit PEDOT on ZnO NR. Unfortunately, at present, no complete solar cells devices were fabricated (ZnO NR – SuMBD organic molecule – PEDOT). Critical issues, that must be solved in order to obtain a working device, concern PEDOT adhesion on TiOPc–functionalized ZnO NR (poor PEDOT wettability of ZnO NR upon TiOPc functionalization), and deposition of metal contact on the PEDOT layer (short circuits have been reported). The research activity of our group in this field is relatively newborn since it started in 2010 and focused mainly in the characterization of starting material (both ZnO nanostructures and organics) so it has to be considered a work in progress activity. Future work will deal with device fabrication upon the resolution of the aforementioned problems.

#### 4.3.5 Final remarks

A directional deposition of TiOPc on ZnO NR using SuMBD technique was demonstrated and a continuous thin absorbing layer (~ 10 nm) is selectively deposited on a side of ZnO NR. This paves the way to a *future* dual functionalization on a single NR in order to use two molecules and hence tailor the hybrid material response. For example, dual molecules can be used to extend the photoanode absorption range (photovoltaic) or to add selectivity (gas sensing). Unfortunately this scenario is not actual since the dual sensitization using TiOPc and TPP was not as successful as the one with TiOPc only. Large aggregates are present and TPP radiative recombination is observed through PL measurement whereas the luminescence of the mere TiOPc was quenched when deposited into ZnO NR. Anyway the ineffectiveness of dual sensitization was ascribed to imperfect TPP coverage, rather than to the dual deposition itself which is a promising frame for future applications.

In any case, with or without dual functionalization, the TiOPc–ZnO hybrid nanostructure shows interesting properties and can be used as photoanode in hybrid excitonic solar cells [122] as well as in TiOPc–based gas sensors [45,123,124], and in quite uncommon applications, like liquid reprography [125]. Moreover, on the contrary of the single constituent materials, the ZnO–TiOPc hybrid structure have been scarcely investigated from both theoretic [126] and applicative point of view [122] allowing attractive research perspectives. Finally, although the directional deposition of porphyrin on ZnO NR is still an open issue and irregular organic aggregates are reported, such hybrid nanostructure can be readily studied for gas sensing [99] as well as singlet oxygen production *i.e.* environmental remediation (photo–degradation of polluting organic compound, water purification) and biomedical (PDT) applications [100–104].

## References

- [1] J. M. Nunzi, *C. R. Phys.*, 2002, **3**, 523
- [2] K. M. Coakley and M. D. McGehee, *Chem. Mater.*, 2004, **16** (23), 4533
- [3] C. J. Brabec, S. Gowrisanker, J. J. M. Halls, D. Laird, S. Jia, S. P. Williams, *Adv. Mater.* 2010, **22**, 3839
- [4] H. Y. Chen et al., *Nature Photonics*, 2009, **3**, 649
- [5] S. H. Park et al., *Nature Photonics*, 2009, **3**, 297
- [6] S. Gunes, H. Neugebauer, and N. S. Sariciftci, *Chem. Rev.*, 2007, **107**, 1324
- [7] H. Hoppe, N.S. Sariciftci, *J. Mater. Res.*, 2004, **19** (7), 1924
- [8] J.T. Chen, C.S. Hsu, *Polym. Chem.*, 2011, **2**, 2707
- [9] J. P. Liu, S. S. Wang, Z. Q. Bian, M. N. Shan, and C. H. Huang, *Chem. Phys. Lett.*, 2009, **470**, 103
- [10] D. Cui, J. Xu, T. Zhu, G. Paradee, S. Ashok, and M. Gerhold, *Appl. Phys. Lett.*, 2006, **88**, 183111
- [11] S. H. Park, H. J. Kim, M.H. Cho, Y. Yi, S.W. Cho, *Appl. Phys. Lett.*, **98**, 2011, 082111
- [12] I. Gur, N. A. Fromer, C.P. Chen, A.G. Kanaras, and A.P. Alivisatos, *Nano Lett.*, 2007, **7** (2), 409
- [13] C. Sanchez, B. Julián, P. Belleville and M. Popall, *J. Mater. Chem.*, 2005, **15**, 3559
- [14] W. J. E. Beek, M.M. Wienk, M. Kemerink, X. Yang, and R.A.J. Janssen, *J. Phys. Chem. B*, 2005, **109** (19), 9505
- [15] J. Liu, E. N. Kadnikova, Y. Liu, M. D. McGehee, and J. Fréchet, *J. Am. Chem. Soc.*, 2004, **126** (31), 9486
- [16] D. C. Olson, J. Piris, R.T. Collins, et al., *Thin Solid Films*, 2006, **496** (1), 26
- [17] P. Ravirajan, A.M. Peiro, M.K. Nazeeruddin, *J. Phys. Chem. B*, 2006, **110** (15), 7635
- [18] W. J. E. Beek, M.M. Wienk, R.A.J. Janssen, *Adv. Funct. Mater.*, 2006, **16** (8), 1112
- [19] K. Takanezawa, K. Hirota, Q.S. Wei, K. Tajima, and K. Hashimoto, *J. Phys. Chem. C*, 2007, **111** (19), 7218
- [20] A. M. Peiro, P. Ravirajan, K. Govender K, *J. Mater. Chem.*, 2005, **16** (21), 2088
- [21] T. Yoshida, M. Iwaya, H. Ando, *Chem. Commun.*, 2004, **4**, 400
- [22] Z. Yin, S. Wu, X. Zhou, X. Huang, Q. Zhang, F. Boey, H. Zhang; et al. *Small*, 2010, **6** (2), 307
- [23] D. C. Olson, S.E. Shaheen, T. Reuben, *J. Phys. Chem. C*, 2008, **111** (44), 16670
- [24] A. L. Briseno, T. W. Holcombe, A. I. Boukai, E. C. Garnett, S. W. Shelton, J. J. M. Frechet, and P. Yang, *Nano Letters*, 2010, **10**, 334
- [25] W. J. E. Beek, M. M. Wienk, R. A. J. Janssen, *Adv. Mater.*, 2004, **16** (12), 1009
- [26] B. C. O'Regan and M. Graetzel, *Nature*, 1991, **335**, 737
- [27] M. Graetzel, *Prog. Photovolt., Res. Appl.*, 2006, **14**, 429
- [28] S. M. Zakeeruddin and M. Graetzel, *Adv. Funct. Mater.*, 2009, **19**, 2187
- [29] Y. Wang, *Sol. Energy Mater. Sol. Cells*, 2009, **93**, 1167
- [30] J. H. Yum, P. Chen, M. Graetzel and M.K. Nazeeruddin, *Chem. Sus. Chem*, 2008, **1**, 699

- [31] E. J. W. Crossland, M. Nedelcu, C. Ducati, S. Ludwigs, M. A. Hillmyer, U. Steiner and H. J. Snaith *Nano Lett.*, 2009, **9** (8), 2813
- [32] N. Robertson, *Angew. Chemie Int. Ed.*, 2006, **45** (15), 2338
- [33] D. P. Hagberg et al., *J. Am. Chem. Soc.*, 2008, **130**, 6259
- [34] S. Altobello, R. Argazzi, S. Caramori, C. Contado, S. Da Fre, P. Rubino, C. Chone, G. Larramona, C.A. Bignozzi, *J. Am. Chem. Soc.*, 2005, **127**, 15342
- [35] B. Li, L. Wang, B. Kang, P. Wang, Y. Qiu, *Solar Energy Materials & Solar Cells* 2006, **90**, 549
- [36] K. Keis, E. Magnusson, H. Lindstrom, S. E. Lindquist, A. Hagfeldt, *Energ. Mat. Sol.*, 2002, **73** (1), 51
- [37] Y. F. Hsu, C. T. Yip, A. B. Djuricic, and W. K. Chan, *J. Appl. Phys.*, 2008, **103**, 083114
- [38] C. Ku and J. Wu, *Appl. Phys. Lett.*, 2007, **91**, 093117
- [39] I. Gonzalez-Valls and M. Lira-Cantu, *Energy Environ. Sci.*, 2009, **2**, 19
- [40] D. Calestani, M. Zha, L. Zanotti, M. Villani, A. Zappettini, *CrystEngComm*, 2011, **13**, 1707
- [41] D. Wei, H.E. Unalan, D. Han, Q. Zhang, L. Niu, G. Amaratunga and T. Ryhanen, *Nanotechnology*, 2008, **19**, 424006
- [42] N. Plank, H.J. Snaith, C. Ducati C, J.S. Bendall, L. Schmidt-Mende and M.E. Welland, *Nanotechnology*, 2008, **19**, 465603
- [43] N. Plank et al, *J. Phys. Chem. C*, 2009, **113**, 18515
- [44] P. Milani, S. Iannotta, *Cluster beam synthesis of nanostructured materials* Springer Verlag, Heidelberg-Berlin (1999)
- [45] F. Siviero, N. Coppede, A. Pallaoro, A.M. Taurino, T. Toccoli, P. Siciliano, S. Iannotta, *Sensors and Actuators B*, 2007, **126**, 214
- [46] T. Toccoli, A. Pallaoro, N. Coppedè, and S. Iannotta, F. De Angelis, L. Mariucci, G. Fortunato, *Appl. Phys. Lett.*, 2006, **88**, 132106
- [47] N. Coppedè, T. Toccoli, A. Pallaoro, F. Siviero, K. Walzer, M. Castriota, E. Cazzanelli, S. Iannotta *J. Phys. Chem. A*, 2007, **111**, 12550
- [48] N. Coppedè, M. Castriota, E. Cazzanelli, S. Forti, G. Tarabella, T. Toccoli, K. Walzer and S. Iannotta *J. Phys. Chem. C*, 2010, **114**, 7038
- [49] F. Cicoira, N. Coppedè, S. Iannotta, R. Martel *Appl. Phys. Lett.*, 2011, **98**, 183303
- [50] S. Iannotta, T. Toccoli *Journal of Polymer Science B: Polymer Physics*, 2003, **41**, 2501
- [51] Q. Zhang, D. Wang, J. Xu, J. Cao, J. Sun, M. Wang, *Mater. Chem. Phys.* 2003, **82**, 525
- [52] S. Yamaguchi, Y. Sasaki, *Chem. Phys. Lett.* 2000, **323**, 35
- [53] T. Nishi, K. Kanai, Y. Ouchi, M.R. Willis, K. Seki, *Chem. Phys.*, 2006, **325**, 121
- [54] H. Tada, H. Touda, M. Takada, K. Matsushige. *Appl. Phys. Lett.*, 2000, **76**, 873
- [55] L. Li, Q. Tang, H. Li, X. Yang, W. Hu, Y. Song, Z. Shuai, W. Xu, Y. Liu, D. Zhu. *Adv. Mater.*, 2007, **19** 2613
- [56] Y. Fujimaki, H. Tadokoro, Y. Oda, H. Yoshioka, T. Homma, H. Moriguchi, K. Watanabe, A. Konishita, N. Hirose, A. Itami, S. Ikeuchi, *J. Imag. Tech.*, 1991, **17**, 202
- [57] A. Yamashita, T. Maruno, T. Hayashi, *J. Phys. Chem.* 1994, **98**, 12695
- [58] M. Brinkmann, Wittmann J., Barthel M., Hanack M., Chaumont C., *Chem. Mater.*, 2002, **14**, 904

- [59] J. Mizuguchi, G. Rihs, H.R. Karfunkel, *J. Phys. Chem.*, 1995, **99**, 16217
- [60] C. L. Kuo, R. C. Wang, J. L. Huang, C. P. Liu, Y. F. Lai, C. Y. Wang and H. C. Chung, *Nanotechnology* 2008, **19**, 285703
- [61] M. Brumbach, D. Placencia, and N. R. Armstrong, *J. Phys. Chem. C*, 2008, **112**, 3142
- [62] Y. S. Chen, P. A. Lee, K. W. Nebesny, N. R. Armstrong *J. Phys. Chem.*, 1996, **100**, 5447
- [63] G. Van de Walle, J. Neugebauer, *Nature*, 2003, **423**, 626
- [64] H. Yanagi, S. Chen, P.A. Lee, K.W. Nebesny, N.R. Armstrong, A. Fujishima, *J. Phys. Chem.*, 1996, **100**, 5447
- [65] L. E. Greene, M. Law, B.D. Yuhua, and P. Yang, *J. Phys. Chem. C*, 2007, **111**, 50
- [66] K. M. Coakley and Michael D. McGehee, *Chem. Mater.*, 2004, **16**, 4533
- [67] C. R. McNeill and N. C. Greenham, *Adv. Mater.*, 2009, **21**, 3840
- [68] C. Goh, S. R. Scully, and M. D. McGehee, *J. Appl. Phys.*, 2007, **101**, 114503
- [69] D. M. Adams, J. Kerimo, E. J. C. Olson, A. Zaban, B. A. Gregg, and P. F. Barbara, *J. Am. Chem. Soc.* 1997, **119**, 10608
- [70] C. R. McNeill, B. Watts, S. Swaraj, H. Ade, L. Thomsen, W. Belcher and P.C. Dastoor, *Nanotechnology*, 2008, **19**, 424015
- [71] M. Nardi, R. Verucchi, R. Tubino, and S. Iannotta, *Phys. Rev. B*, 2009, **79**, 125404
- [72] M. Nardi, R. Verucchi, C. Corradi, M. Pola, M. Casarin, A. Vittadini and S. Iannotta, *Phys. Chem. Chem. Phys.*, 2010, **12**, 871
- [73] J. C. P. Grancho, M.M. Pereira, M.G. Miguel, A.M. Rocha Gonsalves and H.D. Burrows, *Photochemistry and Photobiology*, 2002, **75** (3), 251
- [74] M. Pineiro, M. M. Pereira, A. M. A. Rocha Gonsalves, L. G. Arnaut and S. J. Formosinho, *J. Photochem. Photobiol. A Chem.* 2001, **138**, 147
- [75] J. B. Kim, J. J. Leonard and F. R. Longo, *J. Am. Chem. Soc.*, 1972, **94**, 3986
- [76] P. J. Spellane, M. Gouterman, A. Antipas, S. Kim and Y. C. Liu, *Inorg. Chem.*, 1980, **19**, 386
- [77] M. Gouterman, R. J. Hall, G. E. Khalil, P. C. Martin., E. G. Shankland and R. L. Cerny, *J. Am. Chem. Soc.*, 1989, **111**, 3702
- [78] A. Sen, and V. Krishnan, *J. Chem. Soc. Faraday Trans.*, 1997, **93**, 4281
- [79] K. Walzer, T. Toccoli, A. Pallaoro, R. Verucchi, T. Fritz, A. Leo, A. Boschetti, S. Iannotta, *Surf. Sci.* 2004, **573**, 346
- [80] K. Walzer, T. Toccoli, A. Pallaoro, S. Iannotta, C. Wagner, T. Fritz, *Surf. Sci.*, 2006, **600**, 2064
- [81] S. G. DiMagno, A. K. Wertsching, and C. R. Ross, *J. Am. Chem. Soc.*, 1995, **117**, 8279
- [82] M. K. Geno, J. Halpern, *J. Am. Chem. Soc.*, 1987, **109**, 1238
- [83] A. Eschenmoser, *N.Y. Acad. Sci.*, 1986, **471**, 108
- [84] E. Gudowska-Nowak, M.D. Newton, J. Fajer, *J. Phys. Chem.*, 1990, **94**, 5795
- [85] M. Plato, K. Mobius, M.E. Michel-Beyerle, M.E. Bixon, J. Jortner, *J. Am. Chem. Soc.*, 1988, **110**, 7279
- [86] K. M. Barkigia, L. Chantranupong, K.M. Smith, J. Fajer, *J. Am. Chem. Soc.* 1988, **110**, 7566
- [87] D. Mandon, et al., *Inorg. Chem.* 1992, **31**, 2044
- [88] T. Wondimagegn and A. Ghosh, *J. Phys. Chem. A*, 2000, **104**, 4606

- [89] P. G. Gassman, A. Ghosh, and . Almlo, *J. Am. Chem. Soc.*, 1992, **114**, 9990
- [90] A. K. Perepogu, P.R. Bangal, *J. Chem. Sci.*, 2008, **120** (5), 485
- [91] A. V. Efimov, M. Anikin, N.V. Tkachenko, A.F. Mironov, H. Lemmetyinen, *Chem. Phys. Lett.*, 1998, **289**, 572
- [92] S. Prashanthi, P. H. Kumar, L. Wang, A. K. Perepogu, P. R. Bangal, *J Fluoresc.*, 2010, **20**, 571
- [93] O. Ohno, Y. Kaizu, H. Kobayashi, *J. Chem. Phys.*, 1985, **82**, 1779
- [94] G. G. Gurzadyan, T. H. Tran-Thi, and T. Gustavsson, *J. Chem. Phys.*, 1998, **108**, 385
- [95] L. Bajema, M. Gouterman, C.B. Rose, *J. Mol. Spectrosc.*, 1971, **39**, 421
- [96] A. Marcelli, P. Foggi, L. Moroni, C. Gellini, P. R. Salvi, I. J. Badovinac, *J. Phys. Chem. A*, 2007, **111**, 2276
- [97] Y. Kurabayashi, K. Kikuchi, H. Kokubun, Y. Kaizu, H. Kobayashi, *J. Phys. Chem.*, 1984, **88**, 1308
- [98] X. Li, *Appl. Surf. Sci.*, 2010, **256** (22), 6705
- [99] G. V. Belkova, S.A. Zavyalov, N.N. Glagolev, *Russ. J. Phys. Chem.*, 2010, **84** (1), 129, reported in *AIP Conf. Proc.*, 1137, pp. 349
- [100] M. C. DeRosa, R. J. Crutchley, *Coordination Chemistry Reviews* 2002, **233-234**, 351
- [101] Y. Yamamoto, N. Imai, R. Mashima, R. Konaka, M. Inoue, W. C. Dunlap, *Methods in Enzymology*, 2000, **319**, 29
- [102] Y. Liu, Y. Zhang, S. Wang, C. Pope, and W. Chen, *Appl. Phys. Lett.*, 2008, **92**, 143901
- [103] W. Chen, *Nanoparticle Based Photodynamic Therapy for Cancer Treatment*, in *Cancer Nanotechnology*, American Scientific Publishers, Los Angeles, 2007, Chap. 13, pp. 235
- [104] W. Chen and J. Zhang, *J. Nanosci. Nanotechnol.*, 2006, **6**, 1159
- [105] L. Armelao, F. Heigl, A. Jurgensen, R. I. R. Blyth, T. Regier, X. T. Zhou, and T. K. Sham, *J. Phys. Chem. C*, 2007, **111**, 10194
- [106] R.A. Rosenberg, M. Abu Haija, K. Vijayalakshmi, J. Zhou, S. Xu, and Z.L. Wang, *Appl. Phys. Lett.*, 2009, **95**, 243101
- [107] S. Kishwar, M. H. Asif, O. Nur, M. Willander, P. O. Larsson, *Nanoscale Res. Lett.*, 2010, **5**, 1669
- [108] M. Granstrom, M. Berggren, and O. Ingana, *Science*, 1995, **267**, 1479
- [109] J. Dhanabalan, K. Van Duren, P.A. van Hal, J.L.J. van Dongen, and R.A.J. Janssen, *Adv. Funct. Mater.*, 2001, **11**, 255
- [110] F. Jonas and G.D. Wolf, *U.S. Patent No. 05403467* (1995)
- [111] D. Setiadi, Z. He, J. Hajto, and T.D. Binnie, *Infrared Phys. Technol.*, 1999, **40**, 267
- [112] Y. Xu, M.A.A. Schoonen, *American Mineralogist*, **85**, 2000, 543
- [113] D. Tian, Q. Chen, F. Q. Nie, J. Xu, Y. Song, and L. Jiang, *Adv. Mater.* 2009, **21**, 3744
- [114] H. Yanagi, S. Chen, P. A. Lee, K. W. Nebesny, N. R. Armstrong, A. Fujishima, *J. Phys. Chem.* 1996, **100**, 5447
- [115] J. Hwang, F. Amy, A. Kahn, *Org. Electron.*, 2006, **7**, 387
- [116] A. Elschner *et al.*, *PEDOT*, Taylor and Francis Group, LLC, Boca Raton, 2011
- [117] A. M. Nardes, M. Kemerink, M.M. de Kok, E. Vinken, K. Maturova, and R.A.J. Janssen, *Organic Electronics*, 2008, **9**, 727

- [118] M. M. De Kok, et al., *phys. stat. sol. (a)*, 2004, **201**, 1342
- [119] J. Liu, S. W., Z. Bian, M. Shan, and C. Huangb, *Appl. Phys. Lett.*, 2009, **94**, 173107
- [120] C. H. Hsieh, Y.J. Cheng, P.J. Li, C.H. Chen, M. Dubosc, R.M. Liang, C.S. Hsu, *J. Am. Chem. Soc.* 2010, **132**, 4887
- [121] W. Lu, C. Wang, W. Yue and L. Chen, *Nanoscale*, 2011, **3**, 3631
- [122] L. Heng, D. Tian, L. Chen, J. Su, J. Zhai, D. Han and L. Jiang, *Chem. Commun.*, 2010, **46**, 1162
- [123] M. Bouvet, *Anal Bioanal Chem.*, 2006, **384**, 366
- [124] F. Siviero, N. Coppedè, A.M. Taurino, T. Toccoli, P. Siciliano, S. Iannotta, *Sensors and Actuators B*, 2008, **130**, 405
- [125] D. Tian, Q. Chen, F. Q. Nie, J. Xu, Y. Song, and L. Jiang, *Adv. Mater.*, 2009, **21**, 3744
- [126] P. Palmgren, T. Claesson, A. Önstena, B. Agnarsson, M. Månsson, O. Tjernberga, M. Göthelida, *Surface Science*, 2007, **601** (18), 4222



# 5 Conclusions and future work

---

**Prediction is difficult, especially the future.**

**Niels Bohr**

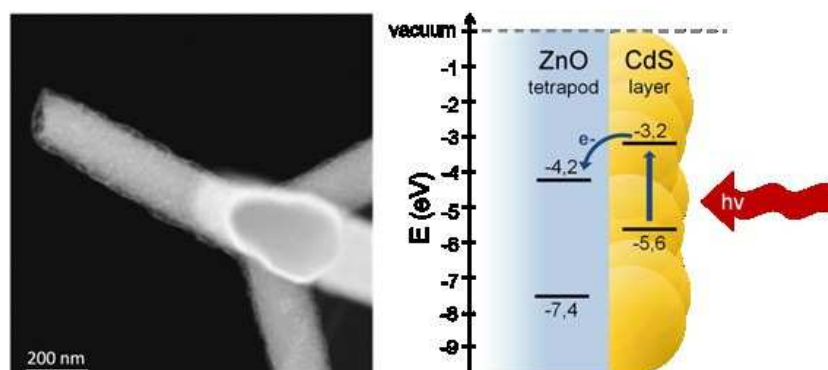
This Thesis has been devoted to the functionalization and characterization of ZnO nanostructures, tetrapods and nanorods in particular. The work took profit from the experience of the research group in the synthesis of different ZnO nanocrystals and their exploitation as gas sensors [1–3], but as of 2009 the functionalization was still unexplored.

Three classes of materials have been chosen to tailor the properties of the ZnO nanostructures: cadmium sulphide as inorganic semiconductor, phthalocyanines and porphyrins as organic semiconductors and magnetite because of its magnetic properties. Although the aforementioned materials are very different, the functionalized nanostructures have been shown to possess interesting properties in common applicative fields, such as light absorption and conversion (*e.g.* photovoltaic, photocatalysis) and gas sensing. Herein conclusions and future perspectives are reported, according to the functionalizing material.

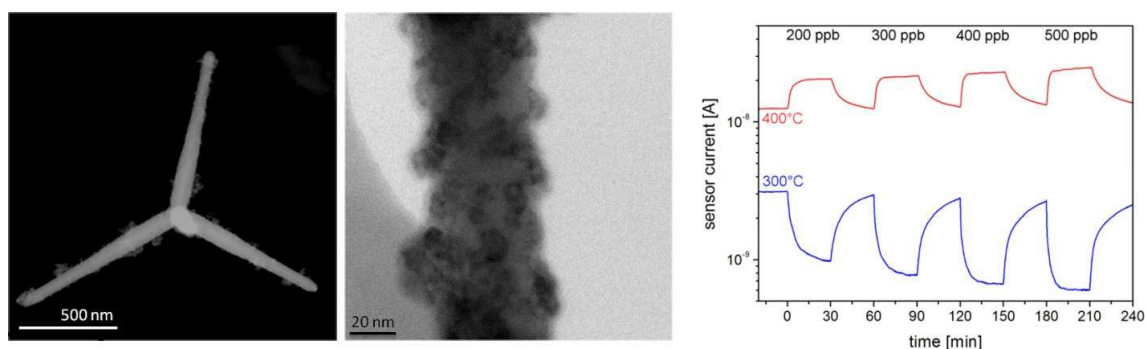
## 5.1 Cadmium sulphide

ZnO tetrapods functionalization has been performed through an optimized chemical bath deposition process [4] which allows an accurate control of the CdS morphology and thickness. Simply varying synthetic parameters (precursors concentrations and temperature) the CdS coverage has been tailored, ranging from small NP decorating ZnO TP (spot-like coverage), to a thin and uniform CdS layer (10 nm) surrounding the ZnO TP (core-shell). It is worth noting that such heterostructures have been synthesized without the need of any surfactant / ligands in order to provide a *clean* interface between CdS and ZnO and hence improve charge transfer across the heterojunction. The CdS functionalization allows to extend the ZnO TP light absorption into the visible range, and the formation of a type-II heterojunction promotes exciton dissociation at the interface and electron transfer from CdS to the ZnO conduction band. Thus the composite material can be employed as photoanode in photovoltaic devices or photo electro-chemical cells, as well as in photocatalytic systems. Our investigations show that the typical CdS luminescence is quenched in the coupled nanostructure and a superior photocatalytic activity is measured with respect to both CdS and ZnO. The type-II heterojunction reduces the electron-hole recombination inside the CdS

and extends hole lifetime, that explains a 15x enhancement in the CdS–ZnO photocatalytic activity with respect to mere CdS nanoparticles (ZnO activity is even lower).



On the other hand, spot–decorated CdS–ZnO nanostructures have been tested in gas sensing applications. Interesting properties arise from the functionalization and an inversion of the chemoresistive response is observed. This peculiar feature is highly desired to overcome the typical lack of selectivity of MOX sensors, so that the proposed nanostructure can be used to distinguish selectively NO<sub>2</sub> among different interfering gases. Finally, the large yield of ZnO TP (multi–gram scale), together with the possibility to tailor the CdS coverage (and hence material properties) in a single–step synthesis, paves the way to possible large–scale integration.



Finally an example of CdS functionalization of ZnO NR has been reported. A modified SILAR technique was chosen to deposit a thin layer of CdS on ZnO NR. The CdS coverage is still not optimized since a core–shell structure has not been achieved yet. A spot–like deposition is observed indeed, but CdS dimensional control is satisfying anyway. Grains size is in the order of a few nanometers (< 10 nm), while aggregates don't exceed 20 nm. Such small dimensions are required to assure an efficient exciton diffusion through CdS grains to ZnO NR. As future perspective, further studies will focus on the creation of a core–shell heterojunction. This geometry is highly desirable for future use in ETA solar cells since it maximizes the visible light collection and reduces the recombination probability between ZnO NR and the chosen hole transporting

material. In addition, core–shell nanostructure of CdS and ZnO have been recently investigated [5–7] as active element for photo–induced water splitting: results are encouraging since an enhancement between 14 and 40 times in hydrogen evolution is observed, compared to the sole CdS and ZnO under the same simulated solar light irradiation [7].

## 5.2 Iron Oxides

Small superparamagnetic magnetite nanoparticles, with mean dimensions up to 10 nm, have been synthesized in both aqueous solution (*via* hydrolysis of Fe(II) precursor and co–precipitation of Fe(II) and Fe(III) salts) and organic solvents (thermal decomposition *via* hot–injection and heating–up methods). All the prepared nanoparticles have good magnetic properties: *i.e.* superparamagnetic behavior with saturation magnetizations above  $50 \text{ A m}^2 \text{ Kg}^{-1}$ . These nanoparticles have been used as *building blocks* for the functionalization of ZnO tetrapods: this results in the creation of a coupled material which still possess all ZnO own attractive features, *e.g.* surface reactivity, strong UV–emission, piezoelectricity etc., together with *added* magnetism. The magnetic response of the coupled compound is ferromagnetic but, considering the very small remanence ( $M_R$ ), the  $\text{Fe}_3\text{O}_4$ –ZnO coupled nanostructures, dispersed in a liquid, don't aggregate because of magnetic dipolar interactions. This paves the way for future use in photocatalytic systems, as well as biomedical applications. Herein the results, perspectives and the open issues are reported, according to the specific synthetic approach.

### Synthesis in aqueous solution

Different capping agents (citric acid, PEG, PVP) were used in order to investigate the possible influence on the NP shape / dimensions and the *affinity* with ZnO tetrapods surface, *i.e.* to promote chemical–driven adhesion. Slightly lower nanoparticles' mean dimensions (5.4 nm) were observed when citric acid is used (ionic surfactant), while 7.5 nm nanoparticles were synthesized using PEG–400 and PVP–10000 (steric surfactants). Despite of different mean dimensions, magnetic properties result comparable among all the prepared samples: saturation magnetization is in the range of  $50 \div 60 \text{ A m}^2 \text{ Kg}^{-1}$ , *i.e.* about 30% lower than bulk magnetite (surfactant weight is not subtracted).

Coupling the as–synthesized magnetite nanoparticles with ZnO tetrapods resulted in several drawbacks. First of all, an amorphous layer caused by the partial decomposition of the capping layer is observed on all samples: the higher the surfactant molecular weight is, the higher is the layer thickness. This feature implies major drawbacks: since almost the whole tetrapod surface is passivated by the amorphous, this prevents potential photocatalytic and gas sensing applications.

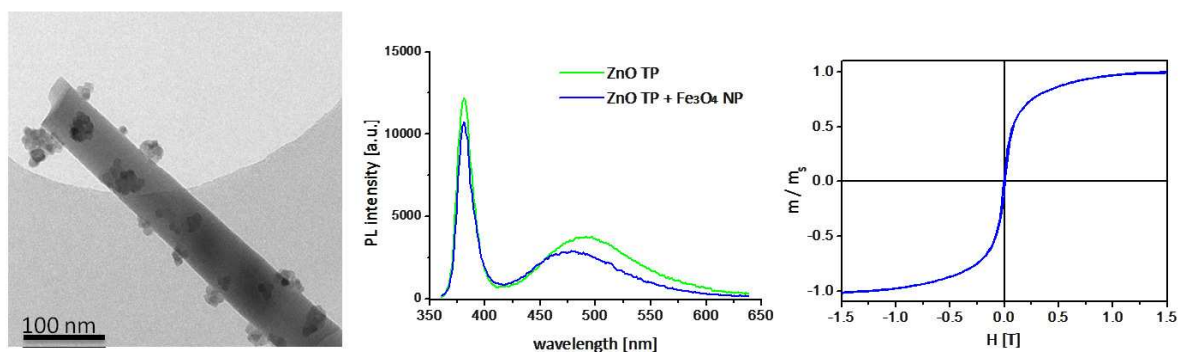
Secondly, the polar groups of the chosen surfactants didn't seem to play a significant role in the adhesion of magnetite to the ZnO surface, in fact magnetite coverage looks comparable among all samples. Finally, aggregation takes place during the heat treatment and nanoparticles coalesce / sinterize as displayed by the increase of mean particles dimensions (up to 24 nm). This results in a ferromagnetic behavior at RT: the coercive field is very low but measurable (17 mT) and the ratio  $M_R / M_S$  is about 2%.

### Synthesis in organic solvents

On the other hand, synthesis in organic solvents, using iron(III) acetylacetonate *via hot-injection*, and, *heating-up* method in particular, improved both the quality of the as-synthesized  $Fe_3O_4$  nanocrystals and the coupling with ZnO TP. The dimensional control is good, and best results have been reported using oleylamine as solvent, surfactant and (mild) reducing agent. Nanoparticles mean dimension resulted to be  $9.4 \pm 1$  nm and a hint of 2D order is observed upon free solvent evaporation, because of VdW interaction between oleylamine hydrophobic tails.

Coupling magnetite nanoparticles with ZnO tetrapods, results in a *extrinsic* magnetic nanostructure which shows a strong UV luminescence (just like ZnO TP) together with sigmoidal  $M(H)$  magnetization curve. This result is particularly attractive since the coupled nanostructure still holds ZnO own properties but can be driven, by the application of an external magnetic field, to a specific target. Moreover the large fraction of ZnO *free* surface allows further functionalizations (*e.g.* porphyrin, as described in the next section).

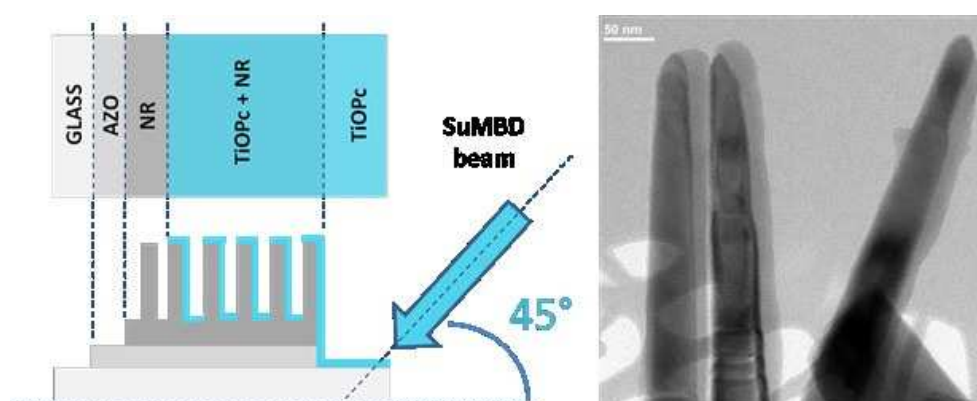
Beside of the great potential, the coupled material can be further improved. As a matter of fact, nanoparticles aggregation is still present on ZnO surface, probably because VdW interaction between oleylamine molecules. A ferromagnetic – rather than superparamagnetic – behavior is observed albeit remanence is very small ( $M_R < 0.5 \text{ A m}^2 \text{ Kg}^{-1}$ ). The bottom line is that ferromagnetism does not prevent possible applications; on the contrary, coupled nanostructures turn out particular interesting in (photo)catalytic systems and nanomedicine (upon non-toxicity verification).



Future work includes the investigation of the *extrinsic* magnetic nanostructure in energy harvesting applications: it would be particularly interesting to put a strain on the  $\text{Fe}_3\text{O}_4$ -functionalized ZnO nanostructures – induced by the application of an external magnetic field ( $\vec{H}$ ) – and consequently measure a piezo-voltage. If  $\vec{H}(x, t)$  varies in space, *i.e.*  $\text{grad}\vec{H} \neq 0$ , then  $\text{Fe}_3\text{O}_4$  nanoparticles are subject to a magnetic force. Thus, the force exerted on magnetite nanoparticles, propagates to the attached ZnO nanostructure (*e.g.* ZnO TP, or vertically aligned ZnO nanorods, grown on AZO substrate [8]) that eventually bends. This causes an accumulation of opposite charges along the ZnO (001) direction and hence a piezo-voltage can be measured (*e.g.* between AZO and ZnO NR tip). Upon verification of the aforementioned working principle, possible future applications include magnetic sensors at the nanoscale, the harvesting of disperse magnetic flux (*e.g.* in electric motors) or novel filter-free photocatalytic systems, where the catalyst is collected by the application of an external magnetic field.

### 5.3 Organics

ZnO nanorods have been sensitized using a tailor-made SuMBD apparatus. Such technique allows a highly-directional deposition of (metallo-)organic molecules and a nanometric control of the growing layer on a variety of different substrates. The selective deposition of titanyl phthalocyanine (TiOPc) on a *single* side of ZnO nanorod has been demonstrated for the first time [9]. The hybrid compound, as well as the organic molecule, have been characterized by absorption spectroscopy and photoluminescence. According to the shape profile of the Q band absorption, features reminiscent of an amorphous phase, combined with a component of phase II, are observed. The presence of a crystalline phase is particular interesting since SuMBD deposition was carried out on substrates at room temperature. STEM, HREM and EDX analyses confirm the directional deposition and photoluminescence studies reveal a quench of the TiOPc emission in the TiOPc-sensitized nanorods. This suggests that the sensitization is effective: the exciton is separated at the interface and the electron is then injected into ZnO conduction band, before recombination takes place inside the organic layer (*i.e.* a type-II hybrid heterojunction). This is crucial for future photovoltaic applications of the organic-inorganic nanostructure as a hybrid photoanode.



Moreover the directional functionalization paves the way to dual-sensitized ZnO architectures: the deposition of two different organic molecules on a single nanorod further enhances the properties of the hybrid nanostructure. A study was carried out using a free-base porphyrin (TPP) as co-absorber, together with TiOPc: unfortunately the porphyrin deposition was not successful and irregular aggregates (in excess of 100 nm) are found on ZnO nanorods surface. In this case, the exciton recombines before reaching the interface and the porphyrin stand-alone emission was observed in the hybrid-nanostructure. This feature has a negative impact on device performance, since it lowers the efficiency of a future solar cell, so that further studies are required in order to improve the TPP deposition and achieve a directional deposition, together with an accurate thickness control (as obtained for TiOPc). Finally, a preliminary study in the deposition of a hole transporting material (PEDOT) was performed and a photovoltaic effect was observed, for the nanorods-PEDOT hybrid junction.

The fabrication of the complete solar cell (ZnO – SuMBD deposited organic molecule – PEDOT) has to be considered as a work in progress activity: further studies will be performed to optimize the technological procedures and obtain the device. Despite the fact that this part of the work has been developed in the frame of a project concerning the photovoltaic application, the hybrid nanostructures – both TiOPc and TPP on ZnO nanorods – are promising building blocks in other applicative fields too, ranging from gas sensing to environmental remediation and nanomedicine. In fact, both ZnO and porphyrins are known to be excellent materials for singlet oxygen production, thus they can be employed for example in photocatalytic systems as well as in photodynamic therapy applications.

In the latter application, a very attractive composite material consists in the porphyrin-sensitization of Fe<sub>3</sub>O<sub>4</sub>-ZnO nanostructures (either in the form of tetrapods, as described in the previous chapter, or nanorods). Such functionalized material can be driven by an external magnetic field to the tumor site and locally *activated* by the use of a X-Rays source. The irradiation triggers the ZnO near band edge (UV) emission that is absorbed by the surrounding organic molecule (*e.g.* porphyrin) [10]. Consequently, excitons are created inside the organic layer and, upon interfacial dissociation, the electron-transfer promotes the formation of singlet oxygen species that, because of their high cytotoxicity, destroy the (tumoral) cells. As recently reported in literature [11], preliminary *in vitro* studies suggest that the cytotoxic activity of ZnO-porphyrin conjugates dramatically exceeds that of porphyrin alone. These results indicate that the coupled nanostructure is a good candidate for photodynamic treatment of tumoral diseases located deep inside the human body, where the photosensitizer cannot be activated by UV-VIS-NIR radiations.

## References

- [1] M. Zha, D. Calestani, A. Zappettini, R. Mosca, M. Mazzera, L. Lazzarini and L. Zanotti, *Nanotechnology*, 2008, **19**, 325603
- [2] L. Lazzarini, G. Salviati, F. Fabbri, M. Zha, D. Calestani, A. Zappettini, T. Sekiguchi and B. Dierre, *ACS Nano*, 2009, **3** (10), 3158
- [3] D. Calestani, M. Zha, R. Mosca, L. Lazzarini, G. Salviati, A. Zappettini, L. Zanotti, *Mater. Res. Soc. Symp. Proc.*, 2009, **1174**, V05-02
- [4] M. Villani, D. Calestani, L. Lazzarini, L. Zanotti, R. Mosca, A. Zappettini, *J. Mater. Chem.*, 2012, in press
- [5] Y. Tak, S. J. Hong, J. S. Lee and K. Yong, *J. Mater. Chem.*, 2009, **19**, 5945–5951
- [6] X. Wang, G. Liu, G. Q. Lu, H. M. Cheng, *international journal of hydrogen energy*, 2010, **35**, 8199 – 8205
- [7] X. Wang, G. Liu, Z. G. Chen, F. Li, L. Wang, G. Q. Lu, H. M. Cheng, *Chem. Commun.*, 2009, 3452–3454
- [8] D. Calestani, M. Z. Zha, L. Zanotti, M. Villani and A. Zappettini, *Cryst. Eng. Comm.*, 2011, **13**, 1707
- [9] N. Coppedè, D. Calestani, M. Villani, M. Nardi, L. Lazzarini, A. Zappettini, S. Iannotta, *J. Phys. Chem. C*, 2012, *submitted*
- [10] W. Chen and J. Zhang, *J. Nanosci. Nanotechnol.*, 2006, **6**, 1159
- [11] Y. Liu, Y. Zhang, S. Wang, C. Pope, and W. Chen, *Appl. Phys. Lett.*, 2008, **92**, 143901

# List of publications

---

1. “Vapour-phase growth, purification and large-area deposition of ZnO tetrapod nanostructures”  
L. Zanotti, D. Calestani, M. Villani, M. Zha, A. Zappettini, and C. Paorici  
*Cryst. Res. Technol.*, 2010, **45** (6), 667 – 671
2. “Pd/PdO functionalization of SnO<sub>2</sub> nanowires and ZnO nanotetrapods”  
C. De Zorzi, G. Rossetto, D. Calestani, M.Z. Zha, A. Zappettini, L. Lazzarini, M. Villani, N. El Habra, L. Zanotti  
*Cryst. Res. Technol.*, 2011, **46** (8), 847 – 851
3. “Low temperature thermal evaporation growth of aligned ZnO nanorods on ZnO film: a growth mechanism promoted by Zn nanoclusters on polar surfaces”  
D. Calestani, M. Z. Zha, L. Zanotti, M. Villani, A. Zappettini  
*CrystEngComm*, 2011, **13**, 1707 – 1712
4. “Aldehyde detection by ZnO tetrapod-based gas sensors”  
D. Calestani, R. Mosca, M. Zanichelli, M. Villani, A. Zappettini  
*J. Mater. Chem.*, 2011, **21**, 15532 – 15536
5. “Non-interacting hard ferromagnetic L1<sub>0</sub> FePt nanoparticles embedded in a carbon matrix”  
M. Solzi, C. Pernechele, G. Calestani, M. Villani, M. Gaboardi and A. Migliori  
*J. Mater. Chem.*, 2011, **21**, 18331 – 18338
6. “Extended functionality of ZnO nanotetrapods by solution-based coupling with CdS nanoparticles”  
M. Villani, D. Calestani, L. Lazzarini, L. Zanotti, R. Mosca, A. Zappettini  
*J. Mater. Chem.*, 2012, *In press*
7. “Solution-free and catalyst-free synthesis of ZnO-based nanostructured TCOs by PED and vapor phase growth techniques”  
D. Calestani, F. Pattini, F. Bissoli, E. Gilioli, M. Villani, A. Zappettini  
*Nanotechnology*, 2012, *accepted with minor revisions*
8. “Directionally selective sensitization of ZnO nanorods by TiOPc: a novel approach to multi functionalized nanosystems”  
N. Coppedè, D. Calestani, M. Villani, M. Nardi, L. Lazzarini, A. Zappettini, S. Iannotta  
*J. Phys. Chem. C*, 2012, *under review*



# Acknowledgements

---

**L'educazione dovrebbe infondere l'idea che l'umanità è una sola famiglia con interessi comuni, e che, di conseguenza, la collaborazione è più importante della competizione**  
Bertrand Russell

Firstly, I would like to express my sincere gratitude to all the research group for the continuous support and encouragement throughout the entire PhD. Dott. Andrea Zappettini and dott. Davide Calestani, who followed my works, are not only mentors but also friends. Prof. Mingzheng Zha, for his courtesy, for giving me invaluable advices, and raising thoughtful questions. Dott. Lucio Zanotti for introducing me to the chemistry laboratory and sharing the research on CdS during the early period of my PhD. Old time friends and now colleagues, dott. Laura Marchini, Nicola Zambelli and Giacomo Benassi, although involved in different scientific topics, for discussing with me encountered problems and giving me unstinting support. Also, I wish to thank dott. Tiziano Rimoldi, who attended his Master Degree training at IMEM and worked together with me in the functionalization of zinc oxide tetrapods with magnetic nanoparticles.

My thanks are also due to all the colleagues who shared part of my work: dott. Nicola Coppedè for the deposition of organic molecules, prof. Gianluca Calestani and dott. Francesco Mezzadri for their help in XRD and their friendship. Dott. Laura Lazzarini and dott. Filippo Fabbri for TEM and FE-SEM analysis. Dott. Francesca Casoli and Valentina Chiesi for magnetic measurements, dott. Paolo Ranzieri for AFM, dott. Roberto Mosca for gas sensors. Last but not least, prof. Anna Painelli and dott. Cristina Sissa for their kind support and constructive advices.

## Un grazie a tutti voi

Sono fermamente convinto che la conoscenza sia un *fatto collettivo*: per dirla come Bernardo di Chartres, siamo nani sulle spalle dei giganti. Per questo vorrei ringraziarvi, in ordine sparso, nella prossima pagina. Voi, che direttamente o vostro malgrado, avete ispirato il mio lavoro, i miei pensieri e, in qualche caso, la mia vita.

Marco

ettor il potlatch galizio il processo barthes la collina del meccanico la madonna di niklashausen rosa luxemburg syd barrett i gelsi mori gli amici cariati this is the greatest place on earth le partite di calcetto nel parcheggio della coop grande incendio un posto per appendere il cappello la pressione bassa il consorzio suonatori indipendenti sensibili alle foglie la mano negrale nubi basse impigliate negli abeti martin heidegger i campi di vicopò vasilij kandinskij apocalypse now jacques derrida giuseppe ungaretti greta e venezia i muri dipinti santa maradona les claypool il 20w marshall la donna di nicolaus roland barthes il livello 57 l'argine di gualtieri i won't go die politely i tramonti muti che si ha pudore di guardare david yow il sogno della merce david cronenberg arnold schönberg il centro giovani mark vladimir majakovskij konna yume wo mita ludwig wittgenstein paolo il ultimo capodanno the guns of brixton fedecostretti a sanguinare il freddo sulle panchine quella rotonda sul mare le notti profonde millenni tanze für euren untergang silence is a dangerous sound mezzanine gary picciotto gli operai del turno del tifo delle 22 alla bormiola in girum imus nocte et consumimur igni sbatti il mostro in prima pagina friedrich nietzsche la pietra di bismantova i pomeriggi di aprile le piante grasse e i pericoli grigi ottusi e pericolosi snoopy yana the day i tried to live the subtle difference between terrorism and inside job la classe operaia va in paradiso pi greco gi rospi nei laghi di montagna allen ginsberg il finnegan's wake ulan bator le upeuctella aspergillum wu ming borgho guazzo making the nature scene sgabruz dedications of symmetry the ex lorenzo il campo da basket in cittadella il 77 quell'emozione sempre più indefinibile carlotta il tempo che scorre lungo i bordi brillare come le mine o le stelle polari sisifo il mezzo di persone che vivono con meno di due dollari al giorno kurt cobain i due mila di györgy ligeti di punk islam la videoteca comunale lovecraft i diritrambi di dioniso la lotta armata al bar iena le ombre stranche berrand russell antonin artaud the waste land cassavetes le ms morbide il inoleum la comune salomé il portatile acer ross e tamboro hans böhm chapel hill le moltitudini le dolomiti del brenta giacomo leopardi chiara e bulgakov full disclosure il kebab di said il circolo di vienna don andrea gallo il divano arancione a fiori l'estetica del novecento i sistemi assommati vita mia a noi due l'avvelenata monica gottlob frege william blake la scala mobile june of 44 ostkreuz barcellona wim mertens alfred jarry a/traverso ideofalce jim morrison joe strummer kari mullins hannarella i precari simona le sinestesia celeste l'autonomia la decrescita o e tancredi albert canus vik artigiani john coltrane ritual de lo habitual la frittata con le cipolle l'odore del pino mugo la cabina telefonica fuori dal cartaino wlr haben wahrheiten fuer dich aufgestellt bruno detassis le sorgenti i labirinti sfioriti del señor matanza palpebrabella i rumori di fondo le nubi a cozzano born annoying john zorn tramonti a torrechiara ai figli degli operai i mercatini nouvelle vague il class walfare darren aronofsky l'ex macello l'equo canone l'odore della terra ulriche meinhof il naso di fausto eddie vedder antonio moresco arthur rimbaud abraham lincoln todo modo jorge luis borges stefano benni kurt gödel il battistero stefano benni kurt gödel tiffano rivolta a salto al cielo giorgio gaber la paletta scheggiata pier paolo pasolini modern money theory prove tecniche di resurrezione daniilo l'emozione plumbea del risveglio cantano notturno di un pastore errante dell'asia eri de luca il parto provinciale returning the screw luigi deleuze la casa dalle finestre che ridono la memoria del ventesimo secolo il mio primo dopoguerra giannaria es chi è stato e chi stato non è repeater ex spectator gill il conflitto nell'epoca della simulazione the love song of alfred prufrock giulia un'irata sensazione di peggioramento was bleibt ist nikonin und gelbe finger zven solidaritay no satelliti could map our veins i miei genitori le case occupate al praterello i chilometri con il walkman nelle orecchie giangiaco feltrinelli i giorni come stanze ost berlin il campo della chiesa le stelle alpine prodotti consuma crepa der gegenstand i coca e rum che sa di benzina ruby soho giovannotto documenti harry bridges virus 15 spigni quella cazzo di tv i turni di notte da greci il gorgo my generation i sogni e i bisogni noam chomsky la montagna sacra douglas hofstadter paola il box degli attrezzi l'acqua che sa di cloro barbara il centro di chopin a tratti moose mordekai levy moses mordekai levy douglas hofstadter paola il box degli attrezzi l'acqua che sa di cloro barbara i grundrisse i contadini della jacquerie sofia eri de luca ubu roi una questione di qualità sonica mario monicelli erica san petronia lori meyers pachyulus communis thomas ethel l'odore dei pomeriggi quando li butti via le due marmotte jail guitar doors le mani sulla città l'atomismo logico le lettere del monumento international labor defense le nottate di donato creti jim hendrix le occupazioni cecilia e il battistero jim morrison joe strummer kari mullins hannarella i precari simona le sinestesia celeste l'autonomia la decrescita o e tancredi albert canus vik artigiani john coltrane ritual de lo habitual la frittata con le cipolle l'odore del pino mugo la cabina telefonica fuori dal cartaino wlr haben wahrheiten fuer dich aufgestellt bruno detassis le sorgenti i labirinti sfioriti del señor matanza palpebrabella i rumori di fondo le nubi a cozzano born annoying john zorn tramonti a torrechiara ai figli degli operai i mercatini nouvelle vague il class walfare darren aronofsky l'ex macello l'equo canone l'odore della terra ulriche meinhof il naso di fausto eddie vedder antonio moresco arthur rimbaud abraham lincoln todo modo jorge luis borges stefano benni kurt gödel il battistero stefano benni kurt gödel tiffano rivolta a salto al cielo giorgio gaber la paletta scheggiata pier paolo pasolini modern money theory prove tecniche di resurrezione daniilo l'emozione plumbea del risveglio cantano notturno di un pastore errante dell'asia eri de luca il parto provinciale returning the screw luigi deleuze la casa dalle finestre che ridono la memoria del ventesimo secolo il mio primo dopoguerra giannaria es chi è stato e chi stato non è repeater ex spectator gill il conflitto nell'epoca della simulazione the love song of alfred prufrock giulia un'irata sensazione di peggioramento was bleibt ist nikonin und gelbe finger zven solidaritay no satelliti could map our veins i miei genitori le case occupate al praterello i chilometri con il walkman nelle orecchie giangiaco feltrinelli i giorni come stanze ost berlin il campo della chiesa le stelle alpine prodotti consuma crepa der gegenstand i coca e rum che sa di benzina ruby soho giovannotto documenti harry bridges virus 15 spigni quella cazzo di tv i turni di notte da greci il gorgo my generation i sogni e i bisogni noam chomsky la montagna sacra douglas hofstadter paola il box degli attrezzi l'acqua che sa di cloro barbara i grundrisse i contadini della jacquerie sofia eri de luca ubu roi una questione di qualità sonica mario monicelli erica san petronia lori meyers pachyulus communis thomas ethel l'odore dei pomeriggi quando li butti via le due marmotte